



**HAL**  
open science

# Fractionalization of pair density waves in cuprate superconductors

Maxence Grandadam

► **To cite this version:**

Maxence Grandadam. Fractionalization of pair density waves in cuprate superconductors. Superconductivity [cond-mat.supr-con]. Université Paris-Saclay, 2021. English. NNT : 2021UPASP116 . tel-03561415

**HAL Id: tel-03561415**

**<https://theses.hal.science/tel-03561415v1>**

Submitted on 8 Feb 2022

**HAL** is a multi-disciplinary open access archive for the deposit and dissemination of scientific research documents, whether they are published or not. The documents may come from teaching and research institutions in France or abroad, or from public or private research centers.

L'archive ouverte pluridisciplinaire **HAL**, est destinée au dépôt et à la diffusion de documents scientifiques de niveau recherche, publiés ou non, émanant des établissements d'enseignement et de recherche français ou étrangers, des laboratoires publics ou privés.

Fractionalization of Pair Density  
Waves in cuprate superconductors  
*Fractionnalisation d'une Onde de Densité de  
Paires dans les cuprates supraconducteurs*

Thèse de doctorat de l'université Paris-Saclay

École Doctorale n° 564, Physique en Île-de-France (PIF)

Spécialité de doctorat: Physique

Unité de recherche: Université Paris-Saclay, CNRS, CEA, Institut de physique théorique,  
91191, Gif-sur-Yvette, France

Référent: Faculté des sciences d'Orsay

Thèse présentée et soutenue à Gif-sur-Yvette, le 08 Novembre 2021, par

**Maxence GRANDADAM**

**Composition du jury**

<b>J. C. Séamus DAVIS</b> Professeur, University of Oxford	Président
<b>Sebastien BURDIN</b> Chargé de Recherche, Laboratoire Ondes et Matière d'Aquitaine, HDR	Rapporteur & Examineur
<b>Frank KRUGER</b> Professeur associé, University College London, HDR	Rapporteur & Examineur

**Direction de la thèse**

<b>Catherine PÉPIN</b> Directrice de Recherche, CEA-Saclay	Directrice de thèse
---	---------------------

**Titre: Fractionnalisation d'une onde de Densité de Paires dans les cuprates supraconducteurs**

**Mots clés :** supraconductivité, cuprates supraconducteurs, systèmes fortement corrélés

**Résumé:** Les cuprates supraconducteurs désignent une classe de matériaux qui ont attiré beaucoup d'attention lorsqu'il a été découvert qu'ils devenaient supraconducteurs à une température supérieure à celle de l'azote liquide. Depuis lors, une quantité importante de travaux, théoriques et expérimentaux, ayant pour but de comprendre le diagramme de phase de ces matériaux ont été conduits. Cependant, il n'y a aujourd'hui toujours pas de consensus sur la nature de la phase de laquelle la supraconductivité émerge, appelée pseudogap. Cette phase n'est pas décrite par la théorie des liquides de Fermi et présente de multiples autres instabilités électroniques en compétition qui sont difficiles à réconcilier dans un seul cadre théorique.

Dans cette thèse, je présente une nouvelle idée pour décrire le pseudogap et la phase supracon-

ductrice associée en utilisant le principe de la fractionnalisation. L'observation récente d'Onde de Densité de Paires, c'est-à-dire de paires électron-électron modulées dans l'espace, nous apprend que la symétrie par translation est, elle aussi, brisée dans le pseudogap. Notre idée est donc que ces Ondes de Densité de Paires sont fractionnalisées en paires électron-électron uniformes, qui sont à l'origine de l'état supraconducteur, et en paires électron-trou modulées qui sont responsables de la brisure de la symétrie par translation. Cette fractionnalisation a de nombreuses conséquences sur les propriétés électroniques qui correspondent aux observations expérimentales faites dans le pseudogap. La présence de ces paires électron-électron présentant une modulation spatiale peut aussi expliquer certains résultats inhabituels sur le transport électrique dans le régime sur-dopé.

**Title:** Fractionalization of Pair Density Waves in cuprate superconductors

**Keywords:** superconductivity, cuprates superconductors, strongly-correlated systems

**Abstract:** Cuprates are materials that have attracted a lot of attention when it was discovered that they become superconducting at temperatures above the boiling point of nitrogen. Since then, a large amount of experimental and theoretical works have been devoted to the understanding of the phase diagram of these materials. One of the main controversial point is the nature of the state from which superconductivity emerges, the pseudogap. Indeed, it defies the Fermi liquid theory for metals and presents a series of competing electronic instabilities that are difficult to disentangle.

In this thesis, I present a new idea to describe the pseudogap phase and the superconducting transition within the framework of fractionalization. The recent observation of Pair Density Wave, *i.e.* modulated particle-particle pairs, on

top of the usual Cooper pairing from conventional superconductivity shows that translation symmetry and pairing are both important to the physics of cuprates. Our idea is based on the fact that this Pair Density Wave is difficult to stabilize, due to multiple reasons such as disorder, and that the system will thus break it down into uniform particle-particle pairs that will condense in the superconducting state and modulated particle-hole pairs that will break the translation symmetry. This fractionalization has strong consequences on the electronic and phononic degrees of freedom that we show matches the puzzling experimental observations in the pseudogap phase. The idea that modulated particle-particle pairs can contribute to the electrical transport outside the pseudogap phase is also explored to explain the anomalous "strange metal" phase above the optimal doping.

Universit  Paris-Saclay

Espace Technologique / B timent Discovery

Route de l'Orme aux Merisiers - RD 128 / 91190 Saint-Aubin, France







# Contents

<b>Synthèse</b>	<b>9</b>
<b>Introduction</b>	<b>15</b>
<b>1 Cuprate superconductors</b>	<b>17</b>
1.1 Unconventional and high-temperatures superconductors . . . . .	17
1.1.1 Bardeen, Cooper, Schrieffer and Onnes . . . . .	17
1.1.2 Non-BCS superconductors . . . . .	18
1.1.3 Anatomy of cuprates . . . . .	20
1.2 Phase diagram and competing orders . . . . .	21
1.2.1 Doping a Mott insulator . . . . .	21
1.2.2 The superconducting state . . . . .	23
1.2.3 Charge Density Wave . . . . .	25
1.3 The Pseudogap . . . . .	28
1.3.1 Electronic properties . . . . .	28
1.3.2 Discrete symmetries and fluctuations . . . . .	30
1.3.3 Pair Density Waves . . . . .	31
1.4 Theoretical Description . . . . .	33
1.4.1 Resonating valence bond and fractionalization . . . . .	33
1.4.2 Numerical developments . . . . .	34
1.4.3 Intertwined orders and Quantum disordered PDW . . . . .	35

<b>2</b>	<b>Theoretical tools</b>	<b>37</b>
2.1	Basic notions . . . . .	37
2.1.1	Second quantization . . . . .	37
2.1.2	Green's functions . . . . .	38
2.1.3	Path-integral formalism . . . . .	39
2.2	Non-interacting systems . . . . .	41
2.2.1	Tight-binding models . . . . .	41
2.3	Interacting systems . . . . .	43
2.3.1	Perturbation expansion . . . . .	43
2.3.2	Mean-field decoupling and BCS theory . . . . .	47
2.4	Fractionalization . . . . .	52
2.4.1	From Hubbard to $t - J$ model . . . . .	52
2.4.2	Gauge theory in cuprates . . . . .	54
<b>3</b>	<b>Fractionalized Pair Density Wave</b>	<b>59</b>
3.1	Effective theories for the pseudogap . . . . .	59
3.1.1	Exact and emergent $SU(2)$ symmetry . . . . .	59
3.1.2	Fractionalization ansatz . . . . .	64
3.1.3	Phenomenological consequences . . . . .	66
3.2	Electronic spectral function in the pseudogap . . . . .	69
3.2.1	Evidence for modulated order . . . . .	69
3.2.2	Microscopic $t-J-V$ model . . . . .	71
3.2.3	Phase and amplitude fluctuations . . . . .	76
3.3	Pole structure of the electronic self-energy . . . . .	80
3.3.1	Electronic spectral function from CDMFT . . . . .	80
3.3.2	Hidden-fermion model . . . . .	82
3.3.3	Study of the pseudogap phase . . . . .	85
3.4	Anomalous phonon softening . . . . .	89

<i>CONTENTS</i>	7
3.4.1 Kohn anomaly . . . . .	89
3.4.2 Phonon renormalization . . . . .	90
3.4.3 Effect of fluctuations . . . . .	93
<b>4 Transport from incoherent bosons</b>	<b>99</b>
4.1 Strange metals . . . . .	99
4.2 Incoherent bosons coupled to fermions . . . . .	102
4.2.1 Effects of fermionic self-energy . . . . .	105
4.2.2 On the fermion-boson vertex corrections . . . . .	107
4.2.3 Boson-boson interactions . . . . .	107
4.3 Transport from incoherent bosons . . . . .	111
4.3.1 Kubo formula . . . . .	112
4.3.2 Static Conductivity – The regimes . . . . .	114
4.4 Effect of magnetic field . . . . .	116
4.4.1 Hall conductivity . . . . .	116
4.4.2 Polarization bubble due to the Zeeman field . . . . .	117
4.4.3 Magnetoresistance . . . . .	119
<b>5 Stacking fault in multi-layer graphene</b>	<b>123</b>
5.1 Lattice effects in the honeycomb lattice . . . . .	123
5.1.1 Edge states with zigzag termination . . . . .	123
5.1.2 Surface state in ABC graphene . . . . .	124
5.2 Stacking fault in multi-layer graphene . . . . .	126
5.2.1 Ribbons with zigzag edges and interfaces . . . . .	127
5.2.2 Ribbons with armchair edges and interfaces . . . . .	130
5.2.3 Finite-size configuration . . . . .	132
<b>Conclusion</b>	<b>135</b>

**Appendices**

<b>A The <math>U(1) \times U(1)</math> theory</b>	<b>137</b>
<b>B CDW gap equation</b>	<b>139</b>
<b>C Boson-Fermion vertex corrections</b>	<b>141</b>
<b>D Fate of bosonic vertex corrections</b>	<b>143</b>

# Synthèse

Les cuprates supraconducteurs ont pris une place centrale dans le milieu de la matière condensée depuis leur découverte en 1986. L'intérêt pour ces matériaux vient de la température à laquelle ils deviennent supraconducteurs avec par exemple le composé YBCO qui fut le premier avec une température de transition au-dessus de la température d'ébullition de l'azote liquide avec  $T_c = 90\text{ K}$ . C'est une avancée majeure pour les potentiels applications puisque le coût pour la réfrigération avec de l'azote liquide est bien inférieur à celui nécessitant de l'hélium liquide. De nos jours, le supraconducteur avec la plus haute température critique à pression ambiante est un cuprate,  $\text{HgBa}_2\text{Ca}_2\text{Cu}_3\text{O}_{8+x}$ , avec  $T_c = 133\text{ K}$ .

Malgré les efforts concentrés sur ces matériaux, il n'y a aujourd'hui toujours pas de consensus sur la raison pour laquelle la température critique pour la transition supraconductrice dans les cuprates est si élevée. De nombreux résultats montrent que la théorie BCS n'est pas applicable pour décrire ces matériaux. Une des raisons qui illustre le changement de paradigme nécessaire est le fait que BCS décrit le phénomène de supraconductivité dans les métaux alors que les cuprates sont, dans leur état naturel, des isolants. Il est en effet nécessaire de changer la densité électronique de celle donnée par la composition chimique originale afin d'obtenir un état supraconducteur. La densité électronique est donc, avec la température, une variable importante pour étudier la physique responsable de la supraconductivité dans les cuprates. Ceci est généralement représenté par le diagramme de phase dopage-température dont un exemple est donné à la Fig.1.

Un élément important de ce diagramme de phase est le nombre d'anomalies, associées aux brisures de diverses symétries discrètes et continues, qui sont observées en plus de la transition supraconductrice. En particulier, de nombreuses symétries discrètes telles que l'inversion par renversement du temps ou la parité sont brisées à une même température qui est supérieure à la température critique. En dessous de cette température, le système n'est pas un isolant, du fait du dopage, mais ne correspond pas non plus à un métal conventionnel. Cette partie du diagramme de phase est désignée comme le "pseudogap" et la compréhension de la nature et de l'origine de ce dernier est une étape essentielle pour pouvoir comprendre la phase supraconductrice qui émerge à plus basse température. On peut également noter la présence dans le diagramme de phase d'une région où la symétrie par translation du réseau cristallin est brisée due à la présence d'ondes de densité de charge ("CDW"). Cette phase ne forme pas d'ordre à longue portée, contrairement aux ordres antiferromagnétique ou supraconducteur, mais dont la présence est récurrente pour toutes les familles de cuprates. C'est l'interaction entre ces différentes phases ordonnées et leurs fluctuations associées qui rend la description du pseudogap si compliquée. Dans cette thèse, je présente une nouvelle idée, qui s'appuie sur les observations expérimentales d'interaction entre l'ordre supra-

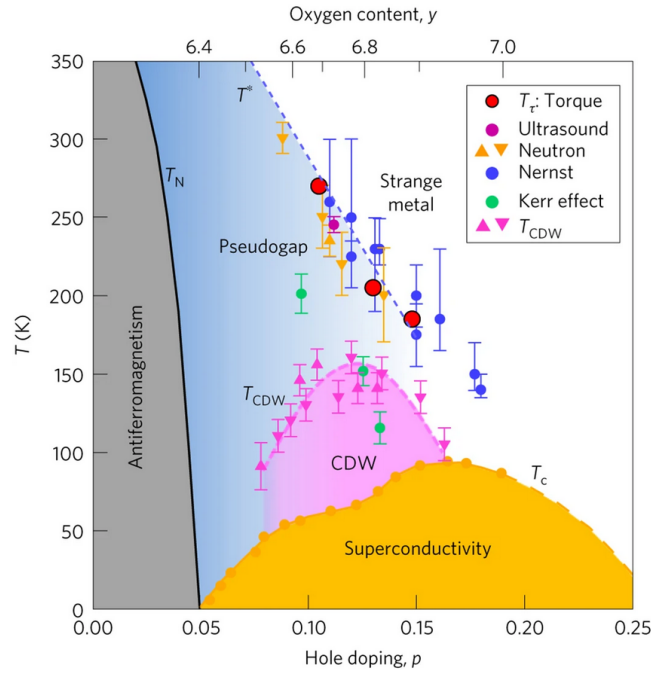


**Figure 1:** Diagramme de phase dopage-température pour le cuprate  $\text{YBa}_2\text{Cu}_3\text{O}_y$  issu de Ref.[32] Les transition vers les états antiferromagnétique et supraconducteur sont bien définis alors que la température associée à l'apparition du pseudogap est plus difficile à mesurer exactement. Cette dernière est cependant détectée par de nombreuses techniques expérimentales différentes comme indiqué dans la légende.

conducteur et les ondes de densité de charge, afin de former une phase avec des caractéristiques similaires au pseudogap observé dans les cuprates. Pour cela, je m'appuie sur un formalisme de théorie de jauge et de champ moyen pour étudier les conséquences de la fractionnalisation d'une onde de densité de paires sur les propriétés électroniques.

Afin de proposer une description des cuprates pertinente, il est important de comprendre les relations entre les trois acteurs principaux que sont le pseudogap, les ondes de densité de charge et la supraconductivité. Une des sondes principales pour cela est la spectroscopie Raman qui permet d'obtenir des informations concernant les excitations collectives des matériaux avec une sélectivité dans la première zone de Brillouin. Cette méthode a en effet été appliquée pour étudier de nombreux composés dans une large gamme de dopage et de température.

Premièrement, il est observé que le rapport entre le gap supraconducteur mesuré et la température critique est bien différent de celui attendu dans le cadre de la théorie BCS. Cela met en avant le caractère non-conventionnel de l'état supraconducteur dans ces matériaux. Plus de précision peuvent être obtenues en distinguant que le gap situé dans la zone nodale est effectivement proportionnel à la température critique mais qu'il y a également une partie du gap, situé dans la zone anti-nodale, qui a une toute autre variation avec le dopage. Le gap anti-nodale est en effet proportionnel à la température à laquelle le pseudogap est observé, indiquant que ces deux phénomènes coexistent toujours même à plus basse température. Enfin, de récentes expériences de spectroscopie Raman ont aussi montré que l'énergie associée aux ondes de densité de charge est très proche de celle associée à la supraconductivité. Considérant que les ondes de densité ne forment pas d'ordre à longue portée cela est une surprise.

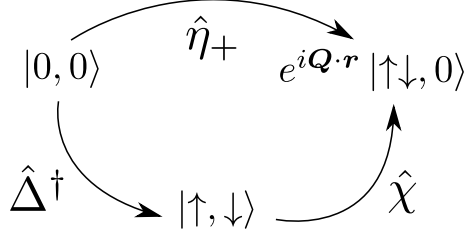


**Figure 2:** Représentation schématique de la relation entre les opérateurs pour l'onde de densité de paires ( $\hat{\eta}$ ), l'onde de densité de charge ( $\hat{\chi}$ ) et la supraconductivité ( $\hat{\Delta}$ ). L'onde de densité de paires brise simultanément la conservation de la charge et la symétrie par translation en créant une paire d'électrons avec une modulation donnée par le vecteur d'onde  $\mathbf{Q}$ . En comparaison, la supraconductivité crée des paires d'électrons de manière uniforme et l'onde de densité de charge brise la symétrie par translation avec une modulation donnée par  $\mathbf{Q}$  sans changer le nombre de charge. Combiner ces deux opérateurs peut alors reconstituer l'effet d'une onde de densité de paires.

Aux vues des observations expérimentales présentées précédemment, je propose dans cette thèse une nouvelle description du pseudogap comme un état obtenu après la fractionnalisation d'un paramètre d'ordre. Les éléments constituant cet état original sont ensuite responsable pour la formation des phases d'ondes de densité de charge et supraconductrice à plus basse température. Le paramètre d'ordre qui permet de briser en même temps la symétrie par translation et la conservation de la charge n'est autre qu'une onde de densité de paires, récemment observée par spectroscopie à effet tunnel dans les cuprates. La relation entre les paramètres d'ordres pour la supraconductivité et les ondes de densité de charge ou de paires est représentée schématiquement dans la Fig.2. La fractionnalisation de l'onde de densité de paires se présente sous la forme

$$\hat{\eta} = [\hat{\Delta}_{ij}, \hat{\chi}_{ij}^\dagger], \quad \hat{\eta}^\dagger = [\hat{\chi}_{ij}, \hat{\Delta}_{ij}^\dagger], \quad (1)$$

où  $\hat{\eta}$ ,  $\hat{\chi}$  et  $\hat{\Delta}$  représentent respectivement les opérateurs pour des ondes de densité de paires, charge et la supraconductivité. Une conséquence de la fractionnalisation est l'introduction d'un degré de liberté de phase additionnel que l'on peut noter si l'on performe simultanément les transformations suivante

$$\hat{\Delta}_{ij} \rightarrow e^{i\theta} \hat{\Delta}_{ij}, \quad \hat{\chi}_{ij} \rightarrow e^{i\theta} \hat{\chi}_{ij}, \quad (2)$$

qui laissent  $\hat{\eta}$  invariant. Cette phase est alors associée à un choix de jauge qui contraint l'amplitude des différents paramètres d'ordre

$$\hat{\Delta}_{ij}^\dagger \hat{\Delta}_{ij} + \hat{\chi}_{ij}^\dagger \hat{\chi}_{ij} = 1. \quad (3)$$

La théorie effective associée aux deux degrés de liberté complexes ( $\hat{\Delta}$  et  $\hat{\chi}$ ) liés par la contrainte Eq.(3) est un modèle chiral donné par

$$S = \int d^d x \frac{1}{2} \sum_{a,b=1}^2 |\omega_{ab}|^2, \quad (4)$$

avec

$$\omega_{ab} = z_a^* \partial_\mu z_b - z_b \partial_\mu z_a^*, \quad (5)$$



où l'on identifie  $z_1 = \Delta_{ij}$ ,  $z_2 = \chi_{ij}$ . Le diagramme de phase résultant de ce modèle chirale comprend deux températures auxquelles  $\chi$  et  $\Delta$  obtiennent une amplitude moyenne non-nulle et une transition de phase lorsque la phase des paramètres d'ordre acquiert une valeur moyenne fixée, identifiée comme la transition supraconductrice.

Il est aussi possible d'étudier les conséquences de cette fractionnalisation sur les propriétés électroniques du système via une théorie de champ moyen. Pour cela on commence avec un modèle contenant une interaction spin-spin et densité-densité donné par

$$H = \sum_{\mathbf{k}} \epsilon_{\mathbf{k}} c_{\mathbf{k}\sigma}^\dagger c_{\mathbf{k}\sigma} + \sum_{\mathbf{k}, \mathbf{k}', \mathbf{q}} \sum_{\alpha, \mu} \left( V_{\mathbf{q}} c_{\mathbf{k}, \alpha}^\dagger c_{\mathbf{k}+\mathbf{q}, \alpha} c_{\mathbf{k}'+\mathbf{q}, \mu}^\dagger c_{\mathbf{k}', \mu} \right) + \sum_{\mathbf{k}, \mathbf{k}', \mathbf{q}} \sum_{\alpha, \beta, \mu, \nu} \left( J_{\mathbf{q}} \boldsymbol{\sigma}_{\alpha\beta} \cdot \boldsymbol{\sigma}_{\mu\nu} c_{\mathbf{k}, \alpha}^\dagger c_{\mathbf{k}+\mathbf{q}, \beta} c_{\mathbf{k}'+\mathbf{q}, \mu}^\dagger c_{\mathbf{k}', \nu} \right). \quad (6)$$

Suivant le formalisme du champ moyen en autorisant un ordre supraconducteur et un ordre d'ondes de densité de charge on obtient alors une action effective

$$S = \int d\tau \sum_{\mathbf{k}, \mathbf{q}} \left( \frac{\Delta_{\mathbf{k}+\mathbf{q}} \Delta_{\mathbf{k}}^*}{J_{\mathbf{q}}^-} + \frac{\chi_{\mathbf{k}+\mathbf{q}} \chi_{\mathbf{k}}^*}{J_{\mathbf{q}}^+} \right) - \text{Tr} \ln \left( i\omega_n - \epsilon_{\mathbf{k}} - \frac{|\Delta_{\mathbf{k}}|^2}{i\omega_n + \epsilon_{\mathbf{k}}} - \frac{|\chi_{\mathbf{k}}|^2}{i\omega_n - \epsilon_{\mathbf{k}+\mathbf{Q}}} \right). \quad (7)$$

Il serait possible d'étudier ici la compétition entre ces deux ordres, mais pour décrire le pseudogap dans l'esprit de la fractionnalisation on s'intéresse au paramètre d'ordre  $|\Psi|^2 = |\Delta|^2 + |\chi|^2$  pour lequel on obtient l'action effective suivante

$$S_{eff} = \int d\tau \sum_{\mathbf{k}, \mathbf{q}} \frac{\Psi_{\mathbf{k}}^\dagger \Psi_{\mathbf{k}+\mathbf{q}}}{\tilde{J}_{\mathbf{q}}} - \text{Tr} \ln(G^{-1}(i\omega_n, \mathbf{k}))$$

$$G^{-1}(i\omega_n, \mathbf{k}) = i\omega_n - \epsilon_{\mathbf{k}} - \frac{|\Psi_{\mathbf{k}}|^2}{2} \left( \frac{1}{i\omega_n + \epsilon_{\mathbf{k}}} + \frac{1}{i\omega_n - \epsilon_{\mathbf{k}+\mathbf{Q}}} \right). \quad (8)$$

Il est ici possible d'obtenir une équation auto-consistante de la forme BCS pour  $|\Psi_{\mathbf{k}}|$  est d'étudier son impact sur la fonction de Green électronique  $G(i\omega_n, \mathbf{k})$ . Le résultat principal est montré à la Fig.3 où l'on observe une très bonne correspondance entre la fonction spectrale en fonction de l'énergie et du moment mesurée expérimentalement est celle obtenue via cette description du pseudogap. Le même formalisme permet également d'expliquer la renormalisation des modes de vibrations observée à la transition supraconductrice. Dans ce cas aussi, la contrainte entre les amplitudes des paramètres d'ordre joue un rôle crucial pour reproduire les données expérimentales. On peut aussi noter que la fonction de Green électronique Eq.(8) peut aussi être comparée aux résultats obtenus par les techniques numériques qui visent à résoudre le modèle de Hubbard directement, tel que le champ moyen dynamique. Bien que ces techniques ne parviennent pas en général à stabiliser les ondes de densité de charge, la structure des pôles de la fonction Green extraite de ces calculs numériques est très similaire à celle obtenue via notre traitement en champ moyen.

L'autre résultat majeur de cette thèse est le fait que la présence de ces ondes de densité de paires sous forme de modes incohérents en dehors du pseudogap peut expliquer la dépendance de la résistivité avec la température. On prend pour cela un propagateur pour ces bosons incohérents

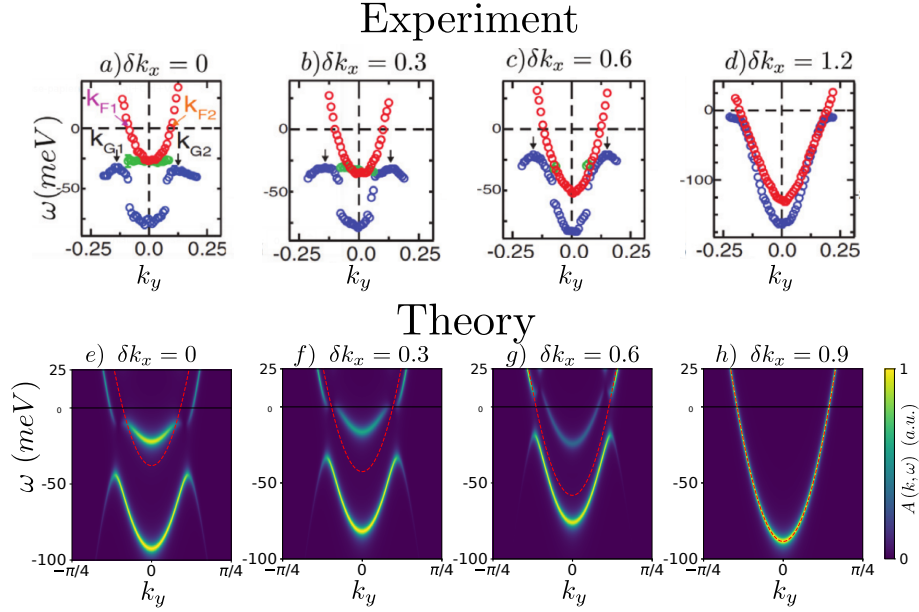


**Figure 3:** (a)-(d) Maximums de la fonction spectral obtenus par ARPES [63] pour  $T > T^*$  (rouge) et  $T < T_c$  (bleu et vert) pour différents  $k_x = \pi - \delta k_x$ . Les arcs de Fermi se terminent à  $\delta k_x = 0.6$  le gap qui persiste à  $\delta k_x = 1.2$  est le gap supraconducteur. (e)-(h) Fonction spectrale obtenue avec la fonction de Green Eq.(8) pour différents  $k_x = \pi - \delta k_x$ . La ligne rouge indique la dispersion électronique lorsque le pseudogap est nul. L'amplitude du pseudogap est prise comme solution de l'équation auto-consistante découlant de Eq.(8) avec  $\mathbf{Q} = (0.2, 0)\pi$ . Adapté de Ref.[135].

une dépendance en énergie dominée par l'amortissement de Landau :

$$\mathcal{D}^{-1}(\mathbf{q}, i\omega_n) = \gamma |\omega_n| + \mathbf{q}^2 + \mu(T).. \quad (9)$$

En utilisant le formalisme de Kubo, qui exprime la conductivité sous la forme d'une expansion diagrammatique, on peut évaluer la contribution de ces bosons de charge 2 en plus de la contribution fermionique. On trouve alors que ces modes incohérents produisent une résistivité qui varie linéairement avec la température sur une large gamme de température. Cette contribution va dominer celle des électrons lorsqu'elle est présente, amenant une déviation de la loi quadratique comme observé expérimentalement.

De nombreux phénomènes liés au pseudogap des cuprates supraconducteurs peuvent donc être décrits si l'on considère cette phase comme étant le résultat de la fractionnalisation d'un paramètre d'ordre. Le candidat naturel du point de vue des symétries et aux vus des récents résultats expérimentaux, est de fractionnaliser une onde de densité de paires qui amène à la formation d'ondes de densité de charge et de supraconductivité à plus basses températures. J'étudie dans cette thèse les conséquences de cette fractionnalisation sur les propriétés électroniques ainsi que sur les modes de vibrations avec de très bonnes comparaisons avec les observations expérimentales. Bien que les méthodes numériques ne parviennent pas à stabiliser les ondes de densité de charge, cette description parvient à expliquer la structure fine de la self-energy obtenue dans des calculs de champ moyen dynamique. Enfin, la présence de ces modes de densité de paires, qui ont une charge 2, en dehors du pseudogap peut également expliquer la déviation de la dépendance quadratique en température de la résistivité.



# Introduction

The main goal of the study of condensed matter systems is to understand and manipulate the different phases that electrons can adopt. In this sense, the discovery of superconductivity more than a hundred years ago was a major breakthrough and it has shaped the field up to now. From a practical aspect, it is a very interesting state of matter as the ability to conduct electricity without resistance would change our everyday life. From a fundamental perspective, the challenges that still exist to understand the phenomenon fully drive physicists to continue the investigation. In this thesis, we will be interested in the modern aspect of superconductivity which is focused on non-conventional superconductors. These are materials that still defy all our attempts to formulate a complete theory that explains their phase diagram. We will focus on a particular family of Copper-based ceramics, the cuprate superconductors, in which superconductivity was discovered in 1986.

Despite the intense focus that has been put on the study of the phase diagram of cuprates, there are still a number of discussion around the nature of the electronic phases that emerge when the system is doped away from half-filling. The most striking evidence for the unconventional nature of the superconducting state is the very high critical temperature ( $\sim 150 K$  in some cuprates) and the enigmatic pseudogap phase to which it is associated. The pseudogap is a region where the system is not described by standard Fermi liquid theory but also do not appear to be in any ordered state, understanding the nature of the pseudogap is important to have a complete understanding of the superconducting phase. In this thesis, we present a new and original idea to describe the pseudogap which is based on the fractionalization of collective modes. The idea of fractionalization is known in condensed matter systems and one of the more striking realizations of such is probably the Fractional Quantum Hall effect where the quasi-particles are seen to have an electric charge of  $1/3$  the one of the bare electrons. Here it is the modulated particle-particle pairs, called Pair Density Waves, that we will fractionalize into uniform particle-particle pairs, know as Cooper pairs and related to the phenomenon of superconductivity, and modulated particle-hole pairs that break the translation symmetry of the system. The consequences of this fractionalization on the electronic degrees of freedom describe a region that we identify with the pseudogap phase.

We start by presenting in Chapter 1 an overview of the field of non-conventional superconductivity and of the phenomenology of cuprates that makes the problem so intricate. We include a review of both the experimental facts as well as the theoretical ideas that were explored in previous work to emphasize that our proposition is based on established ideas on either side. Chapter 2 gives a quick introduction to the main analytical tools and conventions that will be used in this thesis. We also present an example of how fractionalization was used previously to describe the

phase diagram of cuprates.

Chapter 3 is the core of the thesis as we present our new idea on the fractionalization of the Pair Density Waves in cuprates. Starting from the known relation between the different ordered phases observed in the phase diagram, we use an effective theory to get the first phenomenological consequences of our ansatz. We then use mean-field theory and a microscopic model to obtain some stringent features of the pseudogap that are compared to experimental and numerical results. We also explore the so-called Strange metal phase in Chapter 4. This is done by extending our idea for the pseudogap and considering that some incoherent bosons can contribute to the transport properties of the system, explaining the different anomalies observed for temperatures above the superconducting transition. Lastly, we stray away from the field of cuprates in Chapter 5 to explore another promising platform for unconventional superconductivity, multilayer graphene systems. This last study is done by numerical tight-binding calculation and focuses on the effect of stacking faults on the electronic properties of such systems.

# Chapter 1

## Cuprate superconductors

### 1.1 Unconventional and high-temperatures superconductors

#### 1.1.1 Bardeen, Cooper, Schrieffer and Onnes

Superconductivity is a spectacular experimental realisation of a quantum state extending over macroscopic lengths and has always been a wonderful challenge for theoreticians. Its discovery was made possible by the access to very low temperatures when Kammerling Onnes managed to cool down Helium below its boiling point at 4.13 Kelvin. He used these newly available refrigeration capabilities to probe the behaviour of metals at very low temperatures by cooling down elementary Mercury while measuring the change in resistivity of the sample. The sudden vanishing of the resistivity at 4.2  $K$  is so spectacular that it was first thought to be due to a loss of electrical contacts [1]. This is however only one of the tell-tale signatures of superconductivity in metals, the ability for the materials to carry electrical current without any dissipation over macroscopic distances.

Another primary characteristic of superconductors is to expulse any form of magnetic field. This was first reported by W. Meissner and R. Ochsenfeld in 1933 in superconducting tin and lead samples [2]. Thus a superconductor is more than a simple perfect metal and is a distinct phase of matter. This was a major indication on how to describe the superconducting transition which was up to there still unexplained.

Most of the great physicists of the 20<sup>th</sup> century tried to develop a theory of superconductivity at some point. This includes the likes of Einstein, Bohr, Brillouin, Krönig, Bloch, Heisenberg, Born or Feynmann [3]. Some of these attempts still succeeded in describing the phenomenon from a phenomenological point of view such as the work by Fitz and Heinz London in 1935 [4] or the theory by Ginzburg and Landau in 1950 [5] which established the basics for the study of second-order phase transitions still widely used nowadays. A true microscopic understanding of superconductivity was however still missing and the solution would start to appear with the work of L. Cooper on the effect of attractive interactions between electrons [6], called the Cooper problem, in 1956. Showing

that electrons can form pairs when subjected to such attraction was the first step that culminated in the full microscopic theory of superconductivity in 1957 by J. Bardeen, L. Cooper and J. R. Schrieffer and now known as the BCS theory [7, 8]. The principal ingredient for superconductivity in metals is the electron-phonon interaction that leads to an effective attractive interaction between electrons with opposite momenta. These electrons will then form pairs, named Cooper pairs, which will condense in a single, macroscopic, quantum fluid that allows for dissipationless current and perfect diamagnetism.

The agreement between the prediction made using the BCS theory and the experimental results is still nowadays among the best a theory can provide. It requires only one adjustable parameter, usually taken to be the critical temperature which is easily obtained experimentally and is able to explain superconductivity in a large majority of metals. Moreover, the idea of fermions pairing found application in other fields of physics such as superfluidity in  $^3\text{He}$ , neutron stars or quark matter. The discoveries of materials that exhibit a superconducting state continued at a growing rate after the microscopic derivation was given and the access to liquid Helium became more widespread. In fact, most of the metallic alloys have transition temperatures ( $T_c$ ) below 30 K and thus requiring specific cryogenic techniques to study.

### 1.1.2 Non-BCS superconductors

Looking away from the metallic alloys pushed the BCS theory to its limits and it was soon found that some materials exhibit superconducting states that cannot be understood starting from the usual electron-phonon model known up to this point. It is important to note that the superconductivity in these unusual materials is still due to the condensation of Cooper pairs but that the mechanism for the formation of such pairs is different and often remains elusive. This has consequences on several micro and macroscopic quantities depending on the particular physics at play.

One of the first example materials in which the BCS theory is not applicable is probably the organic superconductor  $(\text{TMTSF})_2\text{PF}_6$ , synthesised in 1979 by K. Bechgaard, that has a transition temperature ( $T_c$ ) of 0.9 K under the pressure of 12 kBar [9, 10]. Other Bechgaard salts ( $(\text{TMTSF})_2\text{X}$  with  $\text{X} = \text{PF}_6, \text{ClO}_4, \text{etc...}$ ) have also been shown to have unconventional pairing. In the same year, superconductivity was discovered in a heavy-fermion material  $\text{CeCu}_2\text{Si}_2$  below 0.5 K [11]. This family of materials was already known to have many exotic properties due to the presence of 4*f* and 5*f* electrons in contrast to the usual *d* orbitals governing the physics of metals. The interplay between the itinerant electrons from the metallic orbitals and the highly localized *f* orbitals leads to a renormalization of the mass of the electrons that can increase a hundred times above the bare mass. Another popular family of unconventional superconductors are iron-based superconductors which are relatively more recent. The first member discovered was the iron-pnictide  $\text{LaOFeAs}$  in 2008 with a transition temperature of 38 K [12]. Iron chalcogens ( $\text{FeSe}$ ) have also been found to have a superconducting transition and are generally placed in the same family even though details of the atomic structure can vary. The relative high-temperature of the superconducting transition sparked a lot of interest, especially when a  $T_c$  of 109 K was obtained for thin films of  $\text{FeSe}$  on a  $\text{SrTiO}_3$  substrate [13].

The biggest and most studied family of unconventional superconductors are cuprate materials. Superconductivity was found in  $\text{LaBaCuO}_4$  in 1986 by J.G. Bednorz and K.A. Müller with a critical temperature of  $35\text{ K}$  [14]. Although this was the highest recorded  $T_c$  at the time, it would be quickly outshined by the discovery of Yttrium Barium Copper Oxide (YBCO) the very next year which was the first material to have a superconducting temperature above the boiling point of Nitrogen with  $T_c = 90\text{ K}$  [15]. It quickly became evident that the superconductivity in these materials could not be explained by the BCS theory and the search for both new compounds with even higher critical temperatures and for a theory to explain this phenomenon is still ongoing. The highest critical temperature at ambient pressure is still found in cuprates ( $\text{HgBa}_2\text{Ca}_2\text{Cu}_3\text{O}_{8+x}$  with  $T_c = 133\text{ K}$  [16]).

It is important to mention that high-temperature superconductivity, even though usually associated with unconventional pairing mechanisms, is not forbidden in the BCS theory. In fact, the highest critical temperature was obtained in the BCS superconductors  $\text{H}_3\text{S}$  in 2015 at  $203\text{ K}$  under the pressure of  $90\text{ GPa}$  [17, 18]. There is also a prediction that pure metallic Hydrogen would be superconducting at room temperature but requires even greater pressure [19] and has not been achieved yet.

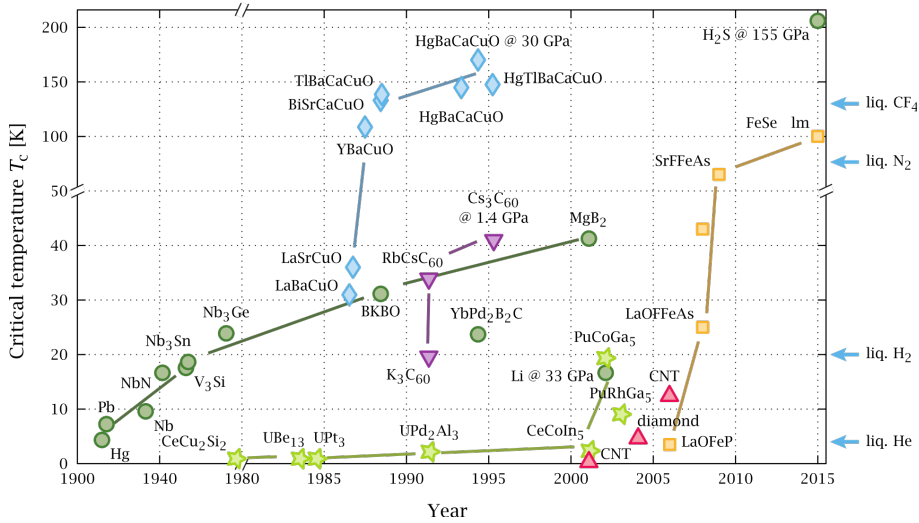


**Figure 1.1:** Critical superconducting temperature for different families of superconductors as they were discovered. Note that some of these results are obtained under pressure. Adapted from Ref.[20].

Even 60 years after the BCS theory and 40 years after the first unconventional superconductors were discovered, there are still new experimental developments that challenge our understanding of superconductivity. The very recent discovery of superconductivity in twisted bilayer graphene [21, 22] is a testimony that we are far from a complete understanding of the phenomenon. One common thread to many unconventional superconductors is the possibilities for multiple different electronic instabilities. In this case, predicting which ordered state the material will be in when cooled down is a formidable task and cooperative or competitive interactions between the different orders are of the greatest importance.



### 1.1.3 Anatomy of cuprates

Cuprate superconductors all share a chemical structure that is at the origin of many of their properties. They are layered materials where copper-oxygen planes are separated by ions such as Yttrium and Barium as represented in the example in Fig.1.2(a). This results in highly anisotropic properties along the direction perpendicular to the  $\text{CuO}_2$  planes and leads us to think most of the physics happens in the two-dimensional square lattice. The resulting first Brillouin zone is a square with momenta going from  $-\frac{\pi}{a_0}$  and  $\frac{\pi}{a_0}$  where  $a_0$  is the lattice spacing that is usually taken to be unity. There are three high symmetry points in the first Brillouin zone named  $\Gamma$ ,  $M$  and  $X$  that are located at the centre, edge and corner of the Brillouin zone respectively (Fig.1.2(b)). The Brillouin zone is also divided between the *nodal region* close to the momenta  $\mathbf{k} = (\pm\frac{\pi}{2}, \pm\frac{\pi}{2}), (\mp\frac{\pi}{2}, \pm\frac{\pi}{2})$  and the *antinodal region* around momenta  $\mathbf{k} = (0, \pm\pi), (\pm\pi, 0)$ . In the study of cuprates, the latter region is the main focus as most of the unconventional properties of the superconducting and normal states are observed there. Note that the presence of the third spatial dimension is needed to obtain any phase transition at finite temperature that breaks a continuous symmetry due to the Mermin-Wagner theorem [23] and we will usually assume that this is the only effect of the weak coupling between the different planes.

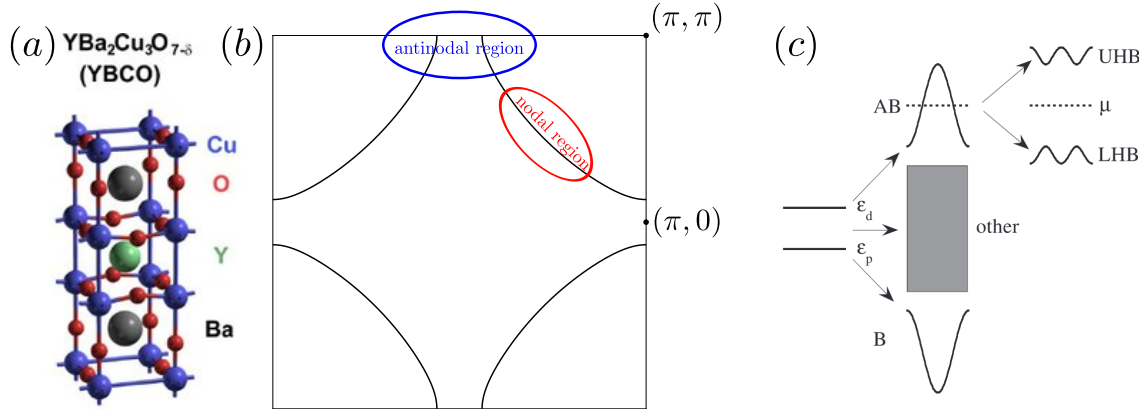


**Figure 1.2:** (a) Crystal structure of a prototypical cuprate. The copper-oxide planes are separated by layers of intercalating ions. Chemical substitution in these insulating planes will change the electron's density in the  $\text{CuO}_2$  planes. Adapted from Ref.[24]. (b) Representation of the first Brillouin zone for the square lattice generally considered for cuprates. We indicate the zone designed as the *antinodal region* around momenta  $\mathbf{k} = (0, \pm\pi), (\pm\pi, 0)$  (blue) and the *nodal region* close to the momenta  $\mathbf{k} = (\pm\frac{\pi}{2}, \pm\frac{\pi}{2}), (\mp\frac{\pi}{2}, \pm\frac{\pi}{2})$  (red). The white line is an example of the location of the Fermi surface for underdoped cuprates. (c) Schematic of the different steps leading to the relevancy of the effective theory with one orbital per site for cuprate superconductors. Adapted from Ref.[25].

Another assumption often made in the study of cuprates is to consider that there is only one orbital per unit cell relevant to the low energy physics. A schematic for the argument is given in Fig.1.2(c) and lies in the way the  $3d^9$  configuration of the copper hybridize with the  $2p^6$  configuration of the oxygen. In particular, the proximity of the  $d$  levels and of the  $p$  levels in energy leads to a bonding state that is fully occupied and below the non-bonding states but, more importantly, a singly occupied anti-bonding state at higher energy [26]. This anti-bonding state has a strong  $3d_{x^2-y^2}$  character and leads to a half-filled band crossing the Fermi level. The highly

metallic nature of this state also gives rise to a high energy penalty for two electrons with opposite spin to occupy it, leading to a high on-site repulsion for between electrons, denoted  $U$ .

Applying the standard band structure theory to this square lattice system with one electron per unit cell would lead us to think that cuprates should be metals. It turns out that the cuprates are insulators with a large gap of order  $3 eV$ . This situation was envisioned way before the discovery of cuprates in part by Mott [27] where an electron-electron repulsion can lead to an insulating behaviour, even for an odd number of electrons per unit cell, giving rise to a Mott insulator. The resulting band structure is composed of a valence band (the lower Hubbard band (LHB)) and a conduction band (the upper Hubbard band (UHB)) separated by a gap of order  $U$  in which lies the chemical potential. The tendency to delocalize the electrons is still present because of the overlap between the different orbital (denoted by  $t$ ) and can be seen through the effective antiferromagnetic interaction that emerges between neighbouring sites. The undoped cuprates, with one electron per site, are thus antiferromagnetic Mott insulators.

## 1.2 Phase diagram and competing orders

### 1.2.1 Doping a Mott insulator

The physics of undoped cuprates is well understood from the early work of Mott and do not show any signs of superconductivity. The incredible complexity usually associated with the cuprates comes from doping, *i.e.* changing the electron density of the parent materials. We are in particular interested in the hole-doped side of the phase diagram, which is obtained by decreasing the number of electrons per unit cell, where the high-temperature superconducting phase emerges. An experimental phase diagram is shown in Fig.1.3, we can see that the critical temperature for the superconducting phase is found to be dome-shaped with a maximum which is referred to as the *optimal* doping. For an electron density lower than the optimal one (overdoped samples) the system is usually found to be a standard metal described by the Fermi liquid theory. Between the half-filling point and the optimal doping (the underdoped region), however, we observe a zoo of unusual properties associated with many different electronic instabilities. These possible orders all manifest below a temperature  $T^*$  which decreases linearly with doping and are a part of the *pseudogap* region. The only long-range orders established in the underdoped cuprates are the antiferromagnetic phase close to half-filling and the superconducting phase. The ordering temperature for the antiferromagnetic phase  $T_{Neel} \sim 300 K$  can be used to estimate the typical scale of the interaction but is usually much lower than the measured value. This is due to the previously mentioned two-dimensional nature of the copper-oxide plane with only weak coupling in the third dimension. This coupling is thus the limiting factor when going through a phase transition and the real scale of the interaction is of order  $1\ 500 K$  [28]. Another important factor in the physics of the pseudogap is the disorder that is present in most materials due to the chemical substitution required to dope the parent compound. This disorder usually strongly affects modulating orders that break translation symmetry [29–31] and all the modulating orders such as the spin density waves, the charge density waves (CDW) or the pair density waves (PDW) have a very short coherence length and/or require external perturbation such as pressure or magnetic field to be stabilized.

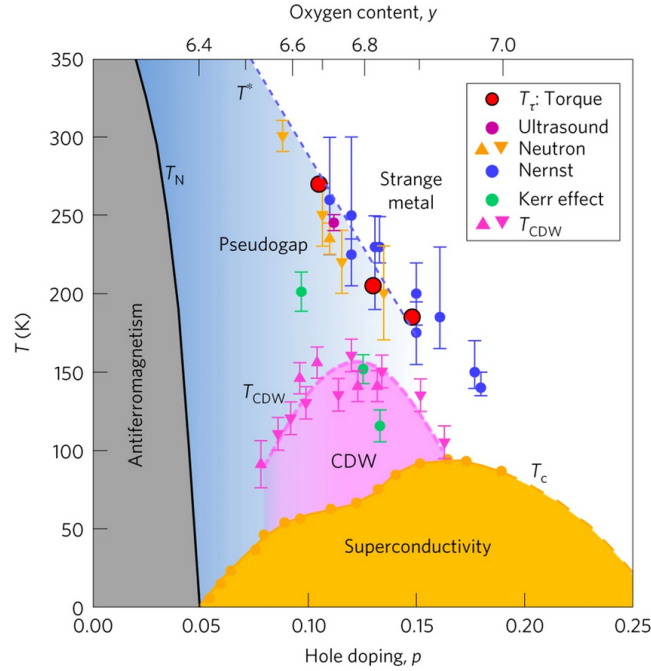


**Figure 1.3:** Experimental Temperature-doping phase diagram of  $\text{YBa}_2\text{Cu}_3\text{O}_y$  from Ref.[32] The transition temperature for the antiferromagnetic and the superconducting states are well known but the pseudogap temperature is more difficult to accurately measure. Note that the different experimental probes susceptible to detect the pseudogap.

The other region of interest in cuprates is the one that is encountered at high temperatures in the proximity of optimal doping. In this region most of the signatures of the pseudogap are gone but, instead of recovering a standard metal, new exotic phenomena are observed. The main indication that we do not recover a Fermi liquid is given by the temperature dependence of the resistivity. In traditional metal, the resistivity grows quadratically with temperature, with a residual value at  $T \rightarrow 0$  being an indication of the disorder in the sample. In this *strange metal* phase, the cuprates are indeed conductors but with a linear dependence of the resistivity with respect to the temperature [33]. This persists over a wide range of temperatures and is often associated with the lack of quasiparticles [33–35]. The connection to the pseudogap is unclear and there is no consensus on the description of this region of the phase diagram up to now.

The high-temperature superconducting state is, in retrospect, one of the less controversial regions of the phase diagram and most of the mystery lies in how it emerges from the enigmatic pseudogap or what is its link to the puzzling strange metal. The amount of experimental data that have been acquired in cuprates over the last 30 years is astounding and it would take too much time trying to present only a fraction of it. Experimental techniques ranging from Inelastic Neutron Scattering, Angle-Resolved Photoemission Spectroscopy, Nuclear Magnetic Resonance or Transport studies have been applied to cuprates and we will only present selected results to describe the main subjects of our theoretical analysis which are the superconducting state, the Charge Density Wave order and the pseudogap.

### 1.2.2 The superconducting state

Superconductivity in cuprates is deemed unconventional as the pairing mechanism is different from the electron-phonon interaction which is at the heart of the BCS theory. The superconducting state is however still the result of the condensation of Cooper pairs and exhibits perfect conduction and a Meissner effect [36] as in more standard superconductors. The origin of the pairing still has consequences on some physical properties of the superconducting state in cuprates.

One way of describing superconductivity is through the idea of a second-order phase transition and its associated order parameter [37]. In the case of superconductivity, the order parameter is usually taken to be the superfluid density which is non-zero only in the superconducting state. This quantity is usually directly related to the superconducting gap  $\Delta$  and we will in the following discussion use the latter one. Note that in systems where fluctuations are important, as in low dimensional systems, it is possible to have a non-zero superconducting gap but to still have a vanishing superfluid density, breaking the equivalence mentioned previously. In this case, the system is not in a superconducting state. In the case of the BCS theory, the superconducting gap can be seen experimentally as a real gap in the electronic spectrum as shown by Scanning Tunneling Spectroscopy [38] (STS). STS is based on the tunnelling effect that can occur between two metals when they are separated by a thin insulating material. In this case, the insulating barrier is the air (or vacuum) that is present between the sample material and a microscopic tip that is approached a few nanometers from the surface to be scanned. When a potential difference is applied between the tip and the sample, the tunnelling processes lead to a current being measured. The variation of this current with the bias voltage is proportional to the density of states (DOS) of the sample at an energy given by the bias voltage, allowing for the direct measurement of the energy dependence of the local density of states.

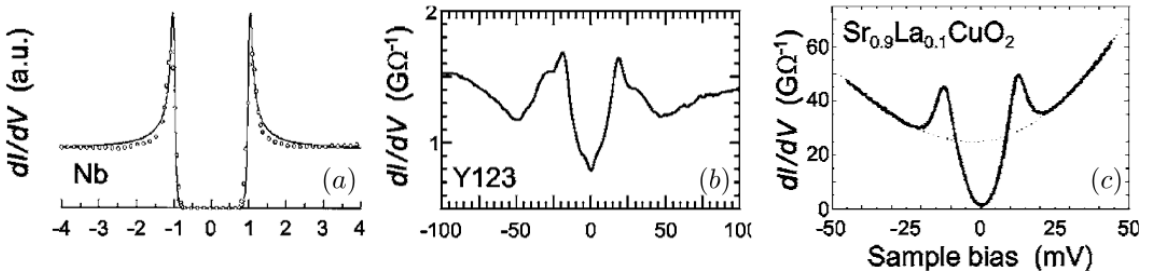


**Figure 1.4:** (a) Differential conductivity  $\frac{dI}{dV}$  as a function of the bias voltage obtained in STS experiments on elemental Niobium which is a BCS superconductor. We see that there is a gap in the electronic density of states, referred to as the superconducting gap, which is a result of the electrons pairing in this energy window. (b) Same quantity measured in the high-temperature superconductor YBa<sub>2</sub>Cu<sub>3</sub>O<sub>y</sub> doped with holes. We see that the density of states close to zero bias has a *V-shape* signature of the d-wave symmetry of the gap in cuprates. (c) We observe the same result in another cuprate material. The d-wave nature of the superconducting gap is a universal feature of the cuprates. Adapted from Ref.[38]

Experimental results in the superconducting state of the BCS superconductor Nb is shown in Fig.1.4(a) and we can clearly see that the DOS is zero in a large energy window around the Fermi level. This gap can be explained by the fact that the electrons close to the Fermi level form Cooper pairs and are not available anymore for tunnelling when the bias voltage is not strong enough to

break the Cooper pairs. Performing the same experiment in cuprate materials shows that even if we observe a vanishing density of states at the Fermi level, there are still occupied states at low energy [38] (Fig.1.4(b) and (c)). This change in the shape of the density of states at low energy is a direct consequence of the anisotropic nature of the superconducting gap in cuprates, in contrast with the BCS theory where the gap is found to be the same whatever the momentum of the electrons forming the Cooper pair is. Because the gap still has to respect the symmetry of the underlying lattice, there are only a number of possibilities for the momentum dependence of  $\Delta_{\mathbf{k}}$ . For cuprates, we have a  $d_{x^2-y^2}$  gap, a name taken from the notation for atomic orbital, which can be written as :

$$\Delta_{\mathbf{k}} = \frac{\Delta_0}{2} (\cos k_x - \cos k_y). \quad (1.1)$$

The superconducting gap will thus be maximum for momenta close to  $(0, \pm\pi)$  and  $(\pm\pi, 0)$  while it vanishes along the diagonal when  $k_x = k_y$ . As a result of these nodal lines, there are electrons at the Fermi level that do not contribute to the pair formation and which lead to the characteristic *V-shape* of the density of states. Moreover, the sign change of the gap between the  $x$ -axis and the  $y$ -axis can be seen as a phase factor added to the amplitude of the gap and has been an efficient wave of validating experimentally the symmetry of the gap through other experimental techniques based on the Josephson effect [39].

Another experimental probe that is able to confirm the symmetry of the superconducting gap is Raman Spectroscopy as it couples directly to the uniform charge susceptibility. When the incoming photon has energy equals to twice the superconducting gap it will trigger a pair breaking effect that will result in a resonance peak in the Raman spectrum for  $\omega = 2\Delta$  [40]. Moreover, by selecting the polarization of the light that is used, Raman spectroscopy can probe selectively some part of the Brillouin zone. It is thus possible to measure the gap in the antinodal region, where it is maximum, and to compare with the results obtained in the nodal region where the gap vanishes. The fact that there is charge excitation with vanishing energy along the diagonal of the Brillouin zone once again affects strongly the shape of the resonance that is observed and is another consequence of the d-wave symmetry of the superconducting gap in cuprates. More puzzling, however, is the doping dependence of the two possible measures of the gap depending on the polarization used. Fig.1.5(c) shows the doping dependence of the nodal gap ( $\Delta_N$ ) measured in the  $B_{2g}$  symmetry and compare it to the antinodal gap ( $\Delta_{AN}$ ) obtained in the  $B_{1g}$  symmetry. The former is directly following the doping dependence of the superconducting critical temperature with the characteristic dome shape. The latter, however, shows a totally different linear dependence with doping, similar to the pseudogap onset temperature. This is the first indication that the superconducting state is still linked to the pseudogap from which it emerges. There are other indications that the pseudogap predominantly affects the antinodal region and some are discussed in more detail in Sec.1.3. We can still use the nodal gap to find the link between  $\Delta_0$  and  $T_c$  and we get  $\frac{2\Delta_0}{k_B T_c} \sim 8$  (Fig.1.5(a)) which is way above the theoretical prediction of  $\frac{2\Delta_0}{k_B T_c} = 4.23$  from BCS theory, confirming the non-conventional nature of the pairing in those materials. In fact, there are still some debates on the eventual link between the antinodal gap observed in the pseudogap and the superconducting state at lower temperatures. This is usually encompassed in a discussion between a “one-gap” versus “two-gap” scenario, *i. e.* whether the phenomenon responsible for the pseudogap is also responsible for the superconducting state (one-gap) or these two states come from different microscopic origins (two-gaps) and could then compete or coexist.

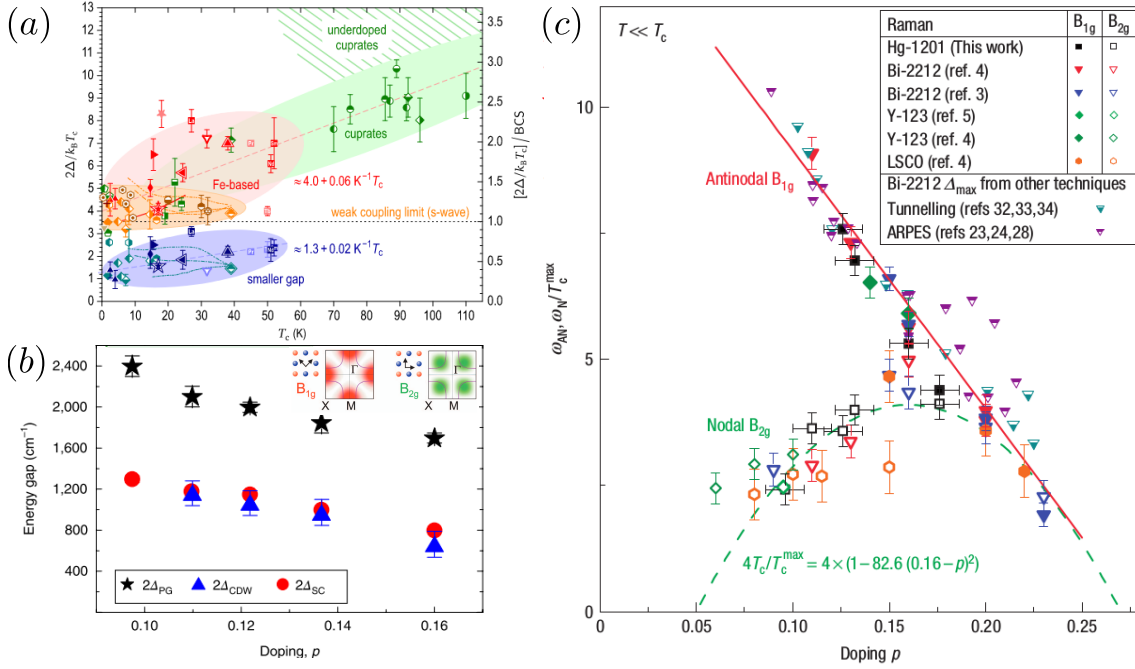


**Figure 1.5:** (a) Superconducting gap to critical temperature ratio  $\frac{2\Delta}{k_B T_c}$  for different families of superconductors. We see that unconventional superconductors such as the iron-based or cuprates generally have a ratio above the one predicted by the BCS theory. This is an important indication that the weak-coupling idea based on the electron-phonon coupling is not valid in these materials. Adapted from Ref.[41]. (b) Energy of the pair breaking peak measured by Raman spectroscopy in the antinodal ( $B_{1g}$ ) region and in the nodal ( $B_{2g}$ ) region. We see that the nodal gap shape dependence with doping as the superconducting temperature  $T_c$ . Meanwhile, the antinodal gap decreases linearly with doping, much like the pseudogap temperature  $T^*$ . Adapted from Ref.[42]. (c) Comparison between the antinodal superconducting gap (red dot) and the nodal CDW gap (blue triangle) obtained by Raman spectroscopy in underdoped HgBa<sub>2</sub>Ca<sub>2</sub>Cu<sub>3</sub>O<sub>8+ $\delta$</sub> . We see that they are both of the same order of magnitude, indicating the importance of the charge modulation phenomenon. Adapted from Ref.[43].

Another important insight given by Raman spectroscopy is the energy scale at which the different phenomenon in the pseudogap occurs. Fig.1.5(b) shows the results obtained by measuring the superconducting pair-breaking peak in the antinodal region and compare it to another pair-breaking peak that is observed in the nodal region. This second peak is observed at a temperature higher than the superconducting transition and is therefore associated with another collective phenomenon. As the onset temperature for this peak coincides with the one at which X-ray diffraction experiments show the CDW, this pair-breaking peak is associated with the modulated particle-hole pairs at the origin of this short-range order in the pseudogap. We can see that both of these excitations have the same energy scale for different doping in the underdoped region, driving us to consider the CDW as an important competitor to superconductivity [43].

### 1.2.3 Charge Density Wave

Multiple modulating orders have been observed at different places in the cuprates phase diagram. The earliest example was found in Lanthanum-based cuprate where *stripes* (one-dimensional modulation) were observed. These stripes showed modulation of both the charge and the spin density at the same time. It was found later that this case is particular to the La-based family of cuprates



while the presence of checkerboard Charge Density Wave is seen ubiquitously in all other families.

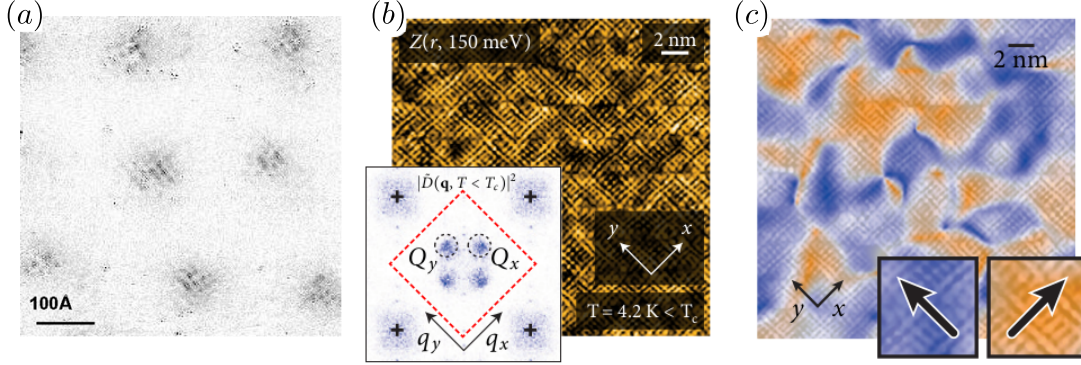


**Figure 1.6:** (a) Observation of the modulation of the electronic density in the superconducting phase. Superconductivity is destroyed locally by applying a small magnetic field and the normal state shows charge modulation in the vortices core. Adapted from Ref.[44]. (b) STS map of the electron-hole asymmetry  $Z(r, V_0) = \left(\frac{dI}{dV}\right)_{V=V_0} / \left(\frac{dI}{dV}\right)_{V=-V_0}$  in the superconducting phase. The inset shows the real part of the Fourier transform on the oxygen's site that exhibits two peaks along the crystal axis. (c) Filtering the original map to keep only the component corresponding to the dotted circle in (b) reveals the unidirectional nature of the modulation. Adapted from Ref.[45].

The first observation of the generic CDW was done in the Bismuth-based cuprate BSCO by Scanning Tunnelling Microscopy [44] (STM). By applying a magnetic field on an optimally doped sample in the superconducting states, one can create vortices where only a quantized number of flux lines can penetrate, destroying the superconducting state. It is then possible to probe the *normal* state behind the Cooper pairs condensate. It was in the core of these vortices that a modulation of the electronic density forming a checkerboard pattern was observed as shown in Fig.1.6(a). This was later expanded further by using resonant inelastic X-ray scattering (RIXS) that detected additional Bragg peaks corresponding to the same charge order as the one observed by STM in the pseudogap region above the superconducting transition. Further studies have since then shown that the CDW order in cuprates is a combination of unidirectional modulations along the crystal axis [45] (Fig.1.6(b)). This order does not show long-range phase coherence and forms puddles between which there are discommensurations (Fig.1.6(c)). The usual order parameter to describe such phase is the amplitude of the electronic modulation at a given wave-vector  $\mathbf{Q}$  written in real space as

$$\chi^{\mathbf{Q}}(\mathbf{r}) = \chi_0 \cos(\mathbf{Q} \cdot \mathbf{r} + \phi). \quad (1.2)$$

The relation between the CDW and the SC is still an open question but there is strong evidence that the two orders are in competition and that suppressing one of them enhances the other. This is already seen in the STM experiment shown in Fig.1.6(a) where destroying superconductivity locally by applying a magnetic field allows the charge modulation to be observed. One can go further and destroy the SC state entirely by applying strong magnetic fields, in this case, a long-range three-dimensional CDW is observed with a critical temperature very close to the zero-field  $T_c$  of superconductivity as shown by the phase diagram in Fig.1.7(a). The study of Quantum Oscillation (QO) in the pseudogap region also shows a Fermi surface reconstruction above a threshold magnetic field [46–53], indicating that the CDW coherence length is large enough. On the other hand, it is possible to suppress the CDW order by applying hydrostatic pressure along the crystal axis. In this case, an increase in  $T_c$  has been reported and is another evidence of the competition between the two orders [54].

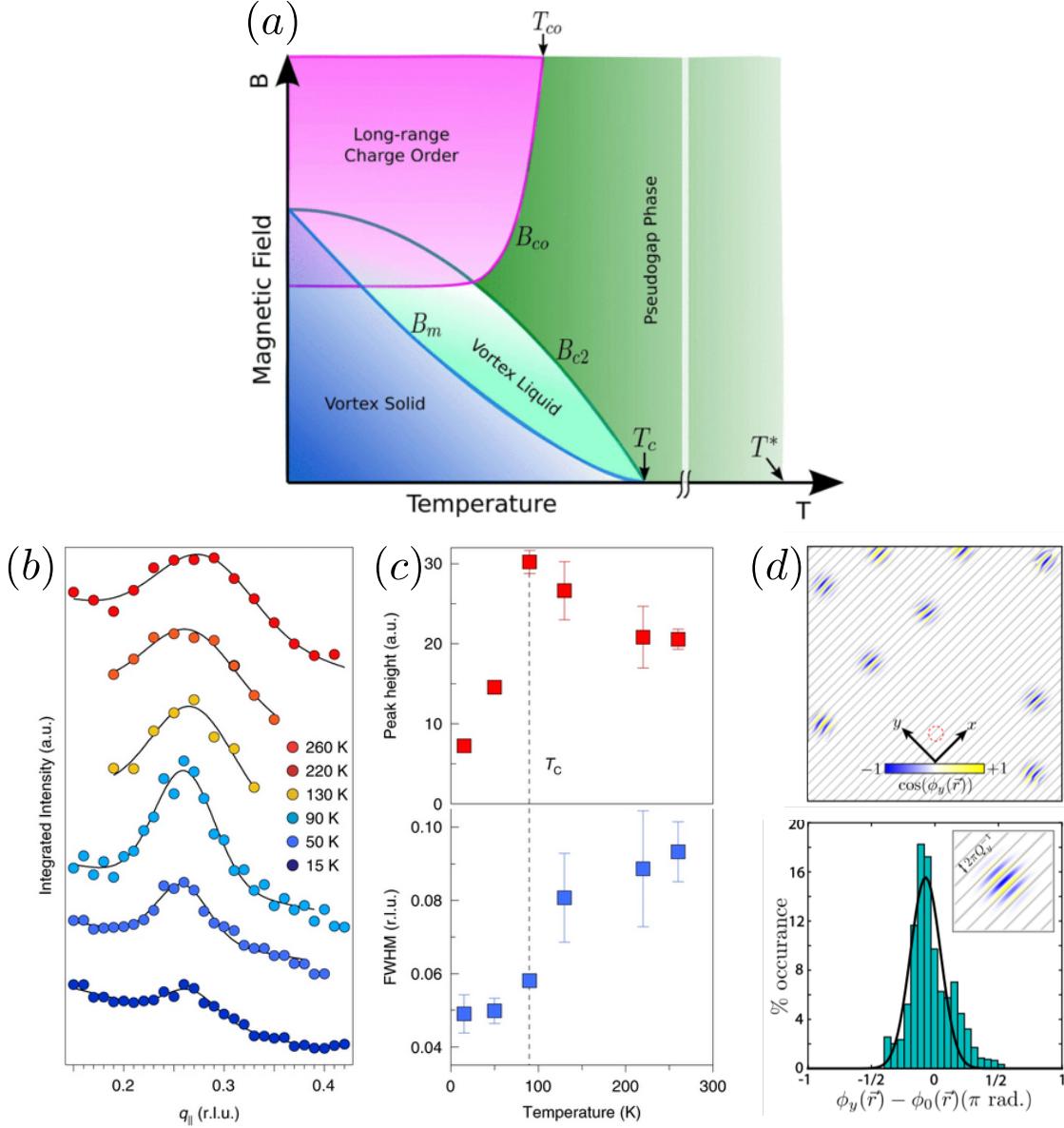


**Figure 1.7:** (a) Schematic Temperature-Magnetic field phase diagram for an underdoped cuprate. We see that for a high magnetic field, the vortex liquid state gives rise to a long-range three-dimensional charge order. The critical temperature for this CDW is almost independent of the magnetic field and very close to the superconducting  $T_c$  at zero field. Adapted from Ref.[55]. (b) CDW peak obtained in RIXS experiments at different temperatures, the black lines are fit using a gaussian shape on top of a linear background. (c) Amplitude and width obtained from the fit in (b). We see that the amplitude is maximum at  $T = T_c$  before decreasing for lower temperature, showing the competition between the two orders. The width of the CDW peak, however, decreases monotonically with temperature with a sharp drop at  $T_c$ . Adapted from Ref.[56]. (d) STM map of the relative phase of the charge order with respect to the lattice in vortices for  $T < T_c$  (top panel). We can see that the distribution of the CDW phases in different vortices (bottom panel) is peaked despite the distance separating the vortices being larger than the expected correlation length for the CDW order. Adapted from Ref.[57].

Even though the CDW and the SC order are in competition, there are also evidences that they coexist in a very peculiar way at low temperature. The first argument for this coexistence is still based on the X-ray experiments that show that the area of the Bragg peak associated with the charge modulation is increasing when the temperature approaches  $T_c$  but remains non-zero in the



superconducting phase (Fig.1.7(b)). Moreover, the width of the CDW peak decreases rapidly when approaching  $T_c$ . The intricate relation is even more visible when looking at the STM results in more detail. In particular, when the phase slip of the CDW with respect to the lattice is measured in different vortices we can see that they form a centred distribution (Fig.1.7(d)) in contrast to the expected uniform distribution of random phase slip. This is surprising as the distance between vortices is much bigger than the phase coherence of the CDW order in the pseudogap region and we would not expect the superconducting transition to affect any of this. The link between the CDW and the SC orders may then be a crucial piece of the puzzle that is the pseudogap.

## 1.3 The Pseudogap

### 1.3.1 Electronic properties

The term *pseudogap* is used in many contexts to designate a loss of density of states at the Fermi level. This definition applies to the pseudogap region in cuprates but it is far from capturing all the unusual phenomenons that are observed in this region of the phase diagram. The pseudogap in cuprates was first characterized by mean of Nuclear Magnetic Resonance (NMR) that measured a decrease of the Knight shift when crossing the  $T^*$  temperature [58, 59]. The Knight shift is a measure of the change of the magnetic environment of the nucleus that is probed and, in metals, is mainly due to the conduction electrons [60]. As such it is related to the density of states at the Fermi level and its decrease at  $T^*$  is a consequence of the loss of electronic states as mentioned previously. This was later confirmed by direct measurement of the density of states by STS as shown in Fig.1.8(a).

More information about this loss of DOS can be obtained by Angle-Resolved Photo-Emission Spectroscopy, an experimental probe based on the inverse photo-electric effect that can study the energy and momentum distribution of the density of states in the Brillouin zone [61]. By irradiating a sample with photons with energy above the work function of the material there is a probability for an electron to be emitted. The energy and angle at which this outgoing electron is extracted from the material are directly related to its energy and momentum eigenstate in the material and the probability of this photon-electron conversion is proportional to the probability of such eigenstate being occupied. This results in ARPES being directly related to the energy and momentum dependent electronic spectral function  $A(\mathbf{k}, \omega)$  which indicates the probability of a state at momentum  $\mathbf{k}$  and energy  $\omega$  to be occupied. Integrating this spectral function over the Brillouin zone recover the DOS discussed previously and integrating over all the negative energies is a measure of the electronic density. For  $T > T^*$ , ARPES can reconstruct the shape of the Fermi surface and show a hole pocket centred around  $\mathbf{k} = (\pi, \pi)$  as shown in Fig.1.8(b) (bottom right). When entering the pseudogap, however, the Fermi surface in the antinodal region is washed out and only Fermi arcs starting from the nodal region remain (Fig.1.8(b) top left). The Fermi surface is no longer a closed surface encompassing the occupied states and the DOS at the Fermi level is effectively decreased. This important change of the electronic properties in the antinodal region in the pseudogap phase is of particular importance as one of the results of the Fermi liquid theory is the relation between the volume enclosed by the Fermi surface and the number of electrons, known

as the Luttinger theorem. With only arcs remaining, it poses the question as to how and if this can be applied in the pseudogap and shows one example of non-Fermi liquid physics.

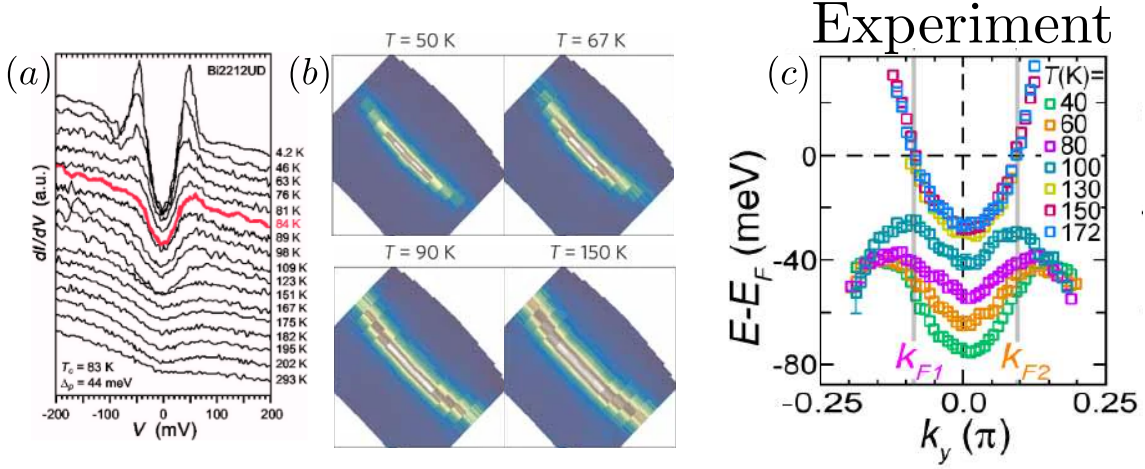


**Figure 1.8:** (a) Density of states measured through the change in the differential current in an STS experiment. Curves at different temperatures are shifted for clarity and the superconducting transition is indicated by the red line. We can see the superconducting gap for  $T < T_c$  but also that a reduced density of states at zero bias persists for  $T_c < T < T^*$ . Adapted from Ref. (b) ARPES results for the electronic spectral function at  $\omega = 0$  different temperatures in the pseudogap phase. We see that the Fermi surface in the antinodal region is washed out as the temperature is decreased. Adapted from Ref.[62]. (c) Change in the band structure at the Brillouin zone edge with temperature when going from the normal state to the superconducting state obtained by ARPES. We see that there are no states closing the Fermi level when  $T < T^*$ , corresponding to the pseudogap. Moreover, the band structure does not change significantly through the superconducting transition except for a slight change in the energy of the bottom of the conduction band. Adapted from Ref.[63].

ARPES can also be used to follow the evolution of the band structure at different temperatures as shown in Fig.1.8(c). One of the momenta is fixed at the edge of the Brillouin zone (here  $k_x = \pi$ ) and we look at the energy at which the electronic spectral function is maximum for different values of  $k_y$ . At the higher temperature,  $T > T^*$ , we observe a band crossing the Fermi level which is consistent with the full Fermi surface mentioned previously. When entering the pseudogap phase, we see that there are no electronic states close to  $E - E_F = 0$ , leading to a gapped band structure. As discussed earlier, this gap is the one responsible for the loss of DOS seen in STS or in NMR experiments and the Fermi surface still consists of Fermi arcs in the nodal region. The other interesting results from this experiment comes from the lowest temperature where  $T < T_c$ . In this case, we see only very small changes in the band structure, indicating that the antinodal superconducting gap is continuously related to the pseudogap. This result confirms the previous observation made by Raman spectroscopy mentioned in Fig.1.5 and we will study it in more detail in Sec.3.2.2.

Another way of measuring the number of carriers is to use transport experiments and in particular the Hall effect. In fact, the slope of the change of resistivity when the applied perpendicular field is changed, called Hall number, is directly related to the number of electrons and holes in the system [64]. Using Hall measurement in overdoped cuprates does give a Hall number that is proportional to  $1 + p$ ,  $p$  being the doping. When entering the pseudogap, however, the Hall number rapidly decreases and becomes proportional to  $p$  [65], indicating once more that the electronic

properties are strongly affected by the pseudogap.

### 1.3.2 Discrete symmetries and fluctuations

On top of the aforementioned electronic properties, the pseudogap is also characterized by the number of symmetries, mostly discrete, that are observed to be broken. Furthermore, fluctuations associated with the different continuous symmetries that we discussed previously also play an important role at finite temperature. Studying these collective effects is important as they are usually universal features of the phase diagram and are less affected by microscopic details such as the changes in the band structure or disorder.

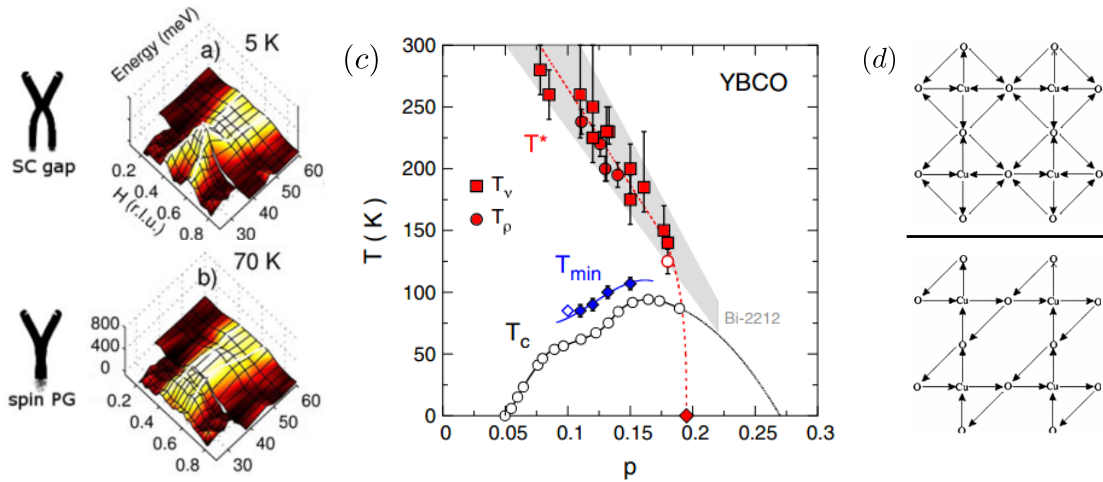


**Figure 1.9:** (a)-(b) Magnetic susceptibility of an underdoped YBCO sample along the  $a^*$  direction for energies above the spin-gap at two different temperatures. In the superconducting phase (top panel) the magnetic mode presents two branches with a positive and a negative dispersion, forming the *hourglass* or X shape of the magnetic susceptibility. When looking in the pseudogap region (bottom panel), the branch with the negative dispersion becomes vertical over a large energy range, forming the Y-shape dispersion. Subtracting the measurement made at low temperature to the high temperature one only shows the downward dispersing branch, showing that the upward branch is unaffected by the superconducting transition. Adapted from Ref.[66]. (c) Phase diagram of underdoped YBCO where the extent over which superconducting fluctuations can be observed is indicated by the blue line  $T_{min}$ . We can see that there is a large part of the pseudogap in which no significant contribution from pairing fluctuations can be observed. Adapted from Ref.[67]. (d) Schematics for the possible intra-unit cell loop current that can arise in the  $\text{CuO}_2$  plane. The presence of the oxygen atoms play a crucial role to allow for this loop-current configuration and it is not definitive whether these can be obtained in the simplified one-band Hubbard model or not. Note that none of these patterns break the translation symmetry from the  $\text{CuO}_2$  lattice and thus do not carry long-range modulation. Adapted from Ref.[68].

The first important fluctuations we want to mention are the antiferromagnetic fluctuations that originate due to the proximity with the Neel state at very low doping. These fluctuations are present in a large part of the phase diagrams and were thought to play a role similar to the phonon of the BCS theory to cause the formation of Cooper pairs [69]. We now know that the situation is more complex but the role of these fluctuations as the primary interaction leading to the formation of ordered states is a common starting point to study the pseudogap phase. The behaviour of the antiferromagnetic fluctuations can be studied from the spin-spin correlation function which is measured by Inelastic Neutron Scattering (INS). Neutrons, being neutral particles, will interact

with the magnetic structure and not the charge distribution in materials in contrast to the photons, used in RIXS for example. In these experiments, it is found that the magnetic susceptibility is gapped, in agreement with the NMR measurement of the Knight shift, and presents a resonance at finite energy around the antiferromagnetic wave-vector  $\mathbf{Q}_{AF} = (\pi, \pi)$ . The dispersion away from this point changes in different parts of the pseudogap. In particular, the  $Y$ -shaped dispersion observed in the pseudogap takes a  $X$ -shaped dispersion below  $T_c$  as shown in Fig.1.9(a)-(b). The downward dispersing branches that is observed in the superconducting state is thought to be the result of a spin-triplet excitation being stabilized at low temperature. Meanwhile, the upward dispersing branch is unaffected by the superconducting transition and is connected to the gapless magnon mode in the antiferromagnetic phase at low doping. There have been extensive studies on the coupling of these spin fluctuations on the single-particle electronic properties in conjunction with other experimental probes such as ARPES [70].

The other fluctuations often considered are the superconducting fluctuations that could originate from the SC state in the underdoped region. This would correspond to Cooper pairs being formed but not having a global phase coherence. The extent to which these fluctuations occur was a controversial subject and the hypothesis that the whole pseudogap could be due to the presence of such incoherent pairs was even considered [71–75]. This was originally supported by the measurement of the Nernst effect [76, 77] but later disputed by other experimental probes. It is nowadays accepted that such fluctuations are limited to a narrow temperature range above  $T_c$  as observed by Nernst measurements in YBCO [67] shown in Fig.1.9(c). This is a strong indication that the pairing fluctuations should not be present in the whole pseudogap region. More recent developments however have observed pairing tendency up to the pseudogap temperature  $T^*$  in pump-probe experiments where the system is taken out of equilibrium [78–80]. These experiments do not however claim that incoherent pairs are present at equilibrium at these temperatures.

The other aspect of the pseudogap region is the number of broken discrete symmetry states that are observed. In fact, it has been experimentally observed that Time-reversal symmetry [81–83] and Parity are broken at  $T^*$ , the  $C_4$  rotational symmetry is also broken in the pseudogap as seen in polarized neutron diffraction [84], torque-magnetometry [32] and optical birefringence measurements [85]. One candidate state to explain the time-reversal symmetry breaking is the intra-unit cell loop current state where phase circulation forming closed loops in the  $\text{CuO}_2$  plaquette leads to effective magnetic moments. Interestingly, these intra-unit cell loop current orders do not generally break the lattice translation symmetry as seen in the example in Fig.1.9 and it is a priori not clear how they could be responsible for the pseudogap. The idea has been extensively studied and is supported by the experimental observations of intra-unit cell magnetic structure by INS [81]. These states with broken discrete symmetries are usually thought to be unable to open a gap in the antinodal region and should thus be considered as a side effect of the pseudogap. There are still theories that pursue the idea of the modulation of intra-unit cell loop current over large scales could be the origin of the pseudogap [68].

### 1.3.3 Pair Density Waves

PDW describes a state that breaks both translation and charge conservation symmetry by having a modulation of the pairing amplitude in real space, much like density is modulated in a CDW state.

The pairing is still associated with electron-electron pairs and the modulation can be identified with the centre-of-mass momentum of the pair. As such, the standard superconducting state is associated with zero centre-of-mass momentum while the PDW as a finite momentum corresponding to the wave-vector of the modulation observed in real space, the associated order parameter can thus be written as

$$\Delta^{\mathbf{Q}}(\mathbf{r}) = \Delta_0 \cos(\mathbf{Q} \cdot \mathbf{r} + \phi), \quad (1.3)$$

where the pairing amplitude  $\Delta_0$  can have a phase changing in space to reflect the orbital symmetry as in the superconducting case (see Sec.1.2.2).

The nature of the translation-breaking state in cuprate superconductors has been questioned by the observation of a modulation of the pairing amplitude in the halo surrounded vortices in the same manner the CDW was first detected. Because it involves particle-particle pairing, the PDW order can couple to the electronic density of states by couplings of the form  $\Delta (\Delta^{\mathbf{Q}})^*$  or  $\Delta^{\mathbf{Q}} (\Delta^{-\mathbf{Q}})^*$ , with  $\Delta$  being associated to uniform particle-particle pairing [86]. The former one will be associated with a modulation of the density with wave-vector  $\mathbf{Q}$  while the second one will induce a modulation of the DOS with a wave-vector of  $2\mathbf{Q}$ . Both wave-vectors have been observed in the modulation of the electronic density of states in a vortex halo, where superconductivity is suppressed but not destroyed as opposed to the vortex core. This is would then correspond to the presence of a PDW with modulation  $\mathbf{Q}$  coexisting with the superconducting state [87].

Other experiments managed to observe the modulation of the pairing amplitude even without magnetic field using Scanning Josephson Tunnelling Microscopy [88], where the standard metallic tip of the STM is replaced by a superconductor. When scanning the surface of a superconducting material, the measured current is given by the Josephson relation and is, among other things, proportional to the pairing amplitude in both the tip and the sample. This allows for the measurement of the pairing amplitude on a nanometer scale without the need to apply an external magnetic field. The original observation pointed toward a PDW having the same modulation wave-vector as the CDW present in the pseudogap region, however, subsequent experiments have shown that it could possibly be that the modulation is twice longer (with a wave-vector twice shorter). This is still a debated point and an important piece of information needed to decipher the link between this PDW and the CDW in the pseudogap.

Other states with modulation of the pairing amplitude were considered theoretically before this observation in cuprates. Most of them, however, require the application of an exterior magnetic field, breaking time-reversal symmetry, to occur. These are referred to as Fulde-Ferrell-Larkin-Ovchinnikov (FFLO) [89, 90] phases and are thought to be relevant in the context of heavy-fermion [91] or organic superconductors [92]. The evidence for such modulation without any magnetic field in cuprates is a strong supporter for the time-reversal conserving version PDW instead of the previously studied FFLO states.

Theoretically, the Pair Density Wave instability is difficult to obtain. Indeed, weak-coupling approaches usually favour the uniform superconducting state and numerous perturbations such as disorder will also have strong adverse effects on the stability of the modulated pairing order. There are unambiguous results in the one-dimensional Kondo-Heisenberg model that shows that there is a stable PDW state at low temperature. The interplay of Luttinger liquid and Kondo physics that leads to this state is, however, difficult to reproduce in higher dimensions. Multiple numerical

studies via variational Monte-Carlo or Gutzwiller projected mean-field based on the  $t - J$  model (a large interaction limit of the Hubbard model) have shown that PDW states are possible but usually have higher energy than the uniform superconducting state [93]. However, all these states are very close in energy and the effect of perturbations such as disorder or the fine details of interlayers coupling are difficult to account for. In general, pair density waves are considered to play a role in the physics of the pseudogap but it is difficult to argue that it is the only instability at play and different scenario of coexistence and/or competition with the other charge density wave or superconducting order are studied. Such works are presented in more detail in Sec.1.4.3

## 1.4 Theoretical Description

### 1.4.1 Resonating valence bond and fractionalization

Although it is believed that the Hubbard model (more details in Sec.2.3) contains all the physics of cuprates, the inability to solve it except in a few specific limits makes the question about how to describe the pseudogap a very present one. The amount of work that has been put in developing theories that can explain the experimental results obtained in underdoped cuprates is fantastic and we will here only present some of them to put our new proposition in the context of earlier and current works.

Historically, one of the most influential ideas to describe the pseudogap of cuprate superconductors was through the Resonating Valence Bond theory [94]. The starting point is the exact ground state in the Mott insulator which is known to be localized electron on every site with antiferromagnetic ordering. The idea is then that the nearest-neighbour correlation that exists between electrons with opposite spin survive when going away from half-filling, forming quantum superposition of singlets at different length scales. When kinetic energy is restored outside the Mott state, these singlets are the building block of the Cooper pairs that forms the high-temperature superconducting state. In this case, the energy scale associated with the superconducting pairing is the same as the one leading the antiferromagnetic state at low doping, explaining the high critical temperature. Formalizing this idea is far from trivial and came later with the introduction of the fractionalization of the electronic degrees of freedom [28, 95–97].

Seeing how the spin and charge degrees of freedom of the electrons behave differently, it was suggested that one should treat them separately. To do so, one can introduce two new quasiparticles, the spinon and the holon, each carrying one of the degrees of freedom from the electron, *i.e.* its spin and its charge respectively. These two new excitations are fundamentally linked one to each other and the information that the two originate from the same electronic quasiparticle is then kept in a strongly fluctuating *emergent* gauge field mediating interaction between the new quasiparticles. It is then possible to study the possible pairing and condensation of spinons and holons to derive the phase diagram as a function of doping. To respect the statistics associated with the fermionic nature of the electron, one of the new quasiparticles has to be a fermion while the other has to be a boson (more details in Sec.2.4.2). The regime in which the fractionalization is valid varies with the choice of which from the spinon or the holon is a fermion but the superconducting phase is always described by the condensation of the bosonic particle and the pairing



of the fermionic ones at the same time.

This spin-charge separation is known to be a good description of the various phenomena in one-dimensional systems as in the Luttinger liquid [98, 99]. Adapting the idea in two dimensions is not straightforward and the study of the pseudogap in this formalism is thus the study of a gauge theory in which the gauge group depends on the flavour of fractionalization that has been used. The idea has had some success in explaining experimental observation such as the superconducting dome and the Fermi arcs but fundamental issues regarding the confining nature of gauge theory, also intensively studied in high-energy physics, makes the progress difficult [100].

## 1.4.2 Numerical developments

Even when resorting to numerical computations, the two-dimensional Hubbard model is a formidable problem. The Hilbert space of quantum systems usually grows as  $4^N$ , where  $N$  is the number of lattice sites considered. This means that the number of states for a two-dimensional system goes from  $4^4 = 256$  for a 2x2 square lattice to  $4^{16} > 4.10^9$  for a 4x4 lattice. The importance of fluctuations in low dimensional systems also requires reasonable sizes to capture all the long-range spatial correlations. Nonetheless, multiple numerical methods have been developed to treat the strongly correlated regime of electronic systems. One prominent technique is the Quantum Monte Carlo (QMC) method and its extensions. It is a stochastic algorithm that will sample the phase space randomly and evaluate various quantities while doing so. It is exact in the limit where the number of sampled points goes to infinity but it allows for a very well-define way of quantifying the error made when taking a finite number of steps. One very powerful application of the QMC technique is in the determinantal, or auxiliary-field, Quantum Monte-Carlo (DQMC) where the interacting part of the problem is treated through a mean-field decomposition in both the spin and charge sector, capturing magnetic order as well as charge modulation or superconductivity [101]. One big hurdle that the DQMC algorithm faces is the “sign-problem” that exist due to the fermionic nature of the electrons [102]. This limits the applicability of DQMC in the Hubbard model away from half-filling, especially for moderate to large interaction strength and low temperature.

Dynamical Mean-Field Theory (DMFT) is another interesting route to approach the problem. The technique is known to be exact in the limit of infinite dimension (or infinite lattice coordination) and focus on the dynamical effects induced by the strong correlations. This is done by mapping the two-dimensional square system onto an impurity problem coupled to a bath [103]. By solving the impurity problem it is thus possible to get the local Green function in the Hubbard model. It is important to note that solving the impurity problem itself is not a trivial task and that this is usually done via Monte-Carlo or exact diagonalisation methods. The main caveat of using this technique in the two-dimensional case is that the role of spatial correlations is ignored. This is an active area of development with improvements such as the cellular DMFT [104, 105] (CDMFT) that use the same mapping but use a small cluster coupled to a bath instead of a single impurity. Including vertex corrections is also a possible route to capture the spatial correlation within this computation scheme [106].

Lastly, there have been insights from real space techniques that are able to give precise information on the scale at which some properties emerge. One popular method is the Density Matrix

Renormalization Group (DMRG) which is exact in one dimension and tackles the exponential growth of the Hilbert space by diagonalizing separately a reduced part of the system by tracing over the density matrix. Applying this procedure iteratively is equivalent to a real space renormalization group procedure and can give good results for the low energy states. This technique is usually limited in higher dimensions where the number of sites in the sub-system still grows quadratically with its size and in the case where there is non-trivial entanglement across the whole system. DMRG still has been widely used to study the Hubbard model in few-leg ladders and has shown the formation of stripes as observed in some cuprates. There are also multiple extensions of DMRG that aim to study two-dimensional systems such as the Projected Entangled Pair States (PEPS) or the Multiscale Entanglement Renormalization Ansatz (MERA) which address the two limitations we mentioned by using the idea of tensor network states [107]. Infinite-PEPS give good variational ground state energy in the strongly-correlated regime of the 2D Hubbard model [108, 109] while MERA has been successfully used in the study of frustrated quantum magnets to study the spin liquid states [110].

Despite the difficulties, these numerical methods are able to extract numerous relevant information from the study of the two-dimensional Hubbard model. The particular case of half-filling is usually used as a benchmark and already reveals non-Fermi liquid behaviour even for weak interactions [111]. Pseudogap-like physics is also observed away from half-filling and a d-wave superconducting state is obtained in DMFT at strong coupling. The case of moderate coupling is more delicate and is still under intense investigation.

### 1.4.3 Intertwined orders and Quantum disordered PDW

Another approach more rooted in the phenomenology of the pseudogap is to consider that there exists preformed Cooper pairs at high temperature, in the pseudogap region, leading to a finite pairing amplitude outside the superconducting phase. These pairs would not condense due to phase fluctuations but still impact the electronic properties. For example, the Fermi arcs are explained by the partial destruction of the superconducting gap above  $T_c$ , the gap vanishing in the nodal region this is where we recover zero-energy electronic states first while the anti-nodal region is still subject to the incoherent pairing [112, 113]. This idea is deeply rooted in the ubiquitous presence of fluctuations in the pseudogap, however, as we mentioned previously in Sec.1.3.2, the observation of superconducting fluctuations only a few tens of Kelvin above  $T_c$  makes it difficult to explain the very high pseudogap temperature  $T^*$ . The idea is still very interesting from a phenomenological point of view and has been extended to include different kinds of preformed pairs to account for the multiple orders observed experimentally [75].

The vast complexity of the phase diagram in cuprates superconductors also pushed theoreticians to look for a higher principle to organize all the different symmetry-broken phases that are experimentally observed. One of the results of these tentatives is the idea of *intertwined* orders, where only a few of the observed ordered states are the true instability of the system but, due to competition or other effects, they combined in different ways to give rise to the whole plethora of phenomena observed [93]. One example is to start with the uniform superconducting state and the PDW state as *parent* phases and to explain the observation of charge density modulation by the coupling of these two orders. The CDW state is then called a *daughter* phase or a *vestigial* order.



In the particular example we choose, this could be obtained by considering both the expectation value of the SC and the PDW order parameters to be zero, *i.e.*

$$\begin{aligned}\langle |\Delta|^2 \rangle &= 0 \\ \langle |\Delta^Q|^2 \rangle &= 0,\end{aligned}\tag{1.4}$$

but to allow for a charge-neutral combination with finite momentum to have a non-vanishing expectation value :

$$\langle \Delta^Q \Delta^* \rangle \neq 0.\tag{1.5}$$

The number and the nature of the vestigial orders are obviously highly dependent on the starting parent phases chosen. This idea does have the benefit to reduce the number of states to consider as long as they can combine to generate the observed symmetry-broken states in the pseudogap. It can however be difficult to justify how the parent phases *intertwined* and how the different vestigial orders organized themselves with temperature and doping.

The difficulty to stabilize the PDW state in theoretical approaches also makes the idea of a peculiar disordered state interesting. The idea was motivated by the possibility of a kinetic-driven Amperean pairing [114] that could lead to a finite pairing correlation with finite centre-of-mass momentum. It was originally derived in a mean-field theory starting from an RVB picture where the spinon pairing was driven by a particular configuration of the emergent gauge field in this theory. This PDW is also directly responsible for the presence of a CDW state with a density modulation twice larger than than the pairing modulation. This charge density wave can be observed even if the PDW order is fluctuating as long as the relative phase fluctuations from  $\Delta^Q$  and  $\Delta^{-Q}$  are zero and is thus closely related to the idea of vestigial orders mentioned previously. The pseudogap is then described by a region where the modulated pairing amplitude is finite but where the order is destroyed by quantum phase fluctuations [115]. We can thus see this line of thought as the intersection of the preformed pairs theories and the intertwined orders theories which provide a microscopic argument starting from the RVB picture.

Our work can be thought of as building upon these previous ideas as it draws the quantum disorder PDW starting point but cast it using a different fractionalization hypothesis. In fact, we will consider that the electron quasiparticles are the good starting point but we notice that the PDW order can be split into two collective modes breaking the charge conservation and the translation symmetry separately, namely a CDW and an SC order. This fractionalization should take place at the pseudogap temperature  $T^*$  and does give Fermi arcs as well as other aspects of the physics of cuprates that we will study in Sec.3.2.1 and Sec.3.4. The region above the superconducting transition is governed by phase fluctuations that play an important role to obtain the pseudogap phenomenology as in the preformed pairs approaches. Lastly, the discrete symmetries such as time-reversal symmetry can be broken by a combination of the SC and CDW fluctuations when none of them is condensed in the spirit of vestigial orders [116]. Note that this approach where collective modes are fractionalized has also been explored starting from spin density wave fluctuations [117].

# Chapter 2

## Theoretical tools

### 2.1 Basic notions

#### 2.1.1 Second quantization

Second quantization and path integral formalism are two natural ways of dealing with many-body problems in quantum mechanics and there exists numerous connections between them. We will here present the important points of both formalisms in order to introduce notations and conventions. Exhaustive derivations of the different properties we will give can be found in Refs.[37, 118, 119] for example.

The starting point for the second quantization formalism is the idea of occupation number representation. It is based on the idea that we can build many-body states  $|\Psi\rangle$  from a complete basis of single-particle states  $\{|\nu_1\rangle, |\nu_2\rangle, \dots\}$  where  $\nu_i$  are quantum numbers labelling the single-particle states. The idea of the occupation number representation is to notice that only the occupied single-particle states are relevant in the description of  $|\Psi\rangle$  and that it is then sufficient to track the number of particles in each of the basis states. We can thus get a basis for the  $n$ -particle states given by

$$|n_{\nu_1}, n_{\nu_2}, \dots\rangle \quad \text{with} \quad \sum_j n_{\nu_j} = n, \quad (2.1)$$

where  $n_{\nu_i}$  is the number of particles in the state  $|\nu_i\rangle$ . We also define number operators  $\hat{n}_{\nu_i}$  whose eigenstates are the states  $|n_{\nu_i}\rangle$  with eigenvalue  $n_{\nu_i}$  and the creation (annihilation) operators  $c_{\nu_i}^\dagger$  ( $c_{\nu_i}$ ) that will change the occupation number by  $+1$  ( $-1$ ) through

$$\begin{aligned} \hat{n}_{\nu_i} |n_{\nu_i}\rangle &= n_{\nu_i} |n_{\nu_i}\rangle \\ c_{\nu_i}^\dagger |n_{\nu_i}\rangle &= \text{cst} |n_{\nu_i} + 1\rangle \quad \text{and} \quad c_{\nu_i} |n_{\nu_i}\rangle = \text{cst} |n_{\nu_i} - 1\rangle. \end{aligned} \quad (2.2)$$

Lastly, the symmetry properties of the many-body states with respect to the exchange of particles

are encoded in the algebra that the creation and annihilation operators obey. For fermions we have

$$\{c_{\nu_i}^\dagger, c_{\nu_j}^\dagger\} = \{c_{\nu_i}, c_{\nu_j}\} = 0 \quad \text{and} \quad \{c_{\nu_i}^\dagger, c_{\nu_j}\} = \delta_{\nu_i, \nu_j}. \quad (2.3)$$

A direct result of this anti-commutation relations is that  $(c_{\nu_i}^\dagger)^2 = 0$  which is a representation of the Pauli principle forbidding two fermions to occupy the same quantum state. The power of the formalism resides in the fact that all one-body operator can be written as quadratic combination of creation and annihilation operators, for which we give examples in Sec.2.2, while two-body operators are given by quartic combinations of  $c^\dagger$  and  $c$  as will be seen in Sec.2.3. The general forms in the basis  $\{|\nu_1\rangle, |\nu_2\rangle, \dots\}$  are

$$\begin{aligned} \hat{O}_{1-body} &= \sum_{i,j} O_{\nu_i, \nu_j} c_{\nu_i}^\dagger c_{\nu_j} \\ \hat{O}_{2-body} &= \sum_{i,j,k,l} O_{\nu_i, \nu_j, \nu_k, \nu_l} c_{\nu_i}^\dagger c_{\nu_j}^\dagger c_{\nu_l} c_{\nu_k} \end{aligned} \quad (2.4)$$

where  $O_{\nu_i, \nu_j}$  and  $O_{\nu_i, \nu_j, \nu_k, \nu_l}$  are the matrix elements of  $\hat{O}$  in the chosen basis. The other interesting properties of the creation operators is that we can easily adapt them to different choice of single-particle state basis. In fact, if we introduce a new single-particle basis  $\{|\mu_0\rangle, |\mu_1\rangle, \dots\}$  we have the following formula for the change of basis

$$c_{\mu_i} = \sum_j \langle \mu_i | \nu_j \rangle c_{\nu_j}. \quad (2.5)$$

We will in the following mainly be interested in systems where spin is a relevant quantum number and we will use the change of basis formula Eq.2.5 to change between a real space representation for the single particle states and the momentum space representation. To do so we only need to know the matrix element  $\langle \mathbf{x} | \mathbf{k} \rangle = e^{i\mathbf{k}\cdot\mathbf{r}}$  which give us the expression for the Fourier transform of annihilation operators

$$c_{\mathbf{k}\sigma} = \frac{1}{\sqrt{N}} \sum_j e^{i\mathbf{k}\cdot\mathbf{r}_j} c_{j\sigma}. \quad (2.6)$$

### 2.1.2 Green's functions

The other tool that we use in order to extract information from many-body Hamiltonians is the Green's function formalism. It comes from the general context of differential equations and can be applied to the time-dependent Schrödinger equation as well as for the time-evolution of many-body wave-functions. There are multiple different Green's functions that can be defined but we will mainly be concerned about the *retarded* electronic Green's function defined as

$$G_{\sigma\sigma'}^{ret}(x, t|x', t') = -i\theta(t-t') \left\langle \left\{ c_{\sigma}(x, t), c_{\sigma'}^\dagger(x', t') \right\} \right\rangle. \quad (2.7)$$

For translational invariant systems, it is often useful to work in momentum space representation where the Green function is diagonal and thus only depends on one momentum, we have a similar definition

$$G_{\sigma\sigma'}^{ret}(\mathbf{k}, t|t') = -i\theta(t-t') \left\langle \left\{ c_{\mathbf{k}\sigma}(t), c_{\mathbf{k}\sigma'}^\dagger(t') \right\} \right\rangle. \quad (2.8)$$

There are multiple ways of obtaining the retarded electronic Green's function or an approximation of it depending on the model studied. One instructive result is the one for non-interacting systems with eigenvalues in momentum space given by a dispersion relation  $\epsilon_{\mathbf{k}}$ , in this case, the single-particle Green's function for a chosen spin species is given by

$$G^{ret}(\mathbf{k}, \omega) = \frac{1}{\omega - \epsilon_{\mathbf{k}} + i\eta}, \quad (2.9)$$

where  $\eta$  is an infinitesimal offset that we need to send to zero. We can then see that the poles of the Green's function on the real axis correspond to the eigenvalue for a state with momentum  $\mathbf{k}$ . This form of the retarded Green's function is of particular importance as it allows us to get an understanding of the electronic spectral function defined by

$$\begin{aligned} A_{\sigma}(\mathbf{k}, \omega) &= -2\text{Im} G_{\sigma}^{ret}(\mathbf{k}, \omega) \\ &= 2\pi\delta(\omega - \epsilon_{\mathbf{k}}) \quad \text{for free electrons.} \end{aligned} \quad (2.10)$$

The electronic spectral function is thus a measure of the probability of an electron to occupy a state at with momentum  $\mathbf{k}$  and energy  $\omega$ . For free electrons it is a Dirac delta at  $\omega = \epsilon_{\mathbf{k}}$  as these are exact eigenstates of the systems. Another useful representation of the Green's function comes from the imaginary-time representation, in which the time coordinate is taken to be a complex number  $\tau \rightarrow it$ . this allows the study of finite-temperature effect and is also a very practical way of performing computations when doing perturbation expansion or treating interactions. The Matsubara Green's function is defined as

$$G(x, \tau | x', \tau') = -\theta(\tau - \tau') \left\langle T_{\tau} \left\{ c_{\sigma}(x, \tau), c_{\sigma'}^{\dagger}(x', \tau') \right\} \right\rangle, \quad (2.11)$$

where  $T_{\tau}$  is a time ordering operator. the imaginary time is limited to value between zero and the inverse temperature  $0 \leq \tau \leq \beta = \frac{1}{k_B T}$  and the electronic Matsubara Green's function is anti-periodic in  $\tau$  with period  $\beta$ . This means that the Matsubara Green's function is only defined for a set of discrete imaginary frequencies  $i\omega_n = \frac{(2n+1)\pi}{\beta}$ . There is an important link between the Matsubara Green's function and the retarded Green's function through analytical continuation  $i\omega_n \rightarrow \omega + i\eta$  which allows us to get physical quantities on the real frequency axis. Care must be taken when doing the analytical continuation as this implies a rotation in the complex planes, any singularities in the complex plane may make the procedure ill-defined. We usually perform this step at the end of the calculation and will mention any difficulty that we may encounter for specific cases.

### 2.1.3 Path-integral formalism

Rewriting many-body problems using the formalism of path integral is interesting as it allows to make use of the whole Quantum Field Theory techniques that have been developed in high-energy physics as well as make connection to the different phenomenon and idea present in classical statistical mechanics. Building the path-integral representation for a many-body problem usually start with the expression of the quantum partition function

$$\mathcal{Z} = \text{Tr} e^{-\beta(\hat{H} - \mu\hat{N})}, \quad (2.12)$$

where we introduced a chemical potential  $\mu$  to work in the grand canonical ensemble with an averaged number of particles  $n$ . The trace in Eq.(2.12) is to be taken over a complete basis of state. Using the notion of fermionic coherent states[37] we can rewrite this expression for the partition function as a functional integral over two complex functions

$$\mathcal{Z} = \int dc dc^* e^{-S(c, c^*)}, \quad \text{with } S[c, c^*] = \int_0^\beta d\tau [c^* \partial_\tau c + H(c, c^*) - \mu N(c, c^*)] \quad (2.13)$$

or in imaginary frequency representation

$$S[c, c^*] = \sum_{\omega_n} \left[ c^* \left( -i\omega_n - \mu + \hat{H}_0 \right) c + \hat{H}_{int}(c, c^*) \right] \quad (2.14)$$

Here it is important to note that to represent the fermionic statistic, the variable  $c^*$  and  $c$  are not ordinary number but *Grassman* variables. They retain the anti-commutation property of the fermionic creation and annihilation operators expressed in Eq.(2.3). The important result regarding the functional integral that appears in the path-integral formalism is the Gaussian integral that describe non-interacting system

$$\mathcal{Z} = \int dc dc^* e^{c^* \hat{H}_0 c} = \text{Det} \left( \hat{H}_0 \right) \quad (2.15)$$

where the determinant is taken over the basis of eigenstates. We can then define the quantum average as

$$\langle \dots \rangle_{S_0} = \text{Det} (S_0)^{-1} \int dc^* dc (\dots) e^{-c^* S_0 c} \quad (2.16)$$

and express it as the functional derivative with respect to external fields, as example for the free fermions

$$\begin{aligned} \langle c_i c_j^* \rangle_{S_0} &= \text{Det} \left( -i\omega_n - \mu + \hat{H}_0 \right)^{-1} \int dc^* dc c_i c_j^* e^{\sum_{\omega_n, i', j'} c_{i'}^* [(-i\omega_n - \mu)\delta_{i', j'} + \hat{H}_{0, i', j'}] c_{j'} - \phi c^* - \phi^* c} \\ &= \mathcal{Z}[0, 0] \left. \frac{\delta^2 \mathcal{Z}[\phi, \phi^*]}{\delta \phi \delta \phi^*} \right|_{\phi, \phi^* = 0} \\ &= \frac{1}{(i\omega_n + \mu) \delta_{i, j} - \hat{H}_{0, i, j}} \end{aligned} \quad (2.17)$$

which is consistent with the result obtained in Eq.(2.9) after analytical continuation and Fourier transform in momentum space.

We will use the tools describe here to formalize the microscopic and effective models we use to pseudogap phase of cuprate superconductors. The simple example we provided here are based on non-interacting systems and were kept general as to not be dependent on the details of the system, we will now give more applied example for both non-interacting (Sec.2.2) and interacting Hamiltonian (Sec.2.3) with a focus on superconductivity. We also come closer to the physics of cuprates in Sec.2.4 with a description of the fractionalization hypothesis coming from the idea of RVB states.

## 2.2 Non-interacting systems

### 2.2.1 Tight-binding models

One of the simplest models that one can write is one considering free electrons in metals. The usual way of representing the periodic potential associated with the lattice of ions in which the electron fluid is placed is by defining localized orbital states (Wannier orbitals) that overlap slightly and allow for electrons to jump from one to another. There can be multiple orbitals per lattice site and a maximum of two electrons per orbital as per the Pauli principle. The tight-binding Hamiltonian is thus given in real space by

$$H_{tb} = - \sum_{i,j,n_1,n_2,\alpha,\beta} t_{ij,n_1n_2,\alpha\beta} \left( c_{in_1\alpha}^\dagger c_{jn_2\beta} + \text{h.c.} \right), \quad (2.18)$$

where  $i$  and  $j$  are lattice site,  $\alpha$  and  $\beta$  are the electrons spin and  $n_1$  and  $n_2$  number the different orbitals. The hopping amplitude  $t_{ij,n_1n_2,\alpha\beta}$  represent the probability for an electron with spin  $\alpha$  in the orbital  $n_1$  at site  $i$  to hop in the orbital  $n_2$  at site  $j$  with spin  $\beta$ . Several simplifications can be made to this general form to treat different type of systems. The first one is to forbid spin-flip processes by requiring that the starting spin  $\alpha$  is the same as the final state spin  $\beta$ . These spin-flip can be necessary when the effect of magnetic field or of spin-orbit coupling are to be considered but we will not be interested in this cases further. We will in fact also consider the hopping amplitude to be spin-independent. One can also consider that the hopping processes only occurs between similar orbitals at different sites. This is equivalent as requiring  $n_1$  to be the same as  $n_2$  and can be justified when the different orbitals are far away in energy such that these hopping events are rare. In the case of cuprates, we will use a single-orbital approximation and thus we will omit the orbital quantum number. Lastly, it is possible to restrict the range over which the hopping is effective by setting  $t_{ij} = 0$  if  $|\mathbf{r}_i - \mathbf{r}_j| > r_{max}$ . The extreme limit of this approximation is to consider only nearest-neighbours hopping, *i.e.*  $t_{ij} = t(\delta_{i,i\pm\hat{x}} + \delta_{i,i\pm\hat{y}})$  where  $\hat{x}$  and  $\hat{y}$  are lattice vectors. This is an approximation that does not reproduce the normal state of cuprates but which does give good results in the low-energy description of graphene for example. The tight-binding model we will consider is thus written

$$H_{tb} = - \sum_{i,j,\sigma} t_{ij} \left( c_{i\sigma}^\dagger c_{j\sigma} + \text{h.c.} \right). \quad (2.19)$$

Note that this model is solely based on the lattice geometry that is contained into the hopping amplitude  $t_{ij}$ , despite this and even if we limits ourselves to two-dimensional systems there are very different results possible. Owing to the translation symmetry of the system we can diagonalize the Hamiltonian by going into momentum space. This is not possible if we want to study finite-size systems as will be explored in Chap.5. To proceed in solving the Hamiltonian in Eq.(2.19) we use the definition of the electronic operators in momentum space given in Eq.(2.6) and get

$$H_{tb} = \sum_{\mathbf{k},\sigma} \epsilon_{\mathbf{k}} c_{\mathbf{k}\sigma}^\dagger c_{\mathbf{k}\sigma}. \quad (2.20)$$

The *electronic dispersion*  $\epsilon_{\mathbf{k}}$  that appears is given by the Fourier transform of the hopping amplitude. In the most simple example of nearest-neighbour hopping on a square lattice this would

yield  $\epsilon_{\mathbf{k}} = -2t(\cos(k_x) + \cos(k_y))$ . During our study of cuprates we will allow for hopping up to the fourth neighbours and use the following electronic dispersion :

$$\begin{aligned} \epsilon_{\mathbf{k}} = & -2t(\cos(k_x) + \cos(k_y)) - 4t'\cos(k_x)\cos(k_y) - 2t''(\cos(2k_x) + \cos(2k_y)) \\ & - 4t'''(\cos(2k_x)\cos(k_y) + \cos(k_x)\cos(2k_y)). \end{aligned} \quad (2.21)$$

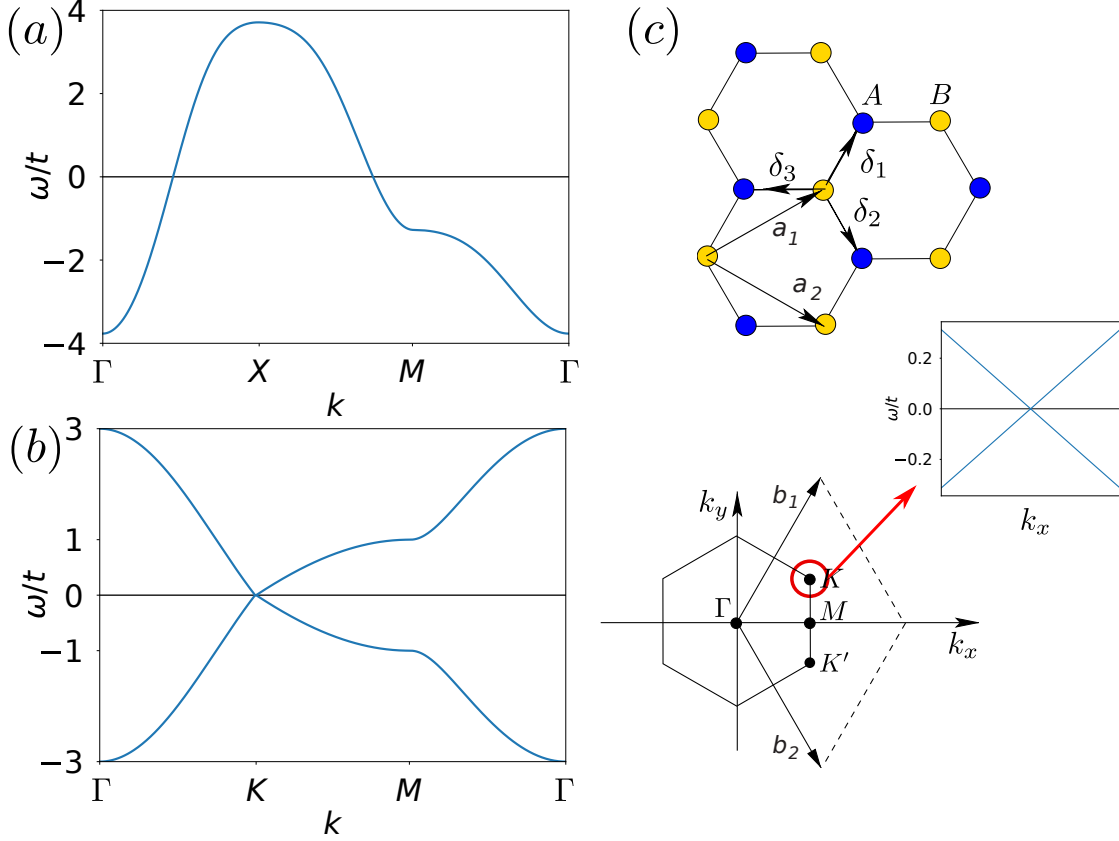


**Figure 2.1:** (a) Band structure for a typical underdoped cuprate dispersion  $\frac{t'}{t} = -0.156$ ,  $\frac{t''}{t} = 0.163$ ,  $\frac{t'''}{t} = -0.0326$  along the high-symmetry point in the Brillouin zone. We observe a hole pocket centred around the X point at momentum  $(\pi, \pi)$ . (b) Band structure for graphene with nearest-neighbour hopping. There are two bands per unit-cell leading to two bands that cross linearly at the K and K' points. Note that in both cases, the bandwidth is equal to  $2zt$  where  $z$  is the coordination number. (c) Top part, honeycomb lattice formed by a triangular lattice with two atoms (A and B) per unit cell. Bottom part, Brillouin zone for the honeycomb lattice with the position of the high symmetry points. Arrow indicates the Dirac point with the inset showing the linear crossing along the  $x$ -axis. Adapted from Ref.[120].

The values of the different hopping amplitudes are obtained from first-principle calculations such as Density Functional Theory or from a fit to ARPES data. We show in Fig.2.1(a) the electronic dispersion for  $\text{Pb}_{0.55}\text{Bi}_{1.5}\text{Sr}_{1.6}\text{La}_{0.4}\text{CuO}_{6+\delta}$  (Bi2201) for a cut along the high-symmetry points in the Brillouin zone where we used the following parameters :  $\frac{t'}{t} = -0.156$ ,  $\frac{t''}{t} = 0.163$ ,  $\frac{t'''}{t} = -0.0326$ . The nearest-neighbour hopping is usually taken as the energy scale in the problem and we can get quantity in absolute energy by using the fact that  $t \sim 300$  meV in most cuprates compound ( $t = 220$  meV in Bi2201). The electron's density  $n$  is given by the number of states

that are present below the Fermi level. It is common to work in the grand canonical ensemble and, instead of fixing  $n$ , use the chemical potential  $\mu$  to get the wanted average density. This is done by adding a term to the tight-binding Hamiltonian

$$H_{tb} \rightarrow H_{tb} - \mu \sum_i (n_{i\uparrow} + n_{i\downarrow}). \quad (2.22)$$

In momentum space this is equivalent to shifting the position of the reference energy, or equivalently to shift the electronic dispersion  $\epsilon_{\mathbf{k}} \rightarrow \epsilon_{\mathbf{k}} - \mu$ .

To highlight the role of the lattice geometry in the electronic properties of materials we also plot the electronic dispersion obtained by considering a honeycomb lattice, as seen in single-layer graphene, in Fig.2.1(b) along the high symmetry points of the hexagonal Brillouin zone (see Fig.2.1(c)). Because the honeycomb lattice is actually a triangular lattice with two atoms per unit cell, the electronic dispersion presents two bands. These bands are crossing at the  $K$  and  $K'$  points, named Dirac points, with a linear dispersion away from them. This linear relation between the momentum and the energy of the electrons eigenstates is responsible for a lot of the physical properties of graphene [120] and is also interesting from the theoretical perspective as a low-energy, continuous, theory for graphene will recover the Lorentz symmetry observed in high-energy physics.

## 2.3 Interacting systems

### 2.3.1 Perturbation expansion

There are multiple ways of implementing interactions in a second quantized Hamiltonian and it is possible to write the interaction term in a form similar to the general hopping term presented in Eq.(2.18). Because we will mostly be interested in the study of cuprate superconductors, we directly start with an approximated interaction that retains only an on-site density-density interaction, called the Hubbard interaction,

$$H_U = U \sum_i n_{i\uparrow} n_{i\downarrow}. \quad (2.23)$$

Note that the interaction term is not quadratic in fermionic operators and thus cannot be cast in to the Hamiltonian matrix form we used in the non-interacting case. We can also see that this on-site interaction is not diagonal in momentum space as

$$H_U = U \sum_{\mathbf{k}, \mathbf{k}', \mathbf{q}} c_{\mathbf{k}'+\mathbf{q}\uparrow}^\dagger c_{\mathbf{k}-\mathbf{q}\downarrow}^\dagger c_{\mathbf{k}\downarrow} c_{\mathbf{k}'\uparrow}, \quad (2.24)$$

and can be interpreted as a scattering event where electrons with opposite spins and momentum  $\mathbf{k}$  and  $\mathbf{k}'$  scatter off of each other and exchange a momentum  $\mathbf{q}$ .

One very natural way of studying interacting problems is to start from the known non-interacting solution and expand around it to capture the effects of interactions. This is a valid approach as long as the ground state of the system does not change drastically when interactions are turned on and gives very good results in describing the electron fluid in metals through the Fermi liquid theory. The caveat of this method is its inability to describe phase transition where the symmetry



of the ground states change when some parameters such as temperature, doping or interaction strength are tuned. We will however see that perturbation expansion can still capture the presence of such phase transition if one knows where to look for it.

We will present here the perturbation expansion for the single-particle Green's function and we thus start by defining the non-interacting Matsubara Green's function

$$G_0(\mathbf{k}, i\omega_n) = (i\omega_n + \epsilon_{\mathbf{k}})^{-1}, \quad (2.25)$$

where  $\omega_n$  is a fermionic Matsubara frequency (see Sec.2.1.2) and  $\epsilon_{\mathbf{k}}$  describe the non-interacting band structure. We will also deviate from the strict Hubbard interaction and consider a more general energy and momentum dependent interaction  $W(i\Omega_n, \mathbf{q})$  where  $\Omega_n$  is a bosonic Matsubara frequency. There are multiple ways of deriving the perturbation series for the electronic Green's function and derivations can be found in Refs.[37, 118] while we start here with the resulting Dyson equation in momentum space which relate the interacting Green's function  $G(i\omega_n, \mathbf{k})$  to the non-interacting  $G_0$ :

$$G(i\omega_n, \mathbf{k}) = G_0(i\omega_n, \mathbf{k}) + G_0(i\omega_n, \mathbf{k}) \Sigma(i\omega_n, \mathbf{k}) G(i\omega_n, \mathbf{k}). \quad (2.26)$$

In the Dyson equation, all the effects of the interactions are captured by the *self-energy* operator  $\Sigma(i\omega_n, \mathbf{k})$ . This equation is exact but it is not possible to compute the self-energy exactly in any realistic problem and approximation on the treatment of the interactions are generally done at the level of the self-energy. We can first note that the Dyson equation can be rewritten as

$$\begin{aligned} G(i\omega_n, \mathbf{k}) &= \frac{G_0(i\omega_n, \mathbf{k})}{1 - G_0(i\omega_n, \mathbf{k}) \Sigma(i\omega_n, \mathbf{k})} = \frac{1}{G_0(i\omega_n, \mathbf{k})^{-1} - \Sigma(i\omega_n, \mathbf{k})} \\ &= \frac{1}{i\omega_n + \epsilon_{\mathbf{k}} - \Sigma(i\omega_n, \mathbf{k})}. \end{aligned} \quad (2.27)$$

Using Eq.(2.25) in the last line allows us to highlight how the interactions, captured by  $\Sigma$  will modify the non-interacting Green's function. The real part of the self-energy will change the band structure by shifting the position of the pole at a given momentum while the imaginary part will induce a finite lifetime for the electronic eigenstates which result in a broadening of the electronic levels. In order to build the perturbation expansion we start by associating a diagrammatic representation for the full and non-interacting Green functions as well as the interaction term :

$$\begin{aligned} G_0(i\omega_n, \mathbf{k}) &= \text{---} \overleftarrow{\omega_n, k} \text{---} & G(i\omega_n, \mathbf{k}) &= \text{====} \overleftarrow{\omega_n, k} \text{====} \\ W(i\Omega_n, \mathbf{q}) &= \text{-----} \Omega_n, q \text{-----} \end{aligned} \quad (2.28)$$

The self-energy is then given by “the sum of all the irreducible diagrams with the external legs

removed” which we build in the following way up to the second order in the interaction :

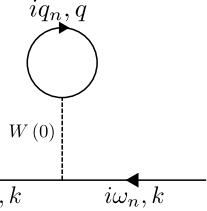
$$\Sigma(i\omega_n, \mathbf{k}) = \text{[diagrammatic expansion]} \quad (2.29)$$

Here we kept the external legs to indicate at which energy and momentum the self-energy is computed but they will not be taken into account in the computation of the diagrams. We see that there are two first order diagrams usually named the Hartree and the Fock term, respectively. There are then six second order diagrams, although some of them can cancel by symmetry depending on the form of the interaction. These diagrams can be thought of as physical scattering processes but they are first and foremost a graphical representation of a mathematical expression. The diagrammatic expansion has to be supplemented by the “Feynman” rules that allows one to evaluate them, for the electron systems these are as follow :

- Multiply each diagram by  $(-1)^F$ ,  $F$  being the number of fermion loops.
- Multiply  $G_0(iq_n, \mathbf{q})$  by  $e^{iq_n \eta}$  in the same time diagram (closed loop with one fermion line).
- Perform summation over each internal momenta and Matsubara frequency and multiply by a factor  $\frac{1}{\beta N}$  where  $\beta = k_B T$  is the inverse temperature and  $N$  is the number of sites.

As an example we can compute the contribution from the Hartree term to the self-energy. This is convenient as the form of the interaction does not play an important role in the final result. In fact, because the incoming and outgoing momenta have to be equal, the transferred momentum through the interaction is zero and the momentum running in the loop is only the internal momentum  $\mathbf{q}$ . Following the Feynman rules given above, we will have a summation over the  $\mathbf{q}$  and an internal fermionic Matsubara energy  $q_n$  and we get an overall factor  $\frac{-1}{\beta N}$ . Using the definitions in E.(2.28)

we get



$$\begin{aligned} \Sigma_{Hartree}(i\omega_n, \mathbf{k}) &= \frac{-1}{\beta N} \sum_{\sigma, \mathbf{q}, i q_n} (-W(0)) G_0(i q_n, \mathbf{q}) e^{i q_n \eta}. \end{aligned} \quad (2.30)$$

The factor  $\eta$  in the exponential is here to ensure the convergence of the Matsubara sum and will be taken to zero at the end of the calculation. The standard techniques to perform this energy integration is to use the equivalence with the integration over a closed contour in the complex plane [37, 118] and we will directly use the result here while converting the finite sum over momenta to a continuous integral :

$$\begin{aligned} \Sigma_{Hartree}(i\omega_n, \mathbf{k}) &= \frac{2W(0)}{\beta} \int \frac{dq}{(2\pi)^d} \sum_{i q_n} \frac{e^{i q_n \eta}}{i q_n - \epsilon_{\mathbf{q}}} \\ &= 2W(0) \int \frac{dq}{(2\pi)^d} n_F(\epsilon_{\mathbf{q}}), \end{aligned}$$

where we introduced the Fermi function  $n_F$  and  $d$  is the spatial dimension of the problem. The integral can be done exactly as it counts the numbers of states that are occupied in the Brillouin zone which is related to the density of electrons  $n$ , leading to the final result

$$\Sigma_{Hartree}(i\omega_n, \mathbf{k}) = W(0) n. \quad (2.31)$$

We can thus see that the Hartree term captures the renormalization of the chemical potential by the uniform part of the interaction  $W(0)$ . The procedure used here can be used to compute all the diagrams but is in practice not tractable for higher-order diagrams when the number of momentum-energy sums increases. In fact, the second-order diagrams shown in Eq.(2.29) already involve three internal momenta. The perturbative expansion of the self-energy is thus exact if one can compute all the diagrams but has to be approximated in all the practical cases.

In the case of small interaction it is possible to truncate the expansion at a given interaction order. In fact, all the diagrams are proportional to  $U^{n_W}$  where  $n_W$  denote the number of interaction lines and  $U$  is the scale of the interaction. As such the contribution of higher-order diagrams will be highly reduced for small interactions.

There is also some families (or topology) of diagrams that can be *resummed* to all orders. This means that we can rewrite the infinite sum of diagrams with the same topology as a series expansion and use this to find a close equation to define a renormalized interaction. One example of this idea is given by the Random Phase Approximation (RPA) [121–123] that is known to give good results in the limit of high density where screening of the interaction is important. RPA is based on the fact that at every order of the expansion we can find diagrams that differ only by the inclusion of

a particle-hole bubble,

$$\Sigma_{RPA} = \text{[diagram 1]} + \text{[diagram 2]} + \text{[diagram 3]} + \text{[diagram 4]} + \dots \quad (2.32)$$

If we focus on this family of diagrams we can rewrite the related self-energy contribution as a first order diagram with a renormalized interaction :

$$\Sigma_{RPA} = \text{[diagram 1]} \times \left( \text{[diagram 1]} + \text{[diagram 2]} + \text{[diagram 3]} + \text{[diagram 4]} + \dots \right) = \text{[diagram 1]} \quad (2.33)$$

This renormalized interaction follows a Dyson like equation that we can invert to get a close expression involving only the bare interaction and the single particle-hole bubble :

$$\begin{aligned} -W_{RPA} &= \text{[diagram 1]} \\ &= \text{[diagram 1]} + \text{[diagram 2]} + \text{[diagram 3]} + \text{[diagram 4]} + \dots \\ &= \text{[diagram 1]} + \text{[diagram 2]} \times \left( \text{[diagram 1]} + \text{[diagram 2]} + \text{[diagram 3]} + \dots \right) \\ &= \text{[diagram 1]} + \text{[diagram 2]} \times \text{[diagram 1]} \\ &= \frac{\text{[diagram 1]}}{1 - \text{[diagram 2]}} \end{aligned} \quad (2.34)$$

Computing the self-energy given in Eq.(2.33) by using the renormalized interaction is thus formally equivalent to taking into account all the diagrams shown in Eq.(2.32) to all order in interaction strength. Limiting the computation of  $\Sigma(i\omega_n, \mathbf{k})$  to this RPA resummation is still a consequent approximation as all the other diagram's topology are ignored. This type of resummation is also available for other family of diagrams such as in the particle-hole or particle-particle ladder approximations [124].

### 2.3.2 Mean-field decoupling and BCS theory

The perturbative expansion we described above is based on the assumption that the ground state, described by the non-interacting  $G_0$ , is not drastically changed when interactions are taken into account. This is however not the case when considering phase transitions, where the symmetry of

the ground state changes, as a function of temperature or interaction strength. We will here give an overview of the mean-field method that can capture such symmetry-breaking ground states and we will apply it to the infamous BCS Hamiltonian to study the superconducting transition.

Thanks to the earlier work on the Cooper problem [6], the idea that an attractive interaction can lead to the formation of pairs of electrons was present when the BCS theory was developed. Some questions remained however, such as how to get electrons, all negatively charged particles, to attract each other and how do these Cooper pairs can lead to a dissipationless current and perfect diamagnetism. We will not answer any of these here as we will start with an effective Hamiltonian that already contains the attractive interaction. We will also not discuss the electromagnetic properties of superconductors but instead, we will be interested in the electronic DOS and the critical temperature. We thus start with a Hamiltonian in momentum space that reads [7] :

$$H_{BCS} = \sum_{\mathbf{k}} \epsilon_{\mathbf{k}} c_{\mathbf{k}\sigma}^{\dagger} c_{\mathbf{k}\sigma} + \sum_{\mathbf{k}, \mathbf{q}} V_{\mathbf{k}, \mathbf{q}} c_{\mathbf{k}\uparrow}^{\dagger} c_{-\mathbf{k}\downarrow}^{\dagger} c_{-\mathbf{q}\downarrow} c_{\mathbf{q}\uparrow} \quad (2.35)$$

The basis of the mean-field approximation lies in the *decoupling* of the interaction term in different channels which depends on which correlations we think are relevant to the physics of the system. For the particular interaction in Eq.(2.35) we obtain

$$\begin{aligned} c_{\mathbf{k}\uparrow}^{\dagger} c_{-\mathbf{k}\downarrow}^{\dagger} c_{-\mathbf{q}\downarrow} c_{\mathbf{q}\uparrow} &\sim \left\langle c_{\mathbf{k}\uparrow}^{\dagger} c_{-\mathbf{k}\downarrow}^{\dagger} \right\rangle c_{-\mathbf{q}\downarrow} c_{\mathbf{q}\uparrow} + c_{\mathbf{k}\uparrow}^{\dagger} c_{-\mathbf{k}\downarrow}^{\dagger} \left\langle c_{-\mathbf{q}\downarrow} c_{\mathbf{q}\uparrow} \right\rangle \\ &- \left\langle c_{\mathbf{k}\uparrow}^{\dagger} c_{-\mathbf{q}\downarrow} \right\rangle c_{-\mathbf{k}\downarrow}^{\dagger} c_{\mathbf{q}\uparrow} - c_{\mathbf{k}\uparrow}^{\dagger} c_{-\mathbf{q}\downarrow} \left\langle c_{-\mathbf{k}\downarrow}^{\dagger} c_{\mathbf{q}\uparrow} \right\rangle \\ &+ \left\langle c_{\mathbf{k}\uparrow}^{\dagger} c_{\mathbf{q}\uparrow} \right\rangle c_{-\mathbf{k}\downarrow}^{\dagger} c_{-\mathbf{q}\downarrow} + c_{\mathbf{k}\uparrow}^{\dagger} c_{\mathbf{q}\uparrow} \left\langle c_{-\mathbf{k}\downarrow}^{\dagger} c_{-\mathbf{q}\downarrow} \right\rangle \end{aligned} \quad (2.36)$$

Replacing the interaction term from Eq.(2.35) by the expression Eq.(2.36) will then yield a quadratic Hamiltonian. There are however two details that prevent the resulting mean-field Hamiltonian  $H_{mf}$  to be solved directly, the first one being the presence of the correlation functions. In fact, we need the system's Green's function to evaluate this correlation value and the Green's function is directly tied to the Hamiltonian. We thus have a self-consistent equation to solve to get the final result. The second details that require our attention is the presence of the particle-particle terms that appears on the first line of our decoupling  $\left\langle c_{\mathbf{k}\uparrow}^{\dagger} c_{-\mathbf{k}\downarrow}^{\dagger} \right\rangle$  and  $\left\langle c_{-\mathbf{q}\downarrow} c_{\mathbf{q}\uparrow} \right\rangle$ . These correlations are usually deemed anomalous because they are directly related to the charge conservation in the system. In fact, a non-zero value of these quantum average means that there is a non-zero overlap between states with different numbers of particles, breaking the charge conservation of the Hamiltonian. This is precisely the symmetry breaking phenomenon we want to describe using mean-field theory. For this, we assume that these correlations are finite and we evaluate them by using the self-consistent equation mentioned previously. It is then important to compare the free energy of the system in the broken symmetry states against the normal state to be sure that the new phase is thermodynamically favored. Before continuing, we can note the the second and third lines in Eq.(2.36) correspond to the Fock and to the Hartree terms respectively, we obtained by treating the interaction in a perturbative expansion in Sec.2.3.1. Those can lead to magnetic or translation symmetry breaking but we will ignore them here to focus on the pairing instability.

We proceed by replacing our interaction term by the mean-field expression retaining only the

pairing terms and get

$$H_{mf} = \sum_{\mathbf{k}} \epsilon_{\mathbf{k}} c_{\mathbf{k}\sigma}^{\dagger} c_{\mathbf{k}\sigma} - \sum_{\mathbf{k}} \left( \Delta_{\mathbf{k}} c_{\mathbf{k}\uparrow}^{\dagger} c_{-\mathbf{k}\downarrow}^{\dagger} + \text{h.c.} \right) - \sum_{\mathbf{k}, \mathbf{q}} V_{\mathbf{k}, \mathbf{q}} \left\langle c_{\mathbf{k}\uparrow}^{\dagger} c_{-\mathbf{k}\downarrow}^{\dagger} \right\rangle \left\langle c_{-\mathbf{q}\downarrow} c_{\mathbf{q}\uparrow} \right\rangle \quad (2.37)$$

where we introduced the gap function :

$$\Delta_{\mathbf{k}} = - \sum_{\mathbf{q}} V_{\mathbf{k}, \mathbf{q}} \left\langle c_{-\mathbf{q}\downarrow} c_{\mathbf{q}\uparrow} \right\rangle. \quad (2.38)$$

We now want to evaluate the correlation in the right-hand side of Eq.(2.38) to obtain the self-consistent equation for our mean-field approximation. There are multiple ways of doing so, either by means of a Bogoliubov transformation [125, 126], minimization of the free energy [118] or by using the Nambu-Gorkov formalism [127, 128]. We will follow a way similar to the latter one by introducing a matrix Green's function

$$\begin{aligned} \hat{G}(\tau, \mathbf{k}) &= \begin{pmatrix} -\left\langle T_{\tau} c_{\mathbf{k}\uparrow}(\tau) c_{\mathbf{k}\uparrow}^{\dagger}(0) \right\rangle & -\left\langle T_{\tau} c_{\mathbf{k}\uparrow}(\tau) c_{-\mathbf{k}\downarrow}(0) \right\rangle \\ -\left\langle T_{\tau} c_{-\mathbf{k}\downarrow}^{\dagger}(\tau) c_{\mathbf{k}\uparrow}^{\dagger}(0) \right\rangle & -\left\langle T_{\tau} c_{-\mathbf{k}\downarrow}^{\dagger}(\tau) c_{-\mathbf{k}\downarrow}(0) \right\rangle \end{pmatrix} \\ &= \begin{pmatrix} G_{\uparrow\uparrow}(\tau, \mathbf{k}) & F_{\downarrow}(\tau, \mathbf{k}) \\ -F_{\downarrow\uparrow}(-\tau, \mathbf{k})^{\dagger} & G_{\downarrow\downarrow}(-\tau, -\mathbf{k})^{\dagger} \end{pmatrix}. \end{aligned} \quad (2.39)$$

It is clear here that the correlation that appears in Eq.(2.38) will be related to the *anomalous* Green's function  $F_{\downarrow\uparrow}(-\tau, \mathbf{k})^{\dagger}$ . We can obtain a close form for the diagonal and off-diagonal terms by considering the equation-of-motion for  $\hat{G}$ . After going to Matsubara frequencies, we obtain

$$\begin{pmatrix} i\omega_n - \epsilon_{\mathbf{k}} & \Delta_{\mathbf{k}} \\ \Delta_{\mathbf{k}}^* & -i\omega_n - \epsilon_{\mathbf{k}} \end{pmatrix} \hat{G}(i\omega_n, \mathbf{k}) = 1. \quad (2.40)$$

We obtain a closed system by taking the top left and bottom left elements of this equation

$$\begin{aligned} &\begin{cases} (i\omega_n - \epsilon_{\mathbf{k}}) G_{\uparrow\uparrow}(i\omega_n, \mathbf{k}) - \Delta_{\mathbf{k}} F_{\downarrow\uparrow}(i\omega_n, \mathbf{k}) = 1 \\ \Delta_{\mathbf{k}}^* G_{\uparrow\uparrow}(i\omega_n, \mathbf{k}) - (i\omega_n + \epsilon_{\mathbf{k}}) F_{\downarrow\uparrow}(i\omega_n, \mathbf{k}) = 0 \end{cases} \\ \Leftrightarrow &\begin{cases} (i\omega_n - \epsilon_{\mathbf{k}}) G_{\uparrow\uparrow}(i\omega_n, \mathbf{k}) - \frac{|\Delta_{\mathbf{k}}|^2 G_{\uparrow\uparrow}(i\omega_n, \mathbf{k})}{i\omega_n + \epsilon_{\mathbf{k}}} = 1 \\ F_{\downarrow\uparrow}(i\omega_n, \mathbf{k}) = \frac{\Delta_{\mathbf{k}}^* G_{\uparrow\uparrow}(i\omega_n, \mathbf{k})}{(i\omega_n + \epsilon_{\mathbf{k}})} \end{cases} \\ \Leftrightarrow &\begin{cases} G_{\uparrow\uparrow}(i\omega_n, \mathbf{k}) = \frac{i\omega_n + \epsilon_{\mathbf{k}}}{(i\omega_n)^2 - \epsilon_{\mathbf{k}}^2 - |\Delta_{\mathbf{k}}|^2} \\ F_{\downarrow\uparrow}(i\omega_n, \mathbf{k}) = \frac{\Delta_{\mathbf{k}}^*}{(i\omega_n)^2 - \epsilon_{\mathbf{k}}^2 - |\Delta_{\mathbf{k}}|^2} \end{cases}. \end{aligned} \quad (2.41)$$

We finally get the electronic Green's function for up-spin electrons, which will be equivalent for down-spin electrons, and the expression for the anomalous Green function.

It is instructive to take a moment to look at how a non-zero pairing amplitude will affect the electronic dispersion. First of all, we can note that the electronic Green's function reduces to

the non-interacting one when  $\Delta_{\mathbf{k}} \rightarrow 0$ . Secondly, we can see that if we make the approximation that the order parameter is independent of momentum, which is a good approximation for the attractive interaction due to electron-phonon coupling, there are no poles of the Green's function for  $\omega < \Delta$ . The band structure can be seen as resulting from the hybridization of an electron band with dispersion  $\epsilon_{\mathbf{k}}$  and a hole band with dispersion  $-\epsilon_{\mathbf{k}}$  with a gap  $\Delta$  opening at the intersection as is shown in Fig.2.2(a). This gap can be directly related to the one seen in STS experiments mentioned in Chap.1. In fact, we can get an expression for the DOS for positive energy in the superconducting state and we find

$$\begin{aligned} \rho(\omega) &= \frac{1}{2\pi N^d} \sum_{\mathbf{k}} A(\mathbf{k}, \omega) \\ &= \frac{-1}{\pi N^d} \sum_{\mathbf{k}} \text{Im} G_{\uparrow\uparrow}^{ret}(\mathbf{k}, \omega) \\ &= \frac{-1}{\pi N^d} \sum_{\mathbf{k}} \text{Im} G_{\uparrow\uparrow}(\mathbf{k}, i\omega_n \rightarrow \omega + i\eta) \\ &= \frac{\omega}{\sqrt{\omega^2 + \Delta^2}} \theta(\omega - \Delta), \end{aligned} \quad (2.42)$$

where  $\theta(x)$  is the Heaviside function. The result is plotted in Fig.2.2(b) and is well understood when compared to the band structure.

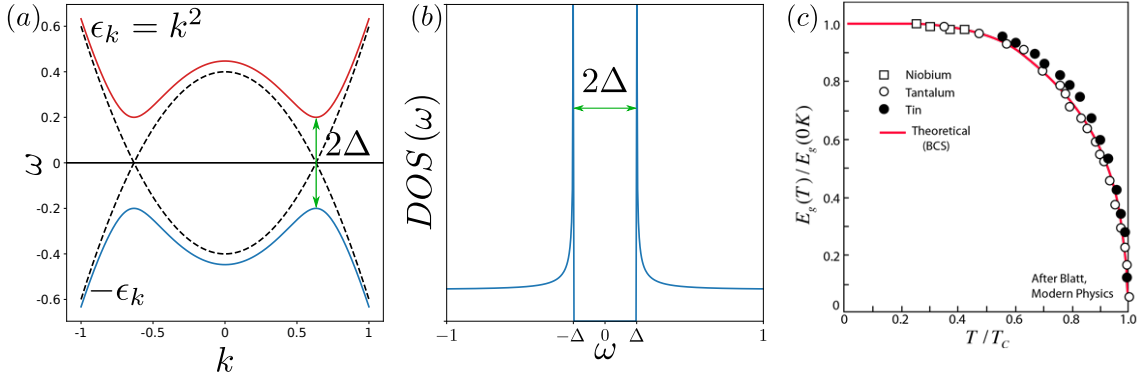


**Figure 2.2:** *a)* Example of the change in the band structure in the superconducting state. The black dashed lines show the original non-interacting band  $\epsilon_{\mathbf{k}} = k^2$  and the equivalent “hole” band  $-\epsilon_{\mathbf{k}}$  which cross at the Fermi level by symmetry as  $\epsilon_{\mathbf{k}_F} = 0 = -\epsilon_{\mathbf{k}_F}$ . In the superconducting state these two bands hybridize with a coupling  $\Delta$ , leading to new quasiparticle bands  $\pm E_{\mathbf{k}} = \pm \sqrt{\epsilon_{\mathbf{k}}^2 + \Delta^2}$  represented by the blue and red lines. These are separated by a direct gap  $2\Delta$ . *b)* DOS in the superconducting state from the BCS theory given by Eq.(2.42). We see that the DOS vanishes for energies below the gap  $|\omega| < \Delta$  in agreement with the band structure from panel (a). This is in very good agreement with the measured DOS in BCS superconductor as presented in Fig.1.4. *c)* Temperature dependence of the superconducting gap obtained from the BCS theory and compared to experimental data from different BCS superconductors. Adapted from Ref.[129].

The anomalous Green's function vanishes when the gap function goes to zero, it is thus only present in the broken-symmetry state. We can now use the result of Eq.(2.41) in Eq.(2.38) to find

a self-consistent equation for  $\Delta_{\mathbf{k}}$ . In fact,

$$\Delta_{\mathbf{k}} = - \sum_{\mathbf{q}} V_{\mathbf{k},\mathbf{q}} \langle c_{-\mathbf{q}\downarrow} c_{\mathbf{q}\uparrow} \rangle = \frac{1}{\beta} \sum_{\mathbf{q}, \omega_n} V_{\mathbf{k},\mathbf{q}} F_{\downarrow\uparrow}^*(i\omega_n, \mathbf{k}) e^{i\omega_n \eta}. \quad (2.43)$$

It is now important to remember that the interaction  $V_{\mathbf{k},\mathbf{q}}$  is taken as being the renormalized interaction due to the electron-phonon scattering [7] and as such is attractive when the characteristic energy scale of the electrons is below the scale of the phonons mediating the interaction, this is expressed by :

$$V_{\mathbf{k},\mathbf{q}} = \begin{cases} -V & \text{if } \epsilon_{\mathbf{k}}, \epsilon_{\mathbf{q}} < \omega_D \\ 0 & \text{otherwise} \end{cases} \quad (2.44)$$

Using Eqs.(2.41) and (2.44) in Eq.(2.43) we get

$$\begin{aligned} \Delta_{\mathbf{k}} &= \frac{-V}{\beta} \sum_{\mathbf{q}}^{\epsilon_{\mathbf{q}} < \omega_D} \sum_{\omega_n} \frac{\Delta_{\mathbf{q}} e^{i\omega_n \eta}}{(i\omega_n)^2 - \epsilon_{\mathbf{q}}^2 - |\Delta_{\mathbf{q}}|^2} \\ &= -V \sum_{\mathbf{q}}^{\epsilon_{\mathbf{q}} < \omega_D} \Delta_{\mathbf{q}} \left( \frac{n_f(E_{\mathbf{q}})}{2E_{\mathbf{q}}} + \frac{n_f(-E_{\mathbf{q}})}{-2E_{\mathbf{q}}} \right) \\ &= V \sum_{\mathbf{q}}^{\epsilon_{\mathbf{q}} < \omega_D} \Delta_{\mathbf{q}} \frac{1 - 2n_f(E_{\mathbf{q}})}{2E_{\mathbf{q}}} \end{aligned} \quad (2.45)$$

where  $E_{\mathbf{k}} = \sqrt{\epsilon_{\mathbf{k}}^2 + |\Delta_{\mathbf{k}}|^2}$  is the electronic dispersion in the superconducting state as given by the poles of  $G_{\uparrow\uparrow}(i\omega_n, \mathbf{k})$ . The solution to the Eq.(2.45) can be found numerically but for the case of momentum independent interaction as we consider here it is usual to assume that the gap function will not depend on momentum, *i.e.*  $\Delta_{\mathbf{k}} \rightarrow \Delta_0$ . we can then simplify both side of the equation and replace the momentum summation by a continuous energy integral to obtain the BCS gap equation:

$$1 = V\rho_0 \int_{-\omega_D}^{\omega_D} d\epsilon_{\mathbf{k}} \frac{\tanh\left(\frac{\beta}{2} \sqrt{\epsilon_{\mathbf{k}}^2 + \Delta_0^2}\right)}{2\sqrt{\epsilon_{\mathbf{k}}^2 + \Delta_0^2}} \quad (2.46)$$

where  $\rho_0$  is the density of states at the Fermi level. The full temperature dependence of the value of the gap function is given by  $\beta = \frac{1}{k_B T}$  in the numerator and the solution as a function of  $T - T_c$  is shown in Fig.2.2(c) and compared to experimental results. We can also derive an analytical solution to this integral equation in two limits, the zero-temperature limit and the vanishing gap limit. Finding the value of the gap  $\Delta_0(0)$  as  $T \rightarrow 0$  is done by noticing that the argument of the hyperbolic tangent is positive and that  $\beta = \frac{1}{k_B T} \rightarrow \infty$ . The numerator of the integrand is thus strictly equal to one and we get

$$\begin{aligned} V\rho_0 \int_{-\omega_D}^{\omega_D} d\epsilon_{\mathbf{k}} \frac{1}{2\sqrt{\epsilon_{\mathbf{k}}^2 + \Delta_0^2}} &= V\rho_0 \sinh^{-1}\left(\frac{\omega_D}{|\Delta_0(0)|}\right) = 1 \\ \xrightarrow{V\rho_0 \ll 1} |\Delta_0(0)| &= 2\omega_D e^{\frac{-1}{V\rho_0}} \end{aligned} \quad (2.47)$$

The approximation  $V\rho_0 \ll 1$  is known as the weak-coupling limit.

The other limit in which the superconducting gap vanishes allow us to get an analytical expression for the critical temperature at which the superconducting temperature takes place. For



this, we consider the limit of Eq.(2.46) when  $\Delta_0 \rightarrow 0^+$  leading to

$$\begin{aligned} V\rho_0 \int_0^{\omega_D} d\epsilon_{\mathbf{k}} \frac{\tanh\left(\frac{\epsilon_{\mathbf{k}}}{2k_B T_c}\right)}{\epsilon_{\mathbf{k}}} &= 1 \\ \longrightarrow k_b T_c &= \frac{2}{\pi} e^{\gamma} \omega_D e^{\frac{-1}{V\rho_0}} \\ &\sim 1.13 \omega_D e^{\frac{-1}{V\rho_0}} \end{aligned} \quad (2.48)$$

Where  $\gamma \sim 0.577$  is the Euler constant. Once again, the result in the weak coupling limit depends only on the three energy scales associated with the strength of the interaction ( $V$ ) and the number of fermions that feels the attractive interaction ( $\rho_0$  and  $\omega_D$ ). We see here that the density of states at the Fermi level plays an important role in determining the critical temperature for the superconducting transition. We also see that the gap-to-temperature ratio is independent of the physical parameters and, when the weak-coupling approximation is valid, gives

$$\frac{2|\Delta_0(0)|}{k_b T_c} \sim 3.53. \quad (2.49)$$

As we discussed in Chap.1, this is valid for a wide range of metallic superconductors and is one example of the power of the BCS theory.

We have here taken the example of a particular interaction that leads to a state breaking the charge conservation symmetry of the Hamiltonian. The mean-field theory can be applied to many other symmetry-breaking states and the difficulty often resides in the choice of the relevant channels to consider. It is also possible to consider multiple possible orders that can be generated by the decoupling of the interaction term but the set of coupled self-consistent equations that are needed to be solved is in general difficult to treat precisely. When looking at the underdoped region in cuprate superconductors, the two main candidates we will consider are the superconducting and the CDW orders while the effect of antiferromagnetism will be captured through the effective interaction. We will treat the competition and coexistence of SC and CDW orders in a mean-field theory in Sec.3.2.2.

## 2.4 Fractionalization

### 2.4.1 From Hubbard to $t - J$ model

The study of cuprate superconductors is usually based on the two-dimensional Hubbard model. It is in fact believed that in the moderate to strong correlation regime, this simple model based on on-site repulsion can capture the pseudogap phenomenology and the high-temperature superconductivity. The Hubbard model [130–132] is simply written in terms of a hopping term analogous to  $H_{tb}$  in Eq.(2.19) and a density-density interaction as presented in Eq.(2.23) yielding

$$H_{\text{Hubbard}} = \sum_{i,j,\sigma} t_{ij} \left( c_{i\sigma}^\dagger c_{j\sigma} + \text{h.c.} \right) + U \sum_i \hat{n}_{i\uparrow} \hat{n}_{i\downarrow} - \mu \sum_i \hat{n}_i. \quad (2.50)$$

To gain insight on the physics captured by the Hubbard model, we start in a way analogous to the study of non-interacting systems by considering the atomic limit, *i.e.* setting the hopping amplitude  $t = 0$ . This is a drastic simplification as it is equivalent to considering only one site and the associated four quantum states. The eigenstates of the Hamiltonian then have eigenvalues that depend in the number of electrons

$$\begin{aligned} \langle \emptyset | H_U | \emptyset \rangle &= 0 & \langle \uparrow\downarrow | H_U | \uparrow\downarrow \rangle &= U - 2\mu \\ \langle \uparrow | H_U | \uparrow \rangle &= -\mu & \langle \downarrow | H_U | \downarrow \rangle &= -\mu \end{aligned} \quad (2.51)$$

The sign of the chemical potential will thus decide if the site is empty ( $\mu < 0$ ) or occupied ( $\mu > 0$ ) in the ground state. Furthermore, there is a energy barrier to get two electrons on the same site given by  $U$ . The solution we obtain in the atomic limit, which present highly localized states separated by an energy gap of order  $U$ , is very different from the solution of the non-interacting tight-binding model we presented in Sec.2.2, showing totally delocalized and gapless continuum of states. The competition between the tendency to delocalize the electron's wavefunction from the hoping term and the localization effect due to the interaction term is at the core of the difficulty in treating the full Hubbard model. Turning on the hopping term can be done in a perturbative way starting from the atomic limit and is a good way to study the very low doping region. For this, we start with a half-filled ground state with as many up and down electrons written as

$$\sum_i (\hat{n}_{i\uparrow} + \hat{n}_{i\downarrow}) |0\rangle = |0\rangle \quad (2.52)$$

Here  $|0\rangle$  design the fact that we have no doubly-occupied sites and it is then easy to see that  $H_U |0\rangle = 0$  and our zeroth-order energy is  $E_0^{(0)} = 0$ . The first-order correction in our perturbation theory is given by :

$$E_0^{(1)} = \langle 0 | H_{tb} | 0 \rangle = 0 \quad (2.53)$$

The first-order correction vanishes because moving a single fermion from the half-filled ground state inevitably lead to a state with a doubly-occupied state and a vacant state and that the overlap  $\langle 0 | 1 \rangle = 0$ . To get a relevant results for our perturbation theory we thus need to go to second order correction for which

$$E_0^{(2)} = \sum_{n \neq 0} \frac{\langle 0 | H_{tb} | n \rangle \langle n | H_{tb} | 0 \rangle}{E_0 - E_n}. \quad (2.54)$$

Because the hopping Hamiltonian only connect states with a number of doubly occupied sites that differs by one, the only non-vanishing contribution to the sum will be given by the term with  $n = 1$ . Moreover, the energy of a state with one doubly-occupied state at zeroth-order is simply given by  $H_U |1\rangle = U$  and we get

$$\begin{aligned} E_0^{(2)} &= \frac{-1}{U} \langle 0 | H_{tb} H_{tb} | 0 \rangle \\ &= \frac{-2t^2}{U} \sum_{i,j} \sum_{\sigma\sigma'} \langle 0 | c_{i\sigma}^\dagger c_{j\sigma} c_{i\sigma'}^\dagger c_{j\sigma'} | 0 \rangle \\ &= \langle 0 | \frac{4t^2}{U} \sum_{i,j} \mathbf{S}_i \cdot \mathbf{S}_j | 0 \rangle \end{aligned} \quad (2.55)$$

we see here that when hopping is turned on on top of a strong on-site repulsion, there is an emergent antiferromagnetic interaction induced by virtual second order hopping between neighbouring sites. This is in agreement with the observation of antiferromagnetic order at half-filling in cuprates. The addition of vacancy, or holes, in this magnetic background is a very non-trivial and exploring the phase diagram away from half-filling is still an open problem. In fact, the technique we applied here is not available anymore as we would have vacancy present in the ground state already and thus the application of the hypothesis we used in Eqs.(2.53) and (2.54) are not necessarily valid anymore.

There is a general way of getting a low-energy effective model at any filling that takes into account the large on-site repulsion via the *Schrieffer-Wolff* transformation. This leads to what is known as the  $t - J$  model which is written as

$$H_{t-J} = P \left( - \sum_{i,j,\sigma} t_{ij} \left( c_{i\sigma}^\dagger c_{j\sigma} + \text{h.c.} \right) + J \sum_{i,j} \mathbf{S}_i \cdot \mathbf{S}_j \right) P \quad (2.56)$$

where the spin-spin interaction is related to the on-site repulsion  $J = 4t^2/U$ . The operators  $P$  are here to indicate that we have excluded all configurations that lead to double occupancy. It is possible in numerical studies to exactly enforce this constraint by explicitly removing those states with two electrons on the same site, however, from an analytical standpoint, it is usually very difficult to take this projection into account despite the importance it can have on the results. The fractionalization of the electronic quasiparticles is one way of treating the no double-occupancy condition that we will review in the next section.

## 2.4.2 Gauge theory in cuprates

The difficulty in treating the projection describe in the previous section can be understood when writing it explicitly in term of electronic operators in real space,

$$\sum_{\sigma} c_{i\sigma}^\dagger c_{i\sigma} \leq 1 \quad \forall i. \quad (2.57)$$

This constraint has to be enforced at every lattice site separately which makes it difficult. One way of handling this strong constraint is by using the slave-boson method that was originally introduced in the study of heavy-fermions. For this we distinguish the different states that the electron operators connect and we assign a new operators to each of these transition [94, 95, 97], for example

$$c_{i\sigma}^\dagger = f_{i\sigma}^\dagger b_i + \sum_{\sigma'} \epsilon_{\sigma\sigma'} f_{i\sigma'}^\dagger d_i^\dagger. \quad (2.58)$$

In fact, the electron's creation operator connects the empty state  $|0\rangle$  and the singly occupied state  $|\sigma\rangle$  as well as the singly-occupied state  $|\sigma'\rangle$  and the doubly-occupied state  $|\sigma\sigma'\rangle$  as shown in Fig.2.3(a). As such the electron's creation operator can be written as destroying the empty state and creating the singly-occupied state, represented by the  $f_{i\sigma}^\dagger b_i$  term, and as destroying a single-occupied state with a different spin to create a doubly-occupied state, given by the term  $\epsilon_{\sigma\sigma'} f_{i\sigma'}^\dagger d_i^\dagger$ . In this case, because a state with two fermions is equivalent to a bosonic state, the

new operators  $b_i$  and  $d_i$  have bosonic statistics and do not carry any spin degree of freedom, they are usually named holon and doublon, respectively. On the other hand, the fermionic  $f_{i,\sigma}$  have no electric charge but carry the spin information and are named spinons. Note that because  $b_i$  and  $d_i$  are bosonic operators we could in principle have an infinite number of them at any given site, to take care of such discrepancy in the Hilbert space of electrons on a lattice and the Hilbert space of one fermion species and two boson species, we need to introduce a constraint on the number of particles at every site,

$$\sum_{\sigma} f_{i\sigma}^{\dagger} f_{i\sigma} + b_i^{\dagger} b_i + d_i^{\dagger} d_i = 1. \quad (2.59)$$

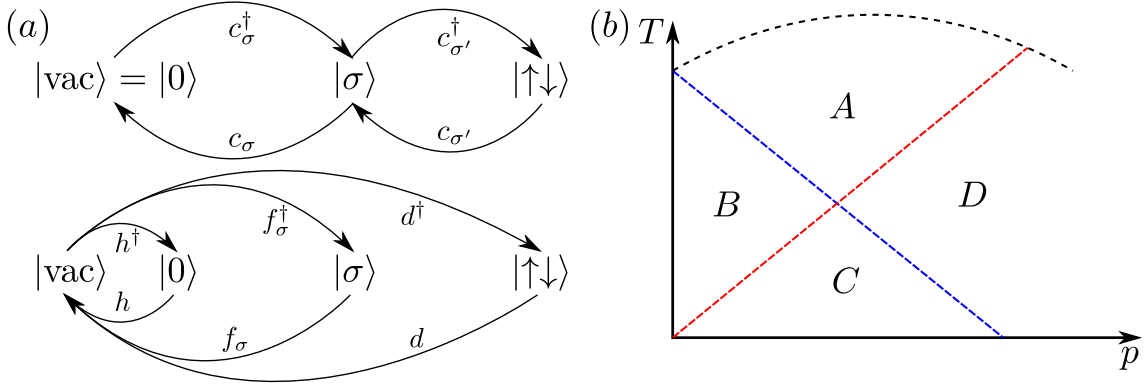


**Figure 2.3:** (a) Schematic for the action of the new  $f, b$  and  $d$  operators and how we can recover the the standard empty, singly and doubly occupied states. Note the the vaccum for these operators is not the empty site in contrast with the canonical fermion operators. (b) Schematic mean-field phase diagram in the fractionalization scenario. We can distinguish four different states with: (A)  $\chi_{ij} \neq 0$ ,  $\Delta_{ij} = 0$ ,  $\langle b_i \rangle = 0$ , (B)  $\chi_{ij} \neq 0$ ,  $\Delta_{ij} \neq 0$ ,  $\langle b_i \rangle = 0$ , (C)  $\chi_{ij} \neq 0$ ,  $\Delta_{ij} \neq 0$ ,  $\langle b_i \rangle \neq 0$ , (D)  $\chi_{ij} \neq 0$ ,  $\Delta_{ij} = 0$ ,  $\langle b_i \rangle \neq 0$ . The different physical properties of these phases are described in the main text. Adapted from Ref.[133].

It is then possible to exclude all the double occupancy by setting the action of  $d_i^{\dagger} |\Psi\rangle = 0$  for any state  $|\Psi\rangle$ , or equivalently, taking an expression for the electron's creation operator and the associated constraint

$$c_{i\sigma}^{\dagger} = f_{i\sigma}^{\dagger} b_i$$

$$\sum_{\sigma} f_{i\sigma}^{\dagger} f_{i\sigma} + b_i^{\dagger} b_i = 1. \quad (2.60)$$

The next step is to use the equality for the electron's operator in Eq.(2.60) in the  $t$ - $J$  Hamiltonian and to implement the associated constraint. This is usually done by introducing a site-dependent Lagrange multiplier in a path-integral formalism leading to the expression for the partition function [28]

$$\mathcal{Z} = \int d\lambda_i db_i db_i^* df_{i,\sigma} df_{i,\sigma}^* \exp \left( - \int_0^{\beta} \mathcal{L}_0 + H_{t-J} d\tau \right). \quad (2.61)$$

where  $\lambda_i$  is the site-dependent Lagrange multiplier and  $\mathcal{L}_0$  capture the time-dependence in the Lagrangian formalism

$$\mathcal{L}_0 = \sum_{i,\sigma} \left( f_{i,\sigma}^* \left( \frac{\partial}{\partial \tau} - \mu \right) f_{i,\sigma} + b_i^* \frac{\partial}{\partial \tau} b_i + i\lambda_i (f_{i,\sigma}^* f_{i,\sigma} + b_i^* b_i - 1) \right) \quad (2.62)$$

As such, performing the functional integral over  $\lambda_i$  in Eq.(2.61) will enforce the no-double occupancy constraint. Replacing the electrons operators in the  $t$ - $J$  Hamiltonian leads to fermion-boson and fermion-fermion coupling. In particular, the hopping term becomes

$$H_{tb} = -t \sum_{i,j,\sigma} (c_{i\sigma}^* c_{j\sigma} + \text{h.c.}) \rightarrow -t \sum_{i,j,\sigma} (f_{i\sigma}^* f_{j\sigma} b_i b_j^* + \text{h.c.}) \quad (2.63)$$

The spin operator that appears in Eq.(2.56) is directly quadratic in fermion operators and the spin-spin interaction leads to

$$\begin{aligned} H_J &= J \sum_{i,j} \mathbf{S}_i \cdot \mathbf{S}_j \\ &\rightarrow \frac{-J}{4} \sum_{i,j} \sum_{\alpha,\beta} f_{i\alpha}^* f_{j\alpha} f_{j\beta}^* f_{i\beta} + (f_{i\uparrow}^* f_{j\downarrow} - f_{i\downarrow}^* f_{j\uparrow}) (f_{j\downarrow} f_{i\uparrow} - f_{j\uparrow} f_{i\downarrow}). \end{aligned} \quad (2.64)$$

Thus, we end up with an effective model of interacting spinons that are linked to free holons by the hopping term and the local constraint encoded in the site-dependent Lagrange multiplier  $\lambda_i$ . This is still a very hard problem to solve but we can note that the spinon-spinon interaction is now an effective attractive interaction  $\frac{-J}{4}$  and it is a sensible idea to start with a mean-field decoupling of the interaction. Looking at Eq.(2.64) there are two channels in which we wish to decouple the interaction term, given by the two mean fields

$$\begin{aligned} \chi_{ij} &= \sum_{\sigma} \langle f_{i\sigma}^* f_{j\sigma} \rangle \\ \Delta_{ij} &= \langle f_{j\downarrow} f_{i\uparrow} - f_{j\uparrow} f_{i\downarrow} \rangle. \end{aligned} \quad (2.65)$$

the mean-field Lagrangian is thus written

$$\begin{aligned} \mathcal{L}_{mf} &= \sum_{i,\sigma} \left( f_{i,\sigma}^* \left( \frac{\partial}{\partial \tau} - \mu \right) f_{i,\sigma} + b_i^* \frac{\partial}{\partial \tau} b_i + i\lambda_i (f_{i,\sigma}^* f_{i,\sigma} + b_i^* b_i - 1) \right) \\ &\quad - t \sum_{i,j,\sigma} (f_{i\sigma}^* f_{j\sigma} b_i b_j^* + \text{h.c.}) - \tilde{J} \sum_{i,j} \left( \chi_{ij}^* \sum_{\sigma} f_{i\sigma}^* f_{j\sigma} + \text{h.c.} \right) \\ &\quad + \tilde{J} \sum_{i,j} (\Delta_{ij} (f_{i\uparrow}^* f_{j\downarrow} - f_{i\downarrow}^* f_{j\uparrow}) + \text{h.c.}). \end{aligned} \quad (2.66)$$

Treating this effective mean-field model still requires approximations, for example on how to treat the holon-spinon coupling or the constraint imposed by  $\lambda_i$ . We can however get insight into the physics of the fractionalization ansatz by imagining the different scenarios possible from Eq.(2.66). Firstly, we note that the first mean-field introduced in Eq.(2.65) can be understood as a renormalization of the spinon hopping, or a Fock shift in conventional notations. Note that this hopping term for spinons is also coupled to the holon hopping through the  $t$  term. In the simplified limit of half-filling in which there is no boson, there are no empty sites, the spinons acquire a Fermi surface and the bandwidth is given by the value of  $\chi_{ij}$  through the value of the interaction  $\tilde{J}$ . This corresponds to the RVB picture originally put forward for the proximity to the Mott insulator and even if subsequent works have found instability related to this spinon Fermi surface [28], it captures the physics of the  $\chi_{ij}$  term well. The second mean-field  $\Delta_{ij}$  represents the possibility for spinons to pair. This is not equivalent to a superconducting state as the spinons do not carry electric

charge but it will induce a gap in the spin excitation spectrum when  $\Delta_{ij} \neq 0$  in the same way the electronic spectrum is gapped in a superconductor (see Sec.2.3.2). The other possibility is the condensation of the holons away from half-filling. Being bosons, there will be a temperature below which Bose-Einstein condensation occurs leading to coherent charge transport, this condensation temperature is usually proportional to the number of bosons and, in our case, to the doping.

One resulting phase diagram is shown in Fig.2.3(b) where we can distinguish four different phases depending on which combination of  $\chi_{ij}$ ,  $\Delta_{ij}$  and  $\langle b_i \rangle$  are non zero. The first important line is the temperature at which the spinon hopping term is non-zero, this is linked to the doping dependence of the spin-spin interaction and is usually suppressed at high doping but also has a contribution from the boson number. In phase *A*,  $\chi_{ij}$  is the only non-vanishing order parameter and we observe spin-charge separation. The spin properties come from the spinon Fermi surface that exists while the charge transport is incoherent, this is sometimes related to the *strange metal* phase of cuprates at optimal doping. The phases that can be found when both  $\chi_{ij}$  and  $\Delta_{ij}$  are non-zero and which is labelled *B* in Fig.2.3(b) is named the *spin-gap* phase. Because the spin excitations are gapped by the spinon pairing but the charge transport is still incoherent this is often associated with the pseudogap region of underdoped cuprates. The onset temperature for the formation of spinon pairs is only related to the spin-spin interaction from the *t-J* model and as such decrease with doping. The high-temperature superconducting phase is then obtained when we have the holons condensation from the spin-gap phase. Indeed, the pairing amplitude  $\langle c_{i\sigma} c_{j-\sigma} \rangle$  can be written in terms of spinon and holons as  $\langle b_i^\dagger f_{i\sigma} b_j^\dagger f_{j-\sigma} \rangle = \langle b_i^\dagger b_j^\dagger \rangle \langle f_{i\sigma} f_{j-\sigma} \rangle$  and is thus non-zero when both  $\langle b_i \rangle$  and  $\Delta_{ij}$  are finite. Because the Bose-Einstein condensation temperature grows with doping and that the spinon pairing temperature decrease monotonously, the resulting superconducting phase has a dome shape in the temperature-doping phase diagram as observed in cuprates and shown in the region *C* in Fig.2.3(b). Lastly, for large doping, the spinon pairing is not effective anymore and we only have a holon condensate and the spinon hopping that are finite. Both charge and spin transport are coherent and the phase is associated with a normal Fermi liquid (phase *D*).

Beyond the phase diagram that emerges from the fractionalization of the electronic degree of freedom, which is quite specific to the approximations done to solve this problem, it is important to note the gauge structure Eq.(2.60) implies. In fact, we can see that when writing the electron creation operator as a product of the holon and spinon operators we introduce a new local and unphysical phase transformation

$$b_i \rightarrow b_i e^{i\theta_i} \quad f_{i\sigma} \rightarrow f_{i\sigma} e^{i\theta_i}. \quad (2.67)$$

This new gauge local transformation is an artefact of our description of the system as the original (physical) electron operator is invariant under such transformation

$$c_{i\sigma}^\dagger = f_{i\sigma}^\dagger b_i \rightarrow f_{i\sigma}^\dagger b_i e^{i\theta_i} e^{-i\theta_i} = c_{i,\sigma}^\dagger \quad (2.68)$$

The constraint given in Eq.(2.60) is also tightly related to this emergent gauge structure as we can see that the Noether charge associated to the new  $U(1)$  symmetry is none other than  $Q_i = \sum_\sigma f_{i\sigma}^\dagger f_{i\sigma} + b_i^\dagger b_i$ . This means that the site-dependent Lagrange multiplier  $\lambda_i$  can be understood as the associated gauge field which couples to the spinons and holons in  $\mathcal{L}_0$  (Eq.(2.62)). Note that the

usual Maxwell term for the dynamic of the gauge field  $\frac{1}{g}F_{\mu\nu}F^{\mu\nu}$  is not present in our derivation of the final action, which can be interpreted as the coupling constant  $g$  being infinite. The same structure will emerge in our description of the pseudogap and will, in the same way, be associated with a constraint that is exactly enforced when the gauge field is integrated out as presented in Sec.3.1.

# Chapter 3

## Fractionalized Pair Density Wave

We now arrive at the core of this thesis where we use the experimental observations presented in Chap.1 and the tools from Chap.2 to build our description of the pseudogap phase in cuprates. Our goal in Sec.3.1 is to build an effective theory to explain the universal features of the phase diagram of underdoped cuprates without precise microscopic details. For this, we start by highlighting the relation between the SC, CDW and PDW states in Sec.3.1.1 by reviewing the case of the attractive Hubbard model and the idea of emergent symmetry where these three states play important roles. Using this and the instructive example of the fractionalization from Sec.2.4.2, we present our fractionalization ansatz for the pseudogap starting from the PDW state in Sec.3.1.2. This mirrors the derivation for Refs.[30, 134] and we give some phenomenological consequences of our effective theory in Sec.3.1.3. We then turn to a more detailed analysis of the single-particle Green's function in Sec.3.2 and Sec.3.3 where, starting from a microscopic model and following the analysis from Ref.[135, 136], we compare the electronic spectral function and the self-energy from our fractionalized PDW to experimental and numerical results. Lastly, in Sec.3.4, we look at the coupling of the electronic degree of freedom to the phonons to elucidate the anomalous phonon softening that is observed in cuprates at the superconducting transition temperature. This was presented in Ref.[137] and use a similar structure as the one we use to explain the ARPES results, giving a body of experiments that can be captured by the same microscopic model.

### 3.1 Effective theories for the pseudogap

#### 3.1.1 Exact and emergent $SU(2)$ symmetry

In order to lay ground for the idea of fractionalization of the PDW order, we start by making the link between the modulated particle-particle order and the more standard SC or CDW orders. Firstly, we define the PDW order parameter with modulation  $\mathbf{Q}$  in real space as the expectation value

$$\Delta_i^{PDW} = \langle c_{i\sigma}^\dagger c_{i-\sigma}^\dagger e^{i\mathbf{Q}\cdot\mathbf{r}_i} \rangle. \quad (3.1)$$



We then see that the PDW state breaks the charge conservation symmetry, as in the superconducting case, but also the translation symmetry due to the modulation wave-vector  $\mathbf{Q}$ . Interestingly, the three local SC, CDW and PDW orders are linked together as they form a closed  $SU(2)$  algebra analogous to the classic spin rotation symmetry. To see this, we will consider briefly the Hubbard model for which this symmetry is exact at half-filling with a specific choice of commensurate charge modulation  $\mathbf{Q} = (\pi, \pi)$ . We start by defining the set of operators

$$\begin{cases} \eta^z = \frac{1}{2} \sum_i c_{i\sigma}^\dagger c_{i\sigma} - 1 \\ \eta^+ = \sum_i e^{i\pi \cdot \mathbf{r}_i} c_{i\uparrow}^\dagger c_{i\downarrow}^\dagger \\ \eta^- = \sum_i e^{-i\pi \cdot \mathbf{r}_i} c_{i\downarrow} c_{i\uparrow} \end{cases} \quad (3.2)$$

These operators satisfy the commutation relations  $[\eta^z, \eta^\pm] = \pm \eta^\pm$  and  $[\eta^+, \eta^-] = \eta^z$  which identifies  $\eta^\pm$  as the raising and lowering operators of the respective  $SU(2)$  algebra generated by  $\{\eta^x, \eta^y, \eta^z\}$ . We can first note that these operators all commute with the Hubbard Hamiltonian and with the standard spin operators  $\{S^x, S^y, S^z\}$

$$[S^\alpha, \eta^\beta] = 0 \quad \text{and} \quad [\eta^\alpha, H] = 0 \quad (3.3)$$

and the model is thus invariant under these two  $SU(2)$  symmetries. Note that the two algebra are not totally independent in the case of the Hubbard model as there exist a  $\mathbb{Z}_2$  transformation called the *Shiba* transformation [138] which maps the spin operators on the  $\eta$  operators while reversing the change of the Hubbard interaction  $U \rightarrow -U$ . These operators will then act on states belonging to a spin  $l$  representation according to the rules

$$\begin{aligned} \eta^z |m\rangle &= m |m\rangle, \\ \eta^\pm |m\rangle &= \sqrt{l(l+1) - m(m \pm 1)} |m \pm 1\rangle. \end{aligned} \quad (3.4)$$

In our case we will be particularly interested in a spin 1 representation for the  $\eta$ -symmetry (also called pseudo-spin symmetry) where the latter acts on the operators

$$\begin{aligned} \Delta_i &= \sum_\sigma \sigma c_{i\sigma}^\dagger c_{i-\sigma}^\dagger, \\ \chi_i &= \sum_\sigma c_{i\sigma}^\dagger c_{i\sigma} e^{i\pi \cdot \mathbf{r}_i}, \\ \Delta_i^* &= \sum_\sigma \sigma c_{i-\sigma} c_{i\sigma}. \end{aligned} \quad (3.5)$$

We thus see that an ordered state with spin aligned along a fixed direction will lead to a superconducting or charge modulating state. The  $\eta$  symmetry is however explicitly broken away from half-filling as the chemical potential term couples directly to one of the generators  $\mu \sum_i n_i \propto \mu \eta^z$ . We could thus rewrite the Hubbard problem as a transverse field spin system where ordering in the  $xy$  plane (corresponding to a superconducting state) competes with a field along the  $z$ -axis due to the chemical potential.

The idea to couple the d-wave superconductor to another ordered state is present in many theories for cuprates. Looking at the phase diagram of the cuprates, one could be convinced that the most prominent features are the antiferromagnetic (AF) phase and the SC phase. Hence as a

natural first guess, the rotation from the SC to the AF state has been tried, leading to an enlarged group of  $SO(5)$  symmetry [139–141], enlarging the space allowed for fluctuations that would lead to the pseudogap regime. The ten generators of the  $SO(5)$  group correspond to transitions between the various states inside the quintuplet  $\Psi_{SO(5)} = (S^x, S^y, S^z, \Delta, \Delta^*)$  (three magnetic states, and two SC states which are complex conjugate of one another). These theories are based on an underlying principle that the two ordered states are nearly degenerate in energy, *i.e.* the symmetry is only weakly broken. The exact symmetry then emerges when the system is perturbed from the ground state by increasing the temperature and the high-temperature region is described by angular fluctuations belonging to the emergent symmetry group.

Later on, theories based on a generalization of the  $U(1)$  gauge theory presented in Sec.2.4.2 to a  $SU(2)$  gauge structure in the pseudo-spin space led to the formation of a flux phase [142], and rotation from the SC state to the flux phase was envisioned. This theory had an emergent  $SU(2)$  symmetry with fluctuations acting as well up to temperatures  $T^*$ .

The ubiquitous observation of charge modulation in the pseudogap region of cuprates by STM [44, 143], NMR [144, 145] and X-ray scattering [146–149] has led people to consider it as a strong competitor to the SC state and a rotation of the SC state towards a CDW state has been proposed [150–154]. At high applied magnetic field, the charge modulations reconstruct the Fermi surface, forming small electron pockets [46–53]. In YBCO, the charge modulations are stabilized as long range uniaxial  $\mathbf{Q} = (Q_0, 0)$  3D order above a certain magnetic threshold [155–157] and the thermodynamic lines can be determined with ultra-sound experiment [158, 159]. The rotation of the SC state to the CDW state is then a generalization of the exact realization presented in Eq.(3.5) to a d-wave order and an incommensurate modulation wave-vector  $(\Delta_{-1}, \Delta_0, \Delta_1)$  with

$$\begin{aligned}\Delta_1 &= \frac{-1}{\sqrt{2}} \hat{d} \sum_{\sigma} \sigma c_{i\sigma}^{\dagger} c_{j-\sigma}^{\dagger}, \\ \Delta_0 &= \frac{1}{2} \hat{d} \sum_{\sigma} \left[ c_{i\sigma}^{\dagger} c_{j\sigma} e^{i\mathbf{Q}\cdot\mathbf{r}} + c_{j\sigma}^{\dagger} c_{i\sigma} e^{-i\mathbf{Q}\cdot\mathbf{r}} \right], \\ \Delta_{-1} &= \frac{1}{\sqrt{2}} \hat{d} \sum_{\sigma} \sigma c_{j-\sigma} c_{i\sigma}\end{aligned}\tag{3.6}$$

where  $\mathbf{r} = (\mathbf{r}_i + \mathbf{r}_j)/2$  and  $\hat{d}$  is the d-wave form factor. The corresponding  $\eta$ -operators that satisfy the  $SU(2)$  algebra are given by

$$\begin{aligned}\eta_+ &= \frac{1}{2} \sum_{\sigma} \sigma [c_{i\sigma}^{\dagger} c_{i-\sigma}^{\dagger} e^{i\mathbf{Q}\cdot\mathbf{r}} + c_{j\sigma}^{\dagger} c_{j-\sigma}^{\dagger} e^{-i\mathbf{Q}\cdot\mathbf{r}}], \\ \eta_- &= \frac{1}{2} \sum_{\sigma} \sigma [c_{i-\sigma} c_{i\sigma} e^{-i\mathbf{Q}\cdot\mathbf{r}} + c_{j-\sigma} c_{j\sigma} e^{i\mathbf{Q}\cdot\mathbf{r}}], \\ \eta_z &= \frac{1}{2} [\eta_+, \eta_-] = \frac{1}{2} \sum_{\sigma} (\hat{n}_{i\sigma} + \hat{n}_{j\sigma} - 1).\end{aligned}\tag{3.7}$$

Note that the CDW state can also be taken to be imaginary leading to a second realization of the  $l = 1$  representation. In general, the two possibilities have to be considered and we thus end up with two copies of the  $SU(2)$  symmetry [30]. The connection between the three states is shown in Fig.3.1(a) and we can see that we can obtain a given state by a combination of different operators,

which will be important in developing the fractionalization idea later on.

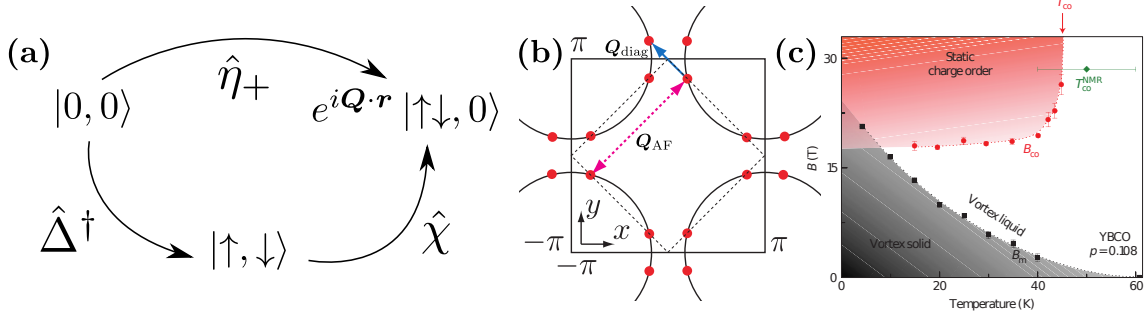


**Figure 3.1:** (a) Schematic on how the SC, CDW and PDW operators connect different states. We have a d-wave SC state that creates particle-particle pair on neighbouring sites while the PDW state is on-site and breaks translation symmetry due to the modulation at wave-vector  $\mathbf{Q}$ . The CDW operator does not change the total number of charge but do connect states with on-site pair and nearest-neighbour pair while also breaking translation symmetry with the same wave-vector as the PDW operator. (b) Schematic of the Brillouin zone where the full black line indicates a typical Fermi surface for underdoped cuprates. The dotted line represents the antiferromagnetic Brillouin zone, *i.e.* points that are related by a translation by the AF wave-vector  $\mathbf{Q}_{\text{AF}} = (\pi, \pi)$ . The hot-spots are points where the Fermi surface intersect the AF Brillouin zone and are shown in red. The symmetry between the SC and CDW states with a diagonal wave-vector connecting the hot-spots ( $\mathbf{Q}_{\text{diag}}$ ) is exact at the hot-spots. Adapted from Ref.[133]. (c) Experimental B-T phase diagram for YBCO where we see a phase with long-range unidirectional charge order at high magnetic fields. The critical magnetic field for the transition from the SC state and the CDW state is almost temperature independent and there is a coexistence phase at low temperature. These two features are recovered in the emergent symmetry theory [55]. Adapted from Ref.[158].

An exact realization of the emergent symmetry has been found when the Fermi surface is reduced to eight “hot spots” (crossing of the Fermi surface and the AF zone boundary as shown in Fig.3.1(b)) and the electrons interact with an AF critical mode in  $d = 2$  [69, 150–152]. In this simple model, the gap equations could be solved showing the exact  $SU(2)$  symmetry between the Cooper pairing and particle-hole channels. They observed some ordering of a composite order parameter, which is a superposition of gaps in the particle-particle and particle-hole channels

$$\hat{\Delta}^* |0\rangle = \sum_{\mathbf{k}\sigma} \left( c_{\mathbf{k}\sigma}^\dagger c_{-\mathbf{k}-\sigma}^\dagger + c_{\mathbf{k}\sigma}^\dagger c_{\mathbf{k}+\mathbf{Q}\sigma} \right) |0\rangle, \quad (3.8)$$

where the modulations in the charge sector occur at a finite diagonal wave vector  $\mathbf{Q}_{\text{diag}} = (Q_x, Q_y)$  (blue arrow in Fig.3.1(b)), where  $Q_x$  and  $Q_y$  are the distance between two hot spots. A composite gap is formed at  $T^*$  with the mean square of the gaps in each channel

$$E^* = \sqrt{|\chi|^2 + |\Delta|^2}, \quad (3.9)$$

where  $\chi$  is the gap in the particle-hole channel whereas  $\Delta$  is the gap in the particle-particle channel. Below  $T^*$ , a great amount of fluctuations are present which are described by the  $O(4)$  non-linear  $\sigma$  model [150, 160, 161]

$$S = 1/2 \int d^d x \sum_{\alpha=1}^4 (\partial_\mu n_\alpha)^2, \quad \text{with } \sum_{\alpha=1}^4 |n_\alpha|^2 = 1. \quad (3.10)$$

with the four fields  $n_\alpha$  given by  $n_1 = (\Delta + \Delta^*)/2$ ,  $n_2 = -i(\Delta - \Delta^*)/2$ ,  $n_3 = (\chi + \chi^*)/2$ ,  $n_4 = -i(\chi - \chi^*)/2$ . The study of the angular fluctuations of this model leads to good agreement with several phenomenological observations, some of which are presented in the following.

### Charge modulations inside the vortex core

At this stage, the model can already explain a few properties of cuprate superconductors. Since the model treats very seriously the competition between CDW and SC pairing order parameters, it predicts charge modulations inside the vortex core [44, 45, 143, 144, 162] (see Sec.1.2.3). Indeed, since the SC order parameter vanishes there, the competing order emerges at the core. The special structure associated with this feature is called a meron, or half skyrmion, in the pseudo-spin space. It can be noted that it is a generic prediction of the theories of emergent symmetries, that the competing order shows up inside the vortex core. For example, the  $SO(5)$  theory predicts AF correlations inside the vortex core [163, 164], whereas the  $SU(2)$  symmetry which rotates superconductivity to the  $\pi$ -flux phase predicts that the  $\pi$ -flux orbital state [28, 165] is present inside the vortex core. Although AF correlations were observed in the vortex core in the La-compounds [166], for YBCO, BSCCO and Hg-series, STM experiments [44, 143] and NMR [162] gave evidence for charge modulations. This ubiquitous observation of charge modulations inside the vortex core is a nice test for the theory of emergent  $SU(2)$  symmetry, but the presence of charge modulations inside the vortex core could also be explained by a strong competition between SC and CDW without invoking any emergent symmetry [167, 168].

### B-T phase diagram

The second set of experimental evidence that can be matched by the idea of emergent symmetry is the phase diagram in the presence of an applied magnetic field as shown in Fig.3.1(c) [55, 158]. For the compound YBCO, a phase diagram could be derived as a function of an applied magnetic field up to roughly  $20T$ . For this specific compound, one observes at  $H_c = 17T$  [158], a second-order phase transition towards a 3D charge order state with one uniaxial vector of modulations [155, 169]. The shape of this transition is very flat in temperature [158, 159], a fact that cannot be accounted for by a simple model of competition between the two orders but can be explained by a spin-flop like transition, where the system suddenly goes from the SC state to the CDW state. The model of pseudo-spin flop comes directly from the expression of the non-linear  $\sigma$  model where the constraint plays the role of the value of the spin in a magnetic spin-flop transition. The pseudo-spin flop transition accounts for the flatness [170] in temperature of the transition, but it does not explain the phase of coexistence [158, 162, 171]. Accounting for this phase requires breaking the exact  $SU(2)$  symmetry underlying the non-linear  $\sigma$  model by an amount of roughly 5%. As a conclusion, an  $SU(2)$  emergent symmetry and its non-linear  $\sigma$  model can account for the whole B-T phase diagram owing to the fact that it is explicitly broken [55].

### Collective modes

An emergent symmetry is characterized by a set of collective modes [172]. Let us assume that the CDW is real, as in the first set of Eq.(3.6). Here the operators  $\eta_+$  and  $\eta_-$  which enable the rotation from the SC to the CDW states are the generators of an  $O(3)$  Lie algebra

$$\mathcal{L} = \begin{pmatrix} 0 & * & * \\ -\frac{i}{2}(\eta_+ - \eta_-) & 0 & * \\ -\eta_z & \frac{1}{2}(\eta_+ + \eta_-) & 0 \end{pmatrix}, \quad (3.11)$$

where the notation  $*$  stands for a hermitian matrix. The structure of  $\mathcal{L}$  in Eq.(3.11) gives rise to collective modes. These collective modes are spin zero, charge two, and reflect the structure of the  $SU(2)$  symmetry. They can be considered as Pair Density Wave (PDW) excitations since they have non zero center of mass wave vector. They could be responsible for the mode observed in the  $A_{1g}$  channel in Raman Scattering [173] and can also be seen by spectroscopy experiments, like X ray, MEELS [174, 175] or soft X-rays [176], where the resolution in  $\mathbf{q}$ -space can be traced. The theory predicts that the mode occurs around the same wave vector as the charge modulations and has a typical linear shape. If the symmetry is explicitly broken, these modes acquire a mass that is proportional to the difference in energy between the SC and CDW states.

### 3.1.2 Fractionalization ansatz

The theory we propose to describe the pseudogap phase is an extension of the previous emergent symmetry idea and is based on the relation that exists between the SC, CDW and PDW states. The physical picture is that the PDW state is an instability of the system but that it cannot form due to frustration induced by disorder, competition with other orders or similar effects. Because it is able to decay into both the particle-particle channel, breaking charge conservation, and a modulated particle-hole channel, breaking translation symmetry, the PDW will fractionalize into an SC and a CDW order when the temperature is lowered. The resulting states will be connected by an emergent  $U(1)$  gauge field as in the electron fractionalization theory (see Sec.2.4.2) that will have multiple consequences that we will explore.

#### Fractionalization of the PDW order and $CP^1$ model

We start by noticing that the relation between the PDW operator from Eq.(3.7) and the SC and CDW operators also leads to the following relations

$$\hat{\eta} = [\hat{\Delta}_{ij}, \hat{\chi}_{ij}^\dagger], \quad \hat{\eta}^\dagger = [\hat{\chi}_{ij}, \hat{\Delta}_{ij}^\dagger], \quad (3.12)$$

as was illustrated in Fig.3.1. In this decomposition, the PDW operator is invariant under the transformation

$$\hat{\Delta}_{ij} \rightarrow e^{i\theta} \hat{\Delta}_{ij}, \quad \hat{\chi}_{ij} \rightarrow e^{i\theta} \hat{\chi}_{ij}. \quad (3.13)$$

The corresponding gauge structure is analogous to Eq.(2.60) and we thus have a constraint in analogy with Eq.(2.60) given by

$$\hat{\Delta}_{ij}^\dagger \hat{\Delta}_{ij} + \hat{\chi}_{ij}^\dagger \hat{\chi}_{ij} = 1. \quad (3.14)$$

In order to construct a field theory, we rewrite the relation Eq.(3.12) as  $\Delta_{PDW} = \Delta\chi^*$ . The typical field theory associated with the decomposition Eq.(3.12) with the constraint Eq.(3.14) that describes two complex fields constrained on a sphere is the rotor model:

$$S = \int d^d x \frac{1}{2} \sum_{a,b=1}^2 |\omega_{ab}|^2, \quad (3.15)$$

where

$$\omega_{ab} = z_a^* \partial_\mu z_b - z_b \partial_\mu z_a^*, \quad (3.16)$$

with here  $z_1 = \Delta_{ij}$ ,  $z_2 = \chi_{ij}$ , ( $z_1^* = \Delta_{ij}^*$ ,  $z_2^* = \chi_{ij}^*$ ). Expanding Eq.(3.15) and using the constraint Eq.(3.14) we get

$$\begin{aligned} S = \int d^d x & [|\partial_\mu \Delta_{ij}|^2 + |\partial_\mu \chi_{ij}|^2 \\ & - (\Delta_{ij} \partial_\mu \Delta_{ij}^* - \chi_{ij}^* \partial_\mu \chi_{ij}) (\Delta_{ij}^* \partial_\mu \Delta_{ij} - \chi_{ij} \partial_\mu \chi_{ij}^*)], \end{aligned} \quad (3.17)$$

where we omitted a possible potential term.

We now note that under the phase transformation  $\Delta_{ij} \rightarrow \Delta_{ij} e^{i\theta}$  and  $\chi_{ij} \rightarrow \chi_{ij} e^{i\theta}$ , which leaves our original PDW field  $\Delta_{PDW}$  unchanged, the second term of Eq.(3.17) then transforms as

$$\begin{aligned} & (\Delta_{ij} \partial_\mu \Delta_{ij}^* - \chi_{ij}^* \partial_\mu \chi_{ij}) \\ & \rightarrow (\Delta_{ij} \partial_\mu \Delta_{ij}^* - \chi_{ij}^* \partial_\mu \chi_{ij}) - i \partial_\mu \theta. \end{aligned} \quad (3.18)$$

Thus we can identify it with a gauge field and rewrite the action Eq.(3.17) as

$$\begin{aligned} \mathcal{S}_{CP^1} &= \int d^d x |\partial_\mu \Psi_{ij}|^2 + \alpha_\mu \bar{\alpha}_\mu \\ &= \int d^d x |D_\mu \Psi_{ij}|^2, \end{aligned} \quad (3.19)$$

where we used the spinor  $\Psi_{ij} = (\Delta_{ij}, \chi_{ij})^T$  and we have introduced the covariant derivative  $D_\mu = \partial_\mu - i\alpha_\mu$ . This action is the one for a  $CP^1$  model and is invariant under the joint transformations

$$\Psi_{ij} \rightarrow e^{i\theta} \Psi_{ij}, \quad \alpha_\mu \rightarrow \alpha_\mu - \partial_\mu \theta, \quad (3.20)$$

reflecting the fact that this phase transformation is introduced by our decomposition Eq.(3.12) and has to leave our original model Eq.(3.15) invariant. Note that in this case, the value of the gauge field  $\alpha_\mu$  is fixed and given by  $\alpha_\mu = -i (\Delta_{ij} \partial_\mu \Delta_{ij}^* - \chi_{ij}^* \partial_\mu \chi_{ij})$ . This is equivalent to considering the global phase of the spinor  $\Psi_{ij}$  as being fixed. Furthermore, the two fields  $\Delta_{ij}$  and  $\chi_{ij}$  are linked by the constraint of Eq.(3.14). We thus recover an effective model which, in analogy with the case of the electrons fractionalization from Sec.2.4.2, has an emergent  $U(1)$  gauge structure associated

to a constraint on the amplitudes of the new fields.

This constraint does not however imply that the SC or CDW orders condense. In fact, just below the pseudogap temperature the amplitude of both  $\Delta_{ij}$  and  $\chi_{ij}$  are still fluctuating. It is only at lower temperatures that these amplitudes become finite. In our case, we can argue on phenomenological grounds that the modulated particle-hole pairs will condense first at a temperature  $T_{co}$ , where charge modulation is observed experimentally. This order is however not a long-range order as we still have fluctuations of the relative phase between the two components of  $\Psi_{ij}$ .

Note that the constraint obtained in Eq.(3.14) is similar to the one that appears in the emergent symmetry idea presented above. Moreover, the effective  $CP^1$  model in Eq.(3.19) can also be shown to be equivalent to an  $O(3)$  non-linear  $\sigma$  model and the phenomenological results described in the previous section, such as the presence of charge modulation in vortex core or the particular shape of the B-T phase diagram, remain valid. We however have a stronger relationship between the SC and CDW orders as the phase fluctuations of both order parameters are linked and will be quenched at the same temperature. This is unexpected as the freezing of the phase of the SC order parameter is usually associated with the fact that the number of particles is not conserved in the SC state while the CDW state is not related to the electromagnetic charge a priori. The freezing of this phase will lead to the superconducting transition at  $T_c$  (see Fig.3.2). This is a unique consequence of the fractionalization hypothesis as the partial freezing of the phase degree of freedom at  $T^*$  will entangle the remaining phase. We also present another alternative way of getting the same effective theory of amplitude and phase constraint from the perspective of a  $U(1) \times U(1)$  gauge theory in Appendix A.

Identifying the general setup presented here with cuprate superconductors we can describe the phase diagram in the underdoped regime when we lower the temperature as described in the next part. We will also revisit the idea of vestigial order where discrete symmetries are broken when the fluctuations of  $\Delta$  and  $\chi$  are linked with for example the time-reversal symmetry breaking associated with intra-unit cell loop currents in cuprates.

### 3.1.3 Phenomenological consequences

#### Phase diagram

With this prelude, we describe the phase diagram of the underdoped cuprates. A first phase transition occurs at  $T^*$  when the global phase  $\theta$  gets frozen and the constraint between the particle-particle pair field  $\Delta_{ij}$  and the particle-hole field  $\chi_{ij}$  sets an energy scale  $E^*$ . The finite amplitude for the spinor  $\Psi_{ij}$  at  $T^*$  does not however mean a condensation of  $|\Delta_{ij}|$  or  $|\chi_{ij}|$  as the constraint in Eq.(3.14) can be satisfied by the fluctuations of both fields. We can thus think that these fields will acquire a finite amplitude at lower temperatures  $T_{co}$  and  $T'_c$  for the CDW and SC amplitudes respectively. In this sense this is similar to a preformed pairs description of the pseudogap phase but where two kinds of pairs, particle-particle and particle-hole, are entangled. Lastly, the remaining relative phase  $\phi$  will get frozen at a lower temperature  $T_c$  which is then identified with the superconducting transition as the EM gauge field gets massive, leading to a Meissner effect [177–179].

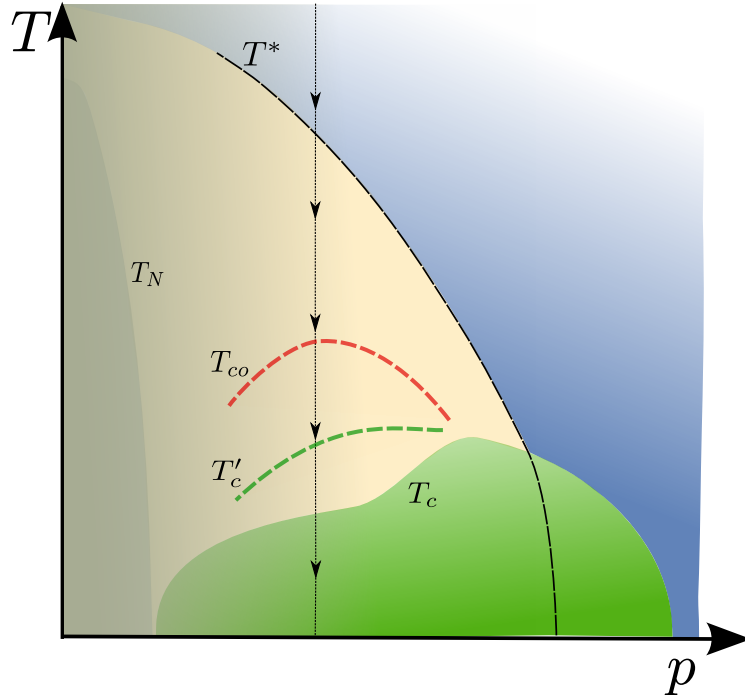


**Figure 3.2:** Schematic temperature ( $T$ )- hole doping ( $p$ ) phase diagram for a cuprate superconductor. As we decrease temperature (black line), we have a first phase transition at  $T^*$ . This sets the pseudogap energy scale and induces a constraint between the two orders as shown in Eq.(3.14). At lower temperatures  $T_{co}$  and  $T'_c$  the amplitudes of the two orders become finite. These are not phase transition but crossover lines. A second transition occurs at  $T_c$ , where the relative phase of the spinor gets frozen. Adapted from Ref.[30]

At  $T_{co}$ , the short-range CDW can be observed in X-ray, STM or NMR measurements due to the pinning of the phase of the CDW order. An NMR perspective on pinning of the charge order in YBCO and its similarity with pinning in layered metals is given in Ref.[180]. Since  $T_{co}$  and  $T'_c$  are mean-field lines, their relative position in the phase diagram depends crucially on the details of the microscopic models. Here, we consider  $T_{co} > T'_c$ . A possible justification comes from the microscopic model (see Sec.3.2.2) we study later on where adding an off-site density-density interaction to the standard  $t$ - $J$  model can lead to an enhanced  $T_{co}$ . Even if the mean-field precursor gaps of both the SC and CDW orders are well defined below  $T'_c$ , the relative phase still fluctuates and thus there is no phase coherence in SC or CDW orders.  $T'_c$  would be related to the onset of the pairing fluctuations as observed in Nernst effect [181], transport studies [182] and Josephson SQUID experiments [183] (see Sec.3.2.3). The relative phase of the two orders gets frozen at a lower temperature  $T_c$ , where the phase coherence sets in for both the SC and CDW orders with the coexistence of both orders. Some signatures of the phase relation between the SC and CDW states can be seen by the observation of the charge order in X-ray [49, 146], STM [143, 184] and NMR [180] measurements and we will discuss the anomalous behaviour of the phonon spectra at  $T_c$  in Sec.3.4. The correlation length of the charge order is not expected to increase for  $T < T_c$  due to the strong competition with the SC state [161, 185] but it does feature a maximum at  $T_c$  [186] showing an intimate connection between the SC and CDW orders. We remark that if the pinning of the CDW order due to disorder is too strong, no superconductivity can emerge below  $T_c$ . Our formalism thus implies that the pinning is present but weaker than the Higgs mechanism giving



rise to a bulk superconductor at  $T_c$ . Lastly, as already noted, since the CDW is a priori a complex field, preemptive orders breaking discrete symmetries like parity, time reversal or lattice rotation, usually associated with  $Q = 0$  orders such as electronic nematicity or loop current states, can be present at higher temperature as in the vestigial order theories [116].

A true long-range charge order, PDW or “super-solid” is never established in the absence of a magnetic field due to the omnipresence of disorder in cuprates. Disorder acts on the charge order as a “random-field” [29]. Following Imry-Ma criterion [31], any strength of “random-field” disorder disrupts the long-range coherence in charge order in dimensions  $d \leq 4$ . This is not the case for the superconducting order as disorder does not directly couple to the superconducting order parameter as “random-fields”. Thus for  $T < T_c$ , the superconducting order shows a true long-range nature in  $d = 3$  or a quasi long-range nature in  $d = 2$ . But, a 3D charge order acquires a true long-range nature only at high magnetic fields when it shows uniaxial behaviour (breaking a nematic discrete symmetry [187]) or in the additional presence of chain-disorder [188]. As a consequence, the PDW order, which is a bilinear combination of the charge order and the superconducting order, can show long-range features only at zero temperature or at high magnetic fields.

### Loop current state

Apart from the finite  $Q$  orders, the pseudogap also hosts  $Q = 0$  orders such as the intra-unit cell loop currents, which break discrete symmetries like parity and time reversal. Within our framework, the loop currents appear as an “auxiliary” or a “preemptive” order [116].

Though the PDW order can be observed only below  $T = T_c$ , the fluctuations of the PDW field in the temperature regime  $T > T_c$  can give rise to auxiliary order parameters. With the motivation to generate a  $Q = 0$  (translationally invariant) emergent loop current order in the pseudogap phase, we construct a secondary order parameter following Ref.[189],

$$l = \left| \Delta_{PDW}^Q \right|^2 - \left| \Delta_{PDW}^{-Q} \right|^2, \quad (3.21)$$

where  $\Delta_{PDW}^Q$  is the amplitude of the PDW field and its value depends on the choice of the modulation wave vector  $Q$ . The PDW field transforms under translation  $T$ , time reversal  $TR$  and parity  $P$  as

$$\begin{aligned} T(\Delta_{PDW}^Q) &= e^{iT \cdot Q} \Delta_{PDW}^Q, \\ TR(\Delta_{PDW}^Q) &= \left( \Delta_{PDW}^{-Q} \right)^*, \\ P(\Delta_{PDW}^Q) &= \Delta_{PDW}^{-Q}. \end{aligned} \quad (3.22)$$

As  $l$  is composed of terms depending on  $\left( \Delta_{PDW}^Q \right)^* \Delta_{PDW}^Q$  and  $\left( \Delta_{PDW}^{-Q} \right)^* \Delta_{PDW}^{-Q}$ , it is a translationally invariant order parameter (under translation  $T(l) = l$ ). The loop current order parameter  $l$  also satisfies,

$$TR(l) = -l \quad P(l) = -l \quad TRP(l) = l. \quad (3.23)$$

Thus, the loop current order parameter defined in Eq. (3.21) satisfies the same symmetries as the magneto-electric loop current state proposed by Varma [190], which is often used to interpret the

intra-unit cell magnetic order seen in polarized elastic neutron scattering measurements [81]. It is important to highlight that the discrete  $Z_2$  symmetries like parity or time-reversal are spontaneously broken by the secondary order parameter  $l$ , which is composed of PDW fluctuations. So, a non-zero average value of  $\langle l \rangle$  does not mean  $\langle \Delta_{PDW}^Q \rangle \neq \langle \Delta_{PDW}^{-Q} \rangle$  (i.e. the PDW ground state does not break parity or time reversal) [189]. Possibilities of preemptive discrete  $Z_2$  symmetry breaking outside the Landau paradigm [191] occurring due to secondary order parameters is already discussed in Refs.[177] and [189]. Interestingly, the preemptive transition occurs at a higher temperature [177] than the primary order transition temperature, thus justifying the presence of loop current state in the  $T > T_c$  region.

## 3.2 Electronic spectral function in the pseudogap

### 3.2.1 Evidence for modulated order

The prime way of studying the effect of the pseudogap is by measuring the momentum and energy dependence of the electronic spectral function  $A(\mathbf{k}, \omega)$  by means of ARPES. By comparing the results obtained at temperatures above  $T^*$  to the result in the pseudogap region or in the superconducting state, we can then try to decipher the effect of each of these transitions. One important experiment in this regard is the one done by R.-H. He *et. al.* [63] on an underdoped Bi2201 sample. They tracked the evolution of the spectral function in the antinodal region, where the pseudogap is known to set in, for temperatures between  $T = 172 K$  down to  $T = 10 K$ . One of the results is the observation of a particle-hole symmetry breaking that appears at the pseudogap transition and is still present in the superconducting state. In contrast, the nodal region, which is still gapless in the pseudogap, do not show such anomaly and is well described by a d-wave superconducting gap for  $T < T_c$ . This particle-hole symmetry breaking was interpreted as the effect of a competing order breaking some combination of translation, rotation and time reversal symmetries. In particular, it was used as a tell-tale signature for the PDW state emerging from the Amperian pairing in Ref.[114]. We will start by giving more details on the results we can extract from the experimental data and we will then show how it can be obtained from our fractionalization ansatz starting from a microscopic Hamiltonian in Sec.3.2.2. Lastly, we give a phenomenological discussion on the effects of the phase and amplitude fluctuations we mentioned in the previous section and how they can be related to the temperature dependence of the spectral function observed experimentally in Sec.3.2.3.

The experimental results we will be interested in are the position of the maximum of the electronic spectral function as a function of energy and momentum along one of the crystal axis in the antinodal region. Fig.3.3(a) shows the different lines along which the measurements have been done. We see that the first cuts C1-C4 are close to the Brillouin zone edge and that they will give information about the effect of the pseudogap on the electronic degrees of freedom. The last cuts C5-C7 are closer to the nodal region and will cross the Fermi arcs where gapless quasiparticle states remain in the pseudogap region. In the superconducting states, these cuts will all show a gapped dispersion except the cut along the C7 line that crosses the diagonal of the Brillouin zone where the SC gap vanishes due to the d-wave symmetry. The position of the maximum of the spectral

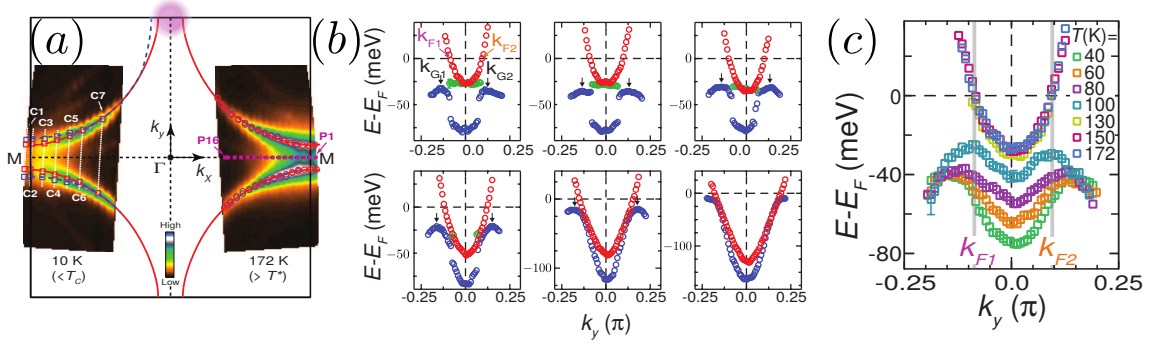


**Figure 3.3:** (a) Electronic spectral function measured at  $\omega = 0$  in the first Brillouin zone for two temperatures, below  $T_c$  (left side) and above  $T^*$  (right side). The white dashed lines indicate the different cuts for which the energy dependence is studied. (b) Energy dependence of the electronic spectral function for cuts C1-C6 from panel (a). The red dots indicate the position of the maximum of the spectral function for  $T > T^*$  while the blue dots show the position of the maximum for  $T < T_c$ . The green dots indicate the position of a broad maximum that is observed only in the superconducting state. The black arrows designate the back-bending of the band below  $T^*$ . (c) Energy dependence of the electronic spectral function for the cut C1 at different temperatures between 172 K and 40 K. We see the pseudogap opening at  $T \sim 130$  K while the superconducting transition does not change the dispersion significantly. The momentum-energy position of the back-bending is stable when the temperature is lowered but the position of the bottom of the band changes continuously. Adapted from Ref.[63].

function along the cuts C1-C6 is shown in Fig.3.3(b) for different temperatures. The red dots indicate the dispersion in the normal state above the pseudogap temperature. This dispersion is gapless for all the cuts. In the first panel, the Fermi momenta  $\mathbf{k}_F$  are defined as the momentum for which the normal state dispersion crosses the Fermi level. The blue dots then show the dispersion at a lower temperature, these do not change much across the superconducting transition except for a slight change in the energy of the bottom of the band as shown in Fig.3.3(c). The main observation is that, in the pseudogap phase, the dispersion shows a *back-bending* at which the slope of the dispersion changes sign. This back-bending occurs at momenta denoted by  $\mathbf{k}_G$  that are shifted with respect to the normal state Fermi momenta  $\mathbf{k}_F$ . This mismatch is the core of our study, it is in fact not possible to obtain this back-bending with  $\mathbf{k}_G \neq \mathbf{k}_F$  by considering a simple superconducting order (see for example Fig.2.2). This is thus taken as the indication that there is another symmetry being broken at the pseudogap transition.

Another observation is the detection of an additional “flat band” designated by the green dots in panel 1-3 of Fig.3.3(b). In contrast with the blue dispersion which varies only slightly below  $T^*$ , this flat band is only observed in the superconducting state and is much broader than the well-defined blue band at higher energy. The position of this broad peak in the spectral function seems to be locked to the energy of the bottom of the normal state dispersion. Superconductivity being generally associated with the opening of a gap at the Fermi level, it is not clear how this band can emerge below  $T_c$  at energies away from the Fermi level. Lastly, the temperature dependence of the band structure shown in Fig.3.3(c) shows that only the position of the bottom of the band changes significantly when the temperature is lowered. In particular, the value of the back-bending momentum  $\mathbf{k}_G$  does not change and the energy at which the latter occurs is also independent of the temperature. This is a strong indication that the phenomenon causing the change in the electronic dispersion at  $T^*$  is still present in the superconducting phase and is still dominating in the antinodal region.

One idea is that this mismatch could be due to the translation symmetry breaking that is known to break the particle-hole symmetry of the band structure. It was however shown that the CDW order observed in cuprate could not alone explain the observed back-bending for the range of momentum at which it is observed [114]. The PDW obtained from the Amperean pairing mechanism yields a similar band structure in the antinodal region and we will here show that our fractionalization ansatz of constrained SC and CDW orders give very good agreement with the experimental data due to the translation and charge conservation symmetry breaking effect.

### 3.2.2 Microscopic $t$ - $J$ - $V$ model

In order to study the effect of our pseudogap ansatz Eq.(3.14) we will start from a microscopic model and use mean-field theory to obtain a self-consistent equation for our pseudogap parameter  $\Psi_{\mathbf{k}}$  in momentum space. We will see that it will have a non-zero amplitude in the antinodal region and leads to the formation of Fermi arcs. Moreover, the electronic dispersion in the pseudogap is in very good agreement with the previous experimental observations.

To study the pseudogap phase of underdoped cuprates we start from the  $t$ - $J$  model (already presented in Sec.2.4.1 to which we add a small nearest-neighbour density-density interaction leading to

$$H_{t-J-V} = - \sum_{i,j,\sigma} t_{ij} \left( c_{i\sigma}^\dagger c_{j\sigma} + \text{h.c.} \right) + \sum_{\langle i,j \rangle} (J S_i \cdot S_j + V n_i n_j). \quad (3.24)$$

The reason for this additional term comes from the symmetry between the SC and CDW order we mentioned in Sec.3.1.1. This exact symmetry is also realized in the  $t$ - $J$  model for some specific point in the momentum space for which the gap equation for the superconducting or charge density wave order parameter is the same. We here break this symmetry with the density-density interaction which will favour the CDW state over the SC states. This is a common way to study the coexistence of both orders [192–194] even though this usually require a critical value of  $V$  to stabilize a coexistence phase while the SC order is still otherwise favoured. The standard  $t$ - $J$  model is also generally accompanied by the projection operators that remove all the states with double occupancy as these are prohibited by the strong on-site repulsion in the Hubbard model. As we discussed in Sec.2.4.2, this projection is difficult to handle analytically and we use here a Gutzwiller mean-field idea. The strong correlations are thus taken into account by a renormalization of the kinetic energy and of the spin-spin interaction by two doping dependent parameters  $g_t$  and  $g_J$  respectively which are given by

$$g_t(p) = \frac{2p}{1+p}, \quad g_J(p) = \frac{4}{(1+p)^2}. \quad (3.25)$$

This is equivalent to projecting out all the states with double-occupancy at the mean-field level. We start by writing the model in momentum space

$$H = \sum_{\mathbf{k}} \epsilon_{\mathbf{k}} c_{\mathbf{k}\sigma}^\dagger c_{\mathbf{k}\sigma} + \sum_{\mathbf{k},\mathbf{k}',\mathbf{q}} \sum_{\alpha,\mu} \left( V_{\mathbf{q}} c_{\mathbf{k},\alpha}^\dagger c_{\mathbf{k}+\mathbf{q},\alpha} c_{\mathbf{k}'+\mathbf{q},\mu}^\dagger c_{\mathbf{k}',\mu} \right) + \sum_{\mathbf{k},\mathbf{k}',\mathbf{q}} \sum_{\alpha,\beta,\mu,\nu} \left( J_{\mathbf{q}} \boldsymbol{\sigma}_{\alpha\beta} \cdot \boldsymbol{\sigma}_{\mu\nu} c_{\mathbf{k},\alpha}^\dagger c_{\mathbf{k}+\mathbf{q},\beta} c_{\mathbf{k}'+\mathbf{q},\mu}^\dagger c_{\mathbf{k}',\nu} \right). \quad (3.26)$$

The electronic dispersion  $\epsilon_{\mathbf{k}}$  is taken to match the dispersion in the normal state obtain by ARPES which yields [63]

$$\begin{aligned} \epsilon_{\mathbf{k}} = & -2t (\cos(k_x) + \cos(k_y)) - 4t' \cos(k_x) \cos(k_y) - 2t'' (\cos(2k_x) + \cos(2k_y)) \\ & - 4t''' (\cos(2k_x) \cos(k_y) + \cos(2k_y) \cos(k_x)) - \mu \end{aligned} \quad (3.27)$$

with  $t = 0.22 \text{ eV}$ ,  $\frac{t'}{t} = -0.156$ ,  $\frac{t''}{t} = 0.163$ ,  $\frac{t'''}{t} = -0.0326$  and  $\mu = -0.24327 \text{ eV}$ . Because the band structure in the real material already include the effect of the renormalization due to the strong electronic correlation, we take this dispersion to already include the effect of  $g_t$ . We then proceed to decouple the two interaction terms in two channel. One will be the pairing channel giving rise to superconductivity while the second one will be related to singlet particle-hole pairs that will give us our CDW order parameter. The different decoupling of the spin-spin and density-density interactions are as follow

$$\begin{aligned} & \sum_{\sigma, \sigma'} \sigma \sigma' \left[ \left\langle c_{\mathbf{k}\sigma}^\dagger c_{\mathbf{k}+\mathbf{q}\sigma} c_{\mathbf{k}'+\mathbf{q}\sigma'}^\dagger c_{\mathbf{k}'\sigma'} \right\rangle \right] \\ = & \sum_{\sigma, \sigma'} \sigma \sigma' \left[ \left\langle c_{\mathbf{k}\sigma}^\dagger c_{\mathbf{k}+\mathbf{q}\sigma} \right\rangle c_{\mathbf{k}'+\mathbf{q}\sigma'}^\dagger c_{\mathbf{k}'\sigma'} + c_{\mathbf{k}\sigma}^\dagger c_{\mathbf{k}+\mathbf{q}\sigma} \left\langle c_{\mathbf{k}'+\mathbf{q}\sigma'}^\dagger c_{\mathbf{k}'\sigma'} \right\rangle \right. \\ & - \left\langle c_{\mathbf{k}\sigma}^\dagger c_{\mathbf{k}'+\mathbf{q}\sigma'}^\dagger \right\rangle c_{\mathbf{k}+\mathbf{q}\sigma} c_{\mathbf{k}'\sigma'} - c_{\mathbf{k}\sigma}^\dagger c_{\mathbf{k}'+\mathbf{q}\sigma'}^\dagger \left\langle c_{\mathbf{k}+\mathbf{q}\sigma} c_{\mathbf{k}'\sigma'} \right\rangle \\ & \left. + \left\langle c_{\mathbf{k}\sigma}^\dagger c_{\mathbf{k}'\sigma'} \right\rangle c_{\mathbf{k}+\mathbf{q}\sigma} c_{\mathbf{k}'+\mathbf{q}\sigma'}^\dagger + c_{\mathbf{k}\sigma}^\dagger c_{\mathbf{k}'\sigma'} \left\langle c_{\mathbf{k}+\mathbf{q}\sigma} c_{\mathbf{k}'+\mathbf{q}\sigma'}^\dagger \right\rangle \right] \end{aligned} \quad (3.28)$$

$$\begin{aligned} \left\langle c_{\mathbf{k}\uparrow}^\dagger c_{\mathbf{k}+\mathbf{q}\downarrow} c_{\mathbf{k}'+\mathbf{q}\downarrow}^\dagger c_{\mathbf{k}'\uparrow} \right\rangle = & \left\langle c_{\mathbf{k}\uparrow}^\dagger c_{\mathbf{k}+\mathbf{q}\downarrow} \right\rangle c_{\mathbf{k}'+\mathbf{q}\downarrow}^\dagger c_{\mathbf{k}'\uparrow} + c_{\mathbf{k}\uparrow}^\dagger c_{\mathbf{k}+\mathbf{q}\downarrow} \left\langle c_{\mathbf{k}'+\mathbf{q}\downarrow}^\dagger c_{\mathbf{k}'\uparrow} \right\rangle \\ & - \left\langle c_{\mathbf{k}\uparrow}^\dagger c_{\mathbf{k}'+\mathbf{q}\downarrow}^\dagger \right\rangle c_{\mathbf{k}+\mathbf{q}\downarrow} c_{\mathbf{k}'\uparrow} - c_{\mathbf{k}\uparrow}^\dagger c_{\mathbf{k}'+\mathbf{q}\downarrow}^\dagger \left\langle c_{\mathbf{k}+\mathbf{q}\downarrow} c_{\mathbf{k}'\uparrow} \right\rangle \\ & + \left\langle c_{\mathbf{k}\uparrow}^\dagger c_{\mathbf{k}'\uparrow} \right\rangle c_{\mathbf{k}+\mathbf{q}\downarrow} c_{\mathbf{k}'+\mathbf{q}\downarrow}^\dagger + c_{\mathbf{k}\uparrow}^\dagger c_{\mathbf{k}'\uparrow} \left\langle c_{\mathbf{k}+\mathbf{q}\downarrow} c_{\mathbf{k}'+\mathbf{q}\downarrow}^\dagger \right\rangle \end{aligned} \quad (3.29)$$

There are numerous possibilities in which we can decouple these interaction terms. In particular, we can see that the first line in Eq.(3.28) will renormalize the band structure and is thus the momentum space representation of the Fock term mentioned in Sec.2.3.1. In the same way, the terms on the last line that are allowed to have  $\sigma \neq \sigma'$  can lead to magnetic order and in particular to antiferromagnetism if the total momentum  $\mathbf{k} - \mathbf{k}' - \mathbf{q} = \pm\boldsymbol{\pi}$ . We will here limit ourselves to a simple singlet pairing and a modulated particle-hole field

$$\begin{aligned} \Delta_{\mathbf{k}} &= \sum_{\sigma} \sigma \langle c_{\mathbf{k}\sigma} c_{-\mathbf{k}-\sigma} \rangle \\ \chi_{\mathbf{k}} &= \sum_{\sigma} \left\langle c_{\mathbf{k}\sigma}^\dagger c_{\mathbf{k}+\mathbf{Q}\sigma} \right\rangle. \end{aligned} \quad (3.30)$$

These two expectations value appears in both decompositions which leads to a coupling constant  $\sim 3J$ . There is however a sign change in the decoupling coming from the density-density interaction in the pairing channel in Eq.(3.28) which will lead to two different coupling constants  $J_-(\mathbf{q}) = 3J_{\mathbf{q}} - V_{\mathbf{q}}$  and  $J_+(\mathbf{q}) = 3J_{\mathbf{q}} + V_{\mathbf{q}}$  for the SC and the CDW order parameters respectively. We can

then write our effective mean-field action in three pieces

$$\begin{aligned}
S &= S_0 + S_\Delta + S_\chi, \tag{3.31} \\
S_0 &= \int d\tau \sum_{\mathbf{k}, \sigma} c_{\mathbf{k}\sigma}^\dagger (i\partial_\tau - \epsilon_{\mathbf{k}}) c_{\mathbf{k}\sigma}, \\
S_\Delta &= \int d\tau \sum_{\mathbf{k}, \mathbf{q}} \left[ \sum_{\sigma} \left( \sigma \Delta_{\mathbf{k}+\mathbf{q}} c_{\mathbf{k}\sigma}^\dagger c_{-\mathbf{k}\bar{\sigma}}^\dagger + \Delta_{\mathbf{k}}^* c_{-\mathbf{k}-\mathbf{q}\bar{\sigma}} c_{\mathbf{k}+\mathbf{q}\sigma} \right) + \frac{\Delta_{\mathbf{k}+\mathbf{q}} \Delta_{\mathbf{k}}^*}{J_{\mathbf{q}}} \right], \\
S_\chi &= \int d\tau \sum_{\mathbf{k}, \mathbf{q}} \left[ \sum_{\sigma} \left( \chi_{\mathbf{k}+\mathbf{q}} c_{\mathbf{k}+\mathbf{Q}\sigma}^\dagger c_{\mathbf{k}\sigma} + \chi_{\mathbf{k}}^* c_{\mathbf{k}+\mathbf{q}\sigma}^\dagger c_{\mathbf{k}+\mathbf{Q}+\mathbf{q}\sigma} \right) + \frac{\chi_{\mathbf{k}+\mathbf{q}} \chi_{\mathbf{k}}^*}{J_{\mathbf{q}}^+} \right].
\end{aligned}$$

The standard procedure to treat the action in Eq.(3.31) is to integrate the fermionic field as we can now use the Gaussian integral result (see Sec.2.1.3) and we get an action solely in terms of the bosonic fields  $\Delta_{\mathbf{k}}$  and  $\chi_{\mathbf{k}}$

$$S = \int d\tau \sum_{\mathbf{k}, \mathbf{q}} \left( \frac{\Delta_{\mathbf{k}+\mathbf{q}} \Delta_{\mathbf{k}}^*}{J_{\mathbf{q}}} + \frac{\chi_{\mathbf{k}+\mathbf{q}} \chi_{\mathbf{k}}^*}{J_{\mathbf{q}}^+} \right) - \text{Tr} \ln \left( i\omega_n - \epsilon_{\mathbf{k}} - \frac{|\Delta_{\mathbf{k}}|^2}{i\omega_n + \epsilon_{\mathbf{k}}} - \frac{|\chi_{\mathbf{k}}|^2}{i\omega_n - \epsilon_{\mathbf{k}+\mathbf{Q}}} \right) \tag{3.32}$$

The self-consistent mean-field equation for the two order parameters can be found by minimizing the variation of the action with respect to the mean-field, *i.e.*

$$\begin{aligned}
\Delta_{\mathbf{k}} &= \frac{-1}{\beta N} \sum_{\mathbf{q}, n} \frac{J_-(\mathbf{q}) \Delta_{\mathbf{k}+\mathbf{q}}}{i\omega_n + \epsilon_{\mathbf{k}+\mathbf{q}}} \frac{1}{i\omega_n - \epsilon_{\mathbf{k}+\mathbf{q}} - \frac{|\Delta_{\mathbf{k}+\mathbf{q}}|^2}{i\omega_n + \epsilon_{\mathbf{k}+\mathbf{q}}} - \frac{|\chi_{\mathbf{k}+\mathbf{q}}|^2}{i\omega_n - \epsilon_{\mathbf{k}+\mathbf{Q}+\mathbf{q}}}}, \\
\chi_{\mathbf{k}} &= \frac{-1}{\beta N} \sum_{\mathbf{q}, n} \frac{J_+(\mathbf{q}) \chi_{\mathbf{k}+\mathbf{q}}}{i\omega_n - \epsilon_{\mathbf{k}+\mathbf{Q}+\mathbf{q}}} \frac{1}{i\omega_n - \epsilon_{\mathbf{k}+\mathbf{q}} - \frac{|\Delta_{\mathbf{k}+\mathbf{q}}|^2}{i\omega_n + \epsilon_{\mathbf{k}+\mathbf{q}}} - \frac{|\chi_{\mathbf{k}+\mathbf{q}}|^2}{i\omega_n - \epsilon_{\mathbf{k}+\mathbf{Q}+\mathbf{q}}}}. \tag{3.33}
\end{aligned}$$

Note that solving these two coupled self-consistent equations would give us information about the competition or coexistence of long-range CDW and SC orders. This is not the description we have in mind for the pseudogap phase but we will still go forward to describe the steps needed to make progress on these gap equations as we will use the same ideas for our pseudogap parameter and it will give us an understanding of the difference between the modulated and the pairing orders. This will also provide us with a basis to compare the solution we will obtain for the pseudogap to the standard competition scenario. We first start by decoupling the two equations by imposing a *strong* competition between the two orders. This is done by considering that only one of the order can have a non-zero expectation value at a given momentum. In fact, the presence of both  $\Delta_{\mathbf{k}}^2$  and  $\chi_{\mathbf{k}}^2$  in the denominator of Eq.(3.33), having a non-zero value for one of the competing order will lower the self-consistent solution for the other. Moreover, the free energy includes term proportional to  $\Delta_{\mathbf{k}}^2$  and  $\chi_{\mathbf{k}}^2$ , meaning that the total energy will be lowered by considering only the largest of the SC or CDW amplitude. We get the decoupled gap equations

$$\begin{aligned}
\Delta_{\mathbf{k}} &= \frac{-1}{\beta N} \sum_{\mathbf{q}, n} \frac{J_-(\mathbf{q}) \Delta_{\mathbf{k}+\mathbf{q}}}{(i\omega_n)^2 - \epsilon_{\mathbf{k}+\mathbf{q}}^2 - \Delta_{\mathbf{k}+\mathbf{q}}^2} \quad \text{if } \Delta_{\mathbf{k}}^2 > \chi_{\mathbf{k}}^2 \text{ else } 0, \\
\chi_{\mathbf{k}} &= \frac{-1}{\beta N} \sum_{\mathbf{q}, n} \frac{J_+(\mathbf{q}) \chi_{\mathbf{k}+\mathbf{q}}}{(i\omega_n - \epsilon_{\mathbf{k}+\mathbf{q}})(i\omega_n - \epsilon_{\mathbf{k}+\mathbf{Q}+\mathbf{q}}) - \chi_{\mathbf{k}+\mathbf{q}}^2} \quad \text{if } \chi_{\mathbf{k}}^2 > \Delta_{\mathbf{k}}^2 \text{ else } 0. \tag{3.34}
\end{aligned}$$

As in the case of the BCS theory, we will now make an approximation on the form of the interaction to continue (see Sec.2.3.2). In our case, we assume that the antiferromagnetic correlations are

dynamic, strongly renormalized, and short-ranged, as given by the phenomenology of neutron scattering studies for cuprates [195]. For this we will take the spin-spin interaction to be peaked around  $\mathbf{Q}_{AF} = (\pi, \pi)$  and finite in a window  $q_{AF}$ . The energy dependence is ignored as we also ignore the energy dependence of the order parameters. As we take the density-density interaction to be small we consider it will not change the momentum space structure of  $J(\mathbf{q})$ . With this, we can restrict the momentum summation in Eq.(3.34) to momenta  $\mathbf{q}$  around  $\mathbf{Q}_{AF}$ . We keep here only the equation for the SC parameter for conciseness while the one treatment of the CDW order is done in Appendix B.

$$\Delta_{\mathbf{k}} = \frac{-1}{\beta N} \sum_{\mathbf{q}, n}^{|q| < q_{AF}} \frac{J_- \Delta_{\mathbf{k}+\mathbf{q}+\mathbf{Q}_{AF}}}{(i\omega_n)^2 - \epsilon_{\mathbf{k}+\mathbf{q}+\mathbf{Q}_{AF}}^2 - \Delta_{\mathbf{k}+\mathbf{q}+\mathbf{Q}_{AF}}^2}. \quad (3.35)$$

One way to continue is to invoke the d-wave symmetry of the SC order parameter to get  $\Delta_{\mathbf{k}+\mathbf{Q}_{AF}} = -\Delta_{\mathbf{k}}$  but as this may not hold for the CDW or pseudogap parameters we will use a general technique and use the self-consistent equation Eq.(3.35) to express  $\Delta_{\mathbf{k}+\mathbf{q}+\mathbf{Q}_{AF}}$  as a function of  $\Delta_{\mathbf{k}+2\mathbf{q}+2\mathbf{Q}_{AF}} \sim \Delta_{\mathbf{k}+\mathbf{q}}$

$$\Delta_{\mathbf{k}} = \frac{1}{(\beta N)^2} \sum_{\mathbf{q}, n}^{|q| < q_{AF}} \frac{J_-}{(i\omega_n)^2 - \tilde{\epsilon}_{\mathbf{k}+\mathbf{q}}^2 - \tilde{\Delta}_{\mathbf{k}+\mathbf{q}}^2} \sum_{\mathbf{q}', m}^{|q'| < q_{AF}} \frac{J_- \Delta_{\mathbf{k}+\mathbf{q}'}}{(i\omega_m)^2 - \epsilon_{\mathbf{k}+\mathbf{q}'}^2 - \Delta_{\mathbf{k}+\mathbf{q}'}^2}, \quad (3.36)$$

where we introduce the notation  $\tilde{f}(\mathbf{k}) = f(\mathbf{k} + \mathbf{Q}_{AF})$ . We now makes the assumption that the width of the spin-spin correlation function being small in momentum space, the order parameter is constant in the region  $|q'| < q_{AF}$  and that the integration over  $q'$  and  $q$  can be taken as independent. This allow us to simplify the order parameter in the numerator on both side and, after performing the analytical Matsubara summation we get

$$1 = \left(\frac{J_-}{N}\right)^2 \sum_{\mathbf{q}} \frac{n_f(\tilde{E}_{+, \mathbf{k}+\mathbf{q}}) - n_f(\tilde{E}_{-, \mathbf{k}+\mathbf{q}})}{\tilde{E}_{+, \mathbf{k}+\mathbf{q}} - \tilde{E}_{-, \mathbf{k}+\mathbf{q}}} \sum_{\mathbf{q}'} \frac{n_f(E_{+, \mathbf{k}+\mathbf{q}'}) - n_f(E_{-, \mathbf{k}+\mathbf{q}'})}{E_{+, \mathbf{k}+\mathbf{q}'} - E_{-, \mathbf{k}+\mathbf{q}'}} \quad (3.37)$$

where for superconductivity  $E_{\pm, \mathbf{k}} = \pm\sqrt{\epsilon_{\mathbf{k}}^2 + \Delta_{\mathbf{k}}^2}$ . We can then rewrite this in a form close to the BCS gap equation Eq.(2.45)

$$1 = \left(\frac{J_-}{4\pi^2}\right)^2 \int_{-q_{AF}/2}^{q_{AF}/2} dq \frac{\tanh\left(\frac{\beta}{2}\tilde{E}_{+, \mathbf{k}+\mathbf{q}}\right)}{2\tilde{E}_{+, \mathbf{k}+\mathbf{q}}} \int_{-q_{AF}/2}^{q_{AF}/2} dq' \frac{\tanh\left(\frac{\beta}{2}E_{+, \mathbf{k}+\mathbf{q}'}\right)}{2E_{+, \mathbf{k}+\mathbf{q}'}}. \quad (3.38)$$

The main difference with the standard BCS gap equation is the dependence of the first integrand upon the shifted  $\tilde{E}_{\mathbf{k}} = \sqrt{\epsilon_{\mathbf{k}+\mathbf{Q}_{AF}}^2 + \Delta_{\mathbf{k}+\mathbf{Q}_{AF}}^2}$  while the second integrand in evaluated at the momentum  $\mathbf{k} + \mathbf{q}'$ . This can be solved by using the self-consistent equation to link  $\Delta_{\mathbf{k}+\mathbf{Q}_{AF}}$  to  $\Delta_{\mathbf{k}}$  once again which will give another integral of form we obtained in Eq.(3.38). Denoting this integral by  $I_{\mathbf{k}}(\Delta)$ , we can write our self-consistency condition as

$$1 = \left(\frac{J_-}{4\pi^2}\right)^2 I_{\mathbf{k}}(\Delta) I_{\mathbf{k}+\mathbf{Q}_{AF}} \left(\frac{-J_-}{4\pi^2} I_{\mathbf{k}}(\Delta)\right), \quad (3.39)$$

$$I_{\mathbf{k}}(\Delta) = \int_{-q_{AF}/2}^{q_{AF}/2} dq \frac{\tanh\left(\frac{\beta}{2}E_{+, \mathbf{k}+\mathbf{q}}\right)}{2E_{+, \mathbf{k}+\mathbf{q}}}. \quad (3.40)$$



This is a complicated integral equation but it is easily amenable to be solved numerically. In fact, for every momentum point  $\mathbf{k}$  we only need to integrate the normal dispersions  $\epsilon_{\mathbf{k}}$  and  $\epsilon_{\mathbf{k}+\mathbf{Q}_{AF}}$  in a circle of diameter  $q_{AF}$ , we can thus find  $\Delta_{\mathbf{k}}$  that satisfy Eq.(3.39) independently for any momentum point in the Brillouin zone. Looking at the integrand in Eq.(3.40), we see that it will be enhanced when  $\mathbf{k}$  is close to  $\mathbf{k}_F$  for which the dispersion vanishes. This leads to the product of integral being important when both  $\mathbf{k}$  and  $\mathbf{k} + \mathbf{Q}_{AF}$  are close to the Fermi surface, this is something that is better realized in the antinodal region than in the nodal region. Thus the superconducting gap will be suppressed close to the diagonal of the Brillouin zone as expected for the case of d-wave symmetry. Note that we can impose the form factor of the superconducting gap at multiple points in this derivation but we wanted to give here a general way to treat the self-consistent equation due to spin fluctuation interaction which is valid for other types of calculations.

Our description of the pseudogap region comes through the constraint that links the SC and CDW amplitude fluctuations as describe in Eq.(3.14). Because we assume that both the SC and CDW orders are fluctuating, the mean-field equations should give us a vanishing solution for  $\Delta$  and  $\chi$ . However, we should have a non-zero value of the pseudogap amplitude given by  $|\Psi|^2 = |\Delta|^2 + |\chi|^2$ . In the spirit of mean-field theory, we write an effective action which is a function of  $\Psi_{\mathbf{k}}$  that we will minimize to get a self-consistent equation that will fix the value of the constraint. This is done by rewriting the mean-field action Eq.(3.31)

$$S_{eff} = \int d\tau \sum_{\mathbf{k}, \mathbf{q}} \frac{\Psi_{\mathbf{k}}^\dagger \Psi_{\mathbf{k}+\mathbf{q}}}{\tilde{J}_{\mathbf{q}}} - \text{Tr} \ln(G^{-1}(i\omega_n, \mathbf{k}))$$

$$G^{-1}(i\omega_n, \mathbf{k}) = i\omega_n - \epsilon_{\mathbf{k}} - \frac{|\Psi_{\mathbf{k}}|^2}{2} \left( \frac{1}{i\omega_n + \epsilon_{\mathbf{k}}} + \frac{1}{i\omega_n - \epsilon_{\mathbf{k}+\mathbf{Q}}} \right). \quad (3.41)$$

Once again differentiating the action with respect to the amplitude of the order parameter (here the pseudogap amplitude) leads to the self-consistent equation

$$|\Psi_{\mathbf{k}}| = \frac{-1}{\beta N} \sum_{i\omega_n, \mathbf{q}} \frac{\tilde{J} \left( i\omega_n + \frac{\tilde{\Delta}_{\mathbf{k}+\mathbf{q}}}{2} \right) |\Psi_{\mathbf{k}+\mathbf{Q}_{AF}}|}{\left( (i\omega_n)^2 - \tilde{\epsilon}_{\mathbf{k}+\mathbf{q}}^2 \right) (i\omega_n - \tilde{\epsilon}_{\mathbf{k}+\mathbf{Q}+\mathbf{q}}) - \left( i\omega_n + \frac{\tilde{\Delta}_{\mathbf{k}+\mathbf{q}}}{2} \right) |\Psi_{\mathbf{k}+\mathbf{Q}_{AF}}|^2} \quad (3.42)$$

where we already used the approximation concerning the form of the interaction and we introduced the notation  $\Delta\epsilon_{\mathbf{k}} = \epsilon_{\mathbf{k}} - \epsilon_{\mathbf{k}+\mathbf{Q}}$ . Note that the coupling constant that appears in the gap equation is  $\frac{1}{\tilde{J}} = \frac{1}{2} \left( \frac{1}{J_+} + \frac{1}{J_-} \right)$  and is thus larger than the coupling constant for the SC order.

Results of this self-consistent equation are shown in Fig.3.4(b) for a modulation wave-vector linking hot-spots along the  $x$  axis. Hot-spots are points of the Fermi surface linked by  $(\pi, \pi)$  and are thus expected to be important due to the form of our interaction. Due to the finite wave-vector of the pseudogap amplitude, the gap equation Eq.(3.42) admits non-zero solution only in the antinodal region (ANR), when this modulation vector links two parts of the Fermi surface. The region close to the Brillouin zone diagonal will thus remain unperturbed by the transition at  $T^*$ . The electronic spectral function  $A(\omega, \mathbf{k}) = -2\text{Im}(G(\omega + i\eta, \mathbf{k}))$  for  $\omega = 0$  and  $\eta \rightarrow 0^+$  shows that the ANR is gapped while the nodal region forms Fermi arcs (Fig.3.4(c)). These arcs terminate close to the hot-spots.

We now look at the reconstructed band structure obtained from the zeros of  $G^{-1}(\mathbf{k}, \omega)$  in the



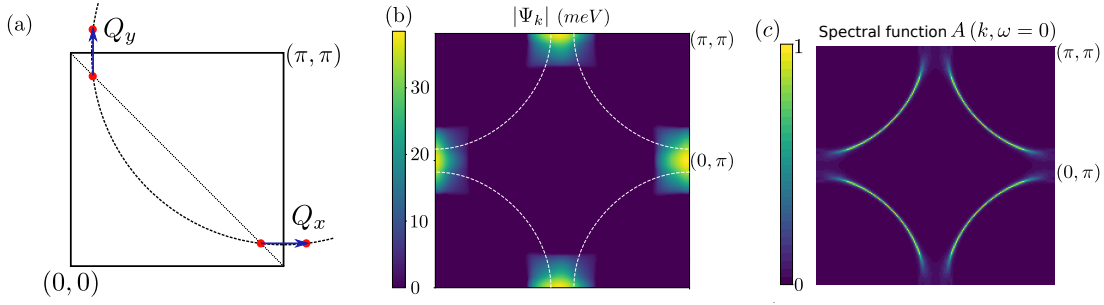


**Figure 3.4:** (a) Schematic representation of the Brillouin zone for cuprates with the modulation wave-vector used in this work. (b) Solution of the gap equation for the pseudogap amplitude Eq.(3.42). Colored regions show non-zero solutions for  $|\Psi_{\mathbf{k}}|$ . We used an axial modulation wave-vector  $Q_x$  relating hot-spots shown in panel (a) and  $J = 300 \text{ meV}$ ,  $V = J/10$  and  $q_{AF} = 0.15 \text{ r.l.u.}$ . The white line indicate the non-interacting Fermi surface. (c) Electronic spectral function  $A(\mathbf{k}, \omega = 0)$  obtained from Eq.(3.41) for  $|\Psi_{\mathbf{k}}|$  given by Eq.(3.42). We see the formation of Fermi arcs as the ANR gets gapped out. We used a broadening factor  $\eta = 5 \text{ meV}$  for numerical purposes. Adapted from Ref.[135]

ANR. From the form of  $G(\mathbf{k}, \omega)$  in Eq.(3.41), we can understand the dispersion as coming from an equal superposition of SC and CDW order in the ANR. We can thus construct the resulting band structure in the pseudogap as the hybridization of the three bands  $\epsilon_{\mathbf{k}}$ , the normal state dispersion,  $-\epsilon_{\mathbf{k}}$  coming from the superconducting order and  $\epsilon_{\mathbf{k}+\mathbf{Q}}$  coming from the modulating order. At the zone boundary ( $k_x = \pi$ ), this results in two bands below the Fermi level shown in Fig.3.5(i) with one of them presenting a back-bending (blue line) indicated by black arrows while the other one (yellow line) present little dispersion around  $k_y = 0$ . In our mean-field description, this back-bending appears as a result of the hybridization between the hole band  $-\epsilon_{\mathbf{k}}$  (green dotted) and the shifted  $\epsilon_{\mathbf{k}+\mathbf{Q}}$  (blue dotted) band in Fig.3.5(i). As such this back-bending will occur at  $k_y = k_G > k_F$  as long as  $\epsilon_{\mathbf{k}+\mathbf{Q}} < \epsilon_{\mathbf{k}}$  which is satisfied for all  $k_x > k_{hot-spot}$ . This means that this anomalous back-bending will persist below  $T_c$  in the ANR but we will recover a standard back-bending at  $k_y = k_F$  in the nodal region as the above condition is not satisfied.

The spectral weight  $A(\mathbf{k}, \omega)$  for each band is obtained for different fixed values of  $k_x = \pi - \delta k_x$  and compared to the experimental dispersion of Ref.[63] (Fig.3.5(a)-(d)). As we get closer to the centre of the Brillouin zone we can see that the energy of the maximum of the band gets closer to the Fermi level leading to the pseudogap closing “from below” (Fig.3.5(e)-(h)) as observed experimentally. Note that we obtain here a gap closing “from below” contrary to what was argued previously for a pure CDW scenario with a modulation along the  $y$  direction [114]. This is because we consider a modulation wave-vector along the  $x$  direction. This same orientation for the modulation wave-vector has been used recently to explain the same ARPES results in Bi2201 through the idea of a quantum disorder PDW [196] and other theoretical approaches such as a superposition of CDW and PDW order [178] or a Resonant Excitonic State [197] used the same wave-vector for the charge order component.

### 3.2.3 Phase and amplitude fluctuations

Our previous description of the band structure in the pseudogap also shows a second band located at the bottom of the non-interacting band. We connect here this band to the flat band observed

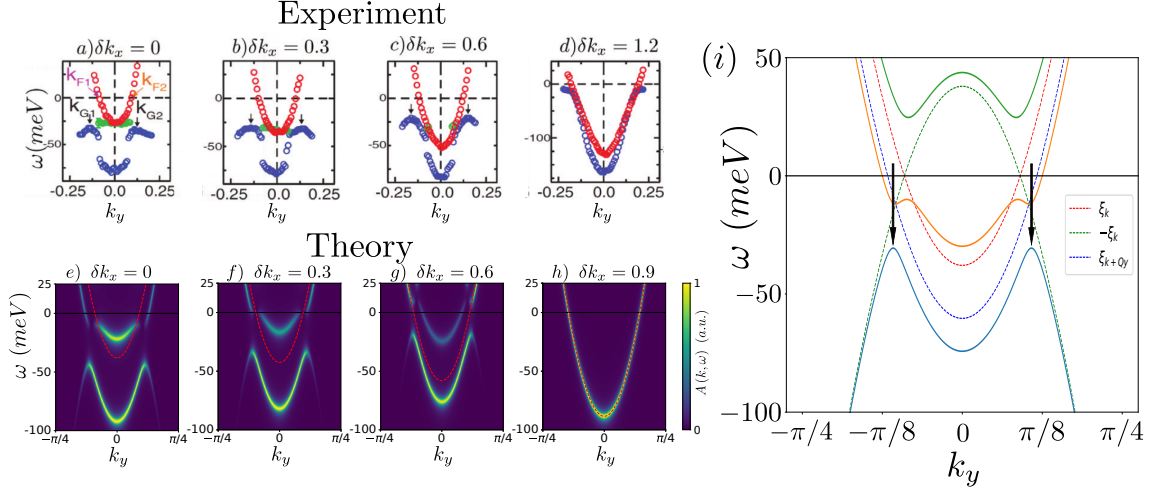


**Figure 3.5:** (a)-(d) Experimental dispersion obtained by ARPES [63] for  $T > T^*$  (red dots) and  $T < T_c$  (blue and green dots) for different cuts at fixed  $k_x = \pi - \delta k_x$ . The Fermi arcs end around  $\delta k_x = 0.6$  and the gap observed in the last panel is the standard nodal d-wave SC. (e)-(h) Theoretical results for the energy dependence of the spectral function  $A(\mathbf{k}, \omega)$  for cuts at fixed  $k_x = \pi - \delta k_x$ . The red dotted line is the non-interacting dispersion. We used the solution of Eq.(3.42) for the pseudogap amplitude and  $Q_x = (0.2, 0)\pi$ . (i) Band structure obtain by the Green's function in Eq.(3.41) for  $k_x = \pi$  and a constant  $|\Psi_{\mathbf{k}}| = 30$  meV. The dotted lines indicate the non-interacting dispersion  $\epsilon_{\mathbf{k}}$  (red), the hole band  $-\epsilon_{\mathbf{k}}$  (green) and the band from the modulating order  $\epsilon_{\mathbf{k}+Q_x}$  (blue). The black arrows point to the back-bending mentioned in the main text. Adapted from Ref.[135].

experimentally below  $T_c$  (green dots in Fig.3.5(a)-(c)) and argue that finite lifetimes for the single-particle and pair excitations lead to this band not being observed above  $T_c$ . For this, we add three phenomenological damping rates  $\Gamma_0$ ,  $\Gamma_1$  and  $\Gamma_2$  in our mean-field Green's function :

$$G^{-1}(i\omega_n, \mathbf{k}) = i\omega_n - \epsilon_{\mathbf{k}} - i\Gamma_0 - \frac{|\Psi_{\mathbf{k}}|^2}{2} \tilde{G}(i\omega_n, \mathbf{k}),$$

$$\tilde{G}(i\omega_n, \mathbf{k}) = (i\omega_n - \epsilon_{\mathbf{k}+Q} + i\Gamma_1)^{-1} + (i\omega_n + \epsilon_{\mathbf{k}} + i\Gamma_2)^{-1}. \quad (3.43)$$

The two factors  $\Gamma_1$  and  $\Gamma_2$  represent the inverse lifetime of particle-hole and particle-particle pairs respectively [73, 74, 198] and can be different as the two species can couple differently to outside perturbations such as disorder. These lifetimes capture the fluctuations in the pseudogap phase and are used in other approaches such as preformed pairs scenarios [112, 113, 199, 200] or appears when considering the effect of gaussian fluctuations [201] on top of mean-field theory. They are expected to be non-zero above  $T_c$  but to vanish at the transition temperature when fluctuations are quenched. The first  $\Gamma_0$  term is a single-particle lifetime that is always non-zero. To understand the effect it has on the electronic spectral function we compute the imaginary part of the retarded Green's function in Eq.(3.43) with  $\Gamma_1$  and  $\Gamma_2$  going to zero

$$-\text{Im}[G(\omega + i\eta, \mathbf{k})] = -\text{Im}\left[\lim_{\eta \rightarrow 0} \frac{1}{\omega - \epsilon_{\mathbf{k}} + i\Gamma_0 - \frac{|\Psi_{\mathbf{k}}|^2}{2} \left(\frac{1}{\omega - \epsilon_{\mathbf{k}+Q} + i\eta} + \frac{1}{\omega + \epsilon_{\mathbf{k}} + i\eta}\right)}\right]$$

$$= \frac{\Gamma_0}{\left[\omega - \epsilon_{\mathbf{k}} - \frac{|\Psi_{\mathbf{k}}|^2}{2} \left(\frac{1}{\omega - \epsilon_{\mathbf{k}+Q}} + \frac{1}{\omega + \epsilon_{\mathbf{k}}}\right)\right]^2 + \Gamma_0^2}$$

$$= \frac{(\omega - \epsilon_{\mathbf{k}+Q})^2 (\omega + \epsilon_{\mathbf{k}})^2 \Gamma_0}{[(\omega - E_{1,\mathbf{k}})(\omega - E_{2,\mathbf{k}})(\omega - E_{3,\mathbf{k}})]^2 + \Gamma_0^2 (\omega - \epsilon_{\mathbf{k}+Q})^2 (\omega + \epsilon_{\mathbf{k}})^2} \quad (3.44)$$

where  $E_{i,\mathbf{k}}$  ( $i = 1, 2, 3$ ) are the new dispersions in the pseudogap state and found as the roots of the denominator. This expression shows that the spectral weight is suppressed when the dispersion is close to the original bands  $-\epsilon_{\mathbf{k}}$  or  $\epsilon_{\mathbf{k}+\mathbf{Q}}$ . This explains the fact that only the bottom of the bands close to  $k_y = 0$  shows a significant spectral weight. The inclusion of finite lifetime will broaden the peak of the spectral function but will do so evenly on the three bands in the pseudogap as the spectral weight for any of the bands is given by

$$\frac{(\omega - \epsilon_{\mathbf{k}+\mathbf{Q}})^2 (\omega + \epsilon_{\mathbf{k}})^2 \Gamma_0}{[(\omega - E_{1,\mathbf{k}}) (\omega - E_{2,\mathbf{k}}) (\omega - E_{3,\mathbf{k}})]^2 + \Gamma_0^2 (\omega - \epsilon_{\mathbf{k}+\mathbf{Q}})^2 (\omega + \epsilon_{\mathbf{k}})^2} \xrightarrow{\omega \rightarrow E_{i,\mathbf{k}}} \frac{1}{\Gamma_0}. \quad (3.45)$$

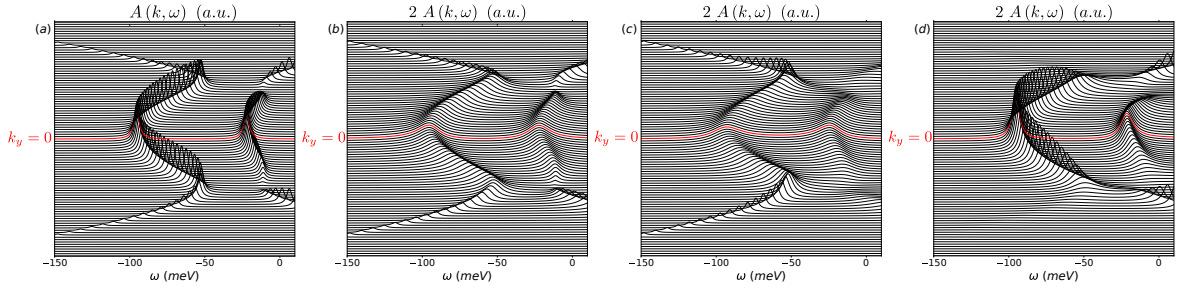


**Figure 3.6:** (a)-(d) Energy dependence of the spectral function at  $k_x = \pi$  for different  $k_y$  between  $-\pi/4$  and  $\pi/4$ , successive lines are shifted for clarity. (a) without any phase fluctuations  $\Gamma_0 = \Gamma_1 = \Gamma_2 = 0$ . We used a broadening  $\eta = 0.002$  eV for numerical purposes. (b) Turning on a finite single-particle lifetime  $\Gamma_0 = 0.02$  eV leads to both bands being broadened in a similar way. (c) In contrast, when we consider only a finite particle-hole lifetime  $\Gamma_1 = 0.02$  eV we see that the dispersion close to  $k_y = 0$  is more strongly affected than the dispersion at higher momenta. The flat band is also more strongly dampened than the main band. (d) The situation is reversed if we consider only a particle-particle lifetime  $\Gamma_2 = 0.02$  eV. The parts of the bands close to  $k_y = 0$  are less affected and still well defined. The flat band is broadened but remains visible. Adapted from Ref.[135].

We can contrast this by looking at the expression of the spectral function when including the finite particle-particle or the finite particle-hole pairs lifetimes. For clarity, we only here consider a finite value for  $\Gamma_1$  while we take  $\Gamma_0 = \Gamma_2 = \eta \rightarrow 0$

$$\begin{aligned} -\text{Im} [G(\omega + i\eta, \mathbf{k})] &= -\text{Im} \left[ \lim_{\eta \rightarrow 0} \frac{1}{\omega - \epsilon_{\mathbf{k}} + i\eta - \frac{|\Psi_{\mathbf{k}}|^2}{2} \left( \frac{1}{\omega - \epsilon_{\mathbf{k}+\mathbf{Q}} + i\Gamma_1} + \frac{1}{\omega + \epsilon_{\mathbf{k}} + i\eta} \right)} \right] \\ &= \frac{\Gamma_1 \frac{|\Psi_{\mathbf{k}}|^2}{2} (\omega + \epsilon_{\mathbf{k}})^2}{[(\omega - E_{1,\mathbf{k}}) (\omega - E_{2,\mathbf{k}}) (\omega - E_{3,\mathbf{k}})]^2 + \left( \omega^2 - \epsilon_{\mathbf{k}}^2 - \frac{|\Psi_{\mathbf{k}}|^2}{2} \right)^2 \Gamma_1^2}. \end{aligned} \quad (3.46)$$

It is more difficult to directly infer the effect of the inverse particle-hole lifetime  $\Gamma_1$  on different portions of the electronic dispersion but we can nonetheless see that there will be an increased spectral weight for the bands that are close to the root of the term proportional to  $\Gamma_1^2$  in the denominator, *i.e.* roots of  $\omega^2 - \epsilon_{\mathbf{k}}^2 - \frac{|\Psi_{\mathbf{k}}|^2}{2}$ . This actually corresponds to the dispersion in a standard superconductor with a gap given by  $\frac{|\Psi_{\mathbf{k}}|^2}{2}$  (see Sec.2.3.2) and will be realized in our 3 bands model for momenta larger than the back-bending momentum as the solution for the electronic dispersion collapses on  $\pm\epsilon_{\mathbf{k}}$  as shown in Fig.3.5(i). This is in agreement with the observation in Fig.3.6(c) that shows that the bands in the pseudogap are broadened close to  $k_y = 0$  when we turn on a

finite value of  $\Gamma_1$  while the shape of the electronic spectral function at higher momenta is mainly unaffected. This also holds for the “flat band” that gets significantly dampened by the particle-hole fluctuations.

The effect of each of these additional terms is depicted in Fig.3.6(a)-(d). As discussed from the result of Eq.(3.44), allowing a non-zero  $\Gamma_0$  will broaden the two bands below the Fermi level in similar ways (Fig.3.6(b)), in contrast to the pair lifetimes which have a very different effect on specific parts of the dispersion. Indeed, Fig.3.6(c) shows that a non-zero  $\Gamma_1$  will strongly suppress the “flat” band close to the Fermi level and also dampens the main band close to  $k_y = 0$ . Turning on the  $\Gamma_2$  term will have the opposite effect as the band far from  $k_y = 0$  gets dampened while the bottom of the flat and main bands remain well defined. The experimental observation of the flat band only close or below  $T_c$  can then be attributed to the presence of a particle-hole pair lifetime in the pseudogap. Note also that due to disorder effect, which couple directly to charge order [29], this lifetime could remain non-zero below  $T_c$  and thus leads to this band remaining broad even in the superconducting state as observed experimentally. Moreover, this description provides a good agreement with the experimental observation that the dispersion in the ANR does not change across the superconducting transition. In our case, the position of the main band does not change with temperature and only the spectral weights of the two bands get modified as the different lifetimes decrease.

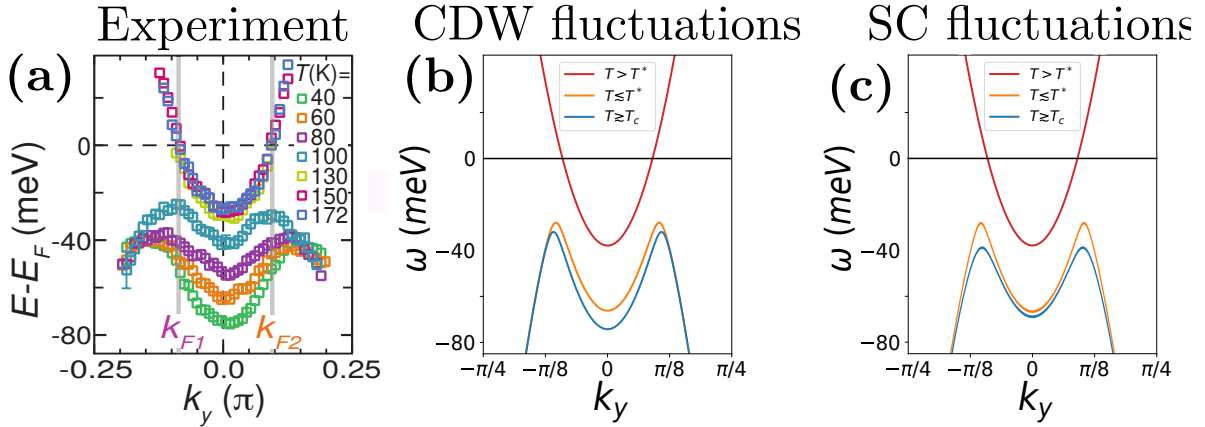


**Figure 3.7:** (a) Experimental measurement for a range of temperature going from above  $T^* \sim 132$  K to  $T \gtrsim T_c \sim 38$  K [63]. (b) The red line indicates the non-interacting band above  $T^*$ . The orange line is the band after the opening of the pseudogap presenting a back-bending shifted from the original Fermi momentum  $k_F$ . When going down in temperature we add a finite mean-field amplitude for the CDW order and obtain the band dispersion represented in blue. The back-bending wave-vector and the gap with respect to the Fermi level are mainly unchanged while the bottom of the band is strongly affected. (c) The red line indicates the non-interacting band above  $T^*$ . The orange line is the band after the opening of the pseudogap presenting a back-bending shifted from the original Fermi momentum  $k_F$ . When going down in temperature we add a finite mean-field amplitude for the SC order and obtain the band dispersion represented in blue. The back-bending wave-vector remain unchanged but the gap with respect to the Fermi level increases rapidly while the bottom of the band is only weakly affected. Adapted from Ref.[135].

Another feature of the temperature dependence measured experimentally for  $T^* > T > T_c$  in the ANR is a significant decrease of the energy of bottom of the band when the temperature is decreased while the maximum energy and the back-bending wave-vector change only slightly

as shown in Fig.3.7(a). We describe here this change in the band structure by adding a finite amplitude for the particle-hole order parameter  $|\chi_{\mathbf{k}}|$ . We then have three different regions such that at  $T > T^*$  we have free electrons. At  $T \lesssim T^*$  where the pseudogap has a finite amplitude but the particle-hole gap is still 0 and at  $T \gtrsim T_c$  where the particle-hole gap is finite. We then obtain the band dispersions shown in Fig.3.7(b). Because the bottom of the band is directly related to the hybridization with the band coming from the charge modulation, it is directly affected by the non-zero value of  $|\chi_{\mathbf{k}}|$ . On the other hand, the back-bending momentum is determined mainly by the value of the modulation wave-vector  $\mathbf{Q}$  and the energy of the maximum comes from the hybridization between the superconducting band  $-\epsilon_{\mathbf{k}}$  and the shifted band  $\epsilon_{\mathbf{k}+\mathbf{Q}}$ , thus related to the value of  $|\Psi_{\mathbf{k}}|$ .

Note that, once again, the superconducting part of the pseudogap plays an opposite role to the CDW part. In fact, allowing a finite value for the particle-particle pair amplitude  $|\Delta_{\mathbf{k}}|$  in the pseudogap phase and distinguishing the same temperature regimes as with the finite particle-hole pair amplitude, we obtain the dispersion shown in Fig.3.7(c). We can then see that the main change with temperature would be the energy at which the back-bending occurs, while the back-bending momentum remains unchanged as discussed previously. If this happens, it should be in a very narrow temperature range above  $T_c$  as the experimental results (Fig.3.7(a)) does not show any sign of it. The fact that  $|\chi_{\mathbf{k}}|$  acquire a quasi long-range component before the  $|\Delta_{\mathbf{k}}|$  is representative of the fact that CDW is observed experimentally at a temperature higher than the temperature for SC fluctuations  $T'_c$ . This long-range component of the CDW order would be the one observed by Raman spectroscopy [43], X-ray [146, 147, 149, 155, 169, 202] and NMR [145, 162, 180, 203] measurements above  $T_c$ .

This particular ARPES experiment is important as it shows the effect that a modulating order can have even without any long-range order on the single-particle quantities as measured by spectroscopy. It was addressed in multiple contexts with the ideas of a quantum disorder PDW [196], the superposition of CDW and PDW order [178] or the Resonant Excitonic States [197]. We showed here that we can reproduce the detailed momentum-energy-temperature dependence of the electronic spectral function starting from a microscopic model treated by mean-field theory considering our superposition of SC and CDW order and some additional phenomenological parameters. In the next section, we use the same setup to show that the Green's function from Eq.(3.41) can be associated with the peculiar pole structure of the electronic self-energy obtained in numerical treatments of the Hubbard model via DMFT.

## 3.3 Pole structure of the electronic self-energy

### 3.3.1 Electronic spectral function from CDMFT

Cluster extension of Dynamical Mean Field Theory (CDMFT) with 2x2 sites gives detailed energy-dependence of the electronic Green's function in the Hubbard model at low doping. Due to the small system size, this is however limited to some specific points of the Brillouin zone. One of the most important results concerns the antinodal point at  $\mathbf{k} = (0, \pi)$  where the pseudogap is observed above the superconducting state. CDMFT allows one to decompose the deviation from the non-

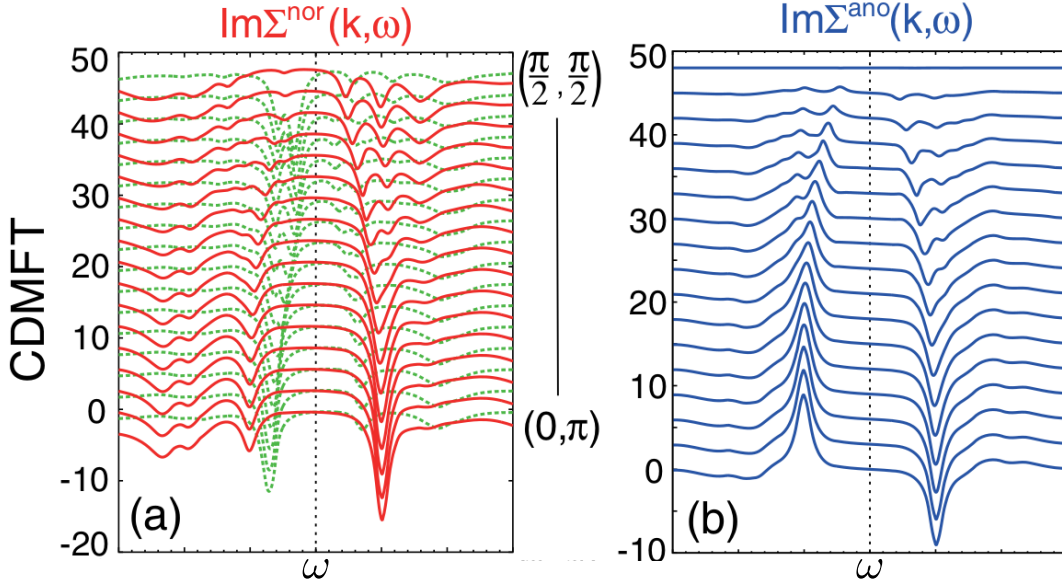


**Figure 3.8:** (a) Normal self-energy (red line) and electronic spectral function (green dotted lines) obtained by CDMFT for momenta on the line  $\mathbf{k} = (0, \pi) - (\pi/2, \pi/2)$ . The self-energy shows two isolated poles in the antinodal region at  $\omega = \pm\omega_0$  but with a clear asymmetry in weight. In the nodal region the peak at positive energy splits. The pole at negative energy is damped and difficult to follow. (b) Anomalous self-energy obtained by CDMFT for the same momenta. It shows pairs of poles at the same position as in the normal part but with an anti-symmetric weight. The same splitting occurs when going from the antinodal to the nodal region. The weight close to  $\mathbf{k} = (\pi/2, \pi/2)$  is close to zero, indicating that the coupling to the hidden-fermion is specific to the antinodal region. Adapted from Ref.[204].

interacting Green's function into two parts: the normal ( $\Sigma_N$ ) and anomalous ( $\Sigma_{AN}$ ) self-energy. The final form of the electronic Green's function is usually given by :

$$G(\mathbf{k}, \omega) = [\omega - \epsilon_{\mathbf{k}} - \Sigma_N(\mathbf{k}, \omega) - W(\mathbf{k}, \omega)]^{-1},$$

$$W(\mathbf{k}, \omega) = \frac{\Sigma_{AN}(\mathbf{k}, \omega)^2}{\omega + \epsilon_{\mathbf{k}} - \Sigma_N(\mathbf{k}, -\omega)^*} \quad (3.47)$$

The anomalous part of the self-energy is directly related to the superconducting order and vanishes outside of the ordered phase but the normal part presents features that lead to the pseudogap in the antinodal region at higher temperatures. Another quantity of interest is the electronic spectral function we already studied in the previous section and which relate directly to ARPES experiment for occupied states ( $\omega < 0$ ). Interestingly there are strong links between the structure in the normal self-energy above and below  $T_c$  as well as a connection with the anomalous self-energy. These seem to indicate that the pseudogap physics is strongly related to the superconducting state.

The energy dependence of the normal self-energy (red lines) and of the electronic spectral function (green dotted line) for momenta on a line from  $\mathbf{k} = (0, \pi)$  to  $\mathbf{k} = (\pi/2, \pi/2)$  is shown in Fig.3.8(a) in the superconducting phase. The distinctive feature of the self-energies in the antinodal region (at  $\mathbf{k} = (0, \pi)$ ) is the two symmetric peaks at low energy. The two poles of  $\Sigma_N$  have a marked weight asymmetry with the pole at  $\omega > 0$  having a larger spectral weight than the one at negative energies. The spectral function plotted at the same momentum (green dotted line in Fig.3.8(a)) presents 3 poles, one at negative energy which is well defined and 2 at positive energies which are broader. In contrast, the two poles of  $\Sigma_{AN}$  shown in Fig.3.8(b) for the same



momenta have the same position as the poles of  $\Sigma_N$  but opposite weight. When going toward the nodal region we observe that the pole at positive energy split into two poles of approximately equal weight. This is also the case for the pole at negative energy even though the vanishing weight close to  $\mathbf{k} = (\pi/2, \pi/2)$  makes it harder to pinpoint the position of the two peaks.

Another crucial piece of information given by CDMFT is the cancellation that occurs between the poles of  $\Sigma_N$  and  $W$ . Indeed it has been observed that, besides having poles at the same energy, the residue of both the normal and the anomalous self-energy at these poles is such that they cancel in the expression of the single-particle Green's function. This has consequences for the electronic spectral function as the poles of the self-energy should correspond to zeros of the spectral function, effectively leading to the splitting of the non-interacting band.

These results were interpreted in terms of "hidden-fermions" which couple to the original electronic degrees of freedom and are themselves susceptible to pairing [204–206]. It is then possible to write a mean-field Hamiltonian for this model and extract analytical expressions for the normal and anomalous self-energy. As we will show in the next section, this construction guarantees the cancellation between  $\Sigma_N$  and  $W$  mentioned earlier. It also displays a structure for both parts of the self-energy in agreement with the numerical results with proper choice for the hidden-fermion. We will present the model and its main features in Sec.3.3.2 and then show how to incorporate our fractionalization idea into the same formalism and compare the results to CDMFT in both the superconducting and the pseudogap states.

### 3.3.2 Hidden-fermion model

We start with the same hidden-fermion model from Ref.[204]. This model describes electrons ( $c_{\mathbf{k}\sigma}^\dagger$ ) on a square lattice coupled to other fermionic excitation ( $f_{\mathbf{k}\sigma}^{\alpha\dagger}$ ):

$$\begin{aligned}
H = & \sum_{\mathbf{k},\sigma} \epsilon_{\mathbf{k}} c_{\mathbf{k}\sigma}^\dagger c_{\mathbf{k}\sigma} + \sum_{\mathbf{k},\sigma} \left( \sigma \Delta_{\mathbf{k}} c_{\mathbf{k}\sigma}^\dagger c_{-\mathbf{k}-\sigma}^\dagger + h.c \right) \\
& + \sum_{\alpha,\mathbf{k},\sigma} \epsilon_{\mathbf{k}}^{f,\alpha} f_{\mathbf{k}\sigma}^{\alpha\dagger} f_{\mathbf{k}\sigma}^\alpha + \sum_{\alpha,\mathbf{k},\sigma} \left( \sigma \Delta_{\mathbf{k}}^{f,\alpha} f_{\mathbf{k}\sigma}^{\alpha\dagger} f_{-\mathbf{k}-\sigma}^\alpha + h.c \right) \\
& + \sum_{\alpha,\mathbf{k},\sigma} \left( V_{\mathbf{k}}^\alpha c_{\mathbf{k}\sigma}^\dagger f_{\mathbf{k}\sigma}^\alpha + h.c \right)
\end{aligned} \tag{3.48}$$

where  $\alpha$  numbers the number of hidden-fermion excitations we consider.

The electronic spectral function can then be obtained and the coupling to the different  $f_{\mathbf{k}\sigma}^\alpha$  excitation leads to a normal and anomalous self-energy given by :

$$\begin{aligned}
\Sigma_N(\mathbf{k}, \omega) &= \sum_{\alpha} \frac{V_{\mathbf{k}}^{\alpha 2} (\omega + \epsilon_{\mathbf{k}}^{f,\alpha})}{\omega^2 - \epsilon_{\mathbf{k}}^{f,\alpha 2} - \Delta_{\mathbf{k}}^{f,\alpha 2}} \\
\Sigma_{AN}(\mathbf{k}, \omega) &= \Delta_{\mathbf{k}} + \sum_{\alpha} \frac{-V_{\mathbf{k}}^{\alpha 2} \Delta_{\mathbf{k}}^{f,\alpha}}{\omega^2 - \epsilon_{\mathbf{k}}^{f,\alpha 2} - \Delta_{\mathbf{k}}^{f,\alpha 2}}
\end{aligned} \tag{3.49}$$

As can be seen from Eq.(3.49) the normal and anomalous part of the self-energy share a similar pole structure which is primarily governed by the choice of  $\Delta_{\mathbf{k}}^{f,\alpha}$  and  $\epsilon_{\mathbf{k}}^\alpha$ . The value of the coupling

between the  $c_{\mathbf{k}\sigma}^\dagger$  and the  $f_{\mathbf{k}\sigma}^{\alpha\dagger}$  fermions only enters in the spectral weight at the different poles as can be seen by computing the residue of the self-energy :

$$\begin{aligned}\text{Res}(\Sigma_N, \pm\omega^\alpha) &= \frac{V_{\mathbf{k}}^{\alpha 2}}{2} \left( 1 \pm \frac{\epsilon_{\mathbf{k}}^{f,\alpha}}{\sqrt{\epsilon_{\mathbf{k}}^{f,\alpha 2} + \Delta_{\mathbf{k}}^{f,\alpha 2}}} \right) \\ \text{Res}(\Sigma_{AN}, \pm\omega^\alpha) &= \mp \frac{V_{\mathbf{k}}^{\alpha 2} \Delta_{\mathbf{k}}^{f,\alpha}}{2\omega^\alpha}\end{aligned}\quad (3.50)$$

We can see that the self-energies have poles due to the hidden-fermions at the energies  $\pm\omega^\alpha = \pm\sqrt{\epsilon_{\mathbf{k}}^{f,\alpha 2} + \Delta_{\mathbf{k}}^{f,\alpha 2}}$ . There is however an important distinction between the normal part and the anomalous part of the self-energy in the weight associated with each of these poles. In fact, the anomalous self-energy has equal and opposite weight at each pole while it depends on the value of  $\epsilon_{\mathbf{k}}^{f,\alpha}$  for the normal self-energy. In particular the sign of  $\epsilon_{\mathbf{k}}^{f,\alpha}$  will determine which of  $\omega^\alpha$  or  $-\omega^\alpha$  has a higher weight. It is also possible to check the cancellation mentioned previously :

$$\begin{aligned}\text{Res}(W, \pm\omega^\alpha) &= \text{Res}\left(\frac{\Sigma_{AN}(\mathbf{k}, \omega)^2}{\omega + \epsilon_{\mathbf{k}} - \Sigma_N(\mathbf{k}, -\omega)^*}, \pm\omega^\alpha\right) \\ &= -\frac{V_{\mathbf{k}}^{\alpha 2}}{2} \left( 1 \pm \frac{\epsilon_{\mathbf{k}}^{f,\alpha}}{\sqrt{\epsilon_{\mathbf{k}}^{f,\alpha 2} + \Delta_{\mathbf{k}}^{f,\alpha 2}}} \right) \\ &= -\text{Res}(\Sigma_N, \pm\omega^\alpha)\end{aligned}\quad (3.51)$$

The original proposition was that only one of these hidden fermionic excitations is relevant to explain the structure of the self-energy at low energy and that identifying  $\epsilon_{\mathbf{k}}^f = z_{\mathbf{k}}\epsilon_{\mathbf{k}+\mathbf{Q}_{AF}} - \mu_f$ , where  $z_{\mathbf{k}}$  is the renormalization factor due to the strong interactions leads to a pole structure analogous to the CDMFT results.

We show in the following that another choice of hidden fermion can lead to a satisfactory comparison with the results obtained by CDMFT but have a different interpretation. Our choice of hidden fermions is based on the previous idea of fractionalization of the PDW order which emphasizes the role of the CDW in the pseudogap. Our analysis will thus be based on the previous hidden-fermion model Eq.(3.48) but we will consider that two fermionic excitation will contribute and identify them with  $f_{\mathbf{k}\sigma}^{\alpha\dagger} = c_{\mathbf{k}+\mathbf{Q}\sigma}^\dagger$  and  $f_{\mathbf{k}\sigma}^{\beta\dagger} = c_{\mathbf{k}-\mathbf{Q}\sigma}^\dagger$ .

We focus on an axial wave-vector that links different parts of the Fermi surface, *i.e.*  $\mathbf{Q} = (\pm Q_0, 0)$  as mentioned in the study of the electronic spectral function from Sec.3.2. We also take into account strong correlations by adding a renormalization factor  $z(\mathbf{k}, \omega)$  that will modify the dispersion of the hidden fermions so that  $\epsilon_{\mathbf{k}}^{f,\alpha} = z\epsilon_{\mathbf{k}+\mathbf{Q}}$  and  $\epsilon_{\mathbf{k}}^{f,\beta} = z\epsilon_{\mathbf{k}-\mathbf{Q}}$  where we took  $z(\mathbf{k}, \omega)$  to be a constant. The bare dispersion is given by taking only nearest and second neighbours hopping  $\epsilon_{\mathbf{k}} = -2t(\cos(k_x) + \cos(k_y)) - 4t'\cos(k_x)\cos(k_y) - \mu$  as to match the one used in the numerical study [204]. We took  $t = 1$  as our energy scale,  $t' = -0.2$  and  $\mu$  is chosen to fix the electron density to  $n = 0.95$  using the Luttinger sum rule in the non-interacting case. Lastly, as we start by investigating the superconducting phase, we take the SC gap with a d-wave form factor  $\Delta_{\mathbf{k}} = \frac{\Delta_0}{2}(\cos(k_x) - \cos(k_y))$  and the other gaps are given by  $\Delta_{\mathbf{k}}^{f,\alpha} = \Delta_{\mathbf{k}+\mathbf{Q}}$  and  $\Delta_{\mathbf{k}}^{f,\beta} = \Delta_{\mathbf{k}-\mathbf{Q}}$ .



### Normal self-energy in the superconducting state

To relate the different features of the normal self-energy to the properties of the hidden fermions we need to study the structure of the normal part of the self-energy given by Eq.(3.49). The positions of the poles are given by  $\omega_{\pm}^{\alpha} = \pm \sqrt{\epsilon_{\mathbf{k}}^{f,\alpha^2} + \Delta_{\mathbf{k}}^{f,\alpha^2}}$  and thus come by pair with symmetric position in energy. The weight associated with each pole is obtained by computing the residue at each of them and is given in Eq.(3.50). The asymmetry in weight is thus controlled by the sign of  $\epsilon_{\mathbf{k}}^{f,\alpha}$  and the value of  $\Delta_{\mathbf{k}}^{f,\alpha}$ . As noted in Ref.[204], the observation that the pole at positive energy has a larger weight than the pole at negative energy in the antinodal region impose the fact that  $\epsilon_{(0,\pi)}^{f,\alpha}$  has to be positive. This constraint is naturally fulfilled in our model when we choose a CDW wave-vector larger than the antinodal Fermi wave-vector which also fits experimental observations.

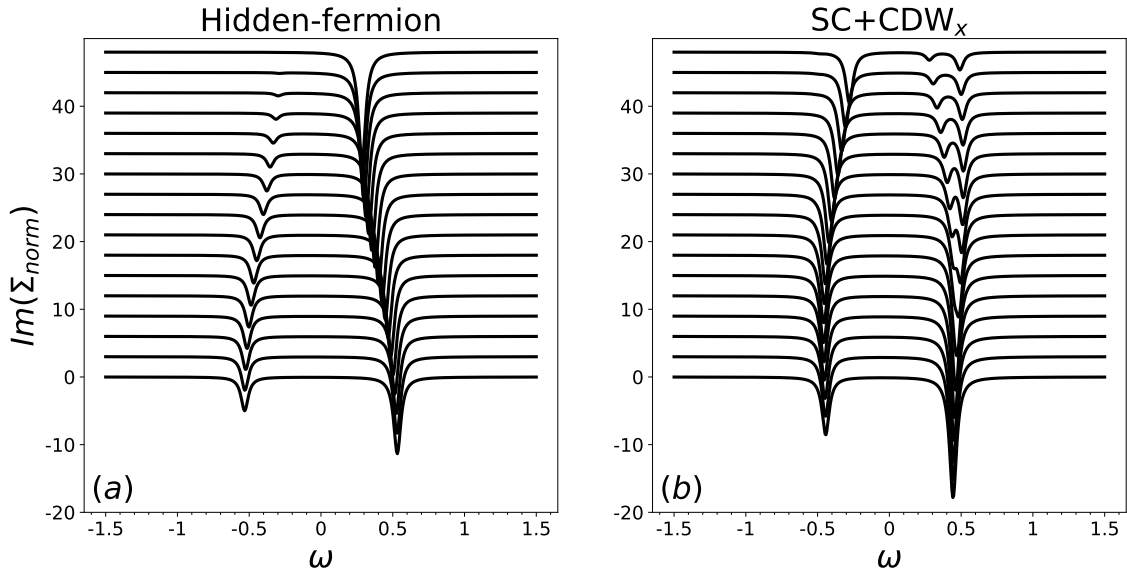


**Figure 3.9:** **(a)** Normal self-energy in the hidden-fermion model of Ref.[204]. The asymmetry in the antinodal region is well reproduced. As there is only one hidden-fermion coupled to electrons it is not possible to recover the splitting in the nodal region. The weight of the positive energy pole is also maximum for  $\mathbf{k} = (\pi/2, \pi/2)$  in contrast to the numerical results shown in Fig.3.8. **(b)** Normal self-energy obtained while considering hidden-fermions due to CDW order with a wave-vector along the  $x$  axis. Due to the symmetry between  $\epsilon_{\mathbf{k}+\mathbf{Q}} = \epsilon_{\mathbf{k}-\mathbf{Q}}$  at  $\mathbf{k} = (0, \pi)$  we only have two visible poles with an asymmetry consistent with the CDMFT results. This symmetry is lost when going to the nodal region and we observe a splitting of the poles. The change of sign of  $\epsilon_{\mathbf{k}-\mathbf{Q}}$  close to  $\mathbf{k} = (\pi/2, \pi/2)$  explains the significant weight for the pole at negative energy. We choose here  $Q_0 = 0.27\pi$ ,  $z = 0.22$ ,  $\Delta_0 = 0.55$ ,  $V_0 = 0.7$  and a numerical broadening factor  $i\eta = 0.03i$ .

The results for the original hidden-fermion idea [204] that identifies  $f_{\mathbf{k}\sigma}^{\alpha\dagger} = c_{\mathbf{k}+\pi\sigma}^{\dagger}$  are shown in Fig.3.9(a) and match multiple characteristics of the numerical results. Notably, the asymmetry in the spectral weight in the antinodal region is well reproduced and the loss of weight for the peak at negative energy is found. Note that, following Eq.(3.50), this happens when  $\epsilon_{\mathbf{k}}^{\alpha}$  is positive. There is thus a crucial role of the added  $\mu_f$  term as the hidden-fermion dispersion  $z_{\mathbf{k}}\epsilon_{\mathbf{k}+\pi}$  alone is negative for  $\mathbf{k} = (0, \pi)$ . The combination of the renormalization induced by  $z_{\mathbf{k}}$  and the positive shift of  $\mu_f$  gives an effective dispersion that is small relative to  $\Delta_{\mathbf{k}}$  and that does not change sign. However, because there is only one hidden fermion it is not possible to capture the splitting in the

nodal region for  $\omega > 0$  and the weight of the positive peak is maximal at  $\mathbf{k} = (\pi/2, \pi/2)$  when the d-wave superconducting gap vanishes, in contrast to the numerical results.

We now turn to the fractionalized PDW hypothesis which gives the same form for the electronic Green's function, in the superconducting phase, to the hidden-fermion model with  $f_{\mathbf{k}\sigma}^{\alpha\dagger} = c_{\mathbf{k}+\mathbf{Q}\sigma}^\dagger$  and  $f_{\mathbf{k}\sigma}^{\beta\dagger} = c_{\mathbf{k}-\mathbf{Q}\sigma}^\dagger$ . Our results for the two hidden fermions coming from the charge order are shown in Fig.3.9(b). At  $\mathbf{k} = (\pi, \pi)$  we can only see a pair of symmetric peaks due to the fact that  $\epsilon_{\mathbf{k}+\mathbf{Q}} = \epsilon_{\mathbf{k}-\mathbf{Q}}$ . Moreover, the charge order wave-vector being larger than the antinodal Fermi momentum means that we have  $\epsilon_{\mathbf{k}\pm\mathbf{Q}} > 0$ . Using the result of Eq.(3.50), this leads to the same weight asymmetry observed in the CDMFT study with the pole at  $+\omega^\alpha$  having a higher weight than the pole at  $-\omega^\alpha$ . When going towards the nodal region the previous symmetry between  $\epsilon_{\mathbf{k}+\mathbf{Q}}$  and  $\epsilon_{\mathbf{k}-\mathbf{Q}}$  is lost and we observe a splitting of the poles at  $\omega > 0$  analogous to the numerical results. It is important to point out that the behaviours of the spectral weight for the two peaks are different. In fact, the pole due to the coupling to  $c_{\mathbf{k}+\mathbf{Q}\sigma}^\dagger$  will have a higher weight at  $-\omega^\alpha$  in the nodal region. This is because  $\epsilon_{\mathbf{k}-\mathbf{Q}}$  will change sign and become negative. Because the pairing gap for the hidden-fermion is taken as  $\Delta_{\mathbf{k}}^{f,\alpha} = \Delta_{\mathbf{k}\pm\mathbf{Q}}$ , there is no cancellation of the weight at  $\mathbf{k} = (\pi/2, \pi/2)$  which result in a non-vanishing weight in the nodal region for the pole at  $\omega < 0$ . Note that we took here a coupling between the electrons and the hidden-fermions to be independent of momentum, *i.e.*  $V_{\mathbf{k}}^{f,\alpha} = V_0$ . This does not impact the position of the poles as shown by Eq.(3.49) but only the weight at each pole (see Eq.(3.50)). Furthermore, results from CDMFT away from the antinodal point  $\mathbf{k} = (0, \pi)$  are extrapolated from the available momentum points. Thus, the discrepancy between the spectral weight in the nodal region can be due to multiple factors.

### 3.3.3 Study of the pseudogap phase

We showed that both the antiferromagnetic hidden-fermion and the fractionalized PDW models give similar results in the superconducting phase. The two models differ strongly in the pseudogap phase where the hidden-fermion model restores the charge conservation symmetry but keeps the coupling between electrons and the hidden fermions unchanged. In contrast, the fractionalization of a Pair Density Wave leads to the superposition of SC and CDW fluctuations that have a strong impact on the electronic spectral functions in the same fashion as we discussed in Sec.3.2.3.

#### Pseudogap in the hidden-fermion model

In the hidden-fermion model, the pseudogap phase is obtained by setting the superconducting order parameters  $\Delta_{\mathbf{k}}$  and  $\Delta_{\mathbf{k}}^{f,\alpha}$  to zero. The remaining part of the self-energy is due to the hybridization to the hidden-fermions through  $V^\alpha$ . The self-energy thus take the form:

$$\begin{aligned}\Sigma_N(\mathbf{k}, \omega) &= \sum_{\alpha} \frac{V_{\mathbf{k}}^{\alpha 2}}{\omega - \epsilon_{\mathbf{k}}^{f,\alpha}} \\ \Sigma_{AN}(\mathbf{k}, \omega) &= 0\end{aligned}\tag{3.52}$$

The structure of the self-energy is then reduced to peaks located at the energy of the hidden-

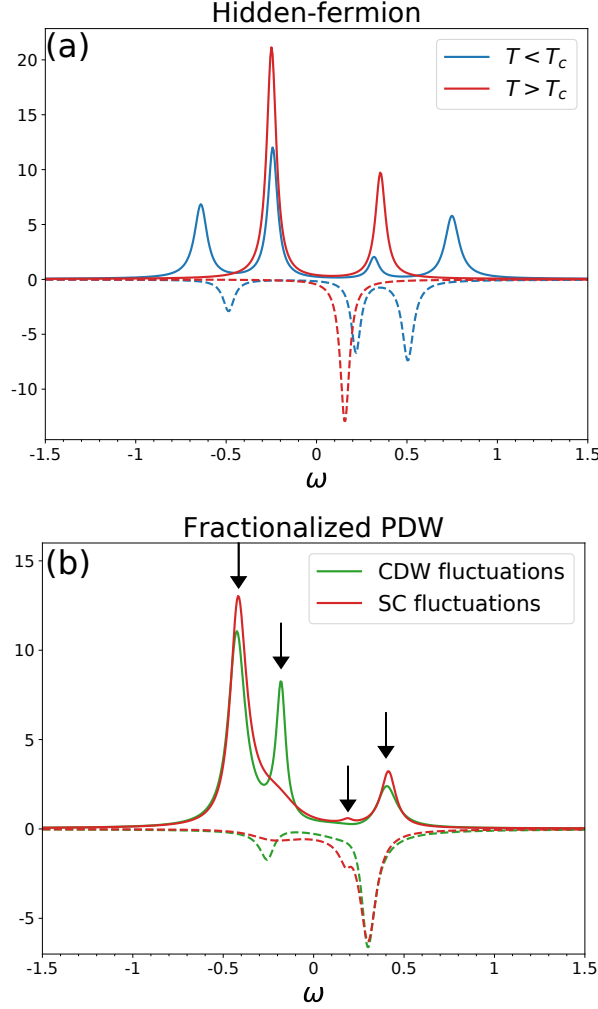


**Figure 3.10:** (a) Electronic spectral function (full line) and self-energy (dotted line) in the pseudogap (red) and superconducting phase (blue) in the hidden-fermion model. Above  $T_c$ , the self-energy is reduced to a single pole at  $\omega = \epsilon_{\mathbf{k} \pm \mathbf{Q}} > 0$  and the resulting electronic spectral function shows 2 poles. There is no spectral weight at  $\omega = 0$  but there will be gapless states away from  $k_x = 0$  in contrast to experimental observations. (b) Electronic spectral function (full line) and self-energy (dotted line) in the pseudogap phase from a fractionalized PDW at  $\mathbf{k} = (0, \pi)$ . Green lines show effects of CDW fluctuations ( $\Gamma_1$ ) while the red lines show the effect of superconducting fluctuations ( $\Gamma_2$ ). Due to the superposition of SC and CDW in the fractionalized PDW idea, the electronic spectral function retains the 4 poles structure seen in the superconducting phase. Finite lifetime for the particle-particle or particle-hole pairs have a much stronger dampening effect in the two poles closest to  $\omega = 0$  which could explain the observed two peaks structure in CDMFT or the single occupied band in ARPES above  $T_c$ . We choose here  $Q_0 = 0.27\pi$ ,  $z = 0.22$ ,  $|\Psi_0| = V_0 = 0.15$ ,  $\Gamma_1 = \Gamma_2 = 0.1$  and a numerical broadening factor  $i\eta = 0.03i$ . Adapted from Ref.[136].

fermions as shown in Fig.3.10(a) (red dotted line). In our case, the self-energy in the antinodal region will display a single peak at  $\omega > 0$  because  $\epsilon_{\pi+Q} = \epsilon_{\pi-Q} > 0$ . This leads to the electronic spectral function having two poles with a vanishing spectral weight at  $\omega = 0$  for  $\mathbf{k} = (0, \pi)$  (red line in Fig.3.10(a)). Note that a non-zero value of hybridization between  $c_{\mathbf{k}\sigma}$  and  $c_{\mathbf{k}+Q\sigma}$  should be interpreted as a long-range CDW at the mean-field level. As such, we should observe a Fermi surface reconstruction with gapless states in the pseudogap phase. This long-range order has only been observed by applying strong magnetic fields [155, 156, 158] in the superconducting phase. Furthermore, the short-range charge order above  $T_c$  is only observed below a transition temperature  $T_{CO}$  which is lower than the pseudogap temperature  $T^*$ . The band structure observed by ARPES does not however show significant change for temperatures in the pseudogap region. It is thus inconsistent to consider that the pseudogap phase is solely due to the charge order.

### Fractionalized Pair Density Wave

To describe the pseudogap phase, we use the same form of the Green's function Eq.(3.43) that was successful in describing the experimental ARPES results for the electronic spectral function [135]. To compare it with the hidden-fermion model, it is equivalent to taking the mean-field amplitude of the SC and CDW gap to be equal while adding finite lifetimes  $\Gamma_1$  and  $\Gamma_2$ . Note that our Green's function does not have any anomalous part which would be a sign for a long-range order in a mean-field description. Because none of the gaps vanishes, the self-energy and the spectral function have the same pole structure in both the pseudogap and the superconducting phases. In fact, the electronic spectral function at  $\mathbf{k} = (0, \pi)$  given in Fig.3.10(b) (full line) with both damping rate  $\Gamma_1$  and  $\Gamma_2$  being turned on alternatively clearly shows 4 poles indicated by arrows. The main observation is that there is a significant reduction in the spectral weight of the two poles at lower energy for both positive and negative energy. This is the same phenomenon that was used to describe the observation of the “flat band” below  $T_c$  by ARPES in Sec.3.2.3. Similarly to this previous study, this description of the pseudogap effectively leads to Fermi arcs and no long-range order is expected. We show the resulting electronic spectral function at  $\omega = 0$  in the antinodal region in Fig.3.11(b). We can see that part of the Fermi surface is washed out even in the absence of fluctuations ( $\Gamma_1 = \Gamma_2 = 0$ ).

Despite having a similar structure for the self-energy in the pseudogap phase, there is an important difference between the structure of the Green's function in our approach and in previous studies based on fractionalization such as the one using a  $SU(2)$  theory [207] of fluctuating antiferromagnetism. In our case, the line of zeros for the real part of the Green's function (black dotted line in Fig.3.11) is very close to the non-interacting Fermi surface. This is in strong contrast to other cases where the Luttinger surface created by interaction with the antiferromagnetic fluctuations intersect the Fermi surface to create small pockets in the nodal region [208].

It is important to note that in order to obtain a good fit with the numerical result obtained by CDMFT, it is necessary here to take a value of  $V^\alpha$  (in the superconducting phase) and  $\Psi$  (in the pseudogap phase) significantly lower than the value of the pairing amplitude  $\Delta$  in the superconducting phase. Indeed, an agreement between the experimental ARPES results and the fractionalized PDW scenario was obtained with the SC and CDW order being very close, a fact supported by Raman experiment in mercury-based cuprate [43]. This would indicate that only

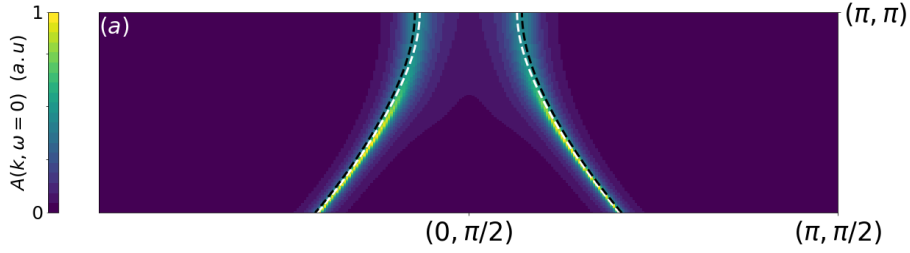


**Figure 3.11:** (a) Electronic spectral function at  $\omega = 0$  for the fractionalized PDW model. The white dotted line indicates the non-interacting Fermi surface while the black dotted line indicates the surface of zeros of the Green's function. We see that the Fermi surface is washed out in the antinodal region. We choose here  $Q_0 = 0.27\pi$ ,  $z = 0.22$ ,  $|\Psi_0| = 0.15$  and a numerical broadening factor  $i\eta = 0.03i$ .

a part of the particle-particle pairs come from the fractionalization while the other part can be described by a standard superconducting condensate. This can also be compared to the two behaviours observed in Raman experiments for the nodal and antinodal part of the superconducting gap [42]. In fact, the nodal gap follows the critical temperature with doping and decreases away from optimal doping while the antinodal gap decreases linearly with doping, following the pseudogap temperature. This imbalance could be here a result of the finite size of the cluster ( $2 \times 2$  sites) used in the CDMFT calculation which is smaller than the wavelength of the charge modulation, thus hindering the formation of modulating orders with periodicity larger than the cluster size.

The results obtained from CDMFT calculations give valuable information on the energy dependence of the electronic Green's function in the doped Hubbard model. This is often limited to specific points in the Brillouin zone which depend on the cluster size. From this, it seems difficult to account for potential modulating orders with a wavelength larger than the cluster size. There is however a large number of experimental evidence [43, 46, 48, 145–147, 149, 155, 156, 180, 202, 203] for these orders to exist and compete in the pseudogap phase of cuprates superconductors. We argued here that despite the numerical limitation, there are signatures of the charge order in the electronic self-energy calculated in CDMFT.

Much like in ARPES experiments, the observations are indirect consequences of the charge order and there is no Fermi surface reconstruction as the charge order remain short-ranged and fluctuating. In the case of ARPES in Bi2201, the main indicators for a modulating order were the back-bending of the band at the Brillouin zone's edge and the specific way the pseudogap was closing close to the nodal region (for more details see Sec.3.2). The limited momentum resolution of CDMFT does not allow for such distinction but the singular pole structure of the self-energy in the antinodal region could itself contain evidence for this modulating order. It is important to note the similarities between the original hidden-fermion from Ref.[204] and our proposition which contains the charge order. In particular both of them give the same result for  $k = (0, \pi)$ . There are however distinctions to be made when going close to the nodal region where the two models differ. The main argument for the CDW scenario is that it allows for the double pole structure observed for  $\omega > 0$  (see Fig.3.9) which is observed numerically. This is to be taken with caution as both the numerical results and the idea of CDW order reaches their limit in the nodal region.

A more convincing argument may come from the electronic spectral function in the pseudogap phase. The original idea for the hidden-fermion is to describe the pseudogap by the absence of

pairing. At the mean-field level, this would lead to a CDW long-range order with the associated Fermi surface reconstruction. The spectral function at the antinodal point does show the 2 poles observed by CDMFT with a vanishing weight at  $\omega = 0$  but there are still gapless states away from  $k_x = 0$ . In contrast, the fractionalized PDW scenario is characterized by the equal superposition of SC and CDW fluctuations in the pseudogap. As such the spectral function has the same structure as in the superconducting state and is fully gapped at the Brillouin zone's edge, leaving Fermi arcs in the nodal region if we include a momentum dependence for the pseudogap order [134, 135]. Taking into account fluctuations in the SC and CDW orders leads to a drastic reduction in the spectral weight of specific poles, giving an effective spectral function with two apparent peaks similar to the phenomenon leading to the formation of the “flat band” in Bi2201 below  $T_c$ .

There are still many differences between the results from CDMFT and the experimental spectral function measured by ARPES. It is however interesting to find common ground to link these two essential techniques to investigate the pseudogap phase of cuprates. The capacity of CDMFT to explore the positive energies which are inaccessible to ARPES and the wide range of doping available to the experiments are complementary to elucidate the pseudogap phase of cuprates.

## 3.4 Anomalous phonon softening

### 3.4.1 Kohn anomaly

The phonon spectrum has been largely studied in metallic systems, where the charge correlations soften the phonon spectrum giving rise to the “Kohn anomaly” [209]. In one dimensional metals [210–212] and in some two-dimensional transition metal dichalcogenides [213], this softening grows towards zero as shown by the black line in Fig.3.12 and a full phonon softening occurs at the CDW wave-vector ( $\mathbf{Q}$ ) below the CDW ordering temperature  $T_{CO}$ . With a similar outlook, the phonon spectrum has been measured in cuprates using different experimental techniques, like inelastic x-ray scattering and inelastic neutron scattering [56, 214–223]. All of these experiments have observed a partial phonon softening, schematically represented by the full red line in Fig.3.12, at the associated wave-vector  $\mathbf{Q}$  in several cuprate families. However, this occurs only below the superconducting transition temperature  $T_c$ , in stark contrast to the metallic systems [212, 213, 224, 225]. The occurrence of phonon softening below  $T_c$  is hence referred to as “anomalous” phonon softening.

The anomalous phonon softening indicates a close connection between the CDW and superconductivity in underdoped cuprates and as such we are interested in the possibility to address this characteristic element of the physics of underdoped cuprates by using the same idea of superposition of SC and CDW fluctuations above  $T_c$  arising from the connection between them within the fractionalized PDW ansatz.

While earlier studies [25, 134, 178, 199] discussed the role of CDW, superconductivity and associated fluctuations on the electronic spectrum, their effect on the bosonic excitations, especially phonons, remains a difficult question and perhaps can give a more complete understanding of the CDW orders in cuprates. Our goal here is to compute the effect of the CDW, superconductivity and thermal fluctuations on the phonon spectrum. Similarly to our study of the electronic spectral

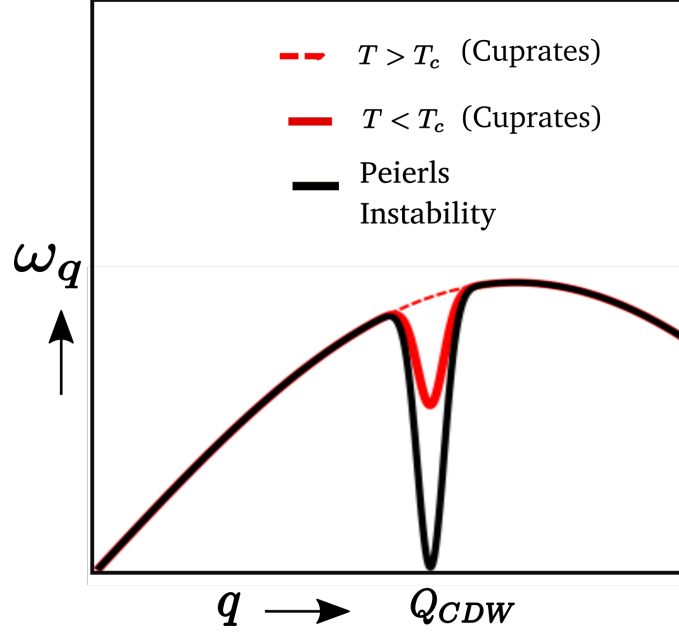


**Figure 3.12:** Schematic representation of a full softening in metals and a partial softening in underdoped cuprates below  $T_c$ . Adapted from Ref.[137].

function, we mimic the fluctuations by introducing an inverse lifetime of quasiparticles [112, 134] and take its temperature dependence phenomenologically [112] based on earlier studies. We will show in Sec.3.4.2 that a strong phonon softening occurs only below  $T_c$  when all fluctuations are quenched, thus explaining the anomalous nature of the phonon softening seen in experiments. Additionally, we also show in Sec.3.4.3 that at low temperatures, different temperature dependences of the superconducting gap and the inverse lifetime of quasiparticle give contrasting effects on the strength of the phonon softening.

### 3.4.2 Phonon renormalization

We start by studying the effect of the SC and CDW orders on the phonon propagator separately and we start with a total Hamiltonian  $H_{tot}$  [226], given by  $H_{tot} = H_e + H_{ph} + H_{e-ph}$ , with,

$$\begin{aligned}
 H_e &= \sum_{\mathbf{k}, \sigma} \epsilon_{\mathbf{k}} c_{\mathbf{k}\sigma}^\dagger c_{\mathbf{k}\sigma} + \sum_{\mathbf{k}, \sigma} (\chi_{\mathbf{k}} c_{\mathbf{k}+\mathbf{Q}\sigma}^\dagger c_{\mathbf{k}\sigma} + h.c.) \\
 &\quad + \sum_{\mathbf{k}} (\Delta_{\mathbf{k}} c_{\mathbf{k}\uparrow}^\dagger c_{-\mathbf{k}\downarrow}^\dagger + h.c.), \\
 H_{ph} &= \sum_{\mathbf{q}} \omega_{\mathbf{q}} (b_{\mathbf{q}}^\dagger b_{\mathbf{q}} + b_{-\mathbf{q}}^\dagger b_{-\mathbf{q}}), \\
 H_{e-ph} &= (g/\sqrt{N}) \sum_{\mathbf{q}} \sum_{\mathbf{k}, \sigma} [c_{\mathbf{k}+\mathbf{q}\sigma}^\dagger c_{\mathbf{k}\sigma} (b_{\mathbf{q}}^\dagger + b_{-\mathbf{q}}) + h.c.],
 \end{aligned} \tag{3.53}$$

where  $H_e$  is an effective mean-field Hamiltonian we used in Sec.3.3 to describe the coexistence of SC and CDW orders at low temperature.  $H_{ph}$  is the Hamiltonian for free phonons with phonon creation operator  $b_{\mathbf{q}}^\dagger$  for wave-vector  $\mathbf{q}$  and frequency  $\omega_{\mathbf{q}}$ .  $H_{e-ph}$  is the Hamiltonian describing electron-phonon interaction with strength  $g$  and  $N$  is the number of lattice sites in the system.

The Green's function corresponding to  $H_e$  is given by  $\hat{G}^{-1}(i\omega_n, \mathbf{k}) = (i\omega_n - \hat{H}_e)$  and has a matrix form in the extended Nambu basis  $\Psi_{\mathbf{k}}^\dagger = (c_{\mathbf{k}\uparrow}^\dagger, c_{-\mathbf{k}\downarrow}, c_{\mathbf{k}+\mathbf{Q}\uparrow}^\dagger, c_{-\mathbf{k}-\mathbf{Q}\downarrow})$  which is given by,

$$G^{-1} = \begin{pmatrix} i\omega_n - \epsilon_{\mathbf{k}} & -\Delta_{\mathbf{k}} & -\chi_{\mathbf{k}} & 0 \\ -\Delta_{\mathbf{k}}^* & i\omega_n + \epsilon_{\mathbf{k}} & 0 & \chi_{\mathbf{k}} \\ -\chi_{\mathbf{k}}^* & 0 & i\omega_n - \epsilon_{\mathbf{k}+\mathbf{Q}} & -\Delta_{\mathbf{k}+\mathbf{Q}} \\ 0 & \chi_{\mathbf{k}}^* & -\Delta_{\mathbf{k}+\mathbf{Q}}^* & i\omega_n + \epsilon_{\mathbf{k}+\mathbf{Q}} \end{pmatrix}. \quad (3.54)$$

Note that taking  $G(i\omega_n, \mathbf{k})_{1,1}$  gives the same Green's function as Eq.(3.41) that we used in the study of the electronic spectral function (Sec.3.2) and of the pole structure of the self-energy (Sec.3.3). We start by considering a d-wave symmetric SC gap, given by  $\Delta_{\mathbf{k}} = (\Delta_{max}/2)[\cos(k_x) - \cos(k_y)]$ , where  $\Delta_{max}$  denotes the maximum gap. Following several theoretical studies [30, 227, 228] and experimental evidences [229, 230], we also take the CDW order parameter with  $\mathbf{Q}$  given by the axial wave-vector connecting two neighboring hot-spots [150]. Moreover, the CDW gap is taken to have a maximum ( $\chi_{max}$ ) at the hot-spots, falling off exponentially away from the hot-spots [30].

The modified electronic spectrum in the presence of SC and CDW orders will renormalize the free phonon propagator,  $D_0(z, \mathbf{q}) = 2\omega_{\mathbf{q}}/(z^2 - \omega_{\mathbf{q}}^2)$ . To analyze this, we write the phonon propagators in matrix form in the ordered phase. The corresponding matrix elements are given by  $D_{m,n}(\mathbf{q}, \tau) = -\langle \mathcal{T} \phi_{\mathbf{q}+m\mathbf{Q}}(\tau) \phi_{\mathbf{q}+n\mathbf{Q}}^\dagger(0) \rangle$ , where  $\mathcal{T}$  is the time-ordering operator [226],  $\phi_{\mathbf{q}}$  is the phonon field operator given by  $b_{\mathbf{q}}^\dagger + b_{-\mathbf{q}}$  and  $m, n = \pm$ . Noting that  $D_{++} \equiv D_{--} := D_1(z, \mathbf{q})$  and  $D_{+-} \equiv D_{-+} := D_2(z, \mathbf{q})$ , we can then write a perturbative expansion in electron-phonon interaction for the renormalized phonon propagator. As given by  $H_{ph}$  in Eq.(3.53), the phonon field  $\phi_{\mathbf{q}}$  couples to an electron-hole pair with momenta  $\mathbf{k} + \mathbf{q}$  and  $\mathbf{k}$  respectively. The simplest correction to the phonon propagator is thus given by the particle-hole bubble

$$\Pi_1(z, \mathbf{q}) = \begin{array}{c} \text{Diagram: A particle-hole bubble diagram. The left wavy line is labeled } Q+q \text{ and the right wavy line is labeled } Q+q. \text{ The top electron line is labeled } k+Q+q \text{ and the bottom electron line is labeled } k. \end{array} \quad (3.55)$$

where we have taken  $\mathbf{q} \rightarrow \mathbf{Q} + \mathbf{q}$  as we expect the softening to occur at the ordering wave-vector. However, in the ordered phase, we can have additional scattering event due to the off-diagonal order. These can be represented using the anomalous part of the Green's function or by considering inclusion of  $\Delta_{\mathbf{k}}$  that will transform an electron line with momentum  $\mathbf{k}$  to a hole line with momentum  $-\mathbf{k}$  or inclusion of  $\chi_{\mathbf{k}}$  which will shift the momentum of the electron line by  $\pm\mathbf{Q}$ . This leads to new polarization bubbles

$$\Pi_2(z, \mathbf{q}) = \begin{array}{c} \text{Diagram: A particle-hole bubble diagram with an off-diagonal scattering event. The left wavy line is labeled } Q+q \text{ and the right wavy line is labeled } Q+q. \text{ The top electron line is labeled } k+Q+q \text{ and the bottom electron line is labeled } -k. \end{array} \quad (3.56)$$

$$\Pi_3(z, \mathbf{q}) = \begin{array}{c} \text{Diagram: A particle-hole bubble diagram with a momentum shift. The left wavy line is labeled } Q+q \text{ and the right wavy line is labeled } -Q+q. \text{ The top electron line is labeled } k+Q+q \text{ and the bottom electron line is labeled } k+Q. \end{array} \quad (3.57)$$

Note that the outgoing propagator in Eq.(3.57) is centered at  $-\mathbf{Q}$  and the diagram actually renor-



malyze the second phonon mode we labelled as  $D_{+-} = D_2(z, \mathbf{q})$ . Lastly, when both  $\Delta_{\mathbf{k}}$  and  $\chi_{\mathbf{k}}$  are non-zero there is the possibility for the inclusion of a term proportional to the product  $\Delta_{\mathbf{k}}\chi_{\mathbf{k}}$  that leads to a polarization bubble

$$\Pi_4(z, \mathbf{q}) = \text{Diagram} \quad (3.58)$$

which once again renormalize the propagator  $D_2(z, \mathbf{q})$ .

We can build the other four expressions starting with a phonon propagator at  $-\mathbf{Q} + \mathbf{q}$  and we finally obtain two coupled Dyson equations for the two phonons mode

$$\begin{aligned} D_1(z, \mathbf{q}) &= D_0(z, \mathbf{q} + \mathbf{Q}) \left[ 1 + \Pi_1(z, \mathbf{q})D_1(z, \mathbf{q}) + \right. \\ &\quad \Pi_2(z, \mathbf{q})D_1(z, \mathbf{q}) + \Pi_3(z, \mathbf{q})D_2(z, \mathbf{q}) + \\ &\quad \left. \Pi_4(z, \mathbf{q})D_2(z, \mathbf{q}) \right], \\ D_2(z, \mathbf{q}) &= D_0(z, \mathbf{q} - \mathbf{Q}) \left[ \Pi_1(z, \mathbf{q})D_2(z, \mathbf{q}) + \Pi_2(z, \mathbf{q})D_2(z, \mathbf{q}) \right. \\ &\quad \left. + \Pi_3(z, \mathbf{q})D_1(z, \mathbf{q}) + \Pi_4(z, \mathbf{q})D_1(z, \mathbf{q}) \right], \end{aligned} \quad (3.59)$$

We obtain the new modes for phonon in the ordered phase by decoupling Eq.(3.59), with the definition  $D_{\pm}(z, \mathbf{q}) = D_1(z, \mathbf{q}) \pm D_2(z, \mathbf{q})$ . We then focus on the expected softening at  $\mathbf{Q}$  and restrict  $\mathbf{q}$  to be small, this allows us to use the approximation that that  $\omega_{\mathbf{Q} \pm \mathbf{q}} \approx \omega_{\mathbf{Q}}$ . Plugging in the form for the free phonon propagator  $D_0(z, \mathbf{q})$ , we obtain the solutions as,

$$D_{\pm}(z, \mathbf{q}) = \frac{2\omega_{\mathbf{Q}}}{z^2 - \omega_{\mathbf{Q}}^2 - 2\omega_{\mathbf{Q}}\Pi_{\pm}(z, \mathbf{q})}, \quad (3.60)$$

where  $\Pi_+ = \Pi_1 + \Pi_2 + \Pi_3 + \Pi_4$  and  $\Pi_- = \Pi_1 + \Pi_2 - \Pi_3 - \Pi_4$ . The dispersion of the new phonon modes correspond to the values of  $z$ , for which denominator of Eq.(3.60) vanishes. Subsequently, taking only  $q$  dependence in  $\Pi$ , the frequency for each mode is given by

$$\Omega_{\pm}^2(q) = \omega_{\mathbf{Q}}^2 + 2\omega_{\mathbf{Q}}\Pi_{\pm}(q). \quad (3.61)$$

These two new phonon modes in Eq.(3.61) with frequency  $\Omega_{\pm}$  signify branching of the free phonon near  $\mathbf{Q}$  due to the presence of CDW and SC orders. We find that the split between  $\Omega_{\pm}$  is proportional to the magnitude of the CDW order. Also, we only plot  $\Pi_{\pm}$  as a function of  $q$ , as the modes  $\Omega_{\pm}(q)$  can be easily identified from the corresponding  $\Pi_{\pm}$  in Eq.(3.61). To quantify the strength of the phonon softening, we look at  $\Pi_{\pm}(q)$  after subtracting  $\Pi_{\pm}(q = -1)$ . In Fig.3.13, we observe that  $\Pi_{\pm}(q)$  decreases strongly within a finite range around  $q = 0$ , with a minimum at  $q = 0$ , readily suggesting a softening of phonon frequency around  $\mathbf{Q}$ . We also observe that away from  $q = 0$ ,  $\Pi_{\pm}(q)$  goes towards zero, implying that we recover the free phonon propagator away from  $\mathbf{Q}$ . This suggests that the effect of CDW and SC orders on the phonon are maximum at  $\mathbf{Q}$  and diminishes away from it as we expected. Additionally, we notice that the suppression of  $\Pi_-$

is larger than the suppression of  $\Pi_+$  and the  $q$  dependence of  $\Pi_{\pm}$  are extremely similar to each other. Hence, for a simpler presentation, we will only plot  $\Pi_-$  as a function of  $q$  in the following study of the effect of the fluctuations.

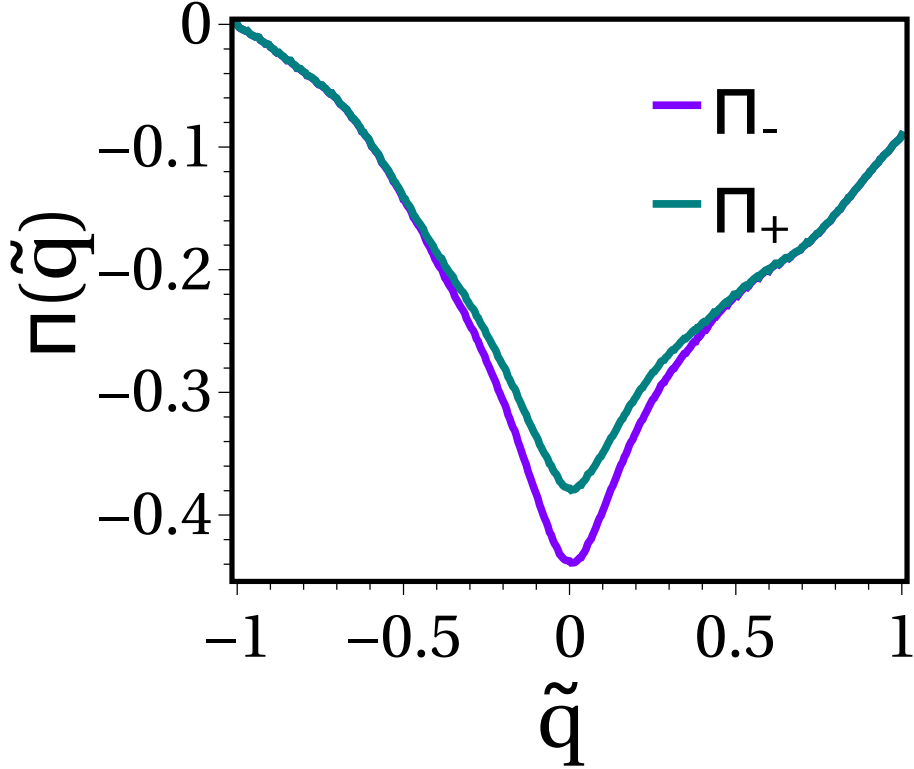


**Figure 3.13:** Plots of the self-energy  $\Pi_{\pm}$  as a function of  $q$  corresponding to the two renormalized phonon modes  $\Omega_{\pm}$  in the presence of  $\chi_{max} = 0.05$  and  $\Delta_{max} = 0.05$ . Both  $\Pi_{\pm}$  exhibit a depletion around  $q = 0$ , implying a softening in the phonon dispersion of the two new modes  $\Omega_{\pm}$  around  $Q$ . Adapted from Ref.[137].

### 3.4.3 Effect of fluctuations

So far, we obtain a phonon softening in the presence of SC and CDW orders. However, to address the anomalous nature of the phonon softening in cuprates, we need to include fluctuation related effects, which we showed played an important role in the description of the electronic spectral function. We once again consider the fluctuations to be captured by a finite lifetime for the particle-particle and particle-hole pairs. We will take the inverse lifetime to be temperature dependent with a large value at high temperatures and a sudden reduction below  $T_c$ , when global phase coherence sets in. We once again use the phase-locking idea to explain that the phase fluctuations of both the particle-particle pairs and the particle-hole pairs are frozen at the superconducting transition.

In order to study the evolution of the phonon softening with temperature, we add the finite inverse lifetime of quasiparticles, given by  $\Gamma$ , pertinent to the fluctuation related effects in the electronic Green's function. The self-energy in Matsubara frequency due to  $\Gamma$  can be written as

$\Sigma = i\Gamma \text{sgn}(\omega_n)$  and the Green's function in Eq. (3.54) will transform as

$$G_{i,j}^{-1}(i\omega_n, \mathbf{k}) \rightarrow G_{i,j}^{-1}(i\omega_n + \Sigma, \mathbf{k}). \quad (3.62)$$

In the presence of  $\Gamma$ , the phonon dispersion will be modified by the real part of  $\Pi(\mathbf{q})$ .

The phonon self-energies  $\Pi_n$  in Eqs.(3.55)-(3.58) now have the following general structure:

$$\sum_{\mathbf{k}, i\omega_n} G_{\mathbf{k}}^a(i\omega_n + i\Gamma \text{sgn}(\omega_n)) G_{\mathbf{k}+\mathbf{q}}^b(i\omega_n + i\Gamma \text{sgn}(\omega_n) + i\epsilon_n), \quad (3.63)$$

where, either of 'a' and 'b' symbolically represents the  $(i, j)^{th}$  element of the Green's function matrix. To evaluate the Matsubara summation in this case, we need to use a contour avoiding the branch cuts defined by  $\text{Im}(z) = 0$  and  $\text{Im}(z + i\epsilon_n) = 0$  as shown in the Fig. 3.14. Using this contour, we arrive at the following integrations,

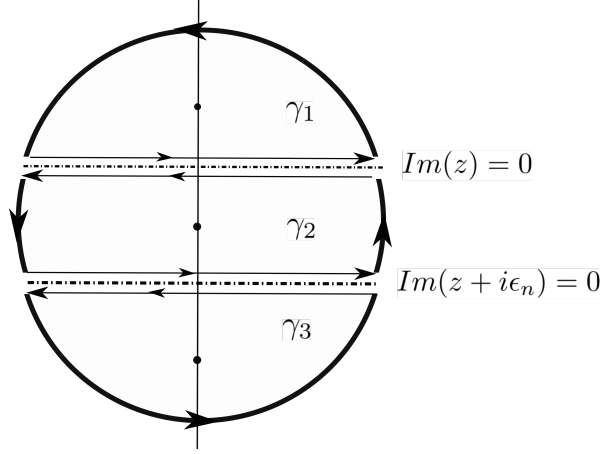


**Figure 3.14:** Contour for complex Matsubara frequency summation:  $\text{Im}(z) = 0$  and  $\text{Im}(z + i\epsilon_n) = 0$  denote the two branch-cuts in the complex plane.  $\gamma_1$ ,  $\gamma_2$  and  $\gamma_3$  are the three contours of integration. Adapted from Ref.[137].

$$\begin{aligned} I_{\gamma_1} &= \sum_{\mathbf{k}} \left[ \int_{-\infty}^{\infty} \frac{d\omega}{2\pi i} n_F(\omega) G_{\mathbf{k}}^a(\omega + i\Gamma) G_{\mathbf{k}+\mathbf{q}}^b(\omega + \epsilon + i\Gamma) \right], \\ I_{\gamma_3} &= - \sum_{\mathbf{k}} \left[ \int_{-\infty}^{\infty} \frac{d\omega}{2\pi i} n_F(\omega) G_{\mathbf{k}}^a(\omega - \epsilon - i\Gamma) G_{\mathbf{k}+\mathbf{q}}^b(\omega - i\Gamma) \right], \\ I_{\gamma_2} &= \sum_{\mathbf{k}} \left[ \int_{-\infty}^{\infty} \frac{d\omega}{2\pi i} n_F(\omega) \left\{ G_{\mathbf{k}}^a(\omega - \epsilon - i\Gamma) G_{\mathbf{k}+\mathbf{q}}^b(\omega + i\Gamma) - G_{\mathbf{k}}^a(\omega - i\Gamma) G_{\mathbf{k}+\mathbf{q}}^b(\omega + \epsilon + i\Gamma) \right\} \right], \end{aligned} \quad (3.64)$$

We treat these integrals in the limit  $T \rightarrow 0$ , where  $I_{\gamma_1}$  and  $I_{\gamma_3}$  in Eq. (3.64) become,

$$\begin{aligned} I_{\gamma_1} &= \sum_{\mathbf{k}} \left[ \int_{-\infty}^0 \frac{d\omega}{2\pi i} G_{\mathbf{k}}^a(\omega + i\Gamma) G_{\mathbf{k}+\mathbf{q}}^b(\omega + \epsilon + i\Gamma) \right] \\ I_{\gamma_3} &= - \sum_{\mathbf{k}} \left[ \int_{-\infty}^0 \frac{d\omega}{2\pi i} G_{\mathbf{k}}^a(\omega - \epsilon - i\Gamma) G_{\mathbf{k}+\mathbf{q}}^b(\omega - i\Gamma) \right]. \end{aligned} \quad (3.65)$$

We replace  $\omega \rightarrow \omega + \epsilon$  in the first term of  $I_{\gamma_2}$  and successively use

$$\lim_{\epsilon \rightarrow 0} \frac{n_F(\omega + \epsilon) - n_F(\omega)}{\epsilon} = -\delta(\omega).$$

Thus,  $I_{\gamma_2}$  in Eq. (3.64) becomes,

$$I_{\gamma_2} = \sum_{\mathbf{k}} \frac{-\epsilon}{2\pi i} [G_{\mathbf{k}}^a(i\Gamma) G_{\mathbf{k}+\mathbf{q}}^b(\epsilon + i\Gamma)]. \quad (3.66)$$

Finally, we evaluate the real frequency ( $\omega$ ) integration in Eq.(3.65) for each of the four self-energies  $\Pi_1$ ,  $\Pi_2$ ,  $\Pi_3$  and  $\Pi_4$  by using,

$$\int_{-\infty}^0 d\omega \left[ \frac{1}{(\omega - x) * (\omega - y)} \right] = \frac{\log[x] - \log[y]}{x - y}, \quad (3.67)$$

where,  $x, y \in \mathbb{C}$ . The summation over  $\mathbf{k}$  is again evaluated using numerical tools. The renormalization of phonon spectrum in this case is given by the real part of the self-energy. The real part of the self-energies are plotted for different set of SC order,  $\Gamma$  and CDW order in Fig.3.15 and Fig.3.16 and we will discuss the results and their relevance for experiments.

To understand the collective effect of the SC gap and  $\Gamma$  on the phonon softening, it is important to disentangle the role played by  $\Gamma$  and the SC gap. Therefore, we start by studying the effect of  $\Gamma$  taking  $\Delta_{max} = 0$ . Fig.3.15(a) shows the variation of  $\Pi(q)$  for four different  $\Gamma$  with  $\chi_{max} = 0.2$ . We notice that for a very small value of  $\Gamma = 0.02$ , there is a significantly strong phonon softening around  $q = 0$ . With increasing  $\Gamma$ , the phonon softening starts to reduce and for a very large  $\Gamma = 1.0$ , the phonon softening gets almost fully suppressed. We also observe that the phonon softening at  $q = 0$  is most strongly affected by  $\Gamma$ . Therefore, for the rest of the analysis, we will concentrate on  $\Pi$  at  $q = 0$  to quantify the phonon softening.

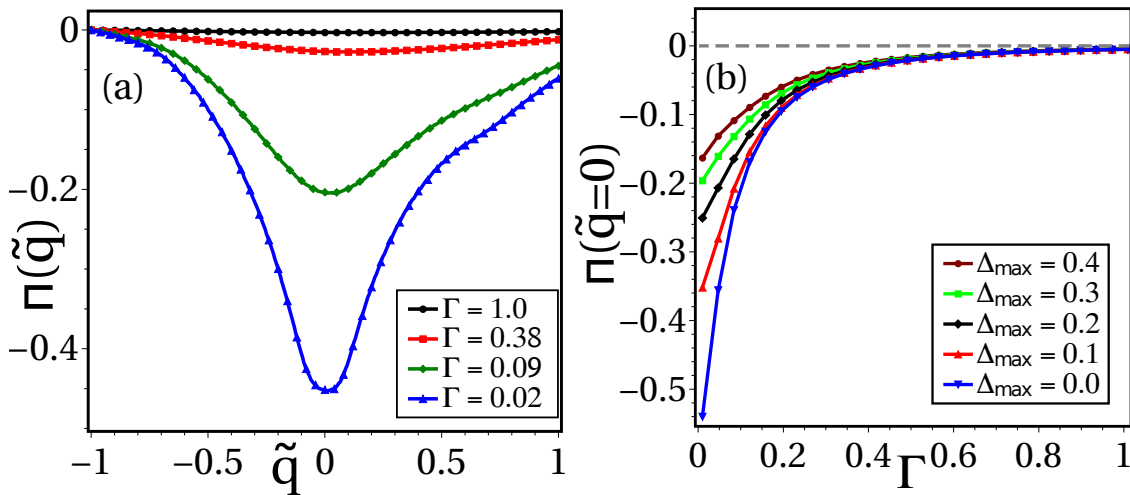


**Figure 3.15:** (a) The variation of  $\Pi(q)$  with  $q$  for four different values of  $\Gamma$  with  $\chi_{max} = 0.2$  and  $\Delta_{max} = 0$ . The plots portray a suppression in phonon softening with increase in  $\Gamma$ . (b) Plots of  $\Pi(q)$  with variation in  $\Gamma$  for five different values of  $\Delta_{max}$  with  $\chi_{max} = 0.2$ . The plots manifest a suppression in phonon softening with an increase in  $\Delta_{max}$ . The effect of  $\Delta_{max}$  is strongest for low  $\Gamma$ , and weakest for high  $\Gamma$ . Adapted from Ref.[137].

Now, we inspect the role of the SC order and the interplay between superconductivity and  $\Gamma$ . In Fig.3.15(b), we plot the variation of  $\Pi(\mathbf{q})$  with  $\Gamma$ , for five different  $\Delta_{max}$  taking  $\chi_{max} = 0.2$ . We notice that  $\Delta_{max}$  has a prominent effect when  $\Gamma$  is very small, as can be seen from the change in  $\Pi(q = 0)$  around  $\Gamma \sim 0.05$ . In this regime,  $\Delta_{max}$  weakens the softening of phonon. A similar effect on phonons in the SC phase has been indicated in conventional s-wave superconductors [231, 232]. With increasing  $\Gamma$ , for example around  $\Gamma \sim 0.3$ , the effect of  $\Delta_{max}$  becomes less significant. Finally, for very large  $\Gamma \simeq 1.0$ , changing  $\Delta_{max}$  has almost no effect as the softening is almost totally suppressed by the fluctuations already. These results highlight two crucial points. First, both superconductivity and  $\Gamma$  suppress the phonon softening. Second, the role of  $\Delta_{max}$  is prominent at low  $\Gamma$ , while negligible for large  $\Gamma$ .

We have seen that the introduction of superconductivity suppresses the phonon softening, while experiments observe a seemingly opposite characteristic of enhancement of phonon softening below  $T_c$ . At this point, we should also notice that  $\Gamma$  suppresses the phonon softening, as shown in Fig.3.15(a). Moreover,  $\Gamma$  is expected to increase with temperature due to an increase in fluctuations, whereas  $\Delta_{max}$  is expected to decrease with temperature, for example in a simple BCS type scenario. Thus, they behave in the opposite manner with temperature.

We consider temperature a phenomenologically temperature dependence for  $\Delta_{max}$  and  $\Gamma$ , similar to the  $T$  dependence extracted from the study from the spectral function in ARPES experiments [112]. The T-dependence of  $\Delta_{max}$  and  $\Gamma$  are shown in Fig.3.16(a). Below  $T_c$ ,  $\Delta_{max}$  decreases slightly with increasing temperature, whereas it remains approximately constant above  $T_c$ . Moreover following indications from Raman spectroscopy [43],  $\chi_{max}$  is taken to be equal to  $\Delta_{max}$ . To illustrate how different temperature dependence of  $\Gamma$  and  $\Delta_{max}$  can give different features in phonon softening, we use four different types of temperature dependence for  $\Gamma$ , denoted by  $\Gamma_1, \Gamma_2, \Gamma_3$  and  $\Gamma_4$  in Fig.3.16(a). Note that, they differ in magnitudes compared to  $\Delta_{max}$ . In all these cases,  $\Gamma$  reduces significantly below  $T_c$ , with the strongest fall in  $\Gamma_4$  and the weakest fall in  $\Gamma_1$ , but still remains finite even in the limit  $T \rightarrow 0$  [233]. Moreover, we considered in all the cases, a linear T-dependence for  $\Gamma$  for  $T > T_c$ , as suggested in some earlier works [234, 235].

In Fig.3.16(b), we plot  $\Pi(q = 0)$  for the parameters in Fig.3.16(a). We start by closely inspecting the  $\Gamma_4$  case in Fig.3.16(b). We observe that the values of  $\Pi(q = 0)$  are close to zero for high temperatures ( $T \gg T_c$ ), implying that the phonon softening is strongly suppressed. Remarkably, we observe that for temperatures  $T \lesssim T_c$ , the values of  $\Pi(q = 0)$  reduce sharply towards more negative values, which suggest that the phonon softening becomes clearly visible at the superconducting transition. But surprisingly, towards further lower temperatures below  $T_c$ ,  $\Pi(q = 0)$  shows an overturn, which implies a suppression in phonon softening. However, the phonon softening below  $T_c$  always remains stronger as compared to  $T > T_c$ . Very similar features have been observed in  $\text{YBa}_2\text{Cu}_3\text{O}_{6+y}$  (YBCO) [214], as shown schematically in Fig.3.16(d). In Fig.3.16(c), we present the full  $q$  dependence of  $\Pi$  at four different temperatures for the case  $\Gamma_4$ . We observe that away from  $q = 0$ , phonon softening is less sensitive to the variation of temperature. Similar feature has been found in experiments [56, 214].

Next, we closely investigate the  $\Gamma_1$  case in Fig. 3.16(b) for  $T \lesssim T_c$ . Very interestingly, the features for  $T \lesssim T_c$  possess marked differences from the  $\Gamma_4$  case. We notice a smoother enhancement in phonon softening just below  $T_c$  ( $T \sim T_c$ ), while the enhancement is more rapid and sharper

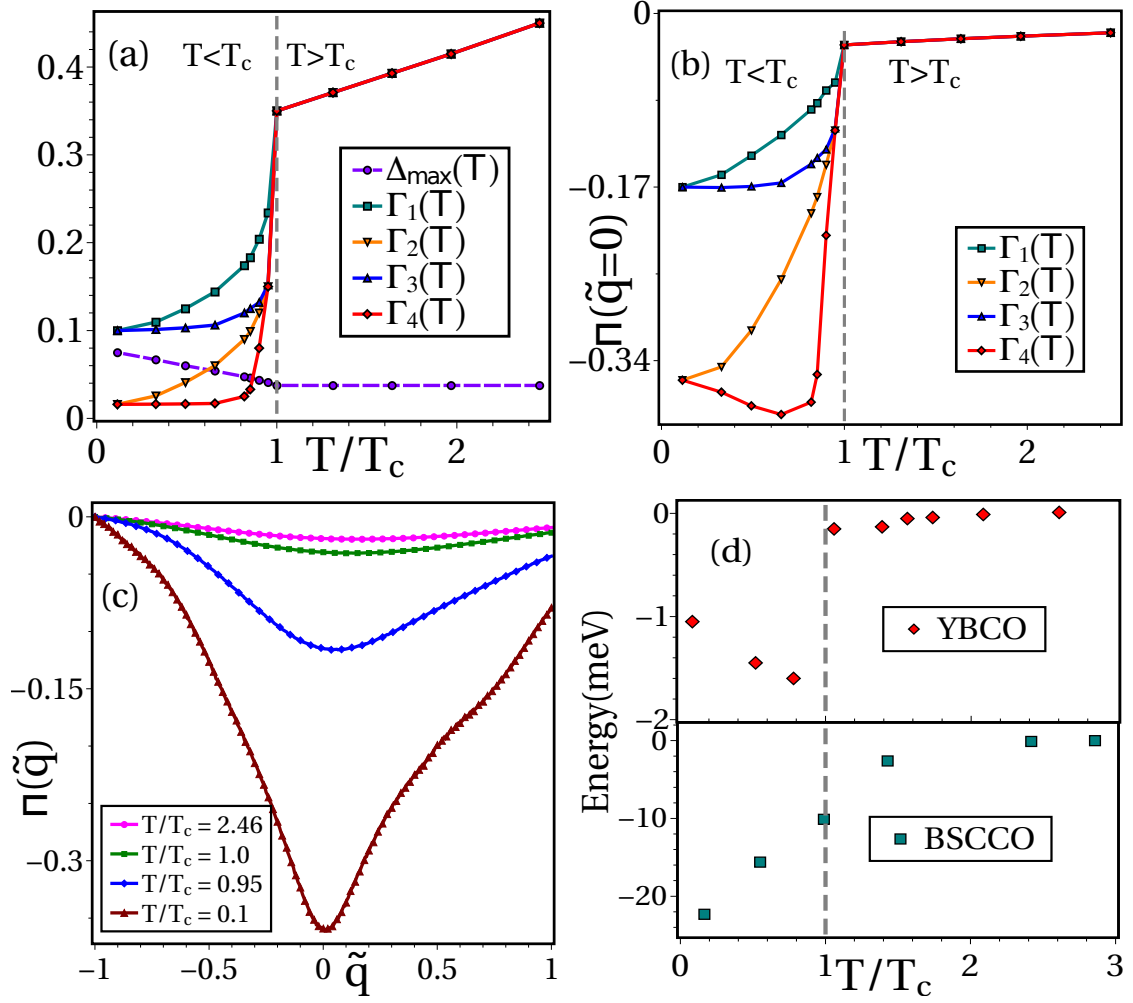


**Figure 3.16:** (a) Different sets of T-dependence for inverse lifetime of quasiparticles denoted by  $\Gamma_1$ ,  $\Gamma_2$ ,  $\Gamma_3$  and  $\Gamma_4$ . The T-dependence of the SC gap is denoted by  $\Delta_{max}(T)$ . In all cases,  $\chi_{max} = \Delta_{max}$ . (b) The T-dependence of  $\Pi(q=0)$  for different parameter sets in (a). A large negative value of  $\Pi(q=0)$  in the regime  $T \lesssim T_c$  implies a strong enhancement of phonon softening, while  $\Pi(q=0) \rightarrow 0$  implies a strong suppression in phonon softening in the regime  $T > T_c$ . (c) The variation of  $\Pi(q)$  with  $q$  at four different temperatures for parameter set  $\Gamma_4$  and  $\Delta_{max}(T)$  shown in (a). (d) Schematic representation of the experimental results of phonon softening at CDW wave-vector for YBCO and BSCCO, adopted from Refs.[56, 137, 214].

for the  $\Gamma_4$  case. In particular, towards lower temperatures ( $T \rightarrow 0$ ), a further enhancement in phonon softening can be noticed in contrast to the suppression observed for  $\Gamma_4$ . Analogous features in phonon softening have been also observed in  $\text{Bi}_2\text{Sr}_2\text{CaCu}_2\text{O}_{8+y}$  (BSCCO) [56], schematically presented in Fig.3.16(d). To demonstrate the different features in phonon softening resulting from an intricate interplay between SC gap and  $\Gamma$  below  $T_c$ , we plot results for two more cases  $\Gamma_2$  and  $\Gamma_3$ , shown in Fig.3.16(b). Below  $T_c$ , for  $\Gamma_2$ , phonon softening sharply enhances than for  $\Gamma_3$  as  $T \rightarrow 0$ .



## Chapter 4

# Transport from incoherent bosons

We present in this chapter new results on the overdoped region of the phase diagrams of cuprates. In fact, in the optimally doped to the slightly overdoped regime, we do not recover a standard Fermi liquid even though the pseudogap is weak or non-existent. The major feature of this new regime is the electrical resistivity which presents an anomalous linear dependence with temperature, in contrast with the quadratic behaviour expected for a conventional metal. As such, this region is dubbed “strange metal” and providing a satisfying description of it seems to be at least as difficult as it is to understand the pseudogap phase. This strange metal regime has also been observed in other materials but our approach here stays close to the idea we discussed for the pseudogap in cuprates. An extensive review of the experimental data on the strange metal would be as long as the first chapter of this thesis so we only give a succinct introduction to the experimental facts and some ideas that were used previously to describe the strange metal in Sec.4.1 before introducing our phenomenological model and the idea of incoherent bosons in Sec.4.2. We then show how we can recover numerous experimental features by using Kubo formalism to compute the conductivity in Sec.4.3 and we study the effect of an external magnetic field in Sec.4.4.

### 4.1 Strange metals

One common thread among diverse strongly correlated materials is the emergence of an anomalous metallic state upon destroying superconductivity [33, 236–238]. The main characteristic of these anomalous states is the scaling of the resistivity  $\rho$  with temperature which differs from the expected  $\rho \sim T^2$  obtained in the Fermi liquid theory. In fact, many materials exhibit a linear scaling of the resistivity in proximity to a superconducting phase as can be seen in Fig.4.1 in three different families of unconventional superconductors, the heavy-fermion material  $\text{CeRh}_6\text{Ge}_4$ , the iron-based superconductor  $\text{BaFe}_2(\text{As}_{1-x}\text{P}_x)_2$  and the cuprate superconductor  $\text{YBa}_2\text{Cu}_3\text{O}_{6.95}$ . These emergent states are referred to as bad metals when the conventional quasiparticle concept becomes invalid at high temperatures [33–35], whereas, in strange metal (SM), such anomaly extends down to very low  $T$  [239]. Particularly in cuprates, the resistivity shows a linear-in- $T$  dependence from low temperature up to the melting point of the material [33, 182, 240–242] over a vast temperature-



doping region, thus manifesting both bad and strange metallic characteristics. Interestingly, for low frequencies, the optical conductivity remarkably follows the classic Drude form [243, 244], which is usually associated with a transport given by semi-classical electrons and should thus be compatible with the Fermi liquid theory.

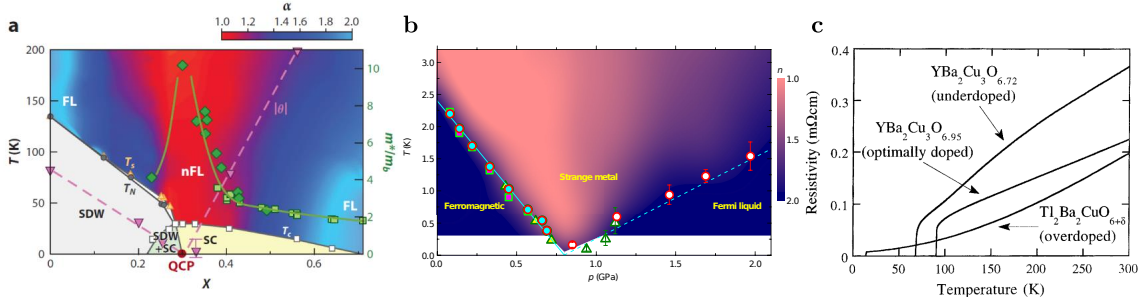


**Figure 4.1:** (a) Phase diagram of BaFe<sub>2</sub>(As<sub>1-x</sub>P<sub>x</sub>)<sub>2</sub>. The colour plot represents the evolution of the exponent  $\alpha$  in  $\rho_{ab}(T) = \rho_0 + AT^\alpha$  while the locations of the structural ( $T_s$ ), magnetic ( $T_N$ ) and superconducting ( $T_c$ ) transitions are determined resistively. The Curie-Weiss temperature  $\theta$  determined by NMR is also indicated (inverted triangles). The green symbols represent  $m^*/m_b$  (right axis) determined by specific heat and quantum oscillation measurements. The putative QCP occurs at  $x_c = 0.3$ . Adapted from Ref.[245]. (b) T-p phase diagram of CeRh<sub>6</sub>Ge<sub>4</sub>. The circles, triangles and squares for pressures below  $p_c$  denote  $T_c$  derived from the resistivity, specific heat (d.c. method), and a.c. heat capacity, respectively. The corresponding symbols above  $p_c$  mark  $T_{FL}$ , below which Fermi-liquid behaviour occurs. The FM transition is suppressed by pressure until the system reaches a QCP at  $p_c \sim 0.8$  GPa. Below  $T_c$ , and at higher pressures below  $T_{FL}$ , Fermi-liquid ground states develop. The colours denote the exponent of  $\rho(T)$  calculated as  $n = d(\log(\rho - \rho_0))/d(\log T)$ , where the Fermi-liquid states with  $n = 2$  are dark blue, and the strange-metal phase near the QCP with  $n = 1$  is shown in pink. Adapted from Ref.[246]. (c) Multiple typical temperature dependences of the resistivity in cuprates as doping is changed. The optimally doped YBa<sub>2</sub>Cu<sub>3</sub>O<sub>6.95</sub> shows the characteristic linear regime observed in the strange metal. Adapted from Ref.[247].

Recently, there has been evidence for the presence of incoherent carriers associated with the strange metal in optimally and over-doped cuprates [248, 249]. Over the region where the dc-resistivity is most linear, there is a significant reduction of the Hall carriers [250, 251], suggesting short-lived carriers responsible for the transport. Furthermore, at high magnetic fields, the magnetoresistance also displays a linear in field evolution in hole-doped cuprates [252, 253] which is further confirmed in other compounds [254–256]. This incoherent contribution to the conductivity is insensitive to the magnetic field’s orientation, again implying a vanishing Hall conductivity [253]. Thus, the mysterious SM phase acquires another element: On the one hand, it shows linear-in- $T$  resistivity with an optical conductivity following the classic Drude form, and with an additional incoherent transport component insensitive to the orientation of the magnetic field. On the other hand, the earlier experimental results in cuprates [257–259] exhibits a second transport time  $\hbar\tau_H^{-1} \sim T^2$  which controls the cotangent of the Hall angle, defined as  $\cot \theta_H = \sigma_{xx}/\sigma_{xy}$  where  $\sigma_{xx}$  and  $\sigma_{xy}$  are, respectively, the longitudinal and the Hall conductivities. A consistent theory for strange metal must reconcile all these unusual behaviours, which still remains a fundamental challenge in condensed matter physics.

Early attempts to demystify the strange metal phase rely on the rationale that the fermionic excitations are primarily responsible for its odd transport properties. These theories capture some basic features of the SM phase; for example, the marginal Fermi liquid theory [235], among others

[260–262], can heuristically describe the temperature dependence of longitudinal conductivity and the Hall angle [263]. More recently, the Hall transport time,  $\tau_H$ , was satisfactorily described by the presence of quasielectrons with an anisotropic transport time around the Fermi surface [264–267]. It is also highlighted that interactions can improve nesting near the hot-spots in the spin fermion model [69, 268], which can lead to  $T$ -linear resistivity with a broad Drude component [269]. Furthermore, such a model can capture the  $T^2$ -dependence of the cotangent of the Hall angle [270]. However, most theories presently encounter difficulties in accounting for all the observed experimental results at the same time. Furthermore, the Drude form of the optical conductivity, along with the recent report of incoherent non-orbital contribution to transport [253] remains to be addressed. Given that situation, a regime of very strong coupling, obtained by either holographic techniques [271–276] or other transport methods [277–282] have been explored to account for some of these observed properties.

To address this challenging problem, an intuitive phenomenological model is imperative. Motivated by the recent discovery of incoherent carriers [248, 249] along with the ubiquitous observations of spatially modulating patterns [88, 283] in the phase diagram of cuprates, we introduce a strange metal model that draws on our previous discussion of the pseudogap and focuses on a bosonic contribution to transport properties. These bosons are remnants of the PDW state we discussed in Chap.3 and consequently carry twice the charge of an electron and include a finite centre-of-mass wave-vector linked to its periodicity.

We propose a phenomenological model consisting of quasielectrons scattering off each other as well as charge-two bosons. The bosons originate from modulated particle-particle pairs of high-energy electrons which interact with the low-energy quasielectrons with strength  $g_I$ , and with themselves with strength  $g_b$ . With the application of an external magnetic field, the corresponding gauge-invariant Hamiltonian is written as

$$\begin{aligned}
\hat{\mathcal{H}} = & \sum_{\mathbf{k}, \alpha} c_{\mathbf{k}, \alpha}^\dagger \left[ \frac{(\mathbf{k} - e\mathbf{A})^2}{2m} - \epsilon_F \right] c_{\mathbf{k}, \alpha} + V_{e-e} \\
& + \sum_{\mathbf{q}} b_{\mathbf{q}}^\dagger \left[ \frac{1}{4} (\mathbf{Q}_0 + \delta\mathbf{q} - 2e\mathbf{A})^2 + \mu_0 \right] b_{\mathbf{q}} \\
& - \frac{1}{2} \sum_{\mathbf{k}, \alpha, \alpha'} c_{\mathbf{k}, \alpha}^\dagger (\vec{\sigma}_{\alpha\alpha'} \cdot \mathbf{H}) c_{\mathbf{k}, \alpha'} + g_b \sum_{\mathbf{q}, \mathbf{p}, \mathbf{k}} b_{\mathbf{k}+\mathbf{q}}^\dagger b_{\mathbf{p}-\mathbf{q}}^\dagger b_{\mathbf{p}} \\
& + g_I \sum_{\mathbf{k}, \mathbf{q}, \alpha} [b_{\mathbf{q}}^\dagger c_{\mathbf{k}, \alpha} c_{-\mathbf{k}+\mathbf{q}, \pm\alpha} + h.c.],
\end{aligned} \tag{4.1}$$

where  $c_{\mathbf{k}, \alpha}^\dagger$  is the creation operator for conduction electrons as before and  $b_{\mathbf{q}}^\dagger$  is the creation operator for charge-two bosons. Our idea is that the finite-momentum Cooper pairing fluctuations, with wave vector  $\mathbf{Q}_0$ , are forming at intermediate temperatures under strong coupling. Once the finite-momentum Cooper pair fluctuations are formed, gauge invariance imposes the vector potential is minimally coupled to the boson momentum  $\mathbf{q}$ . We have then used  $\mathbf{q} = \mathbf{Q}_0 + \delta\mathbf{q}$  such that  $\delta\mathbf{q} \ll \mathbf{Q}_0$  as in the study of the phonon mode. As the fermionic excitations do not play any exotic part in our description of the transport, we take free electrons with  $e$  and  $m$  respectively, the elementary charge and the quasielectron mass, whereas  $\mathbf{A}$  is the vector potential. The quantities  $\epsilon_F$  and  $\mu_0$



We consider the fermions to follow a Fermi liquid behaviour with well defined quasiparticle poles. As such the electronic Green's function  $\mathcal{G}$  is given by

$$\mathcal{G}^{-1}(\mathbf{k}, \epsilon_n) = i\epsilon_n - \epsilon_{\mathbf{k}}, \quad (4.4)$$

where we take for simplicity the dispersion of free fermions  $\epsilon_{\mathbf{k}} = \hbar^2 k^2 / 2m_e$ . For simplicity of notations, we set  $\hbar^2 / 2m_e = 1$ , from now on. In order to perform the Matsubara summation, we go to the complex plane by performing the substitution,  $i\epsilon_n \rightarrow z$ . The first term of the RHS of Eq.(4.3) becomes

$$\Pi(\omega_n, \mathbf{Q}_0) = -\frac{g_I^2}{N} \sum_{\mathbf{k}} \oint_{\mathcal{C}} \frac{dz}{2\pi i} \frac{n_F(z)}{(z + \epsilon_{-\mathbf{k}})(z + i\omega_n - \epsilon_{\mathbf{k} + \mathbf{Q}_0})}. \quad (4.5)$$

The integral is evaluated using the residue theorem and we obtain

$$\Pi(\omega_n, \mathbf{Q}_0) = -g_I^2 \frac{1}{N} \sum_{\mathbf{k}} \frac{1 - n_F(\epsilon_{-\mathbf{k}}) - n_F(\epsilon_{\mathbf{k} + \mathbf{Q}_0})}{i\omega_n - \epsilon_{-\mathbf{k}} - \epsilon_{\mathbf{k} + \mathbf{Q}_0}}. \quad (4.6)$$

As the real part of the self-energy would only shifts the positions of the pole of the bosonic Green's function, we here look at the imaginary part which will give us information about the nature of the quasiparticle spectrum. We perform the analytic continuation by letting  $i\omega_n \rightarrow \omega + i0^+$ , taking the imaginary part then leads to a delta function taken at the pole leading to

$$\begin{aligned} \text{Im } \Pi(\omega, \mathbf{Q}_0) &= \frac{\pi g_I^2}{N} \sum_{\mathbf{k}} [1 - n_F(\epsilon_{-\mathbf{k}}) - n_F(\epsilon_{\mathbf{k} + \mathbf{Q}_0})] \\ &\quad \times \delta(\omega - \epsilon_{-\mathbf{k}} - \epsilon_{\mathbf{k} + \mathbf{Q}_0}). \end{aligned} \quad (4.7)$$

We will obtain the energy dependence of  $\text{Im } \Pi(\omega, \mathbf{Q}_0)$  explicitly after carrying out the momentum summation. We start by treating a simplified case where momenta  $-\mathbf{k}$  and  $\mathbf{k} + \mathbf{Q}_0$  are close to the hot-spots where we can take an approximation for the dispersion before treating the more general case, both leading to the same form for the imaginary part of the self-energy.

### Landau damping for electrons near the hotspots

Here we show that the particle-particle bubble evaluated in the previous section gives a Landau damped form if the electrons lives near the hotspots. We use a linear approximation to write the electronic dispersion near the hotspot as a function of the Fermi velocity and the distance to the hot-spot. Going from one hot-spot to another changes the Fermi velocity in the  $x$  and  $y$  direction from  $(-v_x, v_y) \rightarrow (v_x, v_y)$ . Consequently, the dispersion becomes

$$\begin{aligned} \epsilon_{\mathbf{k}} &= -k_x v_x + k_y v_y, \\ \epsilon_{\mathbf{k} + \mathbf{Q}_0} &= k_x v_x + k_y v_y. \end{aligned} \quad (4.8)$$

Putting these two approximations in Eq.(4.7) we obtain

$$\begin{aligned} \text{Im } \Pi(\omega, \mathbf{Q}_0) &= \frac{\pi g_I^2}{4\pi^2} \int_{-\infty}^{\infty} dk_x \int_{-\infty}^{\infty} dk_y \delta(\omega - 2k_x v_x) \\ &\quad \times [1 - n_F(k_x v_x - k_y v_y) - n_F(k_x v_x + k_y v_y)]. \end{aligned} \quad (4.9)$$

Defining  $\tilde{k}_i = v_i k_i$ , after simplification we obtain

$$\text{Im } \Pi(\omega, \mathbf{Q}_0) = \frac{g_I^2}{16\pi v_x v_y} \int_{-\infty}^{\infty} d\tilde{k}_y \left[ \tanh\left(\frac{\omega/2 - \tilde{k}_y}{2T}\right) + \tanh\left(\frac{\omega/2 + \tilde{k}_y}{2T}\right) \right]. \quad (4.10)$$

In the limit,  $T \rightarrow 0$ , we can approximate  $\tanh(x/T) \approx \text{sgn}(x)$ . In this low-temperature regime, the integrand in the square brackets in Eq. (4.10), has a constant value of  $2\text{sgn}(\omega)$ , when  $\tilde{k}_y$  is restricted between  $(-\omega/2, \omega/2)$ , otherwise it vanishes. Therefore, performing the integration over  $\tilde{k}_y$ , we get

$$\text{Im } \Pi(\omega, \mathbf{Q}_0) = \frac{g_I^2}{8\pi v_x v_y} |\omega|. \quad (4.11)$$

This energy dependence is the standard form for a bosonic mode subject to Landau damping when interacting with the electronic degrees of freedom. We will now show that this result is also valid away from the hotspots and that it is a reasonable approximation for the low-energy dependence of the bosonic propagator after the fermions have been integrated out.

### General case

To obtain an approximate analytical solution in the case where we are away from the hotspots, the  $\mathbf{k}$ -summation is performed by converting it to an integral. We can approximate  $\epsilon_{\mathbf{k}+\mathbf{Q}_0} \approx k^2 + Q_0^2 + 2k_F Q_0 \cos(\theta)$ , where  $\theta$  is the angle between Fermi-momentum  $\mathbf{k}_F$  and the ordering wave-vector,  $\mathbf{Q}_0$ . Furthermore, we use the flat-band approximation with the density of states at the Fermi energy given by  $\mathcal{N}(\epsilon_F)$ , the integral in two dimensions becomes

$$\begin{aligned} \text{Im } \Pi(\omega, \mathbf{Q}_0) &= \frac{g_I^2 \mathcal{N}(\epsilon_F)}{16\pi} \int_0^{2\pi} d\theta \left[ \tanh\left(\frac{\omega + Q_0^2 + 2k_F Q_0 \cos(\theta)}{4T}\right) \right. \\ &\quad \left. + \tanh\left(\frac{\omega - Q_0^2 - 2k_F Q_0 \cos(\theta)}{4T}\right) \right] \end{aligned} \quad (4.12)$$

In the limit,  $T \rightarrow 0$ , we can approximate  $\tanh(x/T) \approx \text{sgn}(x)$ . In this low-temperature regime, the integrand in the square brackets in Eq.(4.12), which we simply denote as  $I(\theta)$  from now on, is approximately given by

$$I(\theta) = \begin{cases} 2 & \text{if } \theta \in \left[ \cos^{-1}\left(\frac{\omega - Q_0^2}{2k_F Q_0}\right), \cos^{-1}\left(\frac{-\omega - Q_0^2}{2k_F Q_0}\right) \right], \\ 2 & \text{if } \theta \in \left[ 2\pi - \cos^{-1}\left(\frac{-\omega - Q_0^2}{2k_F Q_0}\right), 2\pi - \cos^{-1}\left(\frac{\omega - Q_0^2}{2k_F Q_0}\right) \right], \\ 0 & \text{otherwise.} \end{cases} \quad (4.13)$$

The form of  $I(\theta)$  is used to evaluate the integral in Eq.(4.12) and it reads as

$$\text{Im } \Pi(\omega, \mathbf{Q}_0) = \frac{g_I^2 \mathcal{N}(\epsilon_F)}{4\pi} \left[ \cos^{-1} \left( \frac{-\omega - Q_0^2}{2k_F Q_0} \right) - \cos^{-1} \left( \frac{\omega - Q_0^2}{2k_F Q_0} \right) \right]. \quad (4.14)$$

Finally, expanding the function for  $\omega \ll 2k_F Q_0$ , we arrive at the result

$$\text{Im } \Pi(\omega, \mathbf{Q}_0) = \frac{g_I^2 \mathcal{N}(\epsilon_F)}{2\pi} \frac{\omega}{\sqrt{(2k_F Q_0)^2 - Q_0^4}}. \quad (4.15)$$

This shows there is a linear dependence on  $\omega$ . Performing similar calculations for the second term in Eq.(4.3) and the imaginary part of the self-energy reads

$$\text{Im } \Pi(\omega, \mathbf{Q}_0) = \gamma |\omega|, \quad (4.16)$$

with  $\gamma = \frac{g_I^2 \mathcal{N}(\epsilon_F)}{2\pi \sqrt{(2k_F Q_0)^2 - Q_0^4}}$ . We have checked our approximate expression against numerical evaluation of Eq.(4.12). A good agreement between them is observed in Fig.4.2(b) at low temperature, and in Fig.4.2(c) at high temperature with deviations at higher energies.

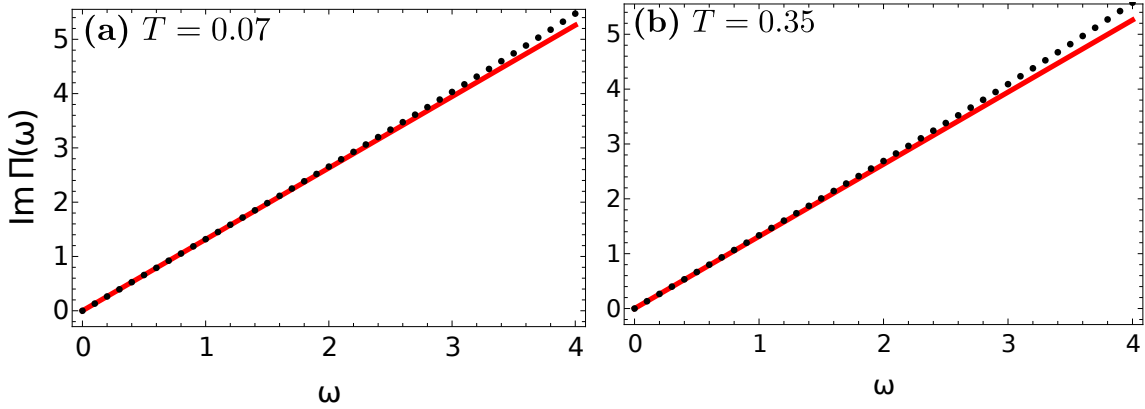


**Figure 4.2:** Comparison of imaginary part of  $\Pi(\omega)$  for numerical and approximate analytical evaluations for low temperature, **(a)**  $T = 0.07$  and  $g_I = 1$ ,  $Q_0 = \pi/2$  **(b)** Same for the higher temperature  $T = 0.35$ . The following physical constants are set to unity:  $\hbar = 1$ ,  $k_B = 1$ , and  $e = 1$ . Adapted from Ref.[284].

### 4.2.1 Effects of fermionic self-energy

In the two computations above, we considered that the fermions were only interacting with the bosonic modes and that the fermion-fermion interactions were weak enough to consider a Fermi liquid behaviour. The strong electronic correlations that govern the pseudogap phase of cuprates could be taken as an argument against our approximation, we show here that the Landau damping form for the renormalized bosonic propagator is robust even in the presence of an arbitrary fermionic self-energy. For simplicity, we use the hot-spots approximation as given in Eq.(4.8) but the result should also hold away from these particular points as the presence of a real part for the self-energy do not change our results.

Suppose this fermionic self-energy arises from a different physical mechanism. Following the notations in Ref.[152], we assume a general form for the fermionic self energy  $\Sigma_\epsilon = |\Sigma(\epsilon)|\text{sgn}(\epsilon)$ . Next, we estimate the particle-particle bubble as given by Eq.(4.2)

$$\Pi(\omega, \mathbf{Q}_0) = \frac{ig_I^2}{8\pi^3 v_x v_y} \int_{-\infty}^{\infty} d\epsilon \int_{-\infty}^{\infty} d\tilde{k}_x \int_{-\infty}^{\infty} d\tilde{k}_y \frac{1}{\left(i\Sigma_\epsilon + \tilde{k}_x - \tilde{k}_y\right) \left(i\Sigma_{\epsilon+\omega} - \tilde{k}_x - \tilde{k}_y\right)}. \quad (4.17)$$

If  $\omega > 0$  the poles of  $\tilde{k}_y$  are in the opposite half-planes if  $\epsilon$  is restricted between  $-\omega \leq \epsilon \leq 0$ . We close the contour in the upper half-plane and obtain

$$\Pi(\omega > 0, \mathbf{Q}_0) = -\frac{g_I^2}{4\pi^2 v_x v_y} \int_{-\omega}^0 d\epsilon \int_{-\infty}^{\infty} d\tilde{k}_x \frac{1}{\left(i\Sigma_\epsilon - i\Sigma_{\epsilon+\omega} + 2\tilde{k}_x\right)}, \quad (4.18)$$

$$\Pi(\omega > 0, \mathbf{Q}_0) = -\frac{g_I^2}{8\pi^2 v_x v_y} \int_{-\omega}^0 d\epsilon \log \left( \frac{i\Sigma_\epsilon - i\Sigma_{\epsilon+\omega} + 2\Lambda}{i\Sigma_\epsilon - i\Sigma_{\epsilon+\omega} - 2\Lambda} \right), \quad (4.19)$$

where  $\Lambda$  is the UV cutoff. If  $\Sigma_\epsilon - \Sigma_{\epsilon+\omega} \ll 2\Lambda$ , then the logarithm can be approximated as  $-i\pi$ . The imaginary part of  $\Pi$  then becomes

$$\text{Im } \Pi(\omega > 0, \mathbf{Q}_0) = \frac{g_I^2}{8\pi v_x v_y} \omega. \quad (4.20)$$

Similarly one can repeat the procedure for  $\omega < 0$  and obtains the same expression with a negative sign, combining these two one can thus write

$$\text{Im } \Pi(\omega, \mathbf{Q}_0) = \frac{g_I^2}{8\pi v_x v_y} |\omega|. \quad (4.21)$$

Therefore, the Landau damping remains unaffected for arbitrary imaginary self-energy corrections. These conclusions remain unaffected if the electrons attain mass away from the putative hot-spots. To recognize this, we introduce in Eq.(4.17) two real terms  $\mu_1$  and  $\mu_2$  as the general mass of the electrons,

$$\Pi(\omega, \mathbf{Q}_0) = \frac{ig_I^2}{8\pi^3 v_x v_y} \int_{-\infty}^{\infty} d\epsilon \int_{-\infty}^{\infty} d\tilde{k}_x \int_{-\infty}^{\infty} d\tilde{k}_y \frac{1}{\left(i\Sigma_\epsilon - \mu_1 + \tilde{k}_x - \tilde{k}_y\right) \left(i\Sigma_{\epsilon+\omega} + \mu_2 - \tilde{k}_x - \tilde{k}_y\right)}. \quad (4.22)$$

Using the same procedure as above we arrive at

$$\Pi(\omega > 0, \mathbf{Q}_0) = -\frac{g_I^2}{8\pi^2 v_x v_y} \int_{-\omega}^0 d\epsilon \log \left( \frac{i\Sigma_\epsilon - i\Sigma_{\epsilon+\omega} - \mu_1 - \mu_2 + 2\Lambda}{i\Sigma_\epsilon - i\Sigma_{\epsilon+\omega} - \mu_1 - \mu_2 - 2\Lambda} \right). \quad (4.23)$$

Again, if  $\Sigma_\epsilon - \Sigma_{\epsilon+\omega} \ll 2\Lambda - \mu_1 - \mu_2$ , we have the same Landau damping form as found in Eq. (4.11) at low energies.

### 4.2.2 On the fermion-boson vertex corrections

Recent studies of the antiferromagnetic QCP [152, 285] in two spatial dimensions obtained that the fermion-boson vertex corrections become relevant at low-energy scales and modify the dynamical exponent close to the QCP. Therefore, it is important to check that these vertex corrections do not spoil our approximations. As the calculations are similar to the one we just carried out and the results do not impact the rest of our discussion we present the details in Appendix C. The main takeaway is that in the case where there are hot-spots linked by the modulation wave-vector  $Q_0$ , there is a logarithmic divergence of the vertex correction at low temperatures. This has however not been seen in numerical Quantum Monte-Carlo studies, suggesting that these corrections are relevant only at very low temperatures at which other many sources of damping with different origins, such as nematic fluctuations, loop-current fluctuations [286], among others exist. These additional fluctuations that emerge in cuprates can also regularize the fermion-boson vertex without changing the transport properties we study here.

To conclude this section, we note that the scattering of the charge-2 bosons with finite center-of-mass momentum leads to a robust form for the self-energy at low energy and justify or starting point for our incoherent boson propagator given by

$$\mathcal{D}^{-1}(\mathbf{q}, i\omega_n) = \gamma |\omega_n| + \mathbf{q}^2 + \mu(T).. \quad (4.24)$$

We will next see how this propagator is renormalized by boson-boson interactions that we will compute in the next section (Sec.4.2.3). We will mainly be interested in the temperature dependence of the “mass” term  $\mu(T)$  which will be important in determining the temperature dependence of the conductivity due to the presence of these bosons as describe in Sec.4.3.

### 4.2.3 Boson-boson interactions

#### Renormalization of the “mass” term – Number of bosons

In this section, we present the detailed evaluation of the leading order term in the self-energy, which renormalizes the bare mass  $\mu(T)$  of the boson and gives the crucial temperature dependence leading to the linear conductivity (see Sec.4.3). Fig.4.3(a) shows the relevant diagram, where the wavy lines represent the bosons, which interact with other bosons with the interaction strength being represented by  $g_b$ . The mass term renormalization is given by the real part of this diagram, i.e.

$$N_b = \frac{g_b}{N\beta} \sum_{q, \omega_n} \frac{1}{\gamma |\omega_n| + q^2 + \mu}. \quad (4.25)$$

The Matsubara summation over  $\omega_n$  is carried out by using the spectral decomposition of the bosonic Green’s function. The spectral function  $\mathcal{A}(E, \mathbf{q})$  is given by [37]

$$\mathcal{A}(\mathbf{q}, E) = -2\text{Im} [\mathcal{D}_R(\mathbf{q}, E)] = -2 \frac{\gamma E}{(\gamma E)^2 + (q^2 + \mu)^2}. \quad (4.26)$$



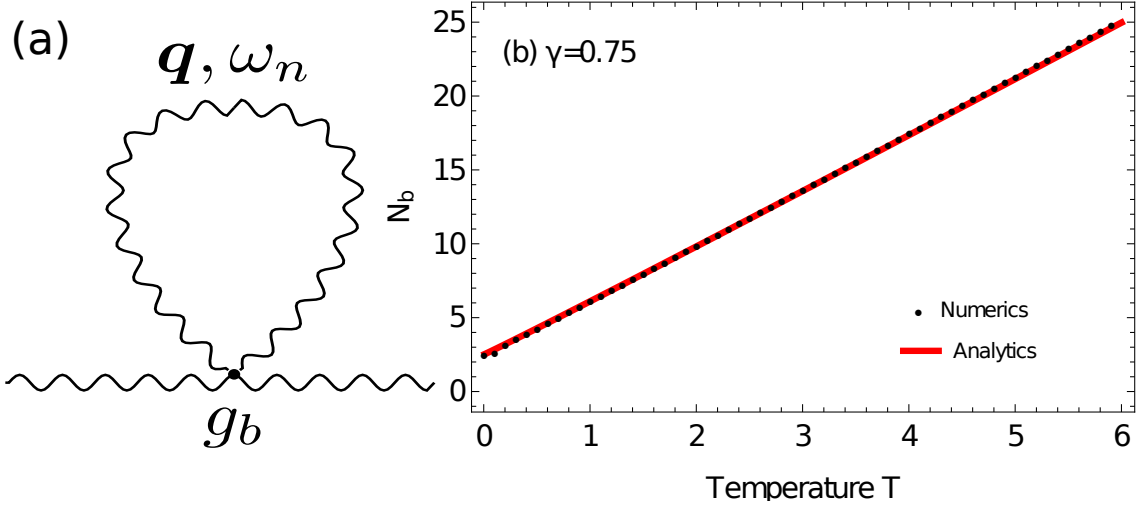


**Figure 4.3:** (a) The first-order diagram of the bosonic self-energy. The wavy lines denote the bosons, which interact with the strength  $g_b$ . (b) The temperature dependence of the number of bosons, evaluated by solving the Eq.(4.29) numerically and compared with the expression arrived at analytically in Eq.(4.33). The perfect match between the two evaluations gives us confidence in our analytical results. The temperature is in the units of  $\mu_0/\gamma$ . Adapted from Ref.[284].

Noting that  $\mathcal{D}(\mathbf{q}, \omega_n) = \int_{-\infty}^{\infty} \frac{dE}{2\pi} \frac{\mathcal{A}(\mathbf{q}, E)}{i\omega_n - E}$ , the summation is taken to the complex plane by promoting  $i\omega_n \rightarrow z$  and  $T \sum_{\omega_n} \rightarrow \oint_{\mathcal{C}} \frac{dz}{2\pi i} n_B(z)$ , where  $\mathcal{C}$  covers the whole of the complex plane. Therefore the expression becomes

$$N_b = \frac{1}{L} \sum_{\mathbf{q}} \oint_{\mathcal{C}} \frac{dz}{2\pi i} \int_{-\infty}^{\infty} \frac{dE}{2\pi} \frac{\mathcal{A}(\mathbf{q}, E) n_B(z)}{z - E}. \quad (4.27)$$

We note that there is one pole in  $z$  and we can thus use the Residue theorem to perform the integral over the complex variable  $z$ , using Eq.(4.26) for the spectral function leads to the expression

$$N_b = -\frac{1}{2\pi} \int_0^{\infty} dq \int_{-\infty}^{\infty} \frac{dE}{2\pi} n_B(E) \frac{\gamma E}{(\gamma E)^2 + (q^2 + \mu)^2}. \quad (4.28)$$

After performing the integral over  $\mathbf{q}$  exactly,  $N_b$  becomes

$$N_b = -\frac{1}{4\pi^2} \int_{-\infty}^{\infty} dE \left[ \frac{\pi}{2} \text{sgn}(E) - \tan^{-1} \left( \frac{\mu}{\gamma T} \right) \right] n_B(E). \quad (4.29)$$

We now approximate the Bose-Einstein distribution as

$$n_B(x) = \begin{cases} 0 & \text{if } x > T, \\ \frac{T}{x} & \text{if } |x| < T, \\ -1 & \text{if } x < -T. \end{cases} \quad (4.30)$$

This allows us to performing the integral in the regime where  $|E| < T$  which leads to a renormalization of the mass term given by

$$N_b^{(1)} = \begin{cases} \frac{T}{4\pi} \log\left(\frac{\gamma T}{\mu}\right) & \text{for } \gamma T \gg \mu, \\ \frac{\mu}{2\pi^2 \gamma} & \text{for } \gamma T \ll \mu. \end{cases} \quad (4.31)$$

Similarly, performing the integral for  $E < -T$ , we obtain

$$N_b^{(2)} = \begin{cases} \frac{1}{4\pi}(\Lambda - T) & \text{for } \gamma T \gg \mu, \\ 0 & \text{for } \gamma T \ll \mu, \end{cases} \quad (4.32)$$

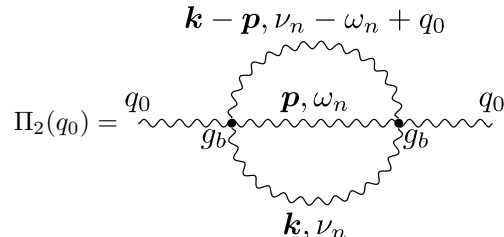
where  $\Lambda$  is the ultraviolet energy cutoff of the system, usually given by the lattice distance. Therefore,  $N_b$  will be independent of temperature in this regime, as  $\Lambda$  will be the dominant energy scale. This gives the number of bosons that condenses to the ground state. The mass term  $\mu$  to the first order is given by setting  $\mu = \mu_0$ , where  $\mu_0$  is the bare mass of the bosons, which is naturally temperature independent. Therefore, to first order in  $g_b$ , we obtain

$$\mu = \begin{cases} \mu_0 + g_b \left( \frac{T}{4\pi} \log\left(\frac{\gamma T}{\mu_0}\right) \right) & \text{for } \gamma T \gg \mu_0, \\ \mu_0 & \text{for } \gamma T \ll \mu_0. \end{cases} \quad (4.33)$$

The constant terms are absorbed in the  $\mu_0$ , which becomes close to zero near the quantum critical point. The temperature dependence of  $N_b$  calculated numerically from Eq. (4.29) and analytical form displayed in Eq. (4.33) matches over a wide range of temperature, as can be seen in Fig.4.3(b)

### Mode-Mode Coupling: Higher order terms in self-energy

The second-order bosonic self-energy diagram – which renormalizes both the mass-term  $\mu$ , and the imaginary term of the bosonic propagator,  $\gamma$  – is denoted by  $\Pi_2(q_0)$  where  $q_0$  is the external frequency. We emphasize that the finite-momentum bosons is dominant around  $Q_0$ , which is different from the external frequency in this diagram,  $q_0$ . The integral is given by

$$\begin{aligned} \Pi_2(q_0) &= \text{Diagram} \\ &= g_b^2 \frac{1}{L^2} \sum_{\mathbf{k}, \mathbf{p}} T^2 \sum_{\omega_n, \nu_n} \mathcal{D}(\nu_n - \omega_n + q_0, \mathbf{k} - \mathbf{p}) \mathcal{D}(\nu_n, \mathbf{k}) \mathcal{D}(\omega_n, \mathbf{p}). \end{aligned} \quad (4.34)$$


Performing the summation over  $\nu_n$  and  $\omega_n$  and using the spectral decomposition, one readily obtains

$$\begin{aligned} \Pi_2(q_0) = \frac{g_b^2}{L^2} \sum_{\mathbf{k}, \mathbf{p}} \int_{-\infty}^{\infty} \frac{dE_1}{2\pi} \frac{dE_2}{2\pi} \frac{dE_3}{2\pi} [\mathcal{A}(E_1, \mathbf{a}) \mathcal{A}(E_2, \mathbf{b}) \mathcal{A}(E_3, \mathbf{d}) (n_B(E_2) - n_B(E_1))] \\ \times \left( \frac{n_B(E_3) - n_B(E_2 - E_1)}{iq_0 - E_1 + E_2 - E_3} \right), \end{aligned} \quad (4.35)$$

where we have defined

$$\mathbf{a} = \mathbf{k}^2 + \mu. \quad (4.36)$$

$$\mathbf{b} = (\mathbf{k} - \mathbf{p})^2 + \mu. \quad (4.37)$$

$$\mathbf{d} = \mathbf{p}^2 + \mu. \quad (4.38)$$

Analytically continuing  $iq_0 \rightarrow q_0 + i0^+$ , the imaginary part of the  $\Pi_2$  becomes

$$\begin{aligned} \text{Im } \Pi_2(q_0) = \frac{-g_b^2 q_0}{8\pi^2 L^2} \sum_{\mathbf{k}, \mathbf{p}} \int_{-\infty}^{\infty} dE_1 dE_2 [\mathcal{A}(E_1, \mathbf{a}) \mathcal{A}(E_2, \mathbf{b}) \mathcal{A}(E_2 - E_1 + q_0, \mathbf{d}) (n_B(E_2) - n_B(E_1))] \\ \frac{\partial n_B}{\partial(E_2 - E_1)}. \end{aligned} \quad (4.39)$$

In the regime where  $|E_2 - E_1| < T$  and expanding the spectral function in the  $q_0 \rightarrow 0$  limit, we obtain

$$\text{Im } \Pi_2(q_0) = \frac{\gamma g_b^2 T q_0}{\pi^2} \frac{1}{L^2} \sum_{\mathbf{k}, \mathbf{p}} \int_{-\infty}^{\infty} dE_1 dE_2 \left[ \frac{\gamma^2 E_1 E_2 \left( \frac{n_B(E_2) - n_B(E_1)}{E_2 - E_1} \right)}{((\gamma E_2)^2 + \mathbf{a}^2)((\gamma E_1)^2 + \mathbf{b}^2)((\gamma(E_2 - E_1))^2 + \mathbf{d}^2)} \right]. \quad (4.40)$$

Next, approximating  $n_B(E)$  by using Eq.(4.30), the integrand will only contribute when both  $|E_1| < T$  and  $|E_2| < T$ . Making a change of variables from  $\tilde{E} = \gamma E$ , we obtain

$$\text{Im } \Pi_2(q_0) = \frac{\gamma g_b^2 T q_0}{\pi^2} \frac{1}{L^2} \sum_{\mathbf{k}, \mathbf{p}} \int_{-\gamma T}^{\gamma T} d\tilde{E}_1 \int_{-\gamma T}^{\gamma T} d\tilde{E}_2 \frac{1}{(\tilde{E}_2^2 + \mathbf{a}^2)(\tilde{E}_1^2 + \mathbf{b}^2)((\tilde{E}_2 - \tilde{E}_1)^2 + \mathbf{d}^2)}. \quad (4.41)$$

Evaluating the integral in the familiar regimes  $\gamma T \gg \mu$  and  $\gamma T \ll \mu$ , we obtain the forms

$$\text{Im } \Pi_2(q_0) = \begin{cases} \frac{\gamma g_b^2 T^2 q_0}{2} \frac{1}{L^2} \sum_{\mathbf{k}, \mathbf{p}} \frac{1}{\mathbf{a}\mathbf{b}\mathbf{d}(\mathbf{a}+\mathbf{b}+\mathbf{d})} & \text{for } \gamma T \gg \mu, \\ \frac{2\gamma^3 g_b^2 T^4 q_0}{\pi^2} \frac{1}{L^2} \sum_{\mathbf{k}, \mathbf{p}} \frac{1}{\mathbf{a}^2 \mathbf{b}^2 \mathbf{d}^2} & \text{for } \gamma T \ll \mu. \end{cases} \quad (4.42)$$

Performing the momentum summation we arrive at expressions for the imaginary part  $\Pi_2$

$$\text{Im } \Pi_2(q_0) = \begin{cases} \frac{c_1 \gamma g_b^2 T^2}{16\pi^3 \mu^2} q_0 & \text{for } \gamma T \gg \mu, \\ \frac{c_2 \gamma^3 g_b^2 T^4}{4\pi^5 \mu^4} q_0 & \text{for } \gamma T \ll \mu, \end{cases} \quad (4.43)$$

where  $c_1 = 0.323$  and  $c_2 = 0.284$  are evaluated numerically. On the other hand, the real part of  $\Pi_2$  can be evaluated by utilizing Kramers-Kronig relations. The external frequency is taken to be small in the above calculations. Thus, a frequency cut-off  $\lambda = \min [\mu, \gamma T]$  is used in the Kramers-Kronig relation. The Kramers-Kronig relation is given by

$$\text{Re } \Pi_2(q_0) = \frac{2}{\pi} \mathcal{P} \int_0^\lambda \frac{\omega \text{Im } \Pi_2(\omega)}{\omega^2 - q_0^2} d\omega. \quad (4.44)$$

Therefore, the real-part of the  $\Pi_2$  becomes

$$\text{Re } \Pi_2(q_0) = \begin{cases} \frac{c_1 \gamma g_b^2 T^2}{8\pi^4 \mu^2} \left( \lambda - q_0 \tanh^{-1} \left( \frac{\lambda}{q_0} \right) \right) & \text{for } \gamma T \gg \mu, \\ \frac{c_2 \gamma^3 g_b^2 T^4}{2\pi^6 \mu^4} \left( \lambda - q_0 \tanh^{-1} \left( \frac{\lambda}{q_0} \right) \right) & \text{for } \gamma T \ll \mu, \end{cases} \quad (4.45)$$

where  $\lambda$  is the cut-off energy scale. Now evaluating the renormalization of the  $\mu$  and  $\gamma$  up to the second order for  $\gamma T \gg \mu_0$ , we get

$$\mu \approx \mu_0 + \frac{g_b}{4\pi} \log \left( \frac{\gamma T}{\mu_0} \right) + \frac{2c_1 \gamma \lambda}{\pi^2 \log^2 (\gamma T / \mu_0)} \quad (4.46)$$

$$\tilde{\gamma} \approx \gamma + \frac{c_1 \gamma}{\pi \log^2 (\gamma T / \mu_0)}. \quad (4.47)$$

Taking the limit  $\gamma T / \mu_0 \gg 1$ , it is clear that the second-order terms are negligible. Next, evaluating the same for  $\gamma T \ll \mu_0$ , we get

$$\mu \approx \mu_0 + \frac{c_2 \lambda (\gamma T)^4}{2\pi^6 \gamma \mu_0^4}, \quad (4.48)$$

$$\tilde{\gamma} \approx \gamma + \frac{c_2 (\gamma T)^3}{4\pi^5 \gamma \mu_0^4}. \quad (4.49)$$

Again, taking the limit  $\gamma T / \mu_0 \ll 1$ , it becomes clear that the higher-order terms are negligible compared to the first-order ones.

### 4.3 Transport from incoherent bosons

We now arrive at the main part of this study. We are interested in the contribution to the transport properties from the incoherent bosons described by the renormalized propagator we obtained in the previous section. For this, we use the idea of linear response theory to compute the current-current correlation. This is embedded in the Kubo formalism that allows us to obtain

the longitudinal conductivity by means of diagrammatic expansion as shown in Sec.4.3.1. We then include the effect of an external magnetic field to obtain a prediction for the Hall conductivity and the magnetoresistance in Secs.4.4.1 and 4.4.3.

### 4.3.1 Kubo formula

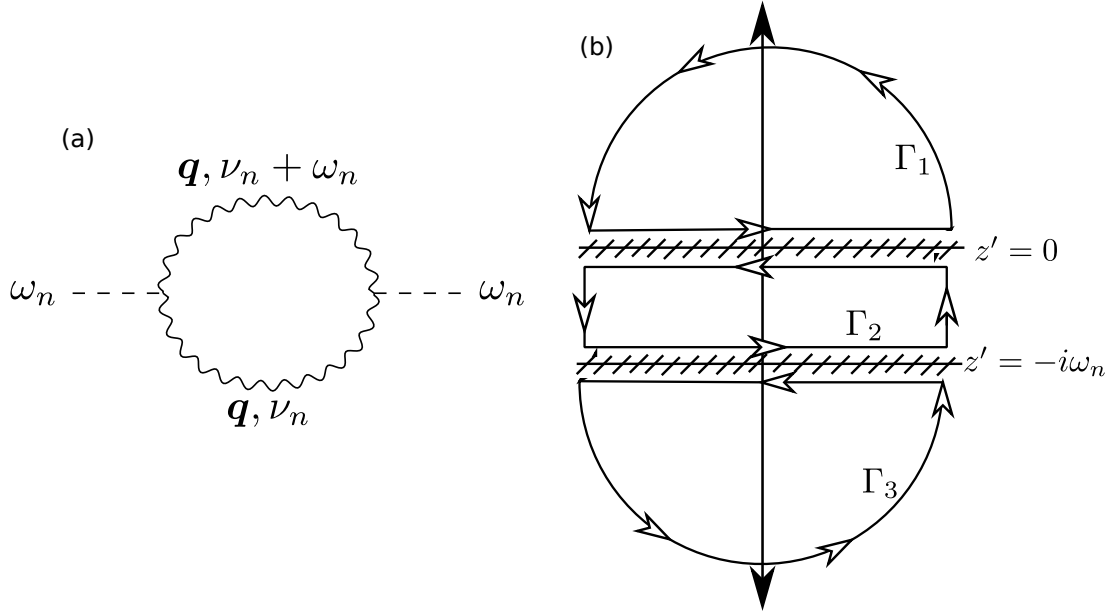


**Figure 4.4:** (a) The leading order diagram to evaluate the conductivity. (b) The contours used to evaluate the Kubo formula for finite-momentum bosons. The two dashed lines are the branch cuts. Adapted from Ref.[284].

The longitudinal conductivity is given in terms of correlation functions  $\mathcal{K}$  by [37]

$$\mathcal{K}(\omega_n) = -T \sum_{\nu_n} \frac{1}{L} \sum_{\mathbf{q}} [\mathcal{D}(\nu_n, \mathbf{q}) + q^2 \mathcal{D}(\nu_n, \mathbf{q}) \mathcal{D}(\nu_n + \omega_n, \mathbf{q})]. \quad (4.50)$$

The first term is the diamagnetic term and the second term is the paramagnetic current-current correlation. The finite-momentum bosons is dominant around  $\mathbf{q} = \mathbf{Q}_0$  so we approximate Eq.(4.50) by

$$\mathcal{K}(\omega_n) \approx -T \sum_{\nu_n} \frac{1}{L} \sum_{\mathbf{q}} [\mathcal{D}(\nu_n, \mathbf{q}) + Q_0^2 \mathcal{D}(\nu_n, \mathbf{q}) \mathcal{D}(\nu_n + \omega_n, \mathbf{q})]. \quad (4.51)$$

The optical conductivity is then evaluated by

$$\sigma(\omega) = - \left. \frac{\mathcal{K}(\omega_n)}{\omega_n} \right|_{i\omega_n \rightarrow \omega + i0^+}. \quad (4.52)$$

The evaluation of the  $\mathcal{K}$  is carried out in the following way: The integral is evaluated in the contour shown in Fig.4.4(b). There are two branch cuts at  $z' = 0$  and  $z' = i\omega_n$ . The integrals over the  $\Gamma_1$  and  $\Gamma_3$  contours cancel the diamagnetic term. Therefore, only the  $\Gamma_2$  contour contributes

to the optical conductivity. The integral becomes

$$\mathcal{K}(\omega_n) = \frac{-Q_0^2}{2\pi i L} \sum_{\mathbf{q}} \oint_{\Gamma_2} \frac{dz n_B(z)}{(i\gamma z + q^2 + \mu)((-iz + \omega_n)\gamma + q^2 + \mu)}. \quad (4.53)$$

The poles of  $z$  lie outside the  $\Gamma_2$  contour and hence the full integrals collapse to the real line integrals along the branch cuts. The resulting expression becomes

$$\mathcal{K}(\omega) = \frac{Q_0^2}{L} \sum_{\mathbf{q}} \frac{1}{2\pi i} \int_{-\infty}^{\infty} dx \frac{n_B(x - \omega/2) - n_B(x + \omega/2)}{(i\gamma x - i\gamma \frac{\omega}{2} + q^2 + \mu)(-i\gamma x - i\gamma \frac{\omega}{2} + q^2 + \mu)}. \quad (4.54)$$

The summation over  $\mathbf{q}$  is converted to an integral and is performed by usual means, i.e.

$$\mathcal{K}(\omega) = -\frac{Q_0^2 \omega}{16\pi^2 \gamma} \int_{-\infty}^{\infty} dx \left( \frac{\partial n_B}{\partial x} \right) \frac{1}{x} \log \left( \frac{-i\gamma x - i\gamma \frac{\omega}{2} + \mu}{i\gamma x - i\gamma \frac{\omega}{2} + \mu} \right). \quad (4.55)$$

From the approximate form of the  $n_B$  given in Eq.(4.30), we obtain

$$\frac{\partial n_B}{\partial x} = \begin{cases} 0 & \text{if } |x| > T, \\ -\frac{T}{x^2} & \text{if } |x| < T. \end{cases} \quad (4.56)$$

Using Eq.(4.56), the optical conductivity becomes

$$\sigma(\omega) = -\frac{iQ_0^2 T}{16\pi^2 \gamma} \int_{-T}^T dx \frac{1}{x^3} \log \left( \frac{-x - \frac{\omega}{2} - \frac{i\mu}{\gamma}}{x - \frac{\omega}{2} - \frac{i\mu}{\gamma}} \right). \quad (4.57)$$

Defining  $\tilde{\mu} = \frac{\omega}{2} + i\frac{\mu}{\gamma}$  and performing the integral, we obtain

$$\begin{aligned} \sigma(\omega) = & -\frac{iQ_0^2 T}{16\pi^2 \gamma} \left[ -\frac{2}{\tilde{\mu} T} + \frac{1}{2\tilde{\mu}^2} \log \left( \frac{\tilde{\mu} + T}{\tilde{\mu} - T} \right) \right. \\ & - \frac{1}{2\tilde{\mu}^2} \log \left( \frac{\tilde{\mu} - T}{\tilde{\mu} + T} \right) + \frac{1}{2T^2} \log \left( \frac{\tilde{\mu} - T}{\tilde{\mu} + T} \right) \\ & \left. - \frac{1}{2T^2} \log \left( \frac{\tilde{\mu} + T}{\tilde{\mu} - T} \right) \right]. \end{aligned} \quad (4.58)$$

We expand the above expression in two regimes: For the first regime,  $T \ll \sqrt{\omega^2/4 + \mu^2/\gamma^2}$  we find that the optical conductivity displays the Drude form

$$\sigma(\omega) = \frac{Q_0^2}{4\pi^2 \mu \left( 1 - i\frac{\gamma\omega}{2\mu} \right)}. \quad (4.59)$$

The Drude conductivity is naturally given by:  $\sigma(\omega) = \sigma_0 \frac{\tau}{1 - i\omega\tau}$ . From that expression, one can easily read off the  $\sigma_0 = \frac{Q_0^2}{2\pi^2 \gamma}$  while the scattering time of the bosons is given by  $\tau = \frac{\gamma}{2\mu}$ . The temperature dependence of the longitudinal conductivity is thus captured by the dependence of the mass term  $\mu$  and  $\gamma$ .

On the other hand, for the second regime  $T \gg \sqrt{\omega^2/4 + \mu^2/\gamma^2}$  the optical conductivity does not exhibit the traditional Drude form

$$\sigma(\omega) = \frac{Q_0^2 \mu}{12\pi^2 \gamma^2 T^2} \left( 1 - i \frac{\gamma \omega}{2\mu} \right). \quad (4.60)$$

In the next section, we discuss the temperature dependence of the dc conductivity and how to understand the phase diagram of cuprates using the different regimes we capture with our approximate analytical treatment.

We can also note that the vertex corrections that could arise due to the boson-boson interaction does not change significantly these results. The calculations for these are presented in Appendix [D](#)

### 4.3.2 Static Conductivity – The regimes

Next, we elaborate on the regimes of the static conductivity. Taking a  $\omega \rightarrow 0$  limit, we obtain the static conductivity in the two theoretical regimes as

$$\rho_{xx}(T) = \begin{cases} \frac{4\pi^2 \mu}{Q_0^2} & \text{for } \gamma T \ll \mu(T), \\ \frac{12\pi^2 \gamma^2 T^2}{Q_0^2 \mu} & \text{for } \gamma T \gg \mu(T). \end{cases} \quad (4.61)$$

The bosonic mass-renormalization is evaluated in Eq.(4.33) and we can see that the transition temperature between our two regimes in Eq.(4.61) also depends on  $\mu(T)$ . To understand when these two distinct regimes are reached, we want to find the temperature scale  $T'_1$ , where

$$\gamma T'_1 = \mu_0 + \tilde{g}_b T'_1 \log(\gamma T'_1 / \mu_0) \quad (4.62)$$

Solving for  $T'_1$ , we get

$$T'_1 = -\frac{\mu_0}{\tilde{g}_b W[-\gamma/\tilde{g}_b \exp(-\gamma/\tilde{g}_b)]}, \quad (4.63)$$

where  $W[x]$  is the Lambert  $W$  function. For different coupling strength  $\tilde{g}_b = g_b/(4\pi)$ , the form for this function is given by

$$W \left[ -\frac{\gamma}{\tilde{g}_b} \exp \left( -\frac{\gamma}{\tilde{g}_b} \right) \right] = \begin{cases} -\frac{\gamma}{\tilde{g}_b} & \text{for } \tilde{g}_b \geq \gamma, \\ -\frac{\gamma}{\tilde{g}_b} \exp \left( -\frac{\gamma}{\tilde{g}_b} \right) & \text{for } \tilde{g}_b < \gamma. \end{cases} \quad (4.64)$$

Putting this in Eq.(4.63), we get the temperature scale

$$T'_1 = \begin{cases} \frac{\mu_0}{\gamma} & \text{for } \tilde{g}_b \geq \gamma, \\ \frac{\mu_0}{\gamma} \exp\left(\frac{\gamma}{\tilde{g}_b}\right) & \text{for } \tilde{g}_b < \gamma. \end{cases} \quad (4.65)$$

This lead to the phase diagram presented in Fig.4.5(a).

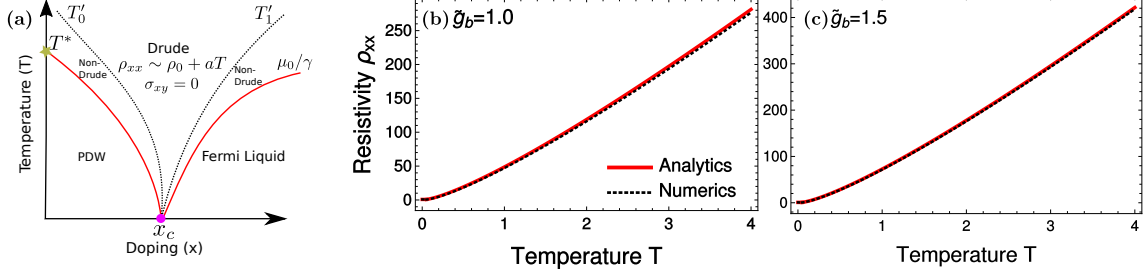


**Figure 4.5:** (a) The phase diagram for the scenario when bosonic interaction strength is weaker than the Landau damping parameter. Here, we have an intermediate regime bounded by the dotted black curve, where the optical conductivity does not conform to the conventional Drude form. This line collapses on the  $\mu_0/\gamma$  line when the boson-boson interaction is strong. (b)-(c) Displays the linear-in- $T$  evolution of resistivity obtained from the analysis of the model. In all the plots, we set the Landau-damping constant equal to  $\gamma = 1.0$  and the temperature independent mass term  $\mu_0 = 0.05$ . The temperature is given in units of  $\mu_0/\gamma$ . Besides, we choose also the input parameters: (b)  $\tilde{g}_b = 1.0$  and (c)  $\tilde{g}_b = 1.5$ . Above  $T > \mu_0/\gamma$  the linear-in- $T$  behavior sets in. We also compare both the numerical and the analytical expressions in these plots which are in good agreement with each others. Adapted from Ref.[284].

It can be seen that if  $\tilde{g}_b \geq \gamma$ , the temperature scale  $T'_1$  collapses on  $\mu_0/\gamma$ . Consequently, we are always in the  $\gamma T < \mu(T)$  regime for strong boson-boson interaction. In other words,  $\gamma T > \mu(T)$  regime is never attained if the coupling between the bosons is stronger than that of the Landau damping coefficient. In this regime, substituting the temperature dependence for  $\mu(T)$  from Eq.(4.33), the static conductivity is given by

$$\rho_{xx}(T) = \begin{cases} \frac{4\pi^2\mu_0}{Q_0^2} + \frac{4\pi^2\tilde{g}_b}{Q_0^2} T \log\left(\frac{\gamma T}{\mu_0}\right) & \text{for } \gamma T \gg \mu_0, \\ \frac{4\pi^2\mu_0}{Q_0^2} & \text{for } \gamma T \ll \mu_0. \end{cases} \quad (4.66)$$

The incoherent charged bosons thus have a linear-in- $T$  resistivity when  $\gamma T \geq \mu_0$ . We have compared the static conductivity given in the above equation against the numerical evaluation for the static limit of Eq.(4.55). This comparison is displayed in Fig.4.5(b) and (c) for two boson-boson interaction strengths. A remarkable match between the two computations over a wide range of temperatures is observed. This regime also corresponds to the Drude form of optical conductivity, as shown in Eq.(4.59). The bosonic contribution becomes independent of temperature below the  $T'_1$  line, however, the presence of conduction electrons will lead to a quadratic  $T$ -dependence of resistivity, just like in the Fermi liquid case.

Interestingly, when the interaction between the bosons is lower than the Landau damping



constant, i.e.,  $\tilde{g}_b < \gamma$ , there will be an intermediate temperature regime,  $\mu_0/\gamma < T < T'_1$ , where  $\gamma T > \mu(T)$ . This is the case explicitly presented in the phase diagram from Fig.4.5(a). The region bounded by the dotted line can harbor a non-Drude like optical conductivity as evaluated in Eq.(4.60). The static conductivity in this limit is given by

$$\rho_{xx}(T) \approx \begin{cases} \frac{12\pi^2\gamma^2}{Q_0^2\tilde{g}_b \log(\gamma T/\mu_0)} T & \text{for } \gamma T \gg \mu_0, \\ \frac{48\pi^3\gamma^2}{Q_0^2\mu_0} T^2 & \text{for } \gamma T \ll \mu_0. \end{cases} \quad (4.67)$$

Consequently, up to logarithmic corrections, we still have a linear-in- $T$  resistivity even when the bosonic interaction strength is weaker than the damping and  $\gamma T > \mu_0$ . However, such linear-in- $T$  resistivity does not subscribe to the Drude form of the optical conductivity. Below this temperature, the incoherent bosons also contribute to the  $T^2$ -resistivity expected in the Fermi-liquid regime. Thus, for weak coupling, the crossover from the strange metallic to Fermi-liquid behaviour occurs through this intermediary region.

In the pseudogap phase, the opening of a gap at the temperature  $T^*$  results from the deconfining transition of the PDW order parameter into the SC and CDW fields. Above  $T^*$ , the incoherent bosons have a bare mass of  $2\mu_0$ . Following the same analysis while using the new bare mass for the bosons leads to similar results with a possible temperature region  $T^* < T < T'_0$  where the non-Drude form of the optical conductivity survives for weakly coupled bosons, i.e.,  $\tilde{g}_b < \gamma$ .

## 4.4 Effect of magnetic field

To get a complete picture of the effect on the transport of the incoherent boson, we now turn to the study of transport in presence of an external magnetic field. We start by showing that the bosons do not contribute to the Hall conductivity in Sec.4.4.1. We then look at how the magnetic field affects the bosonic mass for pairs with both singlet or triplet symmetry. These results are then used in Sec.4.4.3 to study the change in resistivity with a magnetic field. We find that we have multiple regimes possible for pairs with triplet symmetry, some of them compare well with experimental observation but caution must be taken as the triplet pairing is not justified a priori here.

### 4.4.1 Hall conductivity

To discuss the effect of magnetic field, at first order in  $H$ , we calculate the Hall conductivity which is given by

$$\sigma_{xy}^{(1)} = \frac{iH}{\omega_n} T \sum_{\varepsilon_n} \frac{1}{L} \sum_{\mathbf{q}} [q_x \mathcal{D}(\varepsilon_n, \mathbf{q}) \partial_{q_x} \mathcal{D}(\varepsilon_n + \omega_n, \mathbf{q}) - q_y \mathcal{D}(\varepsilon_n, \mathbf{q}) \partial_{q_y} \mathcal{D}(\varepsilon_n + \omega_n, \mathbf{q})]. \quad (4.68)$$

For a particle-hole symmetric theory, the Hall conductivity is naturally expected to vanish. This means that the incoherent bosons at finite- $\mathbf{Q}$  do not contribute to the Hall conductivity. Using the fact that  $\partial_{q_x} \mathcal{D}(x) = q_x \mathcal{D}^2(x)$ , only the wave-vector near  $q_x = Q_0$  will contribute. As a result, we obtain

$$\sigma_{xy}^{(1)}(\omega_n) = \frac{iHQ_0^2}{\omega_n} T \sum_{\varepsilon_n} \frac{1}{L} \sum_{\mathbf{q}} [\mathcal{D}(\varepsilon_n, \mathbf{q}) \mathcal{D}^2(\varepsilon_n + \omega_n, \mathbf{q}) - \mathcal{D}^2(\varepsilon_n, \mathbf{q}) \mathcal{D}(\varepsilon_n + \omega_n, \mathbf{q})]. \quad (4.69)$$

Performing the Matsubara summation by using spectral functions, we arrive at

$$\sigma_{xy}^{(1)}(\omega) = \frac{iHQ_0^2}{L} \sum_{\mathbf{q}} \int_{-\infty}^{\infty} \frac{dE_1}{2\pi} \frac{dE_2}{2\pi} \frac{n_B(E_1) - n_B(E_2)}{\omega(E_1 - E_2 + \omega)} \left( \mathcal{A}(E_1, \mathbf{q}) \tilde{\mathcal{A}}(E_2, \mathbf{q}) - \tilde{\mathcal{A}}(E_1, \mathbf{q}) \mathcal{A}(E_2, \mathbf{q}) \right), \quad (4.70)$$

where  $\mathcal{A}(E, \mathbf{q})$  is given in Eq.(4.26) and the  $\tilde{\mathcal{A}}(E, \mathbf{q})$  is given by

$$\tilde{\mathcal{A}}(q, E) = -2\text{Im} [\mathcal{D}_R^2(E, \mathbf{q})] = -\frac{4\gamma E(q^2 + \mu)}{(\gamma E)^2 + (q^2 + \mu)^2}. \quad (4.71)$$

Therefore, taking the  $\omega \rightarrow 0$ , the expression for the Hall conductivity becomes

$$\sigma_{xy}^{(1)}(0) = \frac{iHQ_0^2}{L} \sum_{\mathbf{q}} \int_{-\infty}^{\infty} \frac{dE_1}{2\pi} \frac{dE_2}{2\pi} \mathcal{A}(E_1, \mathbf{q}) \tilde{\mathcal{A}}(E_2, \mathbf{q}) \left[ \frac{\coth(\frac{E_1}{2T}) - \coth(\frac{E_2}{2T})}{(E_1 - E_2)^2} \right]. \quad (4.72)$$

This can be trivially shown to be exactly zero by noting that the  $\mathcal{A}(E, \mathbf{q})$ ,  $\tilde{\mathcal{A}}(E, \mathbf{q})$  and  $\coth(E)$  are all anti-symmetric functions with respect to  $E$ . Since  $I(-E_1, -E_2) = -I(E_1, E_2)$ , as a consequence, the incoherent bosons will have a vanishing Hall conductivity.

#### 4.4.2 Polarization bubble due to the Zeeman field

Because the incoherent bosons are formed from particle-particle pairs, the presence of an external magnetic field will also affect the mass term  $\mu$ . We compute this renormalization of the mass in the same way as in Sec.4.2.3 by looking at the polarization bubble. We show here that the spin symmetry of the pairs changes drastically the result.

##### Singlet Case

We start by looking at the self-energy contribution due to the Zeeman term for singlet particle-particle pairs. The correction to the mass term is given by

$$\Pi(H, \mathbf{Q}_0) = \frac{g_I^2}{L} \sum_k T \sum_{\varepsilon_n} [\mathcal{G}(-\varepsilon_n, \epsilon_{-\mathbf{k}, \uparrow}) \mathcal{G}(\varepsilon_n, \epsilon_{\mathbf{k}+\mathbf{Q}_0, \downarrow}) - \mathcal{G}(-\varepsilon_n, \epsilon_{-\mathbf{k}, \downarrow}) \mathcal{G}(\varepsilon_n, \epsilon_{\mathbf{k}+\mathbf{Q}_0, \uparrow})], \quad (4.73)$$

where  $\epsilon_{\mathbf{k},\sigma} = k^2 - \sigma H$  where  $\sigma = \pm 1$ . Next, performing the Matsubara summation over  $\varepsilon_n$ , we arrive at the expression which is independent of magnetic field. The mass term thus becomes

$$\mu = \mu_0 + \mu_T, \quad (4.74)$$

where  $\mu_T = \tilde{g}_b T \log(\gamma T / \mu_0)$ . So the mass-term has no contribution from the Zeeman field.

### Triplet Case

Here, we calculate the self-energy correction due to the bosons formed with paired electrons of triplet spin-symmetry. The corresponding expression is given by

$$\Pi(H, \mathbf{Q}_0) = \frac{g_I^2}{L} \sum_{\mathbf{k}} T \sum_{\varepsilon_n} \mathcal{G}(-\varepsilon_n, \epsilon_{-\mathbf{k},\uparrow}) \mathcal{G}(\varepsilon_n, \epsilon_{\mathbf{k}+\mathbf{Q}_0,\uparrow}), \quad (4.75)$$

where again  $\epsilon_{\mathbf{k},\sigma} = k^2 - \sigma H$  where  $\sigma = \pm 1$ . Performing the  $\varepsilon_n$ -summation, we get

$$\Pi(H, \mathbf{Q}_0) = \frac{g_I^2}{L} \sum_{\mathbf{k}} \left\{ \frac{1 - n_F(\epsilon_{\mathbf{k}} - H) - n_F(\epsilon_{\mathbf{k}+\mathbf{Q}_0} - H)}{\epsilon_{\mathbf{k}+\mathbf{Q}_0} + \epsilon_{\mathbf{k}} - 2H} \right\}. \quad (4.76)$$

Next, using a flat band approximation, we can write the momentum summation in the following form

$$\Pi(H, \mathbf{Q}_0) = \frac{\mathcal{N}(\epsilon_F) g_I^2}{4\pi^2} \int_0^{2\pi} d\theta \int_0^\Lambda d\epsilon \frac{\tanh(\frac{\epsilon+\zeta-H}{2T}) + \tanh(\frac{\epsilon-H}{2T})}{2\epsilon + \zeta - 2H}, \quad (4.77)$$

where  $\Lambda$  is the largest energy scale of the system. Additionally, we have substituted  $\zeta \equiv Q_0^2 + 2k_F Q_0 \cos(\theta)$ . Now at  $T \rightarrow 0$ , we will use that  $\tanh(x/T) \rightarrow \text{sgn}(x)$  and then performing the  $\epsilon$ -integral we arrive at

$$\Pi(H, \mathbf{Q}_0) = \frac{\mathcal{N}(\epsilon_F) g_I^2}{4\pi^2} \int_0^{2\pi} d\theta \begin{cases} \log\left(1 - \frac{2H}{\zeta}\right) + \log\left(-\frac{\zeta + 2\Lambda - 2H}{\zeta}\right) & \text{for } \zeta \leq 0, \\ \log\left(\frac{\zeta + 2\Lambda - 2H}{\zeta}\right) & \text{for } \zeta > 0 \text{ and } H - \zeta \leq 0. \end{cases} \quad (4.78)$$

Recall that  $\Lambda$  is the ultraviolet energy cutoff, and hence, expanding in  $H \ll 2k_F Q_0 \ll \Lambda$ , we get

$$\Pi(H, \mathbf{Q}_0) = C - \frac{\mathcal{N}(\epsilon_F) g_I^2}{4\pi^2} \int_{p_1}^{2\pi-p_1} d\theta \frac{2H}{Q_0^2 + 2k_F \cos(\theta)}, \quad (4.79)$$

where  $p_1 \equiv \cos^{-1}(Q_0/(2k_F))$  and  $C$  is the  $H$ -independent constant. Now integrating over  $\theta$ , one

obtains

$$\Pi(H, \mathbf{Q}_0) = C + \frac{2\gamma}{\pi} \coth^{-1} \left( \frac{2k_F + Q_0}{\sqrt{4k_F^2 - Q_0^2}} \right) H, \quad (4.80)$$

where we have used the definition of  $\gamma$  from Eq.(4.16).

The constants can be absorbed in the bare bosonic mass,  $\mu_0$ . Therefore, the total bosonic mass renormalization due to the Zeeman field  $H$ , becomes

$$\mu = \mu_0 + \mu_T + \alpha H, \quad (4.81)$$

where  $\alpha \equiv \frac{2\gamma}{\pi} \coth^{-1} \left( \frac{2k_F + Q_0}{\sqrt{4k_F^2 - Q_0^2}} \right)$  and we also define  $\mu_H \equiv \alpha H$ . Thus, we obtain the mass-renormalization due to the Zeeman field, which is used to evaluate magnetoresistance in the next section.

### 4.4.3 Magnetoresistance

In this section, we explicitly show the calculations to arrive at the magnetoresistance for incoherent bosons. The magnetoresistance quantifies the change of resistance due to the application of the magnetic field and is given by

$$\frac{\Delta\rho_{xx}(H)}{\rho_{xx}(H=0)} = \frac{\rho_{xx}(H) - \rho_{xx}(0)}{\rho_{xx}(0)}. \quad (4.82)$$

The complete resistivity tensor in terms of the conductivity is written as

$$\rho_{xx} = \frac{\sigma_{xx}}{\sigma_{xx}^2 + \sigma_{xy}^2}. \quad (4.83)$$

Notice that, for incoherent transport, we have shown in Sec.4.4.1 that  $\sigma_{xy} = 0$  and hence the expression for the magnetoresistance in terms of conductivity simply reads

$$\frac{\Delta\rho_{xx}(H)}{\rho_{xx}(H=0)} = \frac{\sigma_{xx}(0) - \sigma_{xx}(H)}{\sigma_{xx}(H)}. \quad (4.84)$$

Next, the expression for  $\sigma_{xx} = \sigma_{xx}^{(0)} + \sigma_{xx}^{(2)}$  where  $\sigma_{xx}^{(0)}$  is already calculated in Eq.(4.59). We are thus left with the computation of the second moment of the conductivity  $\sigma_{xx}^{(2)}$ .

#### Second Moment of Conductivity

The second moment of the conductivity, the term proportional to the square of the field strength  $H$ , is given in terms of the bosonic Green's function by

$$\sigma_{xx}^{(2)}(\omega_n) = -\frac{H^2}{\omega_n} \text{Im} \left[ T \sum_{\varepsilon_n} \frac{1}{L} \sum_{\mathbf{q}} \partial_{q_y} \mathcal{D}(\varepsilon_n, \mathbf{q}) \partial_{q_y} \mathcal{D}(\varepsilon_n + \omega_n, \mathbf{q}) \right].$$

Using the form of bosonic propagator  $\mathcal{D}(\omega_n, \mathbf{q})$ , we obtain

$$\sigma_{xx}^{(2)}(\omega_n) = -\frac{4Q_0^2 H^2}{\omega_n} \text{Im} \left[ T \sum_{\varepsilon_n} \frac{1}{L} \sum_{\mathbf{q}} \mathcal{D}^2(\varepsilon_n, \mathbf{q}) \mathcal{D}^2(\varepsilon_n + \omega_n, \mathbf{q}) \right]. \quad (4.85)$$

The spectral function in Eq.(4.71) is used to perform the Matsubara summation over  $\varepsilon_n$ . After analytical continuation, the real part of the second moment of conductivity becomes

$$\sigma_{xx}^{(2)}(\omega_n) = -\frac{4Q_0^2 H^2}{\omega_n L} \sum_{\mathbf{q}} \int_{-\infty}^{\infty} dE_1 \tilde{\mathcal{A}}(E_1, \mathbf{q}) \tilde{\mathcal{A}}(E_1 + \omega, \mathbf{q}) \frac{\partial n_B}{\partial E_1}. \quad (4.86)$$

The Bose function is approximated by Eq.(4.30) and the momentum summation is carried out by replacing  $(q^2 + \mu) = t$ , i.e.,

$$\sigma_{xx}^{(2)}(\omega \rightarrow 0) = -\frac{4TQ_0^2 H^2}{\pi^2} \int_{\mu}^{\infty} t^2 dt \int_{-\infty}^{\infty} dE_1 \frac{\gamma^2}{\{(\gamma E_1)^2 + t^2\}}. \quad (4.87)$$

Finally, performing the integral over  $E_1$  and  $t$ , and then by expanding in the two familiar limits, we obtain the expression for the real part of static second moment of conductivity

$$\sigma_{xx}^{(2)} = \begin{cases} \frac{8\gamma^2 Q_0^2 T^2 H^2}{5\pi^2 \mu^5} & \text{for } \gamma T \ll \mu, \\ \frac{5T\gamma Q_0^2 H^2}{16\pi \mu^4} & \text{for } \gamma T \gg \mu. \end{cases} \quad (4.88)$$

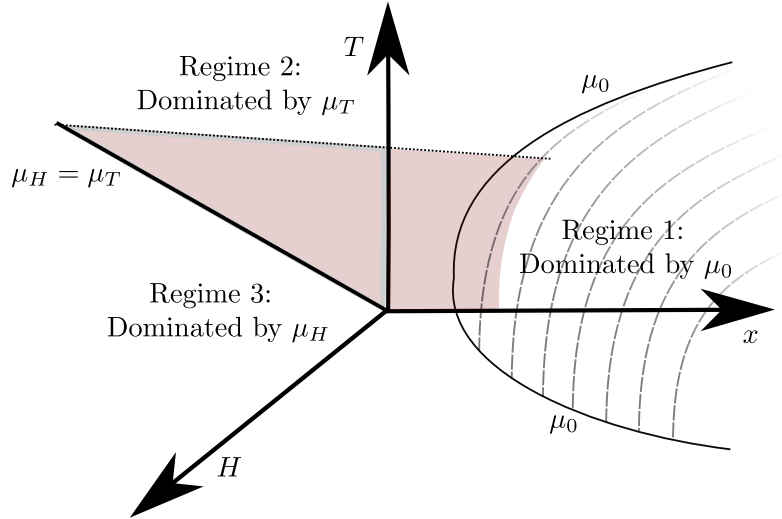


**Figure 4.6:** The figure illustrates the different regimes in the temperature, doping and magnetic field plane. The mass term renormalization for the particle-particle pairs is given by  $\mu = \mu_0 + \mu_T + \mu_H$ . The maximum of the three mass scales determines the regime: In regime 1, the mass is dominated by  $\mu_0$  while in regime 2 and 3 it is dominated by  $\mu_T$  and  $\mu_H$ , respectively. Adapted from Ref.[284].

We now have all the ingredients to understand the change of in magnetoresistance with fields. Indeed, the bosonic mass correction due to the Zeeman field is evaluated in Eq.(4.81). Similarly, the expressions for  $\sigma_{xx}^{(0)}$  in terms of  $\mu$  are evaluated in Eq.(4.61) and the same for  $\sigma_{xx}^{(2)}$  are evaluated

in Eq.(4.88). Notice we have different regimes depending on the renormalization of the mass term from bosonic interactions and the Zeeman field. These regimes are illustrated in Fig.4.6 in the magnetic field, hole doping and temperature plane. The different scenarios arise because the mass term is either dominated  $\mu_0$ ,  $\mu_T$  or  $\mu_H$ . We elaborate on the different possibilities one by one in the following while focusing on the case of triplet symmetry as it induces an additional magnetic field dependence as opposed to the singlet symmetry case.

$$\tilde{g}_b \geq \gamma \text{ and } \mu_T \ll \mu_H$$

First, if the interaction between the bosons is larger than the Landau damping coefficient, i.e.,  $\tilde{g}_b > \gamma$ , we are always in  $\gamma T \ll \mu$ . Additionally, if we are in a regime dominated by the magnetic field scale, i.e.,  $\mu_T \ll \mu_H$  (see regime 3 in Fig.4.6), the mass correction coming from the Zeeman field is given by  $\mu = \mu_0 + \mu_T + \alpha H$  in Eq.(4.81). Therefore, the magnetoresistance evaluates to

$$\frac{\Delta\rho_{xx}(H)}{\rho_{xx}(0)} = \frac{\frac{Q_0^2}{4\pi^2(\mu_0 + \mu_T)} - \frac{Q_0^2}{4\pi^2(\mu_0 + \mu_T + \alpha H)} - \sigma_{xx}^{(2)}(H)}{\frac{Q_0^2}{4\pi^2(\mu_0 + \mu_T + \alpha H)} + \sigma_{xx}^{(2)}(H)}. \quad (4.89)$$

If we take the limit  $\gamma T/\mu \ll 1$  in Eq.(4.88), it is clear that the  $\sigma_{xx}^{(2)}$  becomes negligible. Therefore, the equation for MR becomes

$$\begin{aligned} \frac{\Delta\rho_{xx}(H)}{\rho_{xx}(0)} &\approx \frac{1}{\mu_0 + \mu_T} - \frac{1}{(\mu_0 + \mu_T + \alpha H)}, \\ &\frac{1}{\mu_0 + \mu_T + \alpha H}, \\ \frac{\Delta\rho_{xx}(H)}{\rho_{xx}(0)} &= \frac{\alpha}{\mu_0 + \mu_T} H. \end{aligned} \quad (4.90)$$

Therefore, we obtain a linear-in- $H$  magnetoresistance in the regime 3 of Fig.4.6. Note that  $\mu_H \gg \mu_T$  can be interpreted as  $H \gg \eta T$ , where  $\eta = \frac{\mu_0 + \tilde{g}_b \log(\gamma T/\mu_0)}{\alpha}$ . Thus up to logarithmic corrections  $\eta$  is just a constant. We emphasize that this a similar high-field regime where linear-in- $H$  magnetoresistance is observed experimentally in high field [253].

$$\tilde{g}_b \geq \gamma \text{ and } \mu_T \gg \mu_H$$

Secondly, we still keep the interaction between the bosons stronger than the Landau damping coefficient, i.e.,  $\tilde{g}_b > \gamma$ . However, if the temperature-correction is larger than the magnetic field scale, i.e.,  $\mu_T \gg \mu_H$ , the mass correction coming from the Zeeman field is independent of the field and is given by  $\mu = \mu_0 + \mu_T$  (see regime 2 in Fig.4.6). Consequently, the evaluation of magnetoresistance becomes

$$\frac{\Delta\rho_{xx}(H)}{\rho_{xx}(0)} \approx \frac{\kappa}{\beta} H^2, \quad (4.91)$$

where  $\frac{\kappa}{\beta} \equiv -\frac{32\gamma^2 T^2}{5(\mu_0 + \mu_T)^4}$ . Again for  $\mu_H \ll \mu_T$  can be written as  $H \ll \eta T$ . Therefore, in the low-field regime, we obtain a quadratic  $H$ -dependence of magnetoresistance.

$\tilde{g}_b \geq \gamma$  for  $\mu_T \ll \mu_0$  and  $\mu_H \ll \mu_0$

Similarly, if the temperature or field correction of the bosonic mass term is smaller than the bare bosonic mass, i.e.,  $\mu_T \ll \mu_0$  and  $\mu_H \ll \mu_0$ , the mass correction coming from the Zeeman field is independent of the field and is given by  $\mu = \mu_0$  (see regime 1 in Fig.4.6). Again, the magnetoresistance becomes

$$\frac{\Delta\rho_{xx}(H)}{\rho_{xx}(0)} \approx \frac{\kappa}{\beta} H^2, \quad (4.92)$$

here we get  $\frac{\kappa}{\beta} \equiv -\frac{32\gamma^2 T^2}{5\mu_0^4}$ . So again we have a  $H^2$ -dependence of magnetoresistance in the regime 1 of Fig.4.6. In this regime we have already established the conventional Fermi liquid behavior when discussing the static conductivity in Sec.4.3.

Therefore, when the interaction between the bosons is stronger than the Landau damping coefficient the MR is given by

$$\frac{\Delta\rho_{xx}(H)}{\rho_{xx}(0)} = \begin{cases} \frac{\kappa}{\beta} H^2 & \text{in regimes 1 and 2,} \\ \frac{\alpha}{\mu_0 + \mu_T} H & \text{in regime 3,} \end{cases} \quad (4.93)$$

where the coefficient  $\kappa/\beta$  is different in regimes 1 and 2. Notice that such an  $H$ -evolution of magnetoresistance is recently observed in overdoped cuprates [253].

To summarize this study, we showed that the presence of incoherent modulated particle-particle pairs can affect the transport properties of the system. We considered that these bosons interact with electrons, leading to a Landau damping form for the bosonic propagator, but that the electronic degrees of freedom are not strongly affected by this interaction. The bosons then contribute to a linear temperature dependence of the resistivity on top of the standard  $T^2$  dependence originating from the electrons. If the boson-boson interaction is stronger than the Landau damping parameter, we can thus observe two regimes with either  $T$  or  $T^2$  resistivity leading to a phase diagram schematically represented in Fig.4.5(a). The bosons also lead to an optical conductivity that follows the Drude law while they do not contribute to the Hall conductivity which fits the experimental observations of additional incoherent carriers in overdoped cuprates [248, 249]. Lastly, we showed that we can observe a crossover from a  $H^2$  to  $H$  dependence of the magnetoresistance with the field as observed experimentally [252, 253] but that this requires a triplet symmetry for the pairs which is not supported by any microscopic considerations. The main idea was to present a simple phenomenological understanding of the linear resistivity that may be more accessible than the standard SYK model or holographic approaches.

## Chapter 5

# Stacking fault in multi-layer graphene

This last chapter strays away from the rich case of cuprates to look at another playground where unconventional superconductivity has been observed. In particular, we are interested here in the case of multilayer graphene where lattice effects and impurities can drastically affect the electronic properties of the system. The results presented here are based on numerical tight-binding calculations that allow us to extract the eigenenergies and eigenfunctions of a non-interacting Hamiltonian. We start by presenting known results on the possibility for edge states and surface states due to the specificities of the honeycomb lattice in Sec.5.1. We then come to the new results on the study of stacking faults in multilayer graphene and how impurity states affect the electronic spectrum in Sec.5.2.

## 5.1 Lattice effects in the honeycomb lattice

### 5.1.1 Edge states with zigzag termination

In finite-size systems, the effect of the abrupt termination of the lattice can have strong consequences on the electronic properties [288, 289]. This is striking in graphene where, depending on the geometry of the edges, the density of states changes drastically. The two types of edges that are generally considered are called “zigzag” or “armchair” edges and are represented in Fig.5.1(a) and (b) respectively. The DOS for semi-infinite ribbons is plotted below the lattice schematic and shows finite oscillations away from  $\omega = 0$ . This is because breaking the translation symmetry along one direction means that we only have one momentum direction that is a good quantum number. The Hamiltonian can still be diagonalized in momentum space as explained in Sec.2.2.1 along the infinite direction but not along the finite one, leading to a one-dimensional dispersion with  $2N$  bands,  $N$  being the number of unit cells in the finite direction. The other notable aspect of the DOS is the large peak at  $\omega = 0$  in the zigzag case that is not present in the armchair case. This is due to localized states that appear at the edge of the zigzag ribbon. This result is to be contrasted with the vanishing DOS in the infinite graphene case where only linear band touching occurs at the Fermi level as we showed in Sec.2.2 (Fig.2.1(b)).



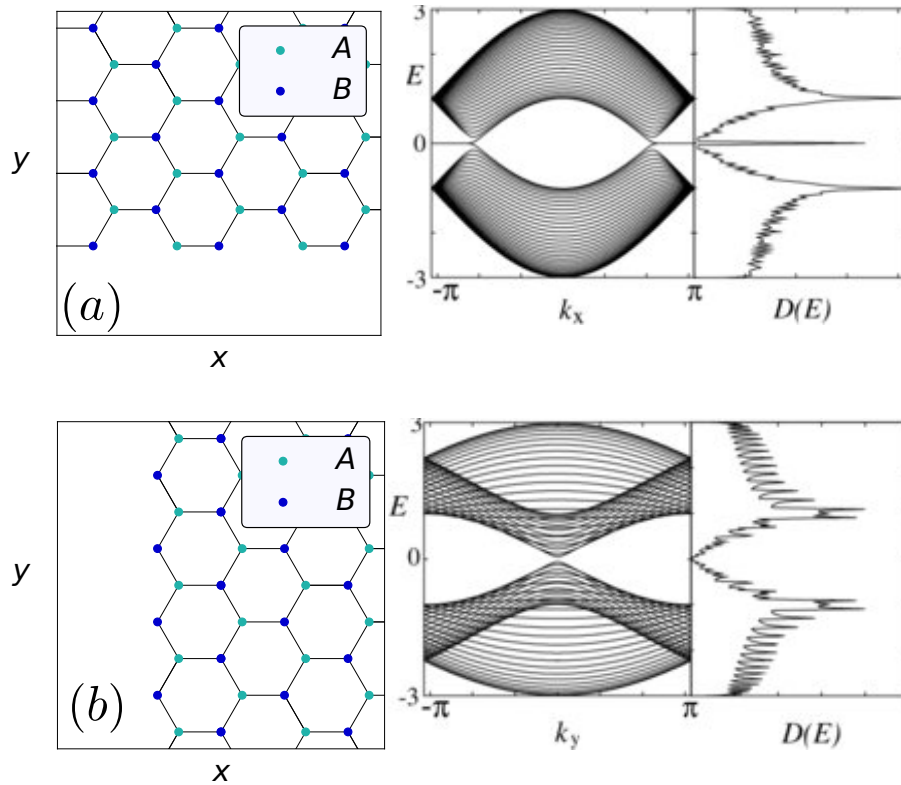


**Figure 5.1:** (a) Armchair termination for a finite size graphene layer. Both  $A$  and  $B$  sublattice atoms are on the edge. The density of states depends on the number of atoms in the perpendicular direction to the edge but shows a vanishing DOS at  $\omega = 0$  as in the infinite layer case. (b) Zigzag termination for a finite size graphene layer. The edge is made of only one sublattice. The density of states depends on the number of atoms in the perpendicular direction to the edge but shows a large increase of the DOS at  $\omega = 0$  indicating the presence of the edge state. DOS adapted from Ref.[287]

### 5.1.2 Surface state in ABC graphene

Another system where this phenomenon can be observed is by using the third dimension to create different termination. This is done in graphene by changing the way the successive graphene layers are stacked on top of one another. Because there are three nonequivalent positions in the triangular unit cell and two atoms per unit cell, there are three different stacking possible. When considering bilayer graphene, the only important choice is between stacking at the same positions in both layers (AA) or a stacking where the second layer is shifted with respect to the first one (AB). When looking at trilayer systems we have even more possibilities, but if we omit stacking with repeated positions in adjacent layers (that are thermodynamically disfavoured) we have once again two main options that are represented in Fig.5.2(a)-(d), one where all the layers have different positions (ABC) and one where the top and bottom layers are equivalent (ABA). Once again these two options have very different electronic properties that can be seen in the infinite two-dimensional plane. The tight-binding Hamiltonians for these trilayer honeycomb lattices are given by:

$$\mathcal{H}(\mathbf{k}) = t_0 \sum_{l=0,1,2} t(\mathbf{k}) c_{\mathbf{k},l,A}^\dagger c_{\mathbf{k},l,B} + h_{inter} + \text{h.c.}, \quad (5.1)$$

with

$$t(\mathbf{k}) = 1 + 2e^{-i\frac{3}{2}a_0k_x} \cos\left(\frac{\sqrt{3}}{2}a_0k_y\right), \quad (5.2)$$

$$h_{inter} = t_1 \left( c_{\mathbf{k},0,B}^\dagger c_{\mathbf{k},1,A} + c_{\mathbf{k},1,A}^\dagger c_{\mathbf{k},2,B} \right) \quad (5.3)$$

for ABA stacking and

$$h_{inter} = t_1 \left( c_{\mathbf{k},0,B}^\dagger c_{\mathbf{k},1,A} + c_{\mathbf{k},1,B}^\dagger c_{\mathbf{k},2,A} \right) \quad (5.4)$$

for ABC stacking. The operator  $c_{\mathbf{k},l,\alpha}^\dagger$  creates an electron on layer  $l$  and sublattice  $\alpha$ , and  $a_0$  is the distance between two neighboring atoms in a honeycomb lattice. In what follows, we take the two hopping parameters to be  $t_0 = 2.6 \text{ eV}$ ,  $t_1 = 0.34 \text{ eV}$ .

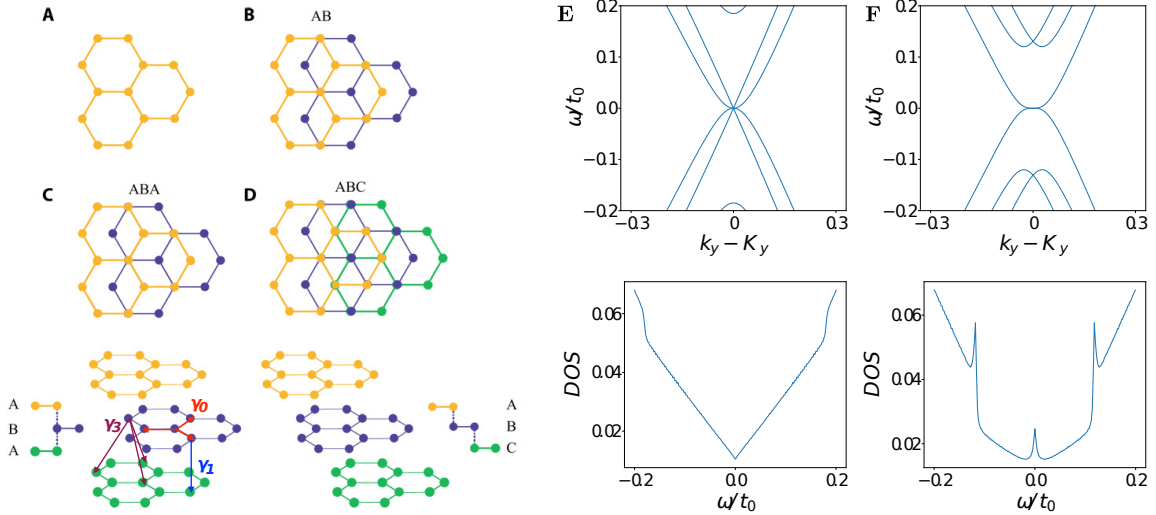


**Figure 5.2:** (A), (B), (C) and (D) How to obtain the two different stacking possibilities for trilayer graphene. The bottom part shows the different out-of-plane hopping and the spatial arrangement of the layer with respect to each other. Adapted from Ref.[290]. (E) Top panel, band structure for ABA graphene close to the Dirac point where we see a linear and quadratic band touching. The corresponding DOS is shown in the bottom panel with the characteristic  $V$ -shape and the vanishing DOS at  $\omega = 0$ . (F) Top panel, band structure for ABC graphene where we see the “flat” bands forming at low energy and touching at  $k_y - K_y = 0$ . The dispersion of these bands goes as  $(k_y - K_y)^N$  where  $N$  is the number of layers. The corresponding DOS (bottom panel) shows an increase in the DOS at  $\omega = 0$  with a  $V$ -shape dependence at higher energies. Note that the low-energy states are localized on the top and bottom layers of the stack. Adapted from Ref.[291]

The band structures obtained by diagonalizing these Hamiltonians are presented in Fig.5.2(e) and (f) for the ABA and ABC stacking respectively. We note that the band structure for the ABA trilayer graphene contains one pair of linear bands and one pair quadratic bands, while the ABC band structure contains two quasi-quadratic bands with an energy gap of about  $0.25t_0$  as well as a lower pair of bands which is not entirely quadratic but flattens close to the Dirac point with an energy dispersion going as  $(k_y - K_y)^3$  creating the precursor of a flat band. This plays an important role in differentiating ABA and ABC stacking in multilayer systems, as the general dispersion for ABC stacking is of the order  $k^N$  with  $N$  the number of layers. This leads to an

enhanced density of states at low energy compared to the ABA case (due to the “flat bands”). We can note that the larger the number of layers, the larger the flat region and its importance [292, 293] to the energy spectrum will be.

As we are working with non-interacting systems, the Matsubara Green’s function is simply given by as:  $G(\mathbf{k}, i\omega_n) = [i\omega_n - \mathcal{H}(\mathbf{k})]^{-1}$ , where  $\omega_n$  denote the Matsubara frequencies. In this study we will mainly be interested by the Density of States (DOS) obtained by integrating  $\mathcal{G}(\mathbf{k}, \omega)$  over the Brillouin zone.

$$DOS(\omega) = -\frac{1}{\pi} \int \frac{d\mathbf{k}}{(2\pi)^2} \text{Im Tr} \mathcal{G}(\mathbf{k}, \omega). \quad (5.5)$$

In the bottom part of Fig.5.2(e) and (f) we plot the DOS for the ABA and ABC trilayer graphene. Note that the DOS for the ABA graphene shows some quasi-V feature close to zero-energy due to the presence of the combination of the quadratic and the linear band, while the ABC graphene shows a small peak at zero-energy due to the incipient flat band, as well as cusps at energies corresponding to the end of the two quadratic bands.

## 5.2 Stacking fault in multi-layer graphene

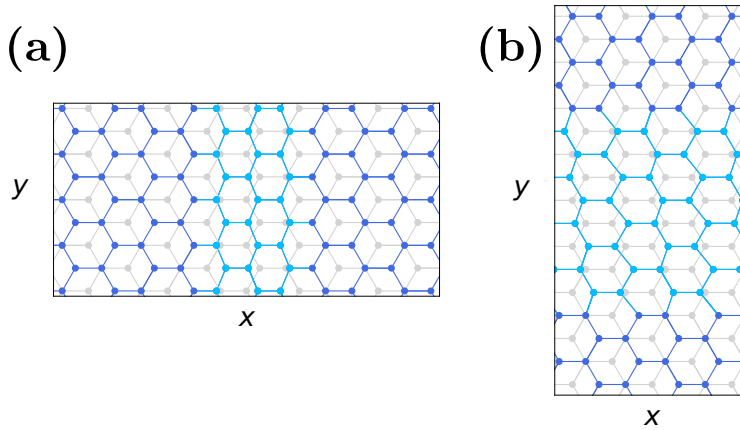


**Figure 5.3:** (a) Schematic representation of the top layer in a ribbon with a stacking fault that preserves the zigzag termination at its edges. We have an ABA stacking on the left side and an ABC stacking on the right side of the defect. (b) Schematic representation of the top layer in a ribbon with a stacking fault that preserves the armchair termination at its edges. We have an ABA stacking on the bottom side and an ABC stacking on the top side of the defect. Adapted from Ref.[291].

Another way of generating interesting localized states is by considering impurities or defects in the lattice structure. Because those effects generally break the translation symmetry, we will work either with one momentum quantum number (as in the zigzag/armchair ribbons example) or entirely in real space by the means of numerical diagonalization of the Hamiltonian. One example of localized impurity states can be found when considering the trilayer graphene systems mentioned previously. Because only the top layer is different between the ABA and ABC stacking orders, we

can consider a *stacking fault*, a defect shifting the top-most C layer to become an A layer. As in the case of the edge state discussed in Sec.5.1, the geometry of the stacking fault will play a role in the physical properties of the systems. We will study here stacking faults that conserve either the zigzag or the armchair termination that are represented in Fig.5.3(a) and (b) respectively. We will first focus on the ribbon geometry for each case before showing some results obtained from a finite-size system.

### 5.2.1 Ribbons with zigzag edges and interfaces

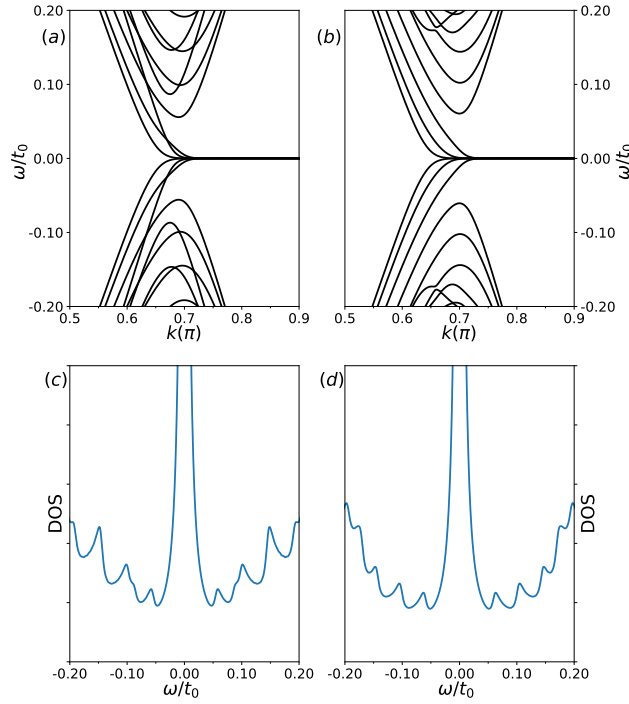


**Figure 5.4:** (a) and (c): Respectively, band structure and density of states for ABA ribbons with zigzag edges. (b) and (d): Respectively, band structure and density of states for ABC ribbons with zigzag edges. We use ribbons with a width of  $78 a_0$  and we consider a numerical broadening  $\eta = 2 \cdot 10^{-3} t_0$  for the density of states. In both cases, we see the presence of flat bands at  $k = \pi$  corresponding to the localized edge modes which give rise to a pronounced peak in the DOS at  $\omega = 0$ . Adapted from Ref.[291].

We start by considering a ribbon that is finite in one direction ( $x$ ) and infinite in the other ( $y$ ), with zigzag edges (see Fig.5.1(b)). Along the finite-size direction, the momentum is no longer a good quantum number and the continuous  $(k_x, k_y)$  band structure is replaced by a quantized set of bands. Thus in Fig.5.4 we plot the band structure of zigzag ABA and ABC ribbons. For the ABA structure, we see two types of quantized modes emerging from the linear and the quadratic band, while for the ABC one we can only see the quantized modes emerging from the lowest band.

It is also known that graphene ribbons with zigzag edges exhibit localized edge states. In a trilayer system, these states exist regardless of the stacking order as can be seen in Fig.5.4: for both ABA and ABC stacking we see that the band structure contains flat bands at zero energy. For each ribbon there are six of those bands, corresponding to the three layers and the two edges of each layer. These states are not topological and can for example move away from zero energy

when we apply an electric field.

The corresponding local DOS (LDOS) depicted in the lower panels of Fig.5.4 shows clearly the zero-energy edge-state peak, as well as the quantized structure of the band structure. Given the effective 1D character of the ribbons, each band will give rise to a peak in the LDOS at the energy corresponding to the bottom-of-the-band (Van Hove singularity) inflexion. This will yield a series of peaks in the LDOS, as visible in the bottom panel of Fig.5.4. The overall trend for the LDOS of the ABA/ABC ribbon is consistent with the LDOS for the infinite ABA/ABC trilayer depicted in Fig.5.2(e) and (f), i.e. a linear dispersion for the ABA ribbon, and a linear dispersion with a smaller slope for the ABC ribbon, jumping abruptly at  $\omega \approx 0.15t_0$ .

When we introduce a stacking fault (see Fig.5.3(a)), the band structure is perturbed, as can be seen in Fig.5.5. Note that because the defect is only localized in the top-most layer, there might be significant hybridization between the two different stacking regions through the bottom layers. Indeed, the bulk bands for the mixed system are no longer similar to the separate ABC/ABA bands but are fully modified by the presence of the defect. To separate the bands coming from the ABC and ABA bulks and those of the interface region we study the effect of the size of the ribbon on the band structure. The idea is that if we change the number of atoms in the bulk, features associated with the edges, as well as with the defect, should remain unchanged. Looking at Fig.5.5, we see that this is indeed the case for the flat bands around  $k = \pi$ . These flat bands can easily be identified with states localized on the edges of the ribbon. Moreover, we note that the lowest-energy bands exhibit a dispersion that is independent of the system size even away from the Dirac point. This size-independent band is peculiar and we argue that it is localized at the interface between the ABA and ABC regions.

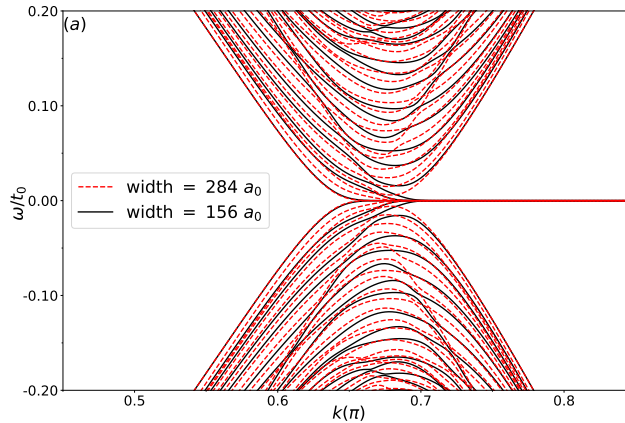


**Figure 5.5:** The band structure for a ribbon with a stacking fault, plotted for two different ribbon widths  $284a_0$  (dashed red) and  $156a_0$  (full black). The flat bands and the lowest-energy bands are independent of the width, while the bulk bands strongly depend on it. Adapted from Ref.[291].

To confirm this observation we study the spectral weight of the different bands as a function of the position on the ribbon. Fig.5.6(a) shows the spectral weight averaged over two unit cells in the stacking fault, while Fig.5.6(b) shows the averaged spectral weight for sites in the bulk on both the ABA and ABC sides of the ribbon. We see that the interface spectral weight is significantly larger for the lowest dispersing energy band, at both positive and negative energies. In contrast, the bulk spectral weight is rather equally distributed on the quantized multiple bands in the Dirac cone with a marked absence of weight on the flat band (localized at the exterior edges) and on the

lowest energy band (localized at the interface). This provides an extra indication that the bands we identified as size-independent are localized on the defect. It is also interesting to note that the situation is less clear for momenta close to the Dirac point where the spectral weight is once again evenly distributed (Fig.5.6(a)) and there are no signs of localized states.

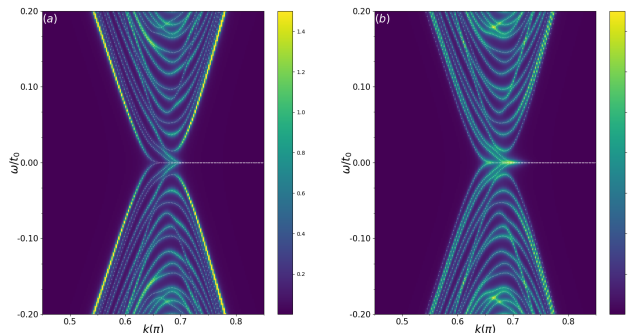


**Figure 5.6:** (a) The eigenstate spectral weight evaluated on sites in the stacking fault. There is a significant weight in the two lowest positive- and negative-energy bands, indicating that these states are localized on the defect. (b) Averaged spectral weight evaluated on sites in the bulk (average of ABA and ABC sides). The ribbon's width is  $156 a_0$  and we used a numerical broadening  $\eta = 3.10^{-3} t_0$ . Adapted from Ref.[291].

Lastly, we look for possible signatures of these states in the density of states as a function of position along the ribbon. We see in Fig.5.7(a) that the local density of states at zero energy is dominated by the edge states. This is due to the flat nature of the edge bands give which rise to a high density of states close to  $\omega = 0$ . This is localized both on the edge but also exhibits significant leaks in the bulk, for the not-too-large system size that we consider. To get a better understanding in Fig.5.7(a) we plot the LDOS as a function of energy in the stacking fault, as well as in the ABA and ABC regions. We thus note that the LDOS in the defect (the region between the white dashed lines in Fig.5.7(a)), as well as in the ABA and ABC regions far from the edges, does still present a significant peak at  $\omega = 0$  that is due to the zigzag edge modes. This makes it hard to separate for example the effect of the bulk ABC zero-energy flat band from that of the zigzag edges.

The dependence of the DOS in the defect on energy (green curve in Fig.5.7(b)) exhibits a roughly linear dependence on energy, similar to that of the bulk ABA region depicted in Fig.5.2; this is consistent with the fact that the defect's spectral weight is maximum on a pair of bands that disperse linearly away from  $k = 0$  (Fig.5.6(a)). These bands decay in intensity close to zero energy, consistent with the reduction in the LDOS of the defect at small energies, as shown in Fig.5.7(b). The bulk ABA preserves also a linear dependence (orange curve in Fig.5.7(b)), modulated by the finite-size effects. The ABC bulk LDOS (Fig.5.7(b) blue curve) also preserves the average ABC uniform bulk dependence depicted in Fig.5.2, i.e a linear dependence with a lower slope for  $0 < \omega < 0.15$  before increasing rapidly.

Note that the LDOS on the interface has roughly the same intensity as in the bulk, the interface does not seem to generate significant interface states localized at the position of the defect.

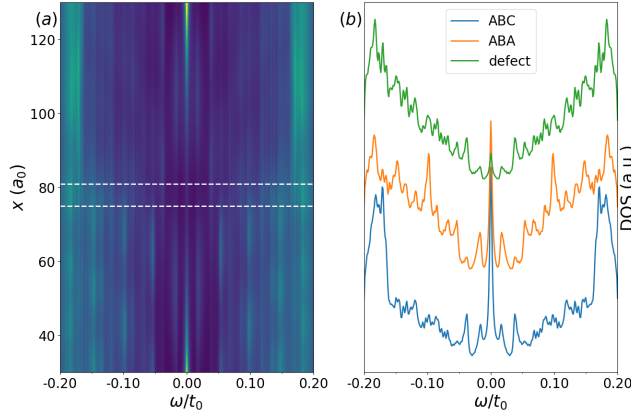


**Figure 5.7:** (a) Local density of states as a function of energy and position along the ribbon. The ABC region corresponds to  $x > 80$  (top of the picture), while the ABA region to  $x < 75$  (bottom of the picture). We left out the ribbon's edges where there is a high density of states due to the edge states in the zigzag geometry. The white dashed lines indicate the position of the stacking fault. (b) Density of states at specific sites. The DOS on the ABA ( $x = 39$ ) and ABC ( $x = 119$ ) sides are taken far from the defect ( $x = 78$ ), in the bulk. The ribbon's width is  $156 a_0$  for both figures. DOS lines are shifted for readability. We used a numerical broadening  $\eta = 2.10^{-3} t_0$ . Adapted from Ref.[291]

## 5.2.2 Ribbons with armchair edges and interfaces

We now perform the same analysis on ribbons with armchair edges. The geometry of the stacking fault is depicted in Fig.5.3(b). In the case of armchair ribbons, there are no edge states and the band structures for the two different stackings are shown in Fig.5.8(a) and (b). Compared to the zigzag case, there is a stronger contrast between the two band structures: for the ABA stacking the linearly-dispersing and the lowest quadratically-dispersing bands seem to be preserved even in the presence of the quantization. The band structure of the ABC-stacked ribbon seems to be affected also much less by the quantization, preserving the  $k^3$ -dispersing bands touching at  $\omega = 0$ ; we thus expect some reminiscence of the flat band signatures (such as a zero-energy peak in the DOS) in this type of geometry. Indeed, while both stackings give rise to zero-energy peaks due to the zero-energy van Hove singularities corresponding to the bottom-of-the-band inflections in the now effectively-1D energy bands, the one corresponding to the ABC stacking is more robust.

The band structure of a ribbon with a stacking fault and armchair edges is shown in Fig.5.9 for two different ribbon widths. Once again the band structure of the combined system cannot be directly traced back to the individual band structures for the ABA and ABC ribbons. Moreover, we can clearly see that the combined-system band structure is not symmetric with respect to  $\omega = 0$ . This symmetry is usually a consequence of the sublattice symmetry that exists in the honeycomb lattice and is broken here due to the particular shape of the impurity (see Fig.5.3(b)). Further studies would be required to fully understand the consequences of this potential explicit symmetry-breaking. The stacking fault gives rise to a distinct signature in the band structure: we can see the formation of two dispersing bands (one for positive and one for negative energies) which seem to be unaffected by the size of the system. This feature indicates that these may indeed be interface bands, and not bulk bands, same as in the zigzag ribbon case. These bands are once more the lowest in energy in the spectrum and have a relatively flat dispersion near  $k = 0$ .

Same as in the zigzag case we also calculate the spectral weight on sites located in the stacking



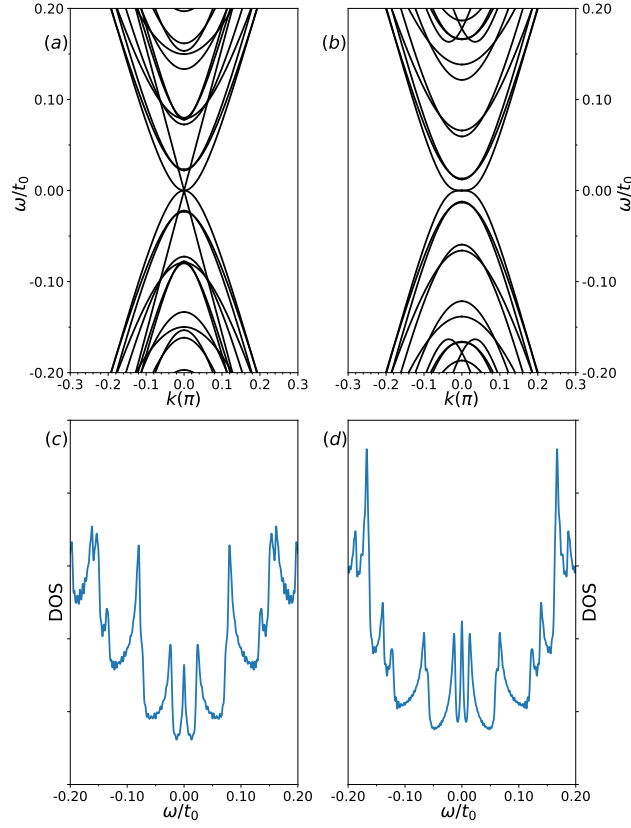


**Figure 5.8:** (a) and (c) Band structure and respectively density of states for ABA ribbons with armchair edges. (b) and (d) Band structure and respectively density of states for ABC ribbons with armchair edges. We used ribbons with a width of  $59 a_0$ , and a numerical broadening  $\eta = 2 \cdot 10^{-3} t_0$  for the density of states. Both stacking seem to exhibit a zero-energy peak in the LDOS, but the ABC stacking one is more robust due to the flatter dispersion around  $k = 0$ . Adapted from Ref.[291]

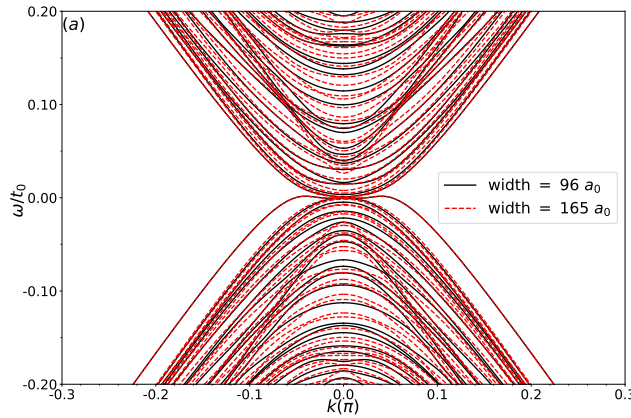


**Figure 5.9:** The band structure for an armchair ribbon with a stacking fault for two different ribbon widths. The lowest-energy dispersing bands are the same for the two different widths, while the bulk bands are different. Adapted from Ref.[291]

fault, and we compare it to the spectral weight in the bulk. This is shown in Fig.5.10: we can see that the interface spectral weight is localized most strongly on the two lowest positive- and negative-energy bands (Fig.5.10a). Moreover, segments from the central band, reminiscent of the linear ABA band, exhibit a very strong intensity at the ABA/ABC interface. On the other hand,



the spectral weight in the bulk (Fig.5.10b) seems evenly distributed, except on the lowest energy band which has very little weight, confirming that this band is an interface band and not a bulk band. We note the strong difference in the scale of the spectral weight between the two figures, indicating that the interface states have much more intensity than the bulk states.

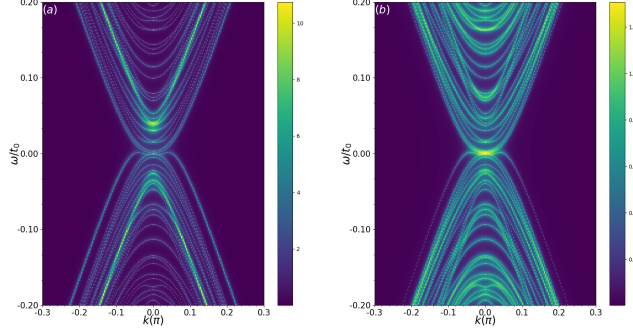


**Figure 5.10:** (a) The eigenstate spectral weight evaluated on sites in the stacking fault. There is a significant weight in the two lowest positive- and negative-energy bands, indicating that these states are localized on the defect. Moreover, reminiscent segments from the linear band arising for a clean ABC structure also shows a very strong intensity on the defect, however, this band is now gapped. (b) Averaged spectral weight evaluated on sites in the bulk (average of ABA and ABC sides). Note the large difference between the scales of the two figures indicating a strong intensity for the states localized on the defect. The ribbon's width is  $96 a_0$  and we used a numerical broadening  $\eta = 3 \cdot 10^{-3} t_0$ . Adapted from Ref.[291]

We also perform an analysis of the LDOS as a function of position (Fig.5.11(a)). This turns out to be very different from the case of the zigzag ribbon, as there are no zero-energy edge states and also there is a higher spectral weight for the states localized on the impurity. We note first that the LDOS in the ABA and the ABC bulk becomes also asymmetric between the positive and negative energies. The ABA LDOS (Fig.5.11(b) orange line) shows only small modifications from the previously studied situations (i.e a linear background plus quantized peaks, see Fig.5.8). The ABC bulk (Fig.5.11(b) blue line) also follows the structure in Fig.5.8, exhibiting a linear slope for  $0 < \omega < 0.15$  before increasing rapidly, as well as a strong zero-energy peak corresponding to the flat band, but with a more pronounced asymmetry between the positive and negative energies, and a reduction in the LDOS at small negative energies.

The averaged DOS in the defect (Fig.5.11(b) green line) shows a reduction in the LDOS around  $\omega = 0$ , and sharp peaks for positive energies  $\omega \approx 0.05$ . This is in agreement with the momentum space analysis (Fig.5.10(a)) where we can see that the spectral weight is maximum on a pair of gapped bands which are reminiscent of the linear ABA bands: the sharp peaks arise at the gap edge of these bands. We also see that the defect DOS is not symmetric with respect to  $\omega = 0$  as expected from the band structure in Fig.5.9. Also, we note the large intensity of the LDOS in the defect which persists at all energies.

### 5.2.3 Finite-size configuration

In this section, we consider instead of an infinite ribbon a finite-size ABA-ABC ribbon. Once again we look at systems with zigzag or armchair terminations, but with finite size in both the  $x$  and  $y$  directions. We thus expect a quantization of the continuous interface bands present in the infinite

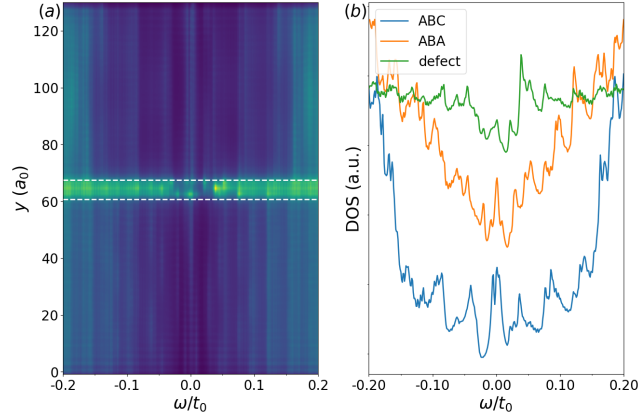


**Figure 5.11:** (a) Local density of states as a function of energy and position along the ribbon. The ABC region corresponds to  $y > 70$  (top of the picture), while the ABA region to  $y < 60$  (bottom of the picture). The white dashed lines indicate the position of the defect. (b) Density of states at specific sites. The DOS on the ABA ( $y = 31$ ) and ABC ( $y = 98$ ) sides are taken far from the defect, in the bulk. The DOS taken on the defect ( $y = 65$ ) is divided by 10 for scaling reasons. The ribbon's width is  $96 a_0$  for both figures. DOS lines are shifted for readability. We used a numerical broadening  $\eta = 2.10^{-3} t_0$ . Adapted from Ref.[291].

ribbon configurations and the appearance of quantized interface levels. Since there is no longer any good momentum quantum number there is no band structure to analyze, but only the LDOS as a function of energy and position.

We start by studying the case of zigzag edges. In Fig.5.12(a) we plot the LDOS as a function of energy along a cut perpendicular to the direction of the stacking fault. We observe some predominant features. First, we note that the edge states, localized at the exterior edges of the sample, continue to exhibit a strong spectral weight even in the finite configuration, this is expected from previous studies of graphene. We can see here that these states also penetrate quite significantly in the bulk ( $\sim 30a_0$ ). The second relevant feature is the formation of the quantized states localized at the ABA/ABC interface, these are just a result of the quantization of the interface bands observed in the previous section. Their intensity once more is not more significant than that of the bulk, indicating that the zigzag interface does not generate strongly localized interface states.

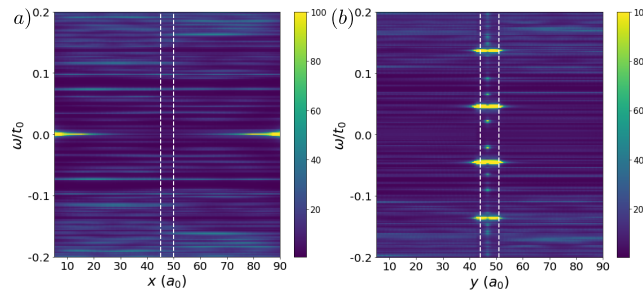


**Figure 5.12:** LDOS as a function of energy and position for a finite-size system with zigzag edges (a) and armchair edges (b). The white dashed lines indicate the position of the defect. The ABA region corresponds to  $x < 45$  (left of the stacking fault), while the ABC region to  $x > 50$  (right of the stacking fault). We used a numerical broadening  $\eta = 1.10^{-3} t_0$  and, for the zigzag ribbon, we have excluded the leftmost and rightmost edges. The length of the ribbons perpendicular to the impurity is  $95a_0$  while the width is  $35a_0$  in both geometries. Adapted from Ref.[291].

We now turn to the case of armchair edges, and in Fig.5.12(d) we plot the LDOS as a function of

energy and position along the  $y$  axis. Here we do not have any zero-energy modes as the armchair edges do not exhibit any localized states. We can see however very clearly the quantization of the energy levels in the stacking fault. The spectral weight associated with these localized states is higher than the spectral weight for delocalized states in the ABC or ABA bulk. This is in agreement with the results for the semi-infinite ribbon presented in Fig.5.11. The limited size for the bulk ABA and ABC stacking regions does not however allow us to have a good quantitative understanding of the low-energy DOS outside the impurity.

The physics of the impurity states can yield non-trivial results, especially when considering the topological properties of the resulting band structure when discrete symmetries are broken. An example is the theoretical and experimental study of topological edge state at AB/BA stacking faults in bilayer graphene [294–297]. Similarly, the topological properties of trilayer ABC graphene can be revealed by applying an electric field gradient between the different layers [298]. Aside from these topological properties, the presence of flat bands is an interesting prospect regarding the potential superconducting instability in these systems [299]. A simple way of understanding this is by considering the scaling of the kinetic energy that comes from the derivative of the dispersion with respect to the momentum at the Fermi level  $\left. \frac{\partial \epsilon_k}{\partial k} \right|_{k_F}$  which is reduced when the band shows a very low dispersion. This can allow for even small interactions to induce phase transitions as the ratio  $E_{interaction}/E_{kinetic}$  becomes more important and is thought to be one of the driving mechanisms in the recent superconducting state in twisted bilayer graphene [21, 22]. The increased density of states at the Fermi level is also an important factor that can favour ordered states such as superconductivity as we showed in the simple BCS approach in Sec.2.3.2. This preliminary study could thus be interesting in the context of the surge in experimental works that look at graphene systems as a platform for unconventional superconductivity.

# Conclusion

To summarize the main point of our new description of the pseudogap, it is important to emphasize the role played by the fractionalization compare to other theories. Indeed, the competition between the SC and the CDW orders is now well-known from the different experimental observations but we argue here that there is more to this relationship between the two orders. In our effective theory from Sec.3.1.2, we see that the competition we obtain is very strong with the local constraint between the two amplitudes. It is also important to note that this constraint is also obeyed by the fluctuations of the orders which are of crucial role in the pseudogap. Moreover, the phase-locking mechanism is a unique signature of our scenario and we suggest that it is at the origin of multiple experimental observations. First of all, the vortex experiment described in Sec.3.1.3 where the phase coherence of the charge order seems to be larger than expected from what is observed above  $T_c$ . Secondly, the phonon softening we studied in Sec.3.4 and which shows that the fluctuations of both the SC and CDW orders need to be quenched at the same time to explain the apparition of this softening at  $T = T_c$ . Lastly, the fluctuations also played a crucial role in describing the temperature dependence of the electronic spectral function in Sec.3.2. We can also note that the PDW order never condenses in our scenario even though it can be observed when both the SC and CDW order have a finite amplitude as their product would also be finite.

We also presented our study of the Strange metal phase in Chap.4 based on the idea that incoherent modulated particle-particle pairs can contribute to the transport properties of the system in the overdoped regime. These incoherent pairs would be related to the PDW which is fractionalized at lower doping but the idea of incoherent carriers was already put forward from the available experimental data. The main reason for the linear-in-T resistivity in our scenario is the Landau damping due to the boson-fermion scattering and the renormalization of the mass of the bosons due to the boson-boson interaction as shown in Sec.4.2. This allows us to obtain in Sec.4.3 a linear temperature dependence for the static conductivity and, when the boson-boson interaction is stronger than the Landau damping, a Drude form for the optical conductivity. These bosons do not however contribute to the Hall conductivity which is in agreement with the loss of Hall carriers observed experimentally. The  $H$  to  $H^2$  scaling to the magnetoresistance can also be recovered if we allow for a triplet symmetry for the pairs as discussed in Sec.4.4. This is a phenomenological model which is simpler than a lot of the other strong coupling theories that have been used to attempt to describe the strange metal phase. It is strongly tied to our description of the pseudogap and could however be difficult to apply to other materials where the same anomalous transport properties are observed.

We can also note that our idea of fractionalization of an order parameter is not unique in the

field of cuprates. In fact, it was recently proposed that the fractionalization of Spin Density Waves [117] could occur outside the antiferromagnetic state, leading to the formation of the pseudogap. In this case, the resulting effective theory is an  $SU(2)$  gauge theory where the Higgs fields are massive which impacts the electronic degrees of freedom. This bears a strong resemblance to our effective theory from Sec.3.1.2, especially when seen from the point of view of a gauge theory as presented in App.A. The idea that the PDW is responsible for the pseudogap is also discussed in other theoretical scenarios as we mentioned in Sec.1.4.3 and our idea is thus at the crossing between the two types of thinking.

The work presented here is based on strong assumptions for the fractionalization which should inherently be a strong coupling phenomenon and that we treated in a mean-field way in most of our work. We think that this is sufficient to give an idea of the consequences of the fractionalization on the electronic and phononic degrees of freedom. It can however be argued that this is not enough to justify the whole setup. To answer such deserved critique, there is a more recent work that proposed to use the Josephson effect [284] to probe the phase relation that is unique to our idea. Observation of this signature would set apart our theory as the phase-locking is a very peculiar effect not present in other widely spread theories. This also showcases the predictive power that our effective theory has. In fact, the constraint on the amplitude *and* on the phase should appear in many different situations and we should now ask what is the correct experiment to confirm or dismiss the theory altogether.

# Appendix A

## The $U(1) \times U(1)$ theory

In this appendix, we show how the constraint between the phase and the amplitude degree of freedom we obtain in our effective theory for the pseudogap can be seen as a consequence of the gauge structure of our ansatz. We start by considering a general action for two complex fields with their respecting gauge degree of freedom,

$$\begin{aligned} \mathcal{S} &= \int d^d x |D_\mu z_1|^2 + |\tilde{D}_\mu z_2|^2, \\ D_\mu &= \partial_\mu - i f_\mu, \quad \tilde{D}_\mu = \partial_\mu - i \tilde{f}_\mu. \end{aligned} \quad (\text{A.1})$$

If we identify the two complex field with our previous order parameters  $z_1 = \Delta_{ij}$  and  $z_2 = \chi_{ij}$  and their respective gauge degree of freedom  $f_\mu = 2A_\mu + \alpha_\mu$  and  $\tilde{f}_\mu = \alpha_\mu$  we can rewrite this action with the spinor

$$\Psi_{ij}^\dagger = (|\Delta_{ij}|e^{i\theta_\Delta}, |\chi_{ij}|e^{i\theta_\chi}) = e^{i\theta} e^{i\tau_z \phi} (|\Delta_{ij}|, |\chi_{ij}|), \quad (\text{A.2})$$

where we have made apparent the global ( $\theta$ ) and the relative ( $\phi$ ) phase between the two component of the spinor and used the third Pauli matrix  $\tau_z$ . We thus end up with an action,

$$\begin{aligned} \mathcal{S} &= \int d^d x |D_\mu \Psi_{ij}|^2 + V(\Psi_{ij}, \Psi_{ij}^\dagger), \\ D_\mu &= \partial_\mu - i a_\mu - i \tau_z b_\mu. \end{aligned} \quad (\text{A.3})$$

where the gauge fields refer this time to the global and relative phases of the spinor and are associated to the following transformations

$$\begin{aligned} \Psi_{ij} &\rightarrow e^{i\theta} \Psi_{ij} & a_\mu &\rightarrow a_\mu + i\partial_\mu \theta, \\ \Psi_{ij} &\rightarrow e^{i\tau_z \phi} \Psi_{ij} & b_\mu &\rightarrow b_\mu + i\partial_\mu \phi. \end{aligned} \quad (\text{A.4})$$

We can also directly relate this new gauge fields to the previous ones

$$a_\mu = A_\mu + \alpha_\mu, \quad b_\mu = A_\mu. \quad (\text{A.5})$$

The action Eq.(A.3) is generic and we didn't impose any constraint between the two fields  $\Delta_{ij}$  and  $\chi_{ij}$  in Eq.(A.3) up to now, this results in the two gauge fields fluctuating.

It is now possible to imagine that a Higgs mechanism will take place at  $T^*$ , freezing one of the phase and giving a mass to the corresponding gauge field. Applying this idea to the global phase  $\theta$  will lead to a mass for the  $a_\mu$  gauge field equal to the spinor amplitude, i.e

$$m_a = |\Psi_{ij}|^2 = \sqrt{|\Delta_{ij}|^2 + |\chi_{ij}|^2} := E^*. \quad (\text{A.6})$$

Hence, we recover a constraint by minimizing the action with respect to a gauge field. We already discussed this phenomenon in the description of the fractionalization of the electronic degree of freedom in Sec.2.4.2. The Lagrange multiplier that was introduced to enforce the constraint on the spinons and holons was identified with a gauge field and integrating over this Lagrange multiplier will realize the constraint exactly. Here we took the reverse path to consider a Higgs mechanism that will freeze the global phase of our spinor and which leads, when the gauge field is integrated out, to a constraint between the amplitudes of the two fields. We end up with a theory of two amplitudes  $|\Delta_{ij}|$ ,  $|\chi_{ij}|$ , linked by a constraint, and one phase  $\phi$  fluctuating. Note that in the case of fractionalization, one of the gauge fields that appears in this theory is *fictitious* as it is not linked to any physical symmetry. The Higgs mechanism here is thus not related to any physical symmetry breaking in contrast to the second transition that could occur when the second phase is frozen which will be equivalent to a standard superconducting transition. This is equivalent, in the pseudogap, to the  $CP^1$  model presented in Sec.3.1.2.

## Appendix B

# CDW gap equation

In this appendix, we show how to get a self-consistent gap equation for the charge order gap from Chap.3. We recall the equation we obtained by minimizing the effective action Eq.(3.32)

$$\chi_{\mathbf{k}} = \frac{-1}{\beta N} \sum_{\mathbf{q}, n}^{|q| < q_{AF}} \frac{J_+ \chi_{\mathbf{k}+\mathbf{q}+\mathbf{Q}_{AF}}}{(i\omega_n + \epsilon_{\mathbf{k}+\mathbf{q}+\mathbf{Q}_{AF}})(i\omega_n + \epsilon_{\mathbf{k}+\mathbf{q}+\mathbf{Q}+\mathbf{Q}_{AF}}) - \chi_{\mathbf{k}+\mathbf{q}+\mathbf{Q}_{AF}}^2}. \quad (\text{B.1})$$

Similarly to the procedure in Sec.3.2.2, we now use the self-consistent equation Eq.(B.1) to express  $\chi_{\mathbf{k}+\mathbf{q}+\mathbf{Q}_{AF}}$  as a function of  $\chi_{\mathbf{k}+2\mathbf{q}+2\mathbf{Q}_{AF}} \sim \chi_{\mathbf{k}+\mathbf{q}}$

$$\chi_{\mathbf{k}} = \frac{1}{(\beta N)^2} \sum_{\mathbf{q}, n}^{|q| < q_{AF}} \frac{J_+}{(i\omega_n + \tilde{\epsilon}_{\mathbf{k}+\mathbf{q}})(i\omega_n + \tilde{\epsilon}_{\mathbf{k}+\mathbf{q}+\mathbf{Q}}) - \tilde{\chi}_{\mathbf{k}+\mathbf{q}}^2} \sum_{\mathbf{q}', m}^{|q'| < q_{AF}} \frac{J_+ \chi_{\mathbf{k}+\mathbf{q}'}}{(i\omega_m + \epsilon_{\mathbf{k}+\mathbf{q}'}) (i\omega_m + \epsilon_{\mathbf{k}+\mathbf{q}'+\mathbf{Q}}) - \chi_{\mathbf{k}+\mathbf{q}'}^2}, \quad (\text{B.2})$$

where we introduced the notation  $f(\tilde{\mathbf{k}}) = f(\mathbf{k} + \mathbf{Q}_{AF})$ . We now makes the assumption that the width of the spin-spin correlation function being small in momentum space, the order parameter is constant in the region  $|\mathbf{q}'| < q_{AF}$  and that the integration over  $\mathbf{q}'$  and  $\mathbf{q}$  can be taken as independent. This allow us to simplify the order parameter in the numerator on both side and, after performing the analytical Matsubara summation we get

$$1 = \left(\frac{J_+}{N}\right)^2 \sum_{\mathbf{q}} \frac{n_f(\tilde{E}_{+, \mathbf{k}+\mathbf{q}}) - n_f(\tilde{E}_{-, \mathbf{k}+\mathbf{q}})}{\tilde{E}_{+, \mathbf{k}+\mathbf{q}} - \tilde{E}_{-, \mathbf{k}+\mathbf{q}}} \sum_{\mathbf{q}'} \frac{n_f(E_{+, \mathbf{k}+\mathbf{q}'}) - n_f(E_{-, \mathbf{k}+\mathbf{q}'})}{E_{+, \mathbf{k}+\mathbf{q}'} - E_{-, \mathbf{k}+\mathbf{q}'}}}, \quad (\text{B.3})$$

where the new dispersion differ from the superconductiviting case,

$$E_{\pm, \mathbf{k}} = \frac{1}{2} \left( \epsilon_{\mathbf{k}} + \epsilon_{\mathbf{k}+\mathbf{Q}} \pm \sqrt{(\epsilon_{\mathbf{k}} - \epsilon_{\mathbf{k}+\mathbf{Q}})^2 + 4\chi_{\mathbf{k}}^2} \right). \quad (\text{B.4})$$

We can then rewrite this in a form close to the BCS gap equation Eq.(2.45)

$$1 = \left(\frac{J_+}{4\pi^2}\right)^2 \int_{-q_{AF}/2}^{q_{AF}/2} dq \frac{\tanh\left(\frac{\beta}{2} \tilde{E}_{+, \mathbf{k}+\mathbf{q}}\right)}{2\tilde{E}_{+, \mathbf{k}+\mathbf{q}}} \int_{-q_{AF}/2}^{q_{AF}/2} dq' \frac{\tanh\left(\frac{\beta}{2} E_{+, \mathbf{k}+\mathbf{q}'}\right)}{2E_{+, \mathbf{k}+\mathbf{q}'}}}, \quad (\text{B.5})$$



The main difference with the standard BCS gap equation is the dependence of the first integrand upon the shifted  $\tilde{E}_{\mathbf{k}} = E_{\mathbf{k}+\mathbf{Q}_{AF}}$  while the second integrand is evaluated at the momentum  $\mathbf{k} + \mathbf{q}'$ . This can be solved by using the self-consistent equation to link  $\chi_{\mathbf{k}+\mathbf{Q}_{AF}}$  to  $\chi_{\mathbf{k}}$  once again which will give another integral of the form we obtained in Eq.(3.38). denoting this integral by  $I_{\mathbf{k}}(\chi)$  this integral we can write our self-consistency condition as

$$1 = \left( \frac{J_+}{4\pi^2} \right)^2 I_{\mathbf{k}}(\chi) I_{\mathbf{k}+\mathbf{Q}_{AF}} \left( \frac{-J_-}{4\pi^2} I_{\mathbf{k}}(\chi) \right), \quad (\text{B.6})$$

$$I_{\mathbf{k}}(\chi) = \int_{-q_{AF}/2}^{q_{AF}/2} dq \frac{\tanh\left(\frac{\beta}{2} E_{+, \mathbf{k}+\mathbf{q}}\right)}{2E_{+, \mathbf{k}+\mathbf{q}}}. \quad (\text{B.7})$$

This is very similar to the result we obtained for the superconducting gap in Eq.(3.39) and we solve it numerically in the same way.

## Appendix C

# Boson-Fermion vertex corrections

In this appendix, we discuss the fate of the boson-fermion vertex correction that could affect the Landau damping we obtained in Sec.4.2. Our calculation for the finite-momentum bosons will follow the results of Ref.[152], and in our study, two different situations can emerge.

In the first one, the bosons cannot generate hot-spots if the wave-vector  $\mathbf{Q}_0$  is either too small or too large to connect distinct parts of the Fermi surface as shown in Fig. (C.1A). Thus, the fermionic propagator reestablishes the Fermi liquid behavior of Eq. (4.4). In this scenario, the Landau damping remains unchanged, whereas the vertex corrections become irrelevant. Hence, the transport properties of the model give the  $T$ -linear behavior of the resistivity and a broad Drude component extending to zero temperature as exhibited in the phase-diagram of Fig. (C.1A).

In the second situation, if the bosonic wave-vector  $\mathbf{Q}_0$  create hot-spots by connecting two distinct parts of the Fermi surface as displayed in Fig. (C.1B), the fermionic self-energy is given by

$$\text{Im } \Sigma(\omega, \mathbf{Q}_0) = C|\omega|^{1/2}\text{sgn}(\omega), \quad (\text{C.1})$$

where  $C$  is just a constant, and the self-energy has a Non-Fermi liquid behavior. Additionally, in this situation, the vertex corrections also become relevant. The integral to evaluate the same is given by

$$\Gamma(0, 0) = \frac{i}{8\pi^3 v_x v_y} \int_{-\infty}^{\infty} dl_{\tau} \int_{-\infty}^{\infty} d\tilde{l}_x \int_{-\infty}^{\infty} d\tilde{l}_y \frac{1}{\left(i\Sigma_{l_{\tau}} + \tilde{l}_x - \tilde{l}_y\right) \left(i\Sigma_{l_{\tau}} - \tilde{l}_x - \tilde{l}_y\right) (\gamma|l_{\tau}| + \tilde{l}_x^2 + \tilde{l}_y^2)}. \quad (\text{C.2})$$

After computing this integral, one obtains a logarithmic divergence from the vertex corrections, thereby affecting the dynamical exponent near the QCP. However, recent sign-problem-free quantum Monte Carlo studies suggest that only within a small temperature regime near the QCP [300] (which is, in fact, too low to be seen in these simulations), these vertex corrections would become relevant which is represented by the blue region of phase-diagram in Fig. (C.1B). Furthermore, before reaching such a low-temperature regime, we point out that this divergence can also be

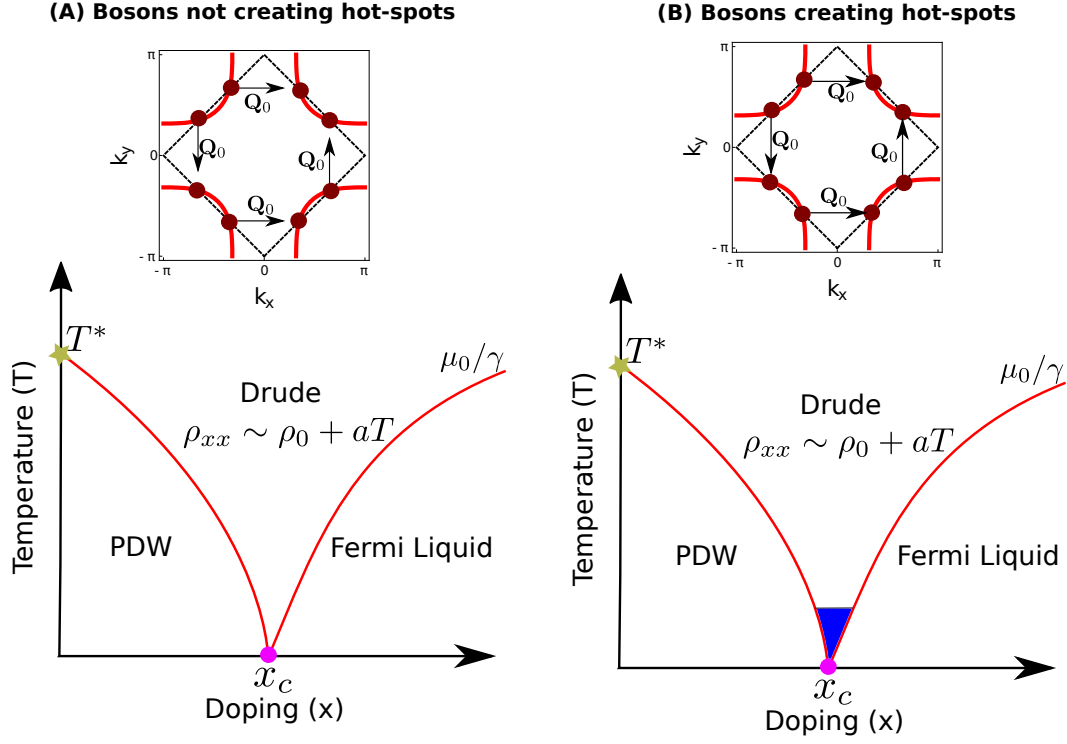


**Figure C.1:** Panel (A) on the left side depicts the scenario when the bosons do not create hot-spots since the bosonic wave-vector  $Q_0$  is smaller than the distinct parts of the Fermi surface. In this scenario, the linear-in- $T$  behavior of resistivity and Drude form of optical conductivity extends to  $T = 0$  at the critical dopings. Panel (B) on the right side presents the scenario when the bosons create hot-spots by connecting the Fermi-surface. In this scenario, the fermion-boson vertex correction becomes relevant and changes the dynamical exponent of the QCP. However, this happens only at low temperatures near the QCP here represented by the blue region. Above this temperature, we can have the same linear-in- $T$  resistivity with Drude conductivity for a broad temperature regime.

regularized by other mechanisms of damping, such that  $\Sigma_\omega \gg C|\omega|^{1/2}\text{sgn}(\omega)$ . In the cuprates these other sources of damping can have many different origins, such as nematic fluctuations, loop-current fluctuations [286], among others. These additional fluctuations that emerge in these materials can also regularize the fermion-boson vertex without changing the transport properties.

## Appendix D

### Fate of bosonic vertex corrections

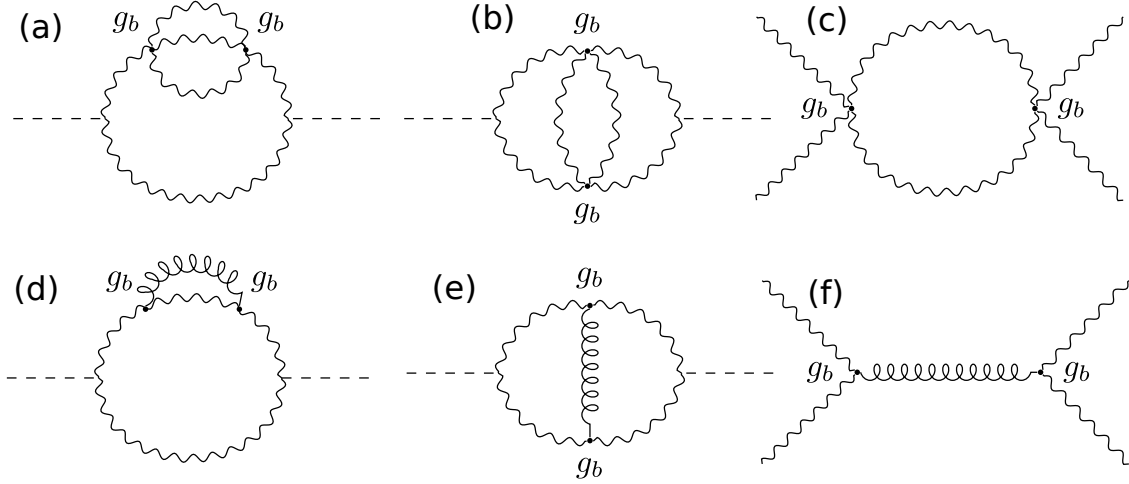


**Figure D.1:** (a) Shows the diagram associated with the current-current correlation function with second order self-energy corrections. (b) Exhibits the same with bosonic vertex corrections. (c) Shows the bosonic bubble that can be replaced with the diagram shown in (f). (d-e) Again shows the current-current correlation function by replacing the bosonic bubble with the curly line.

Here, we discuss the bosonic vertex correction diagram at second-order in  $g_b$  and compare it with the self-energy diagram given by  $\Pi_2$  evaluated in the previous section. The second-order self energy diagram is shown in Fig.D.1(a), whereas the vertex correction diagram is presented in Fig.D.1(b). Next, we replace the boson-boson bubble in Fig.D.1(c) using the curly-line composite propagator, as shown in Fig.D.1(f). After this, it can be readily seen that the diagrams in Fig.D.1(a) and Fig.D.1(b) can be replaced by those in Fig.D.1(d) and Fig.D.1(e), respectively. Subsequently, we define the bosonic composite propagator represented by the curly-line in Fig.D.1(f) as  $\mathcal{F}(\mathbf{q}, \omega)$ . In this notation, the diagram in Fig.D.1(d) becomes

$$\epsilon_1 = \frac{T^2}{L^2} \sum_{\mathbf{k}, \mathbf{q}, \omega_n, \Omega_n} \mathcal{D}^3(\mathbf{k}, \omega) \mathcal{D}(\mathbf{k} + \mathbf{q}, \omega + \Omega) \mathcal{F}(\mathbf{q}, \Omega). \quad (\text{D.1})$$

Similarly, the diagram in Fig.D.1(e) becomes

$$\epsilon_2 = \frac{T^2}{L^2} \sum_{\mathbf{k}, \mathbf{q}, \omega, \Omega} \mathcal{D}^2(\mathbf{k}, \omega) \mathcal{D}^2(\mathbf{k} + \mathbf{q}, \omega + \Omega) \mathcal{F}(\mathbf{q}, \Omega). \quad (\text{D.2})$$

Now, after performing analytical continuation, we obtain using the retarded form of the bosonic Green's function

$$\begin{aligned} T \sum_{\omega_n} \mathcal{D}(\mathbf{k}, \omega) &= \int_{-\infty}^{\infty} \frac{d\omega}{2\pi} \frac{1}{-i\omega + k^2 + \mu} \\ &= i \int_{-\infty}^{\infty} \frac{d\epsilon}{2\pi} \frac{1}{\epsilon + k^2 + \mu}, \end{aligned} \quad (\text{D.3})$$

where in the last step we have made a simple change of variable. From the last definition, it is clear that

$$\frac{\partial \mathcal{D}(\mathbf{k} + \mathbf{q}, \omega + \Omega)}{\partial(-i\omega)} = -\mathcal{D}^2(\mathbf{k} + \mathbf{q}, \omega + \Omega). \quad (\text{D.4})$$

Next, using these previous relations to evaluate  $\epsilon_2$ , we get

$$\epsilon_2 = -\frac{iT}{L^2} \sum_{\mathbf{k}, \mathbf{q}, \Omega} \int_{-\infty}^{\infty} \frac{d\epsilon}{2\pi} \mathcal{D}^2(\mathbf{k}, \epsilon) \partial_{\epsilon} \mathcal{D}(\mathbf{k} + \mathbf{q}, \epsilon + \Omega) \mathcal{F}(\mathbf{q}, \Omega). \quad (\text{D.5})$$

Integrating by parts, we find

$$\epsilon_2 = -2 \frac{iT}{L^2} \sum_{\mathbf{k}, \mathbf{q}, \Omega} \int_{-\infty}^{\infty} \frac{d\epsilon}{2\pi} \mathcal{D}^3(\mathbf{k}, \epsilon) \mathcal{D}(\mathbf{k} + \mathbf{q}, \epsilon + \Omega) \mathcal{F}(\mathbf{q}, \Omega). \quad (\text{D.6})$$

Finally, reverting back to the earlier notation, we get

$$\begin{aligned} \epsilon_2 &= -2 \frac{T^2}{L^2} \sum_{\mathbf{k}, \mathbf{q}, \omega_n, \Omega_n} \mathcal{D}^3(\mathbf{k}, \omega) \mathcal{D}(\mathbf{k} + \mathbf{q}, \omega + \Omega) \mathcal{F}(\mathbf{q}, \Omega) \\ &= -2\epsilon_1. \end{aligned} \quad (\text{D.7})$$

We have already argued in the previous section that the  $\epsilon_1$ -correction due to  $\Pi_2$  is negligible in all regimes. Since we find that  $\epsilon_2$  is of the same order of magnitude as  $\epsilon_1$ , the vertex correction diagram in Fig.D.1(b) can also be safely ignored in our analysis.

# Bibliography

- [1] D. van Delft and P. Kes, *Physics Today* **63**, 38 (2010).
- [2] W. Meissner and R. Ochsenfeld, *Die Naturwissenschaften* **21**, 787 (1933).
- [3] L. N. Cooper and D. Feldman, *BCS: 50 Years* (WORLD SCIENTIFIC, 2010).
- [4] F. London and L. H., *Proceedings of the Royal Society of London. Series A - Mathematical and Physical Sciences* **149**, 71 (1935).
- [5] V. L. Ginzburg and L. D. Landau, *Zh. Eksp. Teor. Fiz.* **20**, 1064 (1950).
- [6] L. N. Cooper, *Physical Review* **104**, 1189 (1956).
- [7] J. Bardeen, L. N. Cooper, and J. R. Schrieffer, *Physical Review* **106**, 162 (1957).
- [8] J. Bardeen, L. N. Cooper, and J. R. Schrieffer, *Phys. Rev.* **108**, 1175 (1957).
- [9] D. Jérôme, A. Mazaud, M. Ribault, and K. Bechgaard, *Journal de Physique Lettres* **41**, 95 (1980).
- [10] J. Singleton and C. Mielke, *Contemporary Physics* **43**, 63 (2002).
- [11] F. Steglich, J. Aarts, C. D. Bredl, W. Lieke, D. Meschede, W. Franz, and H. Schäfer, *Physical Review Letters* **43**, 1892 (1979).
- [12] Y. Kamihara, T. Watanabe, M. Hirano, and H. Hosono, *Journal of the American Chemical Society* **130**, 3296 (2008).
- [13] J.-F. Ge, Z.-L. Liu, C. Liu, C.-L. Gao, D. Qian, Q.-K. Xue, Y. Liu, and J.-F. Jia, *Nature Materials* **14**, 285 (2014).
- [14] J. Bednorz and K. Müller, *Zeitschrift für Physik B Condensed Matter* **64**, 189 (1986).
- [15] M. K. Wu, J. R. Ashburn, C. J. Torng, P. H. Hor, R. L. Meng, L. Gao, Z. J. Huang, Y. Q. Wang, and C. W. Chu, *Physical Review Letters* **58**, 908 (1987).
- [16] A. Schilling, M. Cantoni, J. D. Guo, and H. R. Ott, *Nature* **363**, 56 (1993).
- [17] A. P. Drozdov, M. I. Erements, I. A. Troyan, V. Ksenofontov, and S. I. Shylin, *Nature* **525**, 73 (2015).
- [18] A. Bianconi and T. Jarlborg, *EPL (Europhysics Letters)* **112**, 37001 (2015).
- [19] N. W. Ashcroft, *Physical Review Letters* **21**, 1748 (1968).

- [20] P. J. Ray, *Master's thesis: Structural investigation of  $La(2-x)Sr(x)CuO(4+y)$  - Following staging as a function of temperature*, *Master's thesis* (2016).
- [21] Y. Cao, V. Fatemi, A. Demir, S. Fang, S. L. Tomarken, J. Y. Luo, J. D. Sanchez-Yamagishi, K. Watanabe, T. Taniguchi, E. Kaxiras, R. C. Ashoori, and P. Jarillo-Herrero, *Nature* **556**, 80 (2018).
- [22] Y. Cao, V. Fatemi, S. Fang, K. Watanabe, T. Taniguchi, E. Kaxiras, and P. Jarillo-Herrero, *Nature* **556**, 43 (2018).
- [23] N. D. Mermin and H. Wagner, *Physical Review Letters* **17**, 1133 (1966).
- [24] N. Barisic, M. K. Chan, Y. Li, G. Yu, X. Zhao, M. Dressel, A. Smontara, and M. Greven, *Proceedings of the National Academy of Sciences* **110**, 12235 (2013).
- [25] M. R. Norman and C. Pépin, *Rep. Prog. Phys.* **66**, 1547 (2003).
- [26] W. E. Pickett, *Reviews of Modern Physics* **61**, 433 (1989).
- [27] N. F. Mott, *Proceedings of the Physical Society. Section A* **62**, 416 (1949).
- [28] P. A. Lee, N. Nagaosa, and X.-G. Wen, *Rev. Mod. Phys.* **78**, 17 (2006).
- [29] A. Del Maestro, B. Rosenow, and S. Sachdev, *Phys. Rev. B* **74**, 024520 (2006).
- [30] D. Chakraborty, M. Grandadam, M. H. Hamidian, J. C. S. Davis, Y. Sidis, and C. Pépin, *Phys. Rev. B* **100**, 224511 (2019).
- [31] Y. Imry and S.-k. Ma, *Phys. Rev. Lett.* **35**, 1399 (1975).
- [32] Y. Sato, S. Kasahara, H. Murayama, Y. Kasahara, E. G. Moon, T. Nishizaki, T. Loew, J. Porras, B. Keimer, T. Shibauchi, and Y. Matsuda, *Nature Physics* **13**, 1074 (2017).
- [33] M. Gurvitch and A. T. Fiory, *Phys. Rev. Lett.* **59**, 1337 (1987).
- [34] Emery, V. J. and S. A. Kivelson, *Phys.Rev.Lett.* **74**, 3253 (1995).
- [35] N. Hussey, K. Takenaka, and H. Takagi, *Philosophical Magazine* **84**, 2847 (2004).
- [36] C. L. Smallwood, J. P. Hinton, C. Jozwiak, W. Zhang, J. D. Koralek, H. Eisaki, D.-H. Lee, J. Orenstein, and A. Lanzara, *Science* **336**, 1137 (2012).
- [37] A. Altland, P. Altland, and B. Simons, *Condensed Matter Field Theory* (Cambridge University Press, 2006) p. 265.
- [38] O. Fischer, M. Kugler, I. Maggio-Aprile, C. Berthod, and C. Renner, *Rev. Mod. Phys.* **79**, 353 (2007).
- [39] D. J. V. Harlingen, *Reviews of Modern Physics* **67**, 515 (1995).
- [40] T. P. Devereaux and R. Hackl, *Rev. Mod. Phys.* **79**, 175 (2007).
- [41] D. S. Inosov, J. T. Park, A. Charnukha, Y. Li, A. V. Boris, B. Keimer, and V. Hinkov, *Phys. Rev. B* **83**, 214520 (2011).

- [42] M. Le Tacon, A. Sacuto, A. Georges, G. Kotliar, Y. Gallais, D. Colson, and A. Forget, *Nat. Phys.* **2**, 537 (2006).
- [43] B. Loret, N. Auvray, Y. Gallais, M. Cazayous, A. Forget, D. Colson, M.-H. Julien, I. Paul, M. Civelli, and A. Sacuto, *Nature Physics* , 1 (2019).
- [44] J. E. Hoffman, E. W. Hudson, K. M. Lang, V. Madhavan, H. Eisaki, S. Uchida, and J. C. Davis, *Science* **295**, 466 (2002).
- [45] M. H. Hamidian, S. D. Edkins, C. K. Kim, J. C. Davis, A. P. Mackenzie, H. Eisaki, S. Uchida, M. J. Lawler, E.-A. Kim, S. Sachdev, and K. Fujita, *Nat. Phys.* **12**, 150 (2015).
- [46] N. Doiron-Leyraud, C. Proust, D. LeBoeuf, J. Levallois, J.-B. Bonnemaïson, R. Liang, D. A. Bonn, W. N. Hardy, and L. Taillefer, *Nature* **447**, 565 (2007).
- [47] D. LeBoeuf, N. Doiron-Leyraud, J. Levallois, R. Daou, J. B. Bonnemaïson, N. E. Hussey, L. Balicas, B. J. Ramshaw, R. Liang, D. A. Bonn, W. N. Hardy, S. Adachi, C. Proust, and L. Taillefer, *Nature* **450**, 533 (2007).
- [48] S. E. Sebastian, N. Harrison, R. Liang, D. A. Bonn, W. N. Hardy, C. H. Mielke, and G. G. Lonzarich, *Phys. Rev. Lett.* **108**, 196403 (2012).
- [49] W. Tabis, Y. Li, M. Le Tacon, L. Braicovich, A. Kreyssig, M. Minola, G. Dellea, E. Weschke, M. J. Veit, M. Ramazanoglu, A. I. Goldman, T. Schmitt, G. Ghiringhelli, N. Barišić, M. K. Chan, C. J. Dorow, G. Yu, X. Zhao, B. Keimer, and M. Greven, *Nat. Commun.* **5**, 5875 (2014).
- [50] N. Barišić, S. Badoux, M. K. Chan, C. Dorow, W. Tabis, B. Vignolle, G. Yu, J. Béard, X. Zhao, C. Proust, and M. Greven, *Nature Physics* **9**, 761 (2013).
- [51] G. Grissonnanche and F. Laliberte, (2015), [arXiv:1508.05486](https://arxiv.org/abs/1508.05486) .
- [52] F. Laliberté, J. Chang, N. Doiron-Leyraud, E. Hassinger, R. Daou, M. Rondeau, B. J. Ramshaw, R. Liang, D. A. Bonn, W. N. Hardy, S. Pyon, T. Takayama, H. Takagi, I. Sheikin, L. Malone, C. Proust, K. Behnia, and L. Taillefer, *Nat. Commun.* **2**, 432 (2011).
- [53] J. Chang, R. Daou, C. Proust, D. LeBoeuf, N. Doiron-Leyraud, F. Laliberté, B. Pingault, B. J. Ramshaw, R. Liang, D. A. Bonn, W. N. Hardy, H. Takagi, A. B. Antunes, I. Sheikin, K. Behnia, and L. Taillefer, *Phys. Rev. Lett.* **104**, 057005 (2010).
- [54] N. Auvray, B. Loret, S. Chibani, R. Grasset, Y. Guarnelli, P. Parisiades, A. Forget, D. Colson, M. Cazayous, Y. Gallais, and A. Sacuto, *Physical Review B* **103** (2021), [10.1103/physrevb.103.195130](https://arxiv.org/abs/10.1103/physrevb.103.195130).
- [55] D. Chakraborty, C. Morice, and C. Pépin, *Phys. Rev. B* **97**, 214501 (2018).
- [56] W. S. Lee, K.-J. Zhou, M. Hepting, J. Li, A. Nag, A. C. Walters, M. Garcia-Fernandez, H. C. Robarts, M. Hashimoto, H. Lu, B. Nosarzewski, D. Song, H. Eisaki, Z. X. Shen, B. Moritz, J. Zaanen, and T. P. Devereaux, *Nature Physics* **17**, 53 (2020).
- [57] M. H. Hamidian, S. D. Edkins, K. Fujita, A. Kostin, A. P. Mackenzie, H. Eisaki, S. Uchida, M. J. Lawler, E. A. Kim, S. Sachdev, and J. C. Séamus Davis, arXiv e-prints , [arXiv:1508.00620](https://arxiv.org/abs/1508.00620) (2015), [arXiv:1508.00620 \[cond-mat.supr-con\]](https://arxiv.org/abs/1508.00620) .



- [58] H. Alloul, T. Ohno, and P. Mendels, *Phys. Rev. Lett.* **63**, 1700 (1989).
- [59] W. W. Warren, R. E. Walstedt, G. F. Brennert, R. J. Cava, R. Tycko, R. F. Bell, and G. Dabbagh, *Phys. Rev. Lett.* **62**, 1193 (1989).
- [60] A. J. Freeman, D. D. Koelling, and F. M. Mueller, *Journal of Applied Physics* **41**, 1228 (1970).
- [61] I. M. Vishik, *Reports on Progress in Physics* **81**, 062501 (2018).
- [62] T. J. Reber, N. C. Plumb, Z. Sun, Y. Cao, Q. Wang, K. McElroy, H. Iwasawa, M. Arita, J. S. Wen, Z. J. Xu, G. Gu, Y. Yoshida, H. Eisaki, Y. Aiura, and D. S. Dessau, *Nat. Phys.* **8**, 606 (2012).
- [63] R.-H. He, M. Hashimoto, H. Karapetyan, J. D. Koralek, J. P. Hinton, J. P. Testaud, V. Nathan, Y. Yoshida, H. Yao, K. Tanaka, W. Meevasana, R. G. Moore, D. H. Lu, S.-K. Mo, M. Ishikado, H. Eisaki, Z. Hussain, T. P. Devereaux, S. A. Kivelson, J. Orenstein, A. Kapitulnik, and Z.-X. Shen, *Science* **331**, 1579 (2011).
- [64] H. J. Goldsmid, *Introduction to Thermoelectricity* (Springer Berlin Heidelberg, 2010).
- [65] S. Verret, O. Simard, M. Charlebois, D. Sénéchal, and A. M. S. Tremblay, *Physical Review B* **96**, 125139 (2017).
- [66] V. Hinkov, C. Lin, M. Raichle, B. Keimer, Y. Sidis, P. Bourges, S. Pailhès, and A. Ivanov, *The European Physical Journal Special Topics* **188**, 113 (2010).
- [67] O. Cyr-Choinière, D. LeBoeuf, S. Badoux, S. Dufour-Beauséjour, D. A. Bonn, W. N. Hardy, R. Liang, D. Graf, N. Doiron-Leyraud, and L. Taillefer, *Phys. Rev. B* **98**, 064513 (2018).
- [68] C. M. Varma, *Phys. Rev. B* **73**, 155113 (2006).
- [69] A. Abanov, A. V. Chubukov, and J. Schmalian, *Adv. Phys.* **52**, 119 (2003).
- [70] M. Eschrig, *Advances in Physics* **55**, 47 (2006).
- [71] A. Kanigel, U. Chatterjee, M. Randeria, M. R. Norman, G. Koren, K. Kadowaki, and J. C. Campuzano, *Phys. Rev. Lett.* **101**, 137002 (2008).
- [72] M. Franz and A. J. Millis, *Phys. Rev. B* **58**, 14572 (1998).
- [73] S. Banerjee, T. V. Ramakrishnan, and C. Dasgupta, *Phys. Rev. B* **83**, 024510 (2011).
- [74] S. Banerjee, T. V. Ramakrishnan, and C. Dasgupta, *Phys. Rev. B* **84**, 144525 (2011).
- [75] R. Boyack, C.-T. Wu, P. Scherpelz, and K. Levin, *Physical Review B* **90**, 220513 (2014).
- [76] Z. A. Xu, N. P. Ong, Y. Wang, T. Kakeshita, and S. Uchida, *Nature* **406**, 486 (2000).
- [77] L. Li, Y. Wang, S. Komiya, S. Ono, Y. Ando, G. D. Gu, and N. P. Ong, *Phys. Rev. B* **81**, 054510 (2010).
- [78] S. Rajasekaran, J. Okamoto, L. Mathey, M. Fechner, V. Thampy, G. D. Gu, and A. Cavalleri, *Science* **359**, 575 (2018).

- [79] W. Hu, S. Kaiser, D. Nicoletti, C. R. Hunt, I. Gierz, M. C. Hoffmann, M. Le Tacon, T. Loew, B. Keimer, and A. Cavalleri, *Nature Materials* **13**, 705 (2014).
- [80] D. Fausti, R. Tobey, N. Dean, S. Kaiser, A. Dienst, M. C. Hoffmann, S. Pyon, T. Takayama, H. Takagi, and A. Cavalleri, *Science* **331**, 189 (2011).
- [81] B. Fauqué, Y. Sidis, V. Hinkov, S. Pailhès, C. T. Lin, X. Chaud, and P. Bourges, *Phys. Rev. Lett.* **96**, 197001 (2006).
- [82] P. Bourges, Y. Sidis, and L. Mangin-Thro, *Phys. Rev. B* **98**, 016501 (2018), and references therein.
- [83] L. Zhao, C. A. Belvin, R. Liang, D. A. Bonn, W. N. Hardy, N. P. Armitage, and D. Hsieh, *Nat. Phys.* **13**, 250 (2016).
- [84] L. Mangin-Thro, Y. Li, Y. Sidis, and P. Bourges, *Phys. Rev. Lett.* **118**, 097003 (2017).
- [85] Y. Lubashevsky, L. Pan, T. Kirzhner, G. Koren, and N. Armitage, *Physical Review Letters* **112** (2014), 10.1103/physrevlett.112.147001.
- [86] D. F. Agterberg, J. S. Davis, S. D. Edkins, E. Fradkin, D. J. V. Harlingen, S. A. Kivelson, P. A. Lee, L. Radzihovsky, J. M. Tranquada, and Y. Wang, *Annual Review of Condensed Matter Physics* **11**, 231 (2020).
- [87] S. D. Edkins, A. Kostin, K. Fujita, A. P. Mackenzie, H. Eisaki, S. Uchida, S. Sachdev, M. J. Lawler, E.-A. Kim, J. C. S. Davis, and M. H. Hamidian, *Science* **364**, 976 (2019).
- [88] M. H. Hamidian, S. D. Edkins, S. H. Joo, A. Kostin, H. Eisaki, S. Uchida, M. J. Lawler, E.-A. Kim, A. P. Mackenzie, K. Fujita, J. Lee, and J. C. S. Davis, *Nature* **532**, 343 (2016).
- [89] A. I. Larkin and Y. N. Ovchinnikov, *Zh. Eksp. Teor. Fiz.* **47**, 1136 (1964).
- [90] P. Fulde and R. A. Ferrell, *Phys. Rev.* **135**, A550 (1964).
- [91] Y. Matsuda and H. Shimahara, *Journal of the Physical Society of Japan* **76**, 051005 (2007).
- [92] C. Agosta, *Crystals* **8**, 285 (2018).
- [93] E. Fradkin, S. A. Kivelson, and J. M. Tranquada, *Rev. Mod. Phys.* **87**, 457 (2015).
- [94] P. W. Anderson, *Science* **235**, 1196 (1987).
- [95] G. Baskaran and P. W. Anderson, *Phys. Rev. B* **37**, 580 (1988).
- [96] P. A. Lee and N. Nagaosa, *Phys. Rev. B* **46**, 5621 (1992).
- [97] P. Coleman, *Phys. Rev. B* **29**, 3035 (1984).
- [98] J. M. Luttinger, *Journal of Mathematical Physics* **4**, 1154 (1963).
- [99] F. D. M. Haldane, *Journal of Physics C: Solid State Physics* **14**, 2585 (1981).
- [100] H. Rogalla, *100 years of superconductivity* (CRC Press/Taylor & Francis Group, Boca Raton, 2012).
- [101] J. E. Hirsch, *Physical Review B* **28**, 4059 (1983).

- [102] G. G. Batrouni and P. de Forcrand, *Physical Review B* **48**, 589 (1993).
- [103] A. Georges, G. Kotliar, W. Krauth, and M. J. Rozenberg, *Rev. Mod. Phys.* **68**, 13 (1996).
- [104] G. Kotliar, S. Y. Savrasov, G. Pálsson, and G. Biroli, *Physical Review Letters* **87** (2001).
- [105] T. Maier, M. Jarrell, T. Pruschke, and M. H. Hettler, *Reviews of Modern Physics* **77**, 1027 (2005).
- [106] G. Rohringer, H. Hafermann, A. Toschi, A. Katanin, A. Antipov, M. Katsnelson, A. Lichtenstein, A. Rubtsov, and K. Held, *Reviews of Modern Physics* **90** (2018).
- [107] R. Orús, *Nature Reviews Physics* **1**, 538 (2019).
- [108] P. Corboz, P. Czarnik, G. Kapteijns, and L. Tagliacozzo, *Physical Review X* **8** (2018), [10.1103/physrevx.8.031031](https://doi.org/10.1103/physrevx.8.031031).
- [109] M. Rader and A. M. Läuchli, *Physical Review X* **8** (2018), [10.1103/physrevx.8.031030](https://doi.org/10.1103/physrevx.8.031030).
- [110] G. Evenbly and G. Vidal, *Physical Review Letters* **104** (2010), [10.1103/physrevlett.104.187203](https://doi.org/10.1103/physrevlett.104.187203).
- [111] T. Schäfer, N. Wentzell, F. Šimkovic, Y.-Y. He, C. Hille, M. Klett, C. J. Eckhardt, B. Arzhang, V. Harkov, F.-M. L. Régent, A. Kirsch, Y. Wang, A. J. Kim, E. Kozik, E. A. Stepanov, A. Kauch, S. Andergassen, P. Hansmann, D. Rohe, Y. M. Vil'k, J. P. LeBlanc, S. Zhang, A.-M. Tremblay, M. Ferrero, O. Parcollet, and A. Georges, *Physical Review X* **11** (2021).
- [112] M. R. Norman, M. Randeria, H. Ding, and J. C. Campuzano, *Phys. Rev. B* **57**, R11093 (1998).
- [113] C.-C. Chien, Y. He, Q. Chen, and K. Levin, *Physical Review B* **79**, 214527 (2009).
- [114] P. A. Lee, *Phys. Rev. X* **4**, 031017 (2014).
- [115] Z. Dai, T. Senthil, and P. A. Lee, *Physical Review B* **101** (2020).
- [116] S. Sarkar, D. Chakraborty, and C. Pépin, arXiv e-prints, arXiv:1906.08280 (2019), [arXiv:1906.08280 \[cond-mat.supr-con\]](https://arxiv.org/abs/1906.08280).
- [117] S. Sachdev, H. D. Scammell, M. S. Scheurer, and G. Tarnopolsky, *Phys. Rev. B* **99**, 054516 (2019).
- [118] H. Bruus, *Many-body quantum theory in condensed matter physics : an introduction* (Oxford University Press, Oxford New York, 2004).
- [119] A. M. Tsvelik, *Quantum Field Theory in Condensed Matter Physics* (Cambridge University Press, 2nd ed. (2007)).
- [120] A. H. C. Neto, F. Guinea, N. M. R. Peres, K. S. Novoselov, and A. K. Geim, *Reviews of Modern Physics* **81**, 109 (2009).
- [121] D. Bohm and D. Pines, *Physical Review* **82**, 625 (1951).
- [122] D. Pines and D. Bohm, *Physical Review* **85**, 338 (1952).

- [123] D. Bohm and D. Pines, *Physical Review* **92**, 609 (1953).
- [124] P. Massignan, M. Zaccanti, and G. M. Bruun, *Reports on Progress in Physics* **77**, 034401 (2014).
- [125] N. N. Bogoljubov, *Il Nuovo Cimento* **7**, 794 (1958).
- [126] J. G. Valatin, *Il Nuovo Cimento* **7**, 843 (1958).
- [127] L. P. Gor'kov, *Soviet Phys. JETP* **34**, 735 (1958).
- [128] A. A. Abrikosov, *Methods of quantum field theory in statistical physics* (Dover Publications, New York, 1975).
- [129] F. Blatt, *Modern physics* (McGraw-Hill, New York, 1992).
- [130] J. Hubbard, *Proceedings of the Royal Society of London. Series A. Mathematical and Physical Sciences* **276**, 238 (1963).
- [131] M. C. Gutzwiller, *Physical Review Letters* **10**, 159 (1963).
- [132] J. Kanamori, *Progress of Theoretical Physics* **30**, 275 (1963).
- [133] C. Pépin, D. Chakraborty, M. Grandadam, and S. Sarkar, *Annual Review of Condensed Matter Physics* **11**, 301 (2020).
- [134] M. Grandadam, D. Chakraborty, and C. Pépin, *Journal of Superconductivity and Novel Magnetism* **33**, 2361 (2020).
- [135] M. Grandadam, D. Chakraborty, X. Montiel, and C. Pépin, *Phys. Rev. B* **102**, 121104 (2020).
- [136] M. Grandadam and C. Pépin, *Physical Review B* **103** (2021), 10.1103/physrevb.103.224507.
- [137] S. Sarkar, M. Grandadam, and C. Pépin, *Physical Review Research* **3** (2021), 10.1103/physrevresearch.3.013162.
- [138] F. H. L. Essler, H. Frahm, F. Göhmann, A. Klümper, and V. E. Korepin, *The One-Dimensional Hubbard Model* (Cambridge University Press, 2005).
- [139] E. Demler and S.-C. Zhang, *Phys. Rev. Lett.* **75**, 4126 (1995).
- [140] E. Demler, W. Hanke, and S.-C. Zhang, *Rev. Mod. Phys.* **76**, 909 (2004).
- [141] S.-C. Zhang, *Science* **275**, 1089 (1997).
- [142] P. A. Lee, N. Nagaosa, T.-K. Ng, and X.-G. Wen, *Phys. Rev. B* **57**, 6003 (1998).
- [143] W. D. Wise, M. C. Boyer, K. Chatterjee, T. Kondo, T. Takeuchi, H. Ikuta, Y. Wang, and E. W. Hudson, *Nat. Phys.* **4**, 696 (2008).
- [144] T. Wu, H. Mayaffre, S. Krämer, M. Horvatić, C. Berthier, W. N. Hardy, R. Liang, D. A. Bonn, and M.-H. Julien, [arXiv:1404.1617 \[cond-mat.supr-con\]](https://arxiv.org/abs/1404.1617) (2014).
- [145] T. Wu, H. Mayaffre, S. Krämer, M. Horvatic, C. Berthier, W. N. Hardy, R. Liang, D. A. Bonn, and M.-H. Julien, *Nature* **477**, 191 (2011).

- [146] E. Blackburn, J. Chang, M. Hücker, A. T. Holmes, N. B. Christensen, R. Liang, D. A. Bonn, W. N. Hardy, U. Rütt, O. Gutowski, M. v. Zimmermann, E. M. Forgan, and S. M. Hayden, *Phys. Rev. Lett.* **110**, 137004 (2013).
- [147] S. Blanco-Canosa, A. Frano, T. Loew, Y. Lu, J. Porras, G. Ghiringhelli, M. Minola, C. Mazzoli, L. Braicovich, E. Schierle, E. Weschke, M. Le Tacon, and B. Keimer, *Phys. Rev. Lett.* **110**, 187001 (2013).
- [148] S. Blanco-Canosa, A. Frano, E. Schierle, J. Porras, T. Loew, M. Minola, M. Bluschke, E. Weschke, B. Keimer, and M. Le Tacon, *Phys. Rev. B* **90**, 054513 (2014).
- [149] G. Ghiringhelli, M. Le Tacon, M. Minola, S. Blanco-Canosa, C. Mazzoli, N. B. Brookes, G. M. De Luca, A. Frano, D. G. Hawthorn, F. He, T. Loew, M. M. Sala, D. C. Peets, M. Salluzzo, E. Schierle, R. Sutarto, G. A. Sawatzky, E. Weschke, B. Keimer, and L. Braicovich, *Science* **337**, 821 (2012).
- [150] K. B. Efetov, H. Meier, and C. Pépin, *Nat. Phys.* **9**, 442 (2013).
- [151] C. Pépin, V. S. de Carvalho, T. Kloss, and X. Montiel, *Phys. Rev. B* **90**, 195207 (2014).
- [152] M. A. Metlitski and S. Sachdev, *Phys. Rev. B* **82**, 075128 (2010).
- [153] W. A. Atkinson, A. P. Kampf, and S. Bulut, *New J. Phys.* **17**, 013025 (2015).
- [154] H. Freire, V. S. de Carvalho, and C. Pépin, *Phys. Rev. B* **92**, 045132 (2015).
- [155] S. Gerber, H. Jang, H. Nojiri, S. Matsuzawa, H. Yasumura, D. A. Bonn, R. Liang, W. N. Hardy, Z. Islam, A. Mehta, S. Song, M. Sikorski, D. Stefanescu, Y. Feng, S. A. Kivelson, T. P. Devereaux, Z.-X. Shen, C. C. Kao, W. S. Lee, D. Zhu, and J. S. Lee, *Science* **350**, 949 (2015).
- [156] J. Chang, E. Blackburn, O. Ivashko, A. T. Holmes, N. B. Christensen, M. Huecker, R. Liang, D. A. Bonn, W. N. Hardy, U. Ruett, M. V. Zimmermann, E. M. Forgan, and S. M. Hayden, *Nat. Commun.* **7** (2016), 10.1038/ncomms11494.
- [157] H. Jang, W.-S. Lee, H. Nojiri, S. Matsuzawa, H. Yasumura, L. Nie, A. V. Maharaj, S. Gerber, Y.-J. Liu, A. Mehta, D. A. Bonn, R. Liang, W. N. Hardy, C. A. Burns, Z. Islam, S. Song, J. Hastings, T. P. Devereaux, Z.-X. Shen, S. A. Kivelson, C.-C. Kao, D. Zhu, and J.-S. Lee, *Proc. Natl. Acad. Sci.* **113**, 14645 (2016), <http://www.pnas.org/content/113/51/14645.full.pdf> .
- [158] D. LeBoeuf, S. Kramer, W. N. Hardy, R. Liang, D. A. Bonn, and C. Proust, *Nat. Phys.* **9**, 79 (2013).
- [159] F. Laliberté, M. Frchet, S. Benhabib, B. Borgnic, T. Loew, J. Porras, M. Le Tacon, B. Keimer, S. Wiedmann, C. Proust, and D. LeBoeuf, *npj Quantum Materials* **3**, 11 (2018).
- [160] M. Einenkel, H. Meier, C. Pépin, and K. B. Efetov, *Phys. Rev. B* **90**, 054511 (2014).
- [161] L. E. Hayward, D. G. Hawthorn, R. G. Melko, and S. Sachdev, *Science* **343**, 1336 (2014).
- [162] T. Wu, H. Mayaffre, S. Krämer, M. Horvatić, C. Berthier, P. L. Kuhns, A. P. Reyes, R. Liang, W. N. Hardy, D. A. Bonn, and M.-H. Julien, *Nat. Commun.* **4**, 2113 (2013).

- [163] D. P. Arovas, A. J. Berlinsky, C. Kallin, and S.-C. Zhang, *Phys. Rev. Lett.* **79**, 2871 (1997).
- [164] A. Ghosal, C. Kallin, and A. J. Berlinsky, *Phys. Rev. B* **66**, 214502 (2002).
- [165] P. A. Lee and X.-G. Wen, *Phys. Rev. B* **63**, 224517 (2001).
- [166] B. Lake, G. Aeppli, K. N. Clausen, D. F. McMorrow, K. Lefmann, N. E. Hussey, N. Mangkorntong, M. Nohara, H. Takagi, T. E. Mason, and A. Schröder, *Science* **291**, 1759 (2001), <http://science.sciencemag.org/content/291/5509/1759.full.pdf> .
- [167] S. A. Kivelson, D.-H. Lee, E. Fradkin, and V. Oganesyan, *Phys. Rev. B* **66**, 144516 (2002).
- [168] Y. Zhang, E. Demler, and S. Sachdev, *Phys. Rev. B* **66**, 094501 (2002).
- [169] J. Chang, E. Blackburn, O. Ivashko, A. T. Holmes, N. B. Christensen, M. Hucker, R. Liang, D. A. Bonn, W. N. Hardy, U. Rutt, M. v. Zimmermann, E. M. Forgan, and H. S. M., *Nat. Commun.* **7**, 11494 (2016).
- [170] H. Meier, M. Einenkel, C. Pépin, and K. B. Efetov, *Phys. Rev. B* **88**, 020506 (2013).
- [171] J. Kačmarčík, I. Vinograd, B. Michon, A. Rydh, A. Demuer, R. Zhou, H. Mayaffre, R. Liang, W. N. Hardy, D. A. Bonn, N. Doiron-Leyraud, L. Taillefer, M.-H. Julien, C. Marcenat, and T. Klein, *Phys. Rev. Lett.* **121**, 167002 (2018).
- [172] C. Morice, D. Chakraborty, and C. Pépin, *Phys. Rev. B* **98**, 224514 (2018).
- [173] S. Benhabib, A. Sacuto, M. Civelli, I. Paul, M. Cazayous, Y. Gallais, M. A. Méasson, R. D. Zhong, J. Schneeloch, G. D. Gu, D. Colson, and A. Forget, *Phys. Rev. Lett.* **114**, 147001 (2015).
- [174] S. Vig, A. Kogar, M. Mitrano, A. Husain, L. Venema, M. Rak, V. Mishra, P. Johnson, G. Gu, E. Fradkin, M. Norman, and P. Abbamonte, *SciPost Physics* **3**, 026 (2017).
- [175] M. Mitrano, A. A. Husain, S. Vig, A. Kogar, M. S. Rak, S. I. Rubeck, J. Schmalian, B. Uchoa, J. Schneeloch, R. Zhong, G. D. Gu, and P. Abbamonte, *Proceedings of the National Academy of Sciences* **115**, 5392 (2018).
- [176] L. Chaix, G. Ghiringhelli, Y. Y. Peng, M. Hashimoto, B. Moritz, K. Kummer, N. B. Brookes, Y. He, S. Chen, S. Ishida, Y. Yoshida, H. Eisaki, M. Salluzzo, L. Braicovich, Z.-X. Shen, T. P. Devereaux, and W. S. Lee, *Nature Physics* **13**, 952 (2017).
- [177] Y. Wang and A. Chubukov, *Phys. Rev. B* **90**, 035149 (2014).
- [178] Y. Wang, D. F. Agterberg, and A. Chubukov, *Phys. Rev. Lett.* **114**, 197001 (2015).
- [179] Y. Wang, D. F. Agterberg, and A. Chubukov, *Phys. Rev. B* **91**, 115103 (2015).
- [180] T. Wu, H. Mayaffre, S. Krämer, M. Horvatić, C. Berthier, W. N. Hardy, R. Liang, D. A. Bonn, and M.-H. Julien, *Nature Communications* **6**, 6438 (2015).
- [181] O. Cyr-Choiniere, R. Daou, F. Laliberte, C. Collignon, S. Badoux, D. LeBoeuf, J. Chang, B. J. Ramshaw, D. A. Bonn, W. N. Hardy, R. Liang, J. Q. Yan, J. G. Cheng, J. S. Zhou, J. B. Goodenough, S. Pyon, T. Takayama, H. Takagi, N. Doiron-Leyraud, and L. Taillefer, *Physical Review B* **97**, 064502 (2018).

- [182] F. Rullier-Albenque, H. Alloul, and G. Rikken, *Phys. Rev. B* **84**, 014522 (2011).
- [183] N. Bergeal, J. Lesueur, M. Aprili, G. Faini, J. P. Contour, and B. Leridon, *Nat. Phys.* **4**, 608 (2008).
- [184] C. Howald, H. Eisaki, N. Kaneko, M. Greven, and A. Kapitulnik, *Phys. Rev. B* **67**, 014533 (2003).
- [185] Y. Caplan, G. Wachtel, and D. Orgad, *Phys. Rev. B* **92**, 224504 (2015).
- [186] R. Comin, R. Sutarto, E. H. da Silva Neto, L. Chauviere, R. Liang, W. N. Hardy, D. A. Bonn, F. He, G. A. Sawatzky, and A. Damascelli, *Science* **347**, 1335 (2015).
- [187] L. Nie, G. Tarjus, and S. A. Kivelson, *Proc. Natl. Acad. Sci.* **111**, 7980 (2014).
- [188] Y. Caplan and D. Orgad, *Phys. Rev. Lett.* **119**, 107002 (2017).
- [189] D. F. Agterberg, D. S. Melchert, and M. K. Kashyap, *Phys. Rev. B* **91**, 054502 (2015).
- [190] C. M. Varma, *Phys. Rev. B* **55**, 14554 (1997).
- [191] S. Lee, J. Jung, A. Go, and E.-G. Moon, arXiv e-prints, arXiv:1803.00578 (2018).
- [192] A. Allais, J. Bauer, and S. Sachdev, *Phys. Rev. B* **90**, 155114 (2014).
- [193] A. Allais, J. Bauer, and S. Sachdev, *Indian J. Phys.* **88**, 905 (2014).
- [194] J. D. Sau and S. Sachdev, *Physical Review B* **89** (2014), 10.1103/physrevb.89.075129.
- [195] V. Hinkov, P. Bourges, Y. Pailhès, S. and Sidis, A. Ivanov, C. D. Frost, T. G. Perring, C. T. Lin, D. P. Chen, and B. Keimer, *Nat. Phys.* **3**, 780 (2007).
- [196] Z. Dai, Y.-H. Zhang, T. Senthil, and P. A. Lee, *Phys. Rev. B* **97**, 174511 (2018).
- [197] X. Montiel, T. Kloss, and C. Pépin, *EPL (Europhysics Letters)* **115**, 57001 (2016).
- [198] M. R. Norman, M. Randeria, H. Ding, and J. C. Campuzano, *Phys. Rev. B* **52**, 615 (1995).
- [199] J. C. Campuzano, M. R. Norman, H. Ding, M. Randeria, T. Yokoya, T. Takeuchi, T. Takahashi, T. Mochiku, K. Kadowaki, P. Guptasarma, and D. G. Hinks, *Nature* **392**, 157 (1998).
- [200] J. C. Campuzano, H. Ding, M. R. Norman, and M. Randeira, *Phys. Rev. B* **53**, R14737 (1996).
- [201] L. Benfatto, S. Caprara, and C. D. Castro, *Eur. Phys. J. B* **17**, 95 (2000).
- [202] J. Chang, E. Blackburn, A. T. Holmes, N. B. Christensen, J. Larsen, J. Mesot, R. Liang, D. A. Bonn, W. N. Hardy, A. Watenphul, M. v. Zimmermann, E. M. Forgan, and S. M. Hayden, *Nat. Phys.* **8**, 871 (2012).
- [203] M.-H. Julien, *Science* **350**, 914 (2015).
- [204] S. Sakai, M. Civelli, and M. Imada, *Phys. Rev. Lett.* **116**, 057003 (2016).
- [205] S. Sakai, M. Civelli, and M. Imada, *Physical Review B* **94**, 115130 (2016).
- [206] S. Sakai, M. Civelli, and M. Imada, *Physical Review B* **98**, 195109 (2018).



- [207] M. S. Scheurer, S. Chatterjee, W. Wu, M. Ferrero, A. Georges, and S. Sachdev, *Proceedings of the National Academy of Science* **115**, E3665 (2018).
- [208] K.-Y. Yang, T. M. Rice, and F.-C. Zhang, *Phys. Rev. B* **73**, 174501 (2006).
- [209] E. J. Woll and W. Kohn, *Physical Review* **126**, 1693 (1962).
- [210] B. Renker, H. Rietschel, L. Pintschovius, W. Gläser, P. Brüesch, D. Kuse, and M. J. Rice, *Physical Review Letters* **30**, 1144 (1973).
- [211] K. Carneiro, G. Shirane, S. A. Werner, and S. Kaiser, *Physical Review B* **13**, 4258 (1976).
- [212] J. P. Pouget, B. Hennion, C. Escribe-Filippini, and M. Sato, *Physical Review B* **43**, 8421 (1991).
- [213] J. A. Wilson, F. J. D. Salvo, and S. Mahajan, *Advances in Physics* **50**, 1171 (2001).
- [214] M. Le Tacon, A. Bosak, S. M. Souliou, G. Dellea, T. Loew, R. Heid, K.-P. Bohnen, G. Ghiringhelli, M. Krisch, and B. Keimer, *Nat. Phys.* **10**, 52 (2014).
- [215] E. Blackburn, J. Chang, A. H. Said, B. M. Leu, R. Liang, D. A. Bonn, W. N. Hardy, E. M. Forgan, and S. M. Hayden, *Phys. Rev. B* **88**, 054506 (2013).
- [216] H. Miao, D. Ishikawa, R. Heid, M. L. Tacon, G. Fabbris, D. Meyers, G. Gu, A. Baron, and M. Dean, *Physical Review X* **8** (2018), 10.1103/physrevx.8.011008.
- [217] R. J. McQueeney, Y. Petrov, T. Egami, M. Yethiraj, G. Shirane, and Y. Endoh, *Physical Review Letters* **82**, 628 (1999).
- [218] H. Uchiyama, A. Q. R. Baron, S. Tsutsui, Y. Tanaka, W.-Z. Hu, A. Yamamoto, S. Tajima, and Y. Endoh, *Physical Review Letters* **92** (2004), 10.1103/physrevlett.92.197005.
- [219] D. Reznik, T. Fukuda, D. Lamago, A. Baron, S. Tsutsui, M. Fujita, and K. Yamada, *Journal of Physics and Chemistry of Solids* **69**, 3103 (2008).
- [220] J. Graf, M. d’Astuto, C. Jozwiak, D. R. Garcia, N. L. Saini, M. Krisch, K. Ikeuchi, A. Q. R. Baron, H. Eisaki, and A. Lanzara, *Physical Review Letters* **100** (2008), 10.1103/physrevlett.100.227002.
- [221] M. d’Astuto, G. Dhalenne, J. Graf, M. Hoesch, P. Giura, M. Krisch, P. Berthet, A. Lanzara, and A. Shukla, *Physical Review B* **78** (2008), 10.1103/physrevb.78.140511.
- [222] A. Q. Baron, J. P. Sutter, S. Tsutsui, H. Uchiyama, T. Masui, S. Tajima, R. Heid, and K.-P. Bohnen, *Journal of Physics and Chemistry of Solids* **69**, 3100 (2008).
- [223] M. Raichle, D. Reznik, D. Lamago, R. Heid, Y. Li, M. Bakr, C. Ulrich, V. Hinkov, K. Hradil, C. T. Lin, and B. Keimer, *Physical Review Letters* **107** (2011), 10.1103/physrevlett.107.177004.
- [224] J. E. Lorenzo, R. Currat, P. Monceau, B. Hennion, H. Berger, and F. Levy, *Journal of Physics: Condensed Matter* **10**, 5039 (1998).
- [225] H. Requardt, J. E. Lorenzo, P. Monceau, R. Currat, and M. Krisch, *Physical Review B* **66** (2002), 10.1103/physrevb.66.214303.



- [226] P. Lee, T. Rice, and P. Anderson, *Solid State Communications* **88**, 1001 (1993).
- [227] Y. Wang and A. Chubukov, *Physical Review B* **90**, 2113 (2014).
- [228] D. Chowdhury and S. Sachdev, *Phys. Rev. B* **90**, 134516 (2014).
- [229] E. H. da Silva Neto, P. Aynajian, A. Frano, R. Comin, E. Schierle, E. Weschke, A. Gyenis, J. Wen, J. Schneeloch, Z. Xu, S. Ono, G. Gu, M. Le Tacon, and A. Yazdani, *Science* **343**, 393 (2014).
- [230] R. Comin, A. Frano, M. M. Yee, Y. Yoshida, H. Eisaki, E. Schierle, E. Weschke, R. Sutarto, F. He, A. Soumyanarayanan, Y. He, M. Le Tacon, I. S. Elfimov, J. E. Hoffman, G. A. Sawatzky, B. Keimer, and A. Damascelli, *Science* **343**, 390 (2014).
- [231] J. D. Axe and G. Shirane, *Physical Review B* **8**, 1965 (1973).
- [232] D. Reznik, *Physica C: Superconductivity* **481**, 75 (2012).
- [233] A. V. Chubukov, M. R. Norman, A. J. Millis, and E. Abrahams, *Physical Review B* **76** (2007), 10.1103/physrevb.76.180501.
- [234] A. Kanigel, M. R. Norman, M. Randeria, U. Chatterjee, S. Souma, A. Kaminski, H. M. Fretwell, S. Rosenkranz, M. Shi, T. Sato, T. Takahashi, Z. Z. Li, H. Raffy, K. Kadowaki, D. Hinks, L. Ozyuzer, and J. C. Campuzano, *Nature Physics* **2**, 447 (2006).
- [235] C. M. Varma, P. B. Littlewood, S. Schmitt-Rink, E. Abrahams, and A. E. Ruckenstein, *Phys. Rev. Lett.* **63**, 1996 (1989).
- [236] Y. Cao, D. Chowdhury, D. Rodan-Legrain, O. Rubies-Bigorda, K. Watanabe, T. Taniguchi, T. Senthil, and P. Jarillo-Herrero, *Physical Review Letters* **124**, 076801 (2020).
- [237] G. R. Stewart, *Rev. Mod. Phys.* **73**, 797 (2001).
- [238] A. Rost, S. A. Grigera, J. Bruin, R. Perry, D. Tian, S. Raghu, S. A. Kivelson, and A. Mackenzie, *Proceedings of the National Academy of Sciences* **108**, 16549 (2011).
- [239] R. Cooper, Y. Wang, B. Vignolle, O. Lipscombe, S. Hayden, Y. Tanabe, T. Adachi, Y. Koike, M. Nohara, H. Takagi, *et al.*, *Science* **323**, 603 (2009).
- [240] S. Martin, A. T. Fiory, R. M. Fleming, L. F. Schneemeyer, and J. V. Waszczak, *Phys. Rev. B* **41**, 846 (1990).
- [241] N. E. Hussey, *J. Phys. Condens. Matter* **20**, 123201 (2008).
- [242] F. Rullier-Albenque, H. Alloul, C. Proust, P. Lejay, A. Forget, and D. Colson, *Phys. Rev. Lett.* **99**, 027003 (2007).
- [243] D. Van Der Marel, H. Molegraaf, J. Zaanen, Z. Nussinov, F. Carbone, A. Damascelli, H. Eisaki, M. Greven, P. Kes, and M. Li, *Nature* **425**, 271 (2003).
- [244] J. Zaanen *et al.*, *SciPost Phys* **6**, 061 (2019).
- [245] T. Shibauchi, A. Carrington, and Y. Matsuda, *Annual Review of Condensed Matter Physics* **5**, 113 (2014).

- [246] B. Shen, Y. Zhang, Y. Komijani, M. Nicklas, R. Borth, A. Wang, Y. Chen, Z. Nie, R. Li, X. Lu, H. Lee, M. Smidman, F. Steglich, P. Coleman, and H. Yuan, *Nature* **579**, 51 (2020).
- [247] A. P. Mackenzie, S. R. Julian, D. C. Sinclair, and C. T. Lin, *Physical Review B* **53**, 5848 (1996).
- [248] M. Hashimoto, T. Yoshida, K. Tanaka, A. Fujimori, M. Okusawa, S. Wakimoto, K. Yamada, T. Kakeshita, H. Eisaki, and S. Uchida, *Physical Review B* **79**, 140502 (2009).
- [249] S.-D. Chen, M. Hashimoto, Y. He, D. Song, K.-J. Xu, J.-F. He, T. P. Devereaux, H. Eisaki, D.-H. Lu, J. Zaanen, *et al.*, *Science* **366**, 1099 (2019).
- [250] C. Putzke, S. Benhabib, W. Tabis, J. Ayres, Z. Wang, L. Malone, S. Licciardello, J. Lu, T. Kondo, T. Takeuchi, N. E. Hussey, J. R. Cooper, and A. Carrington, *Nature Physics* **17**, 826 (2021).
- [251] D. Pelc, M. J. Veit, C. J. Dorow, Y. Ge, N. Barišić, and M. Greven, *Phys. Rev. B* **102**, 075114 (2020).
- [252] P. Giraldo-Gallo, J. Galvis, Z. Stegen, K. A. Modic, F. Balakirev, J. Betts, X. Lian, C. Moir, S. Riggs, J. Wu, *et al.*, *Science* **361**, 479 (2018).
- [253] J. Ayres, M. Berben, M. Culo, Y. T. Hsu, E. van Heumen, Y. Huang, J. Zaanen, T. Kondo, T. Takeuchi, J. R. Cooper, C. Putzke, S. Friedemann, A. Carrington, and N. E. Hussey, (2020), [arXiv:2012.01208 \[cond-mat.str-el\]](https://arxiv.org/abs/2012.01208) .
- [254] T. Sarkar, P. Mandal, N. Poniatowski, M. K. Chan, and R. L. Greene, *Science advances* **5**, eaav6753 (2019).
- [255] S. Licciardello, N. Maksimovic, J. Ayres, J. Buhot, M. Čulo, B. Bryant, S. Kasahara, Y. Matsuda, T. Shibauchi, V. Nagarajan, J. G. Analytis, and N. E. Hussey, *Phys. Rev. Research* **1**, 023011 (2019).
- [256] I. M. Hayes, R. D. McDonald, N. P. Breznay, T. Helm, P. J. Moll, M. Wartenbe, A. Shekhter, and J. G. Analytis, *Nature Physics* **12**, 916 (2016).
- [257] J. Clayhold, N. P. Ong, Z. Wang, J. Tarascon, and P. Barboux, *Physical Review B* **39**, 7324 (1989).
- [258] T. Manako, Y. Kubo, and Y. Shimakawa, *Physical Review B* **46**, 11019 (1992).
- [259] N. Barišić, M. Chan, M. Veit, C. Dorow, Y. Ge, Y. Li, W. Tabis, Y. Tang, G. Yu, X. Zhao, *et al.*, *New Journal of Physics* **21**, 113007 (2019).
- [260] P. W. Anderson, *Phys. Rev. Lett.* **67**, 2092 (1991).
- [261] P. A. Casey and P. W. Anderson, *Phys. Rev. Lett.* **106**, 097002 (2011).
- [262] P. Coleman, A. J. Schofield, and A. M. Tsvelik, *Phys. Rev. Lett.* **76**, 1324 (1996).
- [263] E. Abrahams and C. M. Varma, *Phys. Rev. B* **68**, 094502 (2003).
- [264] J. Kokalj and R. H. McKenzie, *Phys. Rev. Lett.* **107**, 147001 (2011).

- [265] J. Kokalj, N. E. Hussey, and R. H. McKenzie, *Phys. Rev. B* **86**, 045132 (2012).
- [266] N. Hussey, H. Gordon-Moys, J. Kokalj, and R. McKenzie, in *J Phys Conf Ser*, Vol. 449 (2013) p. 012004.
- [267] N. Hussey, M. Abdel-Jawad, A. Carrington, A. Mackenzie, and L. Balicas, *Nature* **425**, 814 (2003).
- [268] A. Tsvelik, *Physical Review B* **95**, 201112 (2017).
- [269] L. Classen, N. J. Robinson, and A. M. Tsvelik, *Physical Review B* **99**, 115110 (2019).
- [270] T. M. Rice, N. J. Robinson, and A. M. Tsvelik, *Physical Review B* **96**, 220502 (2017).
- [271] S. A. Hartnoll, A. Lucas, and S. Sachdev, *Holographic quantum matter* (MIT press, 2018).
- [272] T. Faulkner, N. Iqbal, H. Liu, J. McGreevy, and D. Vegh, *Science* **329**, 1043 (2010).
- [273] S. A. Hartnoll, *Nature Physics* **11**, 54 (2015).
- [274] M. Blake and A. Donos, *Physical review letters* **114**, 021601 (2015).
- [275] R. A. Davison, K. Schalm, and J. Zaanen, *Phys. Rev. B* **89**, 245116 (2014).
- [276] A. Amoretti, D. Areán, B. Goutéraux, and D. Musso, *Physical Review Letters* **123**, 211602 (2019).
- [277] X. Wu, X. Chen, C.-M. Jian, Y.-Z. You, and C. Xu, *Physical Review B* **98**, 165117 (2018).
- [278] A. A. Patel, J. McGreevy, D. P. Arovas, and S. Sachdev, *Physical Review X* **8**, 021049 (2018).
- [279] D. Chowdhury and E. Berg, *Phys. Rev. Research* **2**, 013301 (2020).
- [280] I. Paul, C. Pépin, and M. R. Norman, *Phys. Rev. Lett.* **110**, 066402 (2013).
- [281] J. Merino and R. H. McKenzie, *Phys. Rev. B* **61**, 7996 (2000).
- [282] E. W. Huang, R. Sheppard, B. Moritz, and T. P. Devereaux, *Science* **366**, 987 (2019).
- [283] Y. Wang, S. D. Edkins, M. H. Hamidian, J. C. S. Davis, E. Fradkin, and S. A. Kivelson, *Phys. Rev. B* **97**, 174510 (2018).
- [284] A. Banerjee, A. Ferraz, and C. Pépin, (2021), [arXiv:2104.14606 \[cond-mat.supr-con\]](https://arxiv.org/abs/2104.14606) .
- [285] S.-S. Lee, *Annual Review of Condensed Matter Physics* **9**, 227 (2018).
- [286] V. S. de Carvalho, T. Kloss, X. Montiel, H. Freire, and C. Pépin, *Phys. Rev. B* **92**, 075123 (2015).
- [287] K. Wakabayashi, K. ichi Sasaki, T. Nakanishi, and T. Enoki, *Science and Technology of Advanced Materials* **11**, 054504 (2010).
- [288] A. K. Geim and K. S. Novoselov, *Nature Materials* **6**, 183 (2007).
- [289] E. V. Castro, N. Peres, and J. Lopes dos Santos, *EPL (Europhysics Letters)* **84**, 17001 (2008).

- [290] V. Kaladzhyan, S. Pinon, F. Joucken, Z. Ge, E. A. Quezada-Lopez, T. Taniguchi, K. Watanabe, J. V. J. au2, and C. Bena, (2021), [arXiv:2105.08723 \[cond-mat.mes-hall\]](#) .
- [291] M. Grandadam, S. Pinon, C. Bena, and C. Pepin, (2021), [arXiv:2106.15627 \[cond-mat.mes-hall\]](#) .
- [292] D. Pierucci, H. Sediri, M. Hajlaoui, J.-C. Girard, T. Brumme, M. Calandra, E. Velez-Fort, G. Patriarche, M. G. Silly, G. Ferro, V. Soulière, M. Marangolo, F. Sirotti, F. Mauri, and A. Ouerghi, *ACS Nano* **9**, 5432 (2015).
- [293] A. Yacoby, *Nature Phys* **7**, 925 (2011).
- [294] I. Martin, Y. M. Blanter, and A. F. Morpurgo, *Phys. Rev. Lett.* **100**, 036804 (2008).
- [295] L.-J. Yin, H. Jiang, J.-B. Qiao, and L. He, *Nat. Comm.* **7**, 11760 (2016).
- [296] A. Vaezi, Y. Liang, D. H. Ngai, L. Yang, and E.-A. Kim, *Phys. Rev. X* **3**, 021018 (2013).
- [297] F. Zhang, A. H. MacDonald, and E. J. Mele, *Proceedings of the National Academy of Sciences* **110**, 10546–10551 (2013).
- [298] J. Jung, F. Zhang, Z. Qiao, and A. H. MacDonald, *Phys. Rev. B* **84**, 075418 (2011).
- [299] N. B. Kopnin, T. T. Heikkilä, and G. E. Volovik, *Physical Review B* **83** (2011), [10.1103/physrevb.83.220503](#).
- [300] M. H. Gerlach, Y. Schattner, E. Berg, and S. Trebst, *Physical Review B* **95**, 035124 (2017).